NUCLEAR SPIN TRANSFER STUDIES OF CHEMICAL REACTIONS IN LIVING SYSTEMS

by

Eric W. McFarland

B.S. (1980), M.S. (1982) University of California, Berkeley

SUBMITTED TO THE DEPARTMENT OF HEALTH SCIENCES AND TECHNOLOGY IN PARTIAL FULFILLMENT OF THE REQUIREMENTS FOR THE DEGREE OF

DOCTOR OF PHILOSOPHY IN

MEDICAL ENGINEERING

at the

MASSACHUSETTS INSTITUTE OF TECHNOLOGY

April 1987

Signature of Author _____
Department of Health Sciences and Technology
April 15, 1987

Certified by _____
Martin J. Kushmerick, M.D.,Ph.D.
Thesis Supervisor

Accepted by _____
Roger G. Mark, M.D.,Ph.D.
Chairman, Departmental Graduate Committee

Nuclear Spin Transfer Studies of Chemical Reactions
in Living Systems

by

Eric W. McFarland

Submitted to the Department of Health Sciences and Technology on April 15, 1987 in partial fulfillment of the requirements for the degree of DOCTOR OF PHILOSOPHY IN MEDICAL ENGINEERING.

Abstract

Non-invasive nuclear magnetic resonance (NMR) spin transfer techniques were applied *in vivo* to study chemical reaction rates. Previous studies typically modeled *in vivo* reactions as simple two site systems with only chemical exchange acting to influence the spin states. In complex biological systems there is evidence that heteronuclear and homonuclear dipolar coupling occurs as well as physical or physiological separation of reacting systems into compartments. In addition, multiple site exchange is likely in most pathways. These effects on the NMR determined flux were analyzed and found to introduce significant technique dependent errors. A transient spin labeling method was used that minimizes the errors and gives reliable quantitative unidirectional exchange fluxes.

Creatine kinase (CK) catalyzes the ^{31}P exchange between phosphocreatine, PCr, and ATP. The CK reaction can be used to calculate the micromolar quantities of ADP in mammalian muscle if the reaction can be shown to be in equilibrium. ^{31}P NMR studies of the molecular flux (PCr -->ATP) through CK have been performed by several groups with conflicting results that challenge the conventional role of CK in muscle and suggest that the reaction may not be in equilibrium. The blood perfused cat soleus was studied at rest and under graded levels of steady-state stimulation designed to increase total cellular ATPase activities more than 10-fold. 1)The forward and reverse fluxes were found to be equal. 2)The [ATP] was found to remain constant throughout the range of electrical stimulations, [PCr] declined and [Pi] increased stoichiometrically to steady-state levels that depended on the stimulation rate. 3)The NMR derived rate constant, which is a measure of the ratio of unidirectional chemical flux to NMR visible substrate concentration, increased with stimulation; however, the flux was found to remain constant. This

result is contrary to reports where the CK flux was found to vary significantly with small changes in ATPase activity and PCr/ATP in heart and amphibian muscle. These results exclude the kind of requisite functional coupling between mitochondria and the myofibrills implied by the 'PCr shuttle' model, but are completely consistent with the properties expected of CK in a homogeneous solution. Resting [ADP] was calculated from the CK equilibrium to be 15uM at rest, rising to above 140uM with stimulation. If the myokinase reaction is assumed to be near equilibrium, [AMP] will be less than 0.1 uM in the resting soleus. These low levels have important regulatory implications for metabolic pathways.

Finally, a method was developed to spatially encode reaction kinetic information and produce NMR images sensitive to chemical exchange. Microscopic images were produced reflecting chemical exchange as a function of spatial position. These images demonstrate a means of investigating kinetic heterogeneity and compartmentation of reactions that occur in both living and non-living systems.

Thesis Supervisor: Martin J. Kushmerick, M.D.,Ph.D.
Title: Director NMR Research, Brigham and Women's Hospital, Associate Professor of Physiology and Biophysics, Department of Radiology, Harvard Medical School

Acknowledgments

This project would not have been completed without the help of several colleagues and members of the Francis Bitter National Magnet Laboratory support staff. I thank Dr. Leo Neuringer for his support and encouragement throughout the project and his review and comments of this text. Dr. Tim Moerland and Dr. Joseph Krisanda were essential to the success of the perfused soleus preparation. I am grateful to Dr. David Ruben for his software expertise, Dr. Gary Zientara for help with image processing, Vincent Carabillo for electronics advice, and Paul Sassone for his skill in probe fabrication. I am also grateful to Dr. Mirko Hrovat for many thought provoking late-night discussions. The careful reviewing of this manuscript by Dr. David Holtzman, Dr. Bruce Rosen, and Dr. Jason Koutcher was appreciated. Finally, I sincerely appreciate the advice, encouragement, and surgical skill of my advisor Dr. Martin Kushmerick.

Financial support for this project was provided in part by 1) Harvard-MIT Division of Health Sciences and Technology Medical Engineering-Medical Physics Fellowship Program. 2) Young Men's Philanthropic League. 3) Department of Radiology, Harvard Medical School. 4) National Institute of Health grant, RR-00995, 5) Field Effects Inc., Acton, MA., 6) Muscular Dystrophy Association.

Table of Contents

List of Symbols and Abbreviations

Chemical flux, (moles-sec^{-1}).	γ
Magnetization flux, (sec^{-1}).	ψ
Ratio of chemical exchage rate to relaxation = k*T_1.	α
Adenosine diphosphate.	ADP
Adenylate kinase.	AK
Adenosine triphosphate.	ATP
Vector field produced by conductor carrying a unit current.	B/i
Spin flip angle, (radians).	β
Magnetic field produced by conductor carrying a unit current.	B/i
Bovine serum albumin.	BSA
Autocorrelation function.	C(t)
Chemical exchange magnetic resonance imaging.	CHEMI
Creatine phosphokinase.	CK
Image pixel intensity.	D(r)
Dithiothrietol.	DTT
Ethylenediamine tetraacetate.	EDTA
Free induction decay.	FID
Filling factor.	ff
Magnetic field gradient, (Gauss/cm).	G
Gyromagnetic ratio, (Khz/Gauss).	γ
Gibb's free energy, (KJ/mole).	ΔG
Gibb's function determined at 25°C, 1 atm,(KJ/mole).	ΔG_o
Static magnetic field strength, (Tesla).	H_o
Time varying magnetic field strength, (Tesla).	H_1
Planck's constant, 6.626 x 10^{-34} Joule-sec.	h
nuclear angular momentum.	J
Chemical equilbrium constant.	K
Geometric coupling constant for magnetic flux linkage.	κ
Ratio of chemical flux, to chemical concentration, (sec^{-1}).	k_{ij}
Inductance, (henry).	L
Equilibrium longitudinal magnetization of species i.	M_{i_o}
Net magnetization of species i.	M_i
Morpholinopropane/sulfonic acid.	MOP's
Nuclear dipole moment.	μ
Nicotinamide adenine dinucleotide.	NAD
Nicotinamide adenine dinucleotide, reduced form.	NADH
Nuclear Magnetic Resonance.	NMR

Nuclear Overhauser Effect.	NOE
Phosphocreatine.	PCr
1,4-Piperazinediethane sulfonic acid	PIPES
Phosphorylation potential, [ATP]/([ADP][Pi]).	pp
Phenylphosphonic acid.	PPA
Parts per million.	ppm
Nuclear spin density, (nuclei/vol).	ρ
Quality factor of r.f. coil loaded, Q_l, and unloaded, Q_o.	Q
Spatial coordinate.	r
Lattice relaxation rate for nuclear species i, $1/T_1$, (sec^{-1}).	R_i
Resistance, (ohms).	R
Radiofrequency.	r.f.
Recycle delay, time between pulses (sec).	RD
Nuclear magnetic resonance signal, S(t), S(w).	S
Standard error.	SE
Steady-state saturation transfer experiment, type A.	SSA
Steady-state saturation transfer experiment, type B.	SSB
Dipolar coupling constant between M_i and M_j, (sec^{-1}).	σ_{ij}
Signal-to-noise ratio.	SNR
Lattice relaxation time constant, (sec.).	T_1
Spin-spin relaxation time constant, (sec.).	T_2
Spin echo delay time (msec).	T_E
Repeat time = RD.	T_R
Volume.	V
Molecular oxygen consumption.	V_{O_2}
Frequency, (hertz).	ω
Chemical species i.	X_i

CHAPTER 1:
INTRODUCTION

1.1 Motivation

The usual assumption linking *in vitro* biochemistry to cellular biology is that chemical reactions in cells can be reproduced *in vitro*. It is often taken for granted that living systems behave as well mixed solutions because, for lack of a satisfactory measurement technique, this hypothesis has remained untested. Recently, nuclear magnetic resonance (NMR) has evolved from an *in vitro* analytical chemistry tool to an exciting method for studying biochemistry non-invasively in living tissue. Compounds containing phosphorus (^{31}P) are especially suited to NMR investigations. Phosphoenergetic studies of intact muscle have produced several important results characterizing changes in the relative levels of key ^{31}P containing metabolites during physiological perturbations (58,22,93,25,109).

The molecular flux through specialized biochemical pathways can be obtained using NMR by "labeling" the magnetization of a substrate and observing the transfer of the labeled magnetization to the product (spin transfer). It is possible to obtain dynamic physical chemical information concerning the maintenance of steady-state and functional relationships between the fluxes and function. Studies measuring the molecular flux of the creatine phosphokinase (CK) catalyzed phosphoryl transfer between adenosine triphosphate (ATP) and phosphocreatine (PCr) have received the greatest attention (43,103,93,88,2).

Interest in the CK reaction stems from its central role in maintenance of

nearly constant levels of ATP in excitable tissue and the ability to calculate the NMR invisible ADP levels from the CK equilibrium. That the CK catalyzed exchange is one of the few reactions observable in living cells by NMR is also likely responsible for the large number of studies. Unfortunately, rates of exchange published by several groups measured in identical preparations of perfused heart muscle show tremendous variation; conclusions, based on these data, challenging the classical role of creatine kinase are controversial. Additionally, several studies have questioned the equilibrium of the CK exchange thereby invalidating calculations of intracellular ADP (43,103,2,13,14,97). The failure of previous investigations to accurately characterize, in living muscle, the chemical exchange between ATP and PCr; and the need for accurate flux information to define the role of CK in muscle and study the influence of its substrates on oxidative metabolism, has stimulated this research.

Essential to meaningful interpretation of NMR spin transfer kinetic data is: a) a correct mathematical description of the chemical system. b) a complete account of all nuclear spin interactions, and c) consideration of the fundamental limits of sensitivity of the NMR technique. Drawing on the history of success of *in vitro* NMR rate measurements, physiologists and biochemists have applied NMR to living tissue and interpreted data based on oversimplified models. The most obvious complication characteristic of most tissue is macroscopic heterogeneity of cell type that prevents understanding of cellular level processes.

The data obtained from intact tissue consists of a global average of the many fundamentally and functionally different cell types composing muscle and other organs. Unfortunately, NMR measurements of chemical species at the millimolar concentrations characteristic of most metabolites have intrinsically low signal-to-noise ratios (SNR's). Reliably fitting this data to complicated models is

problematic. Conflicting data is often attributed to mysterious "NMR invisible pools" or ill-defined "functional metabolic compartments." The potential for nuclear interactions in enzymatic reactions that transfer spin without chemical exchange has also been ignored. Specifically, dipolar interactions, commonly encountered in biochemical studies, have not been included in tissue models. This study begins by extending the early work to include a more realistic account of the complex interactions likely to be present in physiological NMR spin transfer studies. Realizing that a complete biochemical and physical description of the system is unlikely, a specific protocol for molecular flux measurements is described in Chapter 3 that has a minimal dependency on the details of a model. The technique is calibrated and applied in Chapter 4 to the kinetics of CK in stimulated skeletal muscle. Finally, to address the issue of tissue heterogeneity a method of obtaining microscopically resolved chemical flux information and thereby producing a chemical exchange image is proposed in Chapter 5.

1.2 NMR Applications to Mammalian Muscle Phosphoenergetics

Chemomechanical conversion of chemical potential energy to work in muscle occurs over a large dynamic range of chemical activity. Mammalian skeletal muscle energy utilization can transiently increase nearly a hundredfold between the resting and stimulated state. Maintenance of a high rate of energy usage requires regulation of oxidative metabolism to provide adequate chemical potential energy in the form of high-energy phosphate compounds, ATP, and PCr. Transfer, addition, or hydrolysis of phosphate groups on these molecules are the basic reactions of cellular energetics. Cells can modulate the extent of storage or expenditure of energy by variation of the free energy of ATP hydrolysis. At a given pH:

(1.1) $\Delta G = \Delta G^{o} - RT^{*}\{ \ln([ATP]) - \ln([ADP]^{*}[Pi]) \}$

The sensitivity of ΔG, and the phosphorylation potential {PP= [ATP]/([ADP][Pi])}, to intracellular content has been well established *in vitro* (80). Quantification of [ATP], [ADP], and Pi levels following metabolic excursions allows the determination of ΔG and provides a measure of cellular energy status.

Examination of the living system is essential to test the relationship between the *in vitro* and the *in vivo* state. Experimental procedures designed to measure conditions *in vivo* rely on rapid fixation and freezing. The inability of these techniques to adequately preserve the levels of key metabolic control variable(s), ADP, Pi, and NAD/NADH among others, is documented (1,82) and has led to the development of non-invasive techniques for intracellular metabolic monitoring.

In the 1970's NMR was applied *in vivo* and shown to provide a unique, albeit limited, opportunity for metabolic studies (58). The NMR visible isotope ^{31}P accounts for 100% of the naturally occurring phosphorus and allows unique visualization of the relative concentrations of ATP, PCR, Pi, and in certain preparations a number of other metabolically important compounds, for example; phosphoethanolamine, glycerolphosphocholine, and ribose phosphate. Studies to date have generally been directed toward measurement of relative metabolite levels following physiological perturbation.

An enormous fund of literature has developed with results of NMR studies quantifying ^{31}P containing compounds in different organs under a variety of conditions. These studies have provided a few unexpected observations of phosphate metabolite concentrations that have yet to be adequately explained. Non-NMR studies had previously set [ADP] in the range of 500-1000 uM (111).

Because ADP in resting muscle cannot be directly measured by NMR, its concentration is thought to be below 100 micromolar (uM). Inorganic phosphate (Pi) levels in properly perfused tissue and intact organs were found to be significantly lower than the levels predicted from freeze clamping experiments (1). Both of these compounds are thought to have important regulatory functions and, perhaps more importantly, their levels allow precise calculation of ΔG for ATP hydrolysis within the cytoplasm. Together, the overestimates of Pi and ADP have led to calculated values of the cellular phosphorylation potential and ΔG of ATP hydrolysis, Equation 1.1, that underestimated the energy potential of muscle.

The *in vitro* enzymatic studies of the phosphate converting enzymes, creatine kinase and actomyosin ATPase, show marked sensitivity of catalytic activity to experimental conditions (124,29). Accurate reproduction of intracellular conditions or substrate levels is not possible, thus the value of *in vitro* studies in predicting *in vivo* reaction dynamics is unknown and the role of the many possible controlling substances equivocal. Considerable effort is presently focused on accurate *in vivo* determination of cellular enzyme kinetics.

Under certain conditions, NMR can be used to measure unidirectional molecular exchange fluxes. Together with the NMR determined metabolite concentrations, flux determinations allow the study of reaction dynamics. Recently, the effects of chemical exchange on the NMR signal have been exploited *in vivo* (43,5). In ^{31}P NMR the importance of chemical exchange cannot be understated. In Figure 1.1 a typical ^{31}P spectra is shown from a perfused soleus preparation as described in Chapter 4. All compounds with visible resonances exhibit exchange phenomena that dramatically affect the characteristics of the spectrum. Downfield the Pi resonance is located at a frequency dependent on the pH of the intracellular milieu as described in the first ^{31}P study of living cells (99).

The Pi resonance frequency is the weighted average of the two distinct frequencies of the ^{31}P's in the conjugate acid-base pair $H_2PO_4^{-1}$ and HPO_4^{-2} in "fast" proton exchange. Measurement of the Pi resonance provides a non-invasive measure of intracellular pH.

The resonances due to γ, and β ATP phosphates are in "fast and "intermediate" exchange with the divalent cation magnesium, (Mg^{++}). The NMR observation of the chemical exchange between the ATP and Mg++ allows the determination of a lower limit for skeletal muscle intracellular [Mg^{++}] of 0.5mM. At this concentration over 93% of cellular ATP is in the form of an ATP-Mg complex, which is the true substrate of many ATP utilizing reactions (80).

The ATP resonances illustrate that "speed" of the exchange is relative to the ratio of the resonance frequency difference between the product and reactant, (ω_1 - ω_2), and the characteristic rate constant k_{12}, which is inversely proportional to the lifetime of state 1. If $(\omega_1 - \omega_2)/k_{12} >> 1$ the exchange is said to be "slow" and two peaks at ω_1 and ω_2 will be seen. If $(\omega_1 - \omega_2)/k_{12} << 1$, then the exchange is "fast," and one peak is observed at a frequency that reflects a weighted average of ω_1 and ω_2. The broader β-ATP resonance is in the intermediate range where the single peak of fast exchange is increased in width. At slower exchange rates the peak broadens out and separates into two relatively long-lived species at ω_1 and ω_2 (slow exchange).

The γ-ATP phosphate is involved additionally in "slow" exchange with the PCr resonance through CK. Competing reactions involving the γ-P of ATP must be considered in some cells and include the Pi transfer through cellular ATPase's (120) and ADP ^{31}P exchange through adenylate kinase (AK) (21). If the near equilibrium condition for CK and AK reactions can be established, indirect monitoring of the NMR invisible species ADP and AMP is possible using the corresponding

equilibrium relationships.

Accurate measurements of ATP <--> PCr exchange rates are necessary to establish the validity of the near equilibrium assumption and to compare the properties of the enzyme *in vitro* to those observed *in vivo*. NMR kinetic measurements will also provide evidence of linkage between CK flux and ATPase activity, which is an issue in the identification of the role of PCr in muscle. Though only a limited number of reactions can be studied, spin transfer can provide thermodynamic and flux information *in vivo* which is unique and important.

When the correct model of the chemical exchange is known, additional information can be obtained by perturbing the metabolite levels, pH, and temperature of the system. Variations in the NMR determined flux can be ascribed to metabolite changes and/or variations in the catalytic activity of the enzyme itself. In the studies outlined in Chapter 4 phosphoryl transfer through CK in mammalian slow-twitch muscle was examined. A variety of system stresses were applied to confirm that the enzyme dynamics in the integrated living system were identical to those found *in vitro*.

The expectations of the quality of NMR spin transfer data should be tempered by the difficulty in obtaining high accuracy from a fundamentally insensitive measurement technique. Determination of realistic *in vivo* resolution limits and optimized methods of data collection was an additional goal of this research.

1.3 Background Principles

The phenomena of nuclear magnetic resonance was predicted and observed more than 40 years ago (46,15,16,108). Initially a probe of nuclear structure, the spectroscopic method has since been used for such diverse studies as oil exploration, flow quantification, thermography, chemical reaction studies, and medical imaging. Well developed classical and quantum descriptions have been published in hundreds of papers and textbooks. The fundamental physics have been worked out, and only expressions useful for extension of the basic theory to exchanging biological systems will be reproduced here.

Used most commonly as an analytical chemistry tool, NMR relies on the magnetic moment, μ, of nuclei with net angular momentum, J. In the presence of a static magnetic field, H_o, allowed spin states are defined with small energy differences proportional to the field strength. For nuclei with spin quantum number 1/2 (including ^1H, ^{31}P) there are two allowed states with an energy level spacing of $\Delta E = \gamma * H_o * h$, where h is Planck's constant. The energy associated with μ is proportional to the field strength and tiny relative to the thermal kinetic energy which works to equilibrate the spin states. At H_o= 1 Tesla (T), $E_{mag}/E_{kin} \sim 10^{-7}$. It is because the energy difference is so small that the NMR technique is relatively insensitive and predominantly limited by the signal-to-noise ratio (SNR). In bulk matter containing nuclei with magnetic moments, the slight difference in populations of the states gives rise to a net polarization, M_o, aligned parallel to H_o at equilibrium. At 25°C 1cc of water has a net magnetic moment of approximately $5x10^{-11}$Joules/Tesla.

Typically, coordinates are assigned with the z axis parallel to H_o. Following perturbation of M_o from its equilibrium orientation, the transient behavior is described by the classical Bloch equations (15,16).

$$\text{a)}\ \dot{M}_z = R^*(M_o - M_z) + \gamma^*(\bar{M} \times \bar{H})_z$$

$$(1.2)\quad \text{b)}\ \dot{M}_x = -M_x/T_2 + \gamma^*(\bar{M} \times \bar{H})_x$$

$$\text{c)}\ \dot{M}_y = -M_y/T_2 + \gamma^*(\bar{M} \times \bar{H})_y$$

Where H is the total external magnetic field composed of H_o and, during excitation, a radiofrequency (r.f.) field, H_1 applied perpendicular to H_o. $R=1/T_1$ and $1/T_2$ refer to environment specific spin-lattice and spin-spin relaxation rates respectively. $H_1(t)$ applied orthogonal to H_o for a short time, t_p (usec), at a frequency, ω, will tip the magnetization, about the axis of H_1, through an angle $\beta=H_1{}^*\gamma^*t_p$. The resonance frequency, ω, is related to nuclear properties and the field strength by, $\omega=\gamma^*H_o$. After the r.f. excitation the component of magnetization parallel to H_o, M_z, will return to equilibrium as :

$$(1.3)\quad M(t) = M_o[1 - (1-\cos(\beta)\exp(-t^*R))]$$

From this "relaxation" behavior the characteristic T_1 of the system can be obtained revealing, in many cases, information about the local chemical environment. It will be shown below how slow chemical exchange will alter this simple behavior allowing extraction of reaction information.

Typically M_z is monitored at time t by nearly instantaneously tipping it into the x-y plane with a 90^o pulse where it precesses about $H_o k$ at its Larmor frequency, ω. A current is induced in a conducting coil surrounding the object by the time varying magnetic field produced by the precessing magnetization. The time varying current is the measured NMR signal, S(t). Fourier transformation of

the signal results in a frequency domain spectrum with an approximately Lorentzian absorption mode (Real) lineshape, S(w). S(w) is the characteristic resonance peak of NMR spectroscopy. From the height or area of the resonance peak obtained from a living system, concentrations of the nuclei can be determined. The metabolite concentrations are related directly to the resonance peaks. Only nuclei within mobile molecules are accounted for in the typical spectrum, and species bound to structural elements (bone ^{31}P) or large macromolecules (phospholipid) will not produce sharp resonance lines. Additionally, ligands (adenosine phosphates) residing on macromolecules (ATPases, actin) for times long compared to the T_2 relaxation time will be undetected. In this most basic application NMR provides a means of non-invasively determining the relative concentrations of mobile metabolites that have unique resonances.

1.4 Chemical Exchange

The first theoretical formulation and practical application of NMR to the study of chemical exchange came less than 8 years after the discovery of the phenomena itself (50). In 1958, Harden McConnell investigated the effects of chemical exchange on the NMR signal and generalized the original Bloch equations to include "spin transfer" between exchanging species (90). Chemical exchange could be monitored either by effects on transverse or longitudinal relaxation. The McConnell equations described the general case and predicted how the effective T_2 or T_1 values would reflect exchange. Gutowski and others focused on transverse magnetization effects and monitored rate constants by the linewidths of the exchanging resonances (51). These "T_2 methods" were most applicable to fast exchange, which is characterized by state lifetimes less than approximately 1 second. At slower rates the linewidth increase due to exchange becomes negligible

compared to the natural linewidth. This limitation is especially important in biological tissue where linewidths are practically limited to 0.05 hertz per megahertz (ppm). That the linewidth quantitatively measured fast exchange was confirmed in several published studies comparing the NMR derived rate constants to those obtained using non-NMR methods (85,52,64).

This study focuses on a second approach, following directly from the McConnell equations, that allows monitoring of "slow" exchange processes by effects on the longitudinal magnetization (z component) of one distinct species, M_i, following perturbation of another, M_j. Several metabolically important reactions have rates falling in the slow range. To date, the most successful applications of NMR rate measurements *in vivo* have been for ^{31}P slow exchange reactions through creatine kinase (43,103,93,88,2) adenylate kinase (21), and arginine kinase (20).

Slow exchange methods can be implemented in two-dimensional schemes, whereby complex, multi-site exchanges can be visualized in complex spectra (10). In systems of few resolvable resonances these methods have been shown to be less efficient than the one-dimensional techniques described below (19).

The original McConnell expressions describing the dynamics of a perturbed spin system undergoing two-site chemical exchange are most commonly used (90). However, a slightly different formalism will be used here to stress the important distinction between the chemical flux, γ_{ij}, from chemical species X_i to species X_j, and the magnetization flux, Ψ_{ij}, from M_i to M_j. The first assumption is that the measured magnetization in a fully relaxed system, M_{i_o}, is proportional to the chemical concentration, $X_i = c^*M_{i_o}$. Also chemical steady-state will be assumed with all X_i's constant in time. The steady-state chemical flux then is related to the magnetization flux by

$$(1.4) \qquad \Psi_{ij_o} = \gamma_{ij} * (M_{i_o}/X_i) = k_{ij} * M_{i_o}$$

The ratio of the true chemical flux to the chemical concentration is a constant for a given steady-state system. This ratio will be referred to as the NMR derived rate constant, $k_{ij}=\gamma_{ij}/X_i$. k is only a constant with respect to magnetization; perturbation of the spins has no effect on the chemistry. Note that nothing has been implied about the reaction mechanism and that k will not necessarily be constant for different steady-state conditions where γ_{ij} and X_i may take on different values.

Following perturbation, the magnetization of species i may be reduced from its equilibrium value, M_{i_o} to M_i. Though the chemical flux. γ, remains unchanged the magnetization flux is reduced by

$$(1.5) \qquad \Psi_{ij} = \Psi_{ij_o} * (M_i/M_{i_o}) = k_{ij} * M_i$$

Ψ_{ij} is still related to the chemical flux through k_{ij} and the equilibrium magnetization, M_{i_o}.

The original modified Bloch equations described the balance of magnetization flux to and from species i through exchange together with the restoration of equilibrium through relaxation (90).

$$(1.6a) \qquad dM_i/dt = R_i(M_{i_o} - M_i) - M_i * k_{ij} + M_j * k_{ji}$$

$$(1.6b) \qquad dM_j/dt = R_j(M_{j_o} - M_j) - M_j{*}k_{ji} + M_i{*}k_{ij}$$

The conditions for slow chemical exchange to be measurable by NMR spin transfer are:

1) At least one product and one reactant have NMR distinguishable resonances. This requires a minimum species lifetime $\tau = 1/k > 1/(\omega_1 - \omega_2)$.

2) The ratio of τ/T_1 should be approximately 1. The slowest reactions measurable will depend on T_1. Systems with state lifetimes much longer than T_1 will not be practically measurable.

The NMR derived rate constant k_{ij} is often referred to as the "pseudo" first-order rate constant because of the units (sec^{-1}). For many reactions this seemingly simple constant masks the actual higher order rate constant and the details of the enzymatic reaction since it simply reflects the steady-state chemical flux per unit NMR visible substrate. k_{ij} often contains a dependency on NMR invisible substances and contributions from non-exchange effects. In Chapter 2 this limitation is addressed together with the theoretical and practical efficiencies of NMR kinetic experiments.

The two-site model was later extended to describe n-site exchange (116,45). In addition to chemical exchange and lattice relaxation, dipolar coupling is a significant mechanism of transferring magnetization. To include homonuclear and heteronuclear dipolar coupling in exchanging systems, the modified Bloch equations can be further generalized to include the important cross relaxation between spins, σ_{ij}. Other treatments have lumped exchange and dipolar interactions into a single cross-relaxation effect (102); however, it is useful to separate the processes to use

the results to test specific system models. The time dependence of M_z for the ith species is given by

$$(1.7) \qquad M_i=[R_i+ \sum_j(\psi_{ij_o}/M_{i_o})]*(M_{i_o}-M_i) -- \sum_j[((\psi_{ji_o}/M_{j_o})-\sigma_{ji})*(M_{j_o}-M_j)]$$

or in compact form

$$(1.8) \qquad \dot{M} = \bar{A} * \overline{(M_o - M)} \qquad \text{or}$$

$$(1.9) \qquad \begin{vmatrix} \dot{M}_1 \\ \dot{M}_2 \\ \dot{M}_3 \\ \\ \\ \\ \dot{M}_n \end{vmatrix} = \begin{vmatrix} R_1+\sum k_{ij} & \sigma_{21}-k_{21} & \sigma_{31}-k_{31} & \cdots & \sigma_{n1}-k_{n1} \\ \sigma_{12}-k_{12} & R_2+\sum k_{ij} & & & \cdot \\ \sigma_{13}-k_{13} & \sigma_{23}-k_{23} & R_3+\sum k_{ij} & \cdot & \cdot \\ \cdot & & & & \\ \cdot & & & & \\ \cdot & & & & \\ \sigma_{1n}-k_{1n} & \cdots \sigma_{2n}-k_{2n} & \cdots & \cdot & R_n+\sum k_{nj} \end{vmatrix} \begin{vmatrix} M_{1_o}-M_1 \\ M_{2_o}-M_2 \\ M_{3_o}-M_3 \\ \\ \\ \\ M_{n_o}-M_n \end{vmatrix}$$

where

$$(1.10) \qquad k_{ij} = \psi_{ij_o}/M_{i_o}$$

Now A is not symmetric and is not necessarily diagonalizable. However there are special cases of biochemical importance where the system of equations can be solved or at least simplified. If equilibrium is assumed for all exchanges throughout the system $M_{i_o}*k_{ij} = M_{j_o}*k_{ji}$ and the cross relaxation terms are related by the relationship $\sigma_{ij}*M_{i_o} = \sigma_{ji}*M_{j_o}$. A becomes symmetric and can be diagonalized.

The real eigenfunctions can then be readily obtained. The well-known solution has the form:

$$(1.11) \qquad \overline{(M_o - M)} = \bar{D}*\bar{E}$$

For the commonly treated two-site exchange, $X_a <--> X_b$, the solution is:

$$(1.12) \qquad M_i(t) = C_1*e^{-\lambda_1 t} + C_2*e^{-\lambda_2 t}$$

where $$\lambda_{(\frac{1}{2})} = 0.5*[(k_{1a}+k_{1b}) \; (\mp) \; [(k_{1a}-k_{1b})^2+4k_a k_b]^{1/2}$$

and $$C_{(\frac{1}{2})} = [-][(-\lambda_{(\frac{2}{1})}+k_{1a})(M_{a_\infty} - M_{a_o}) - k_b((M_{b_\infty} - M_{b_o})]/(\lambda_2 - \lambda_1)$$

and $$k_{1a} = k_a + 1/T_{1_a} \text{ and } k_{1b} = k_b + 1/T_{1_b}$$

In principle, a single perturbation of the spin system will allow monitoring of the time dependencies of the longitudinal magnetizations. A converging least-squares analysis of the response will provide a complete determination of the elements of A, a_{ij}'s. Note that it is not possible to separate the cross relaxation σ_{ij} from the a_{ij}'s, and the characteristic rates of the system will be composed of mixtures of lattice relaxation, dipolar cross relaxation, and chemical exchange. In practice unless the eigenvalues all differ by at least a factor of 4, a solution of the system is not possible (81). To extract the individual k_{ij}'s in an n-site exchange, n selective experiments are required (45).

The generality of the above expressions should be appreciated. Compartments of NMR indistinguishable nuclei are accounted for by simply

superimposing solutions for the individual compartments. Diffusion processes occurring on the spin transfer time scale are given by equating k_{ij} of each a_{ij} term to the (diffusion constant)/(intercompartment distance). Heteronuclear and homonuclear interactions without chemical exchange are treated with k=0. These cases will be made clear in Chapter 2 in specific examples.

1.5 Spin Transfer Experiments

There are three basic classes of perturbations that can be applied to a spin system in one-dimensional Fourier transform spectroscopy: a) non-selective broadband excitation "hard pulse," b) frequency selective excitation pulses, and the c) frequency selective saturation pulse, "soft pulse." Using combinations of these perturbations, practical kinetic methods fall into two classes, steady-state experiments and transient experiments.

STEADY-STATE SATURATION TRANSFER: In the steady-state experiment of a two-site exchange ($X_1 <--> X_2$), first described by Forsen and Hoffman (39,40), a low power ($H_1{}^*\gamma << \omega_1-\omega_2$) r.f. magnetic field is applied perpendicular to the static field at the resonance frequency of M_1, ω_1. The field is applied for a time, t_s, to remove the net magnetization of the selected resonance, $M_1=0$, $\Psi_{12}=0$, and to equilibrate the exchanging states ($t_s > 3/(R+k)$). For ^{31}P *in vivo* spectroscopy at 146 Mhz, $R=1/T_1$ has a value of approximately 0.3 seconds and for commonly studied reactions, k ranges from 0.3 to 0.1 sec^{-1}. A saturation pulse of from 5 to 7 seconds is required to establish steady-state.

$$(1.13) \qquad \dot{M}_2=0=R_2{}^*(M_{2_o} - M_2) - \Psi_{21}$$

Transfer of saturation occurs through chemical exchange reducing the magnitude of

M_2. In the absence of cross relaxation, (σ=0), the steady-state solution is

$$(1.14) \qquad M_{2_{sat}} = M_{2_o}/(1 + k_{21}/R_2)$$

A similar reduced expression is obtained in n-site exchange in the absence of cross relaxation when all but one of the resonances are saturated (39). The chemical flux is obtained from the product $X_2{}^*k_{21}=\tau_{21}$.

For steady-state experiments it is useful to define α_{ij} as:

$$(1.15) \qquad \alpha_{ij} = \psi_{ij_o}/(R_i{}^*M_{io}) = k_{ij}/R_i$$

α gives the relative magnitudes of chemical exchange magnetization transfer to relaxation recovery of magnetization.

Isolation of the exchange terms, k_{ij} from α, requires an independent determination of R_i or R_i+k_{ij}. Two practical implementations of the steady-state experiment are typically used in two-site systems. The first method follows the approach of the system to steady-state by using increasingly long periods of saturation, t_{sat} at ω_1, Figure 1.2c. This procedure will be referred to as SSA. The initial conditions for Equation 1.6 used in the SSA experiment are that complete saturation of a single resonance occurs instantaneously, $M_1(t=0) = 0$, and that the other resonance is unpreturbed, $M_2(t=0)=M_2(t<0)$. The approach of M_2 to steady-state is monitored by a β degree pulse to sample the z magnetization and follows:

$$(1.16) \qquad M_2(t)=M_{2_{sat}} + (M_{2o}-M_{2_{sat}})\exp\{-t_{sat}{}^*(k_{21}+R_2)\}$$

From data obtained for several values of t_{sat} the parameters $M_{2_{sat}}$, k_{21}, and R_2 are obtained.

In the second type of experiment, SSB, the steady-state value of M_2 is measured with and without r.f. saturation of M_1, Figure 1.2d. From Equation 1.12 the value of $\alpha_{21}=k_{21}/R_2$ is obtained. Secondly, the relaxation behavior of $M_2(t)$ is measured in an inversion recovery experiment while M_1 is continuously saturated, Figure 1.2d, to obtain R_2 separate from k. With the initial conditions following saturation, $M_1=0$, and $M_2(t=0)= M_{2_{sat}}*\cos(\beta)$ for a inverting pulse angle $2*\beta$, Equation 1.6 has the solution

$$(1.17) \qquad M_2(t)=M_{2_{sat}}*\{1 + \cos(\beta-1)\exp(-t(R_2+k_{21}))\}$$

The effective relaxation rate is determined, $R_2 + k_{21}$, and used together with k_{21}/R_2 to obtain separately, k_{21}, R_2 and the fluxes $\gamma_{21}=N_{2_o}*k_{21}$, and $\Psi_{21}=M_{2_o}*k_{21}$

TRANSIENT SPIN TRANSFER: The transient kinetic experiment is performed by measuring the evolution of M(t), described by Equation 1.8, following a short ($t<<R$ or K) selective perturbation, Figure 1.2a,b. Typically, a single resonance is inverted and the "inversion transfer" used to determine k (30). Rate constants can be obtained by fitting the data to the complete solutions, Equation 1.11, or by using linear approximations. Figure 1.3 illustrates the behavior of an M_1 <---> M_2 exchanging system following selective inversion of M_1 using a pulse sequence such as that described in Figure 1.2b. The exchange process transfers inverted magnetization from M_1 to M_2, reducing M_2 from the equilibrium value. Simultaneously, the competing process of spin-lattice relaxation, R_2, acts to restore equilibrium conditions. The exchange effectively increases the rate of M_1 relaxation

by transferring relaxed, non-inverted spins from M_2, which increases the longitudinal component of M_1 together with the lattice relaxation effects.

The SSA, SSB, and transient experiments have been applied *in vivo* to measure biochemical reaction unidirectional fluxes. Considerably more effort has been devoted to studies using the SSA experiment primarily because of its relative ease of implementation and data analysis. Considering the wide variation in observed kinetic data obtained from similar preparations reported by several institutions, it is useful to reconsider the assumptions required for applicability of the methods and the simplified solutions. In ^{31}P studies of CK exchange simple two- or, more recently, three-site exchange has been assumed. Data have been analyzed treating the tissue as a single well-stirred compartment without spin-spin interactions or diffusion. Additionally, ideal initial conditions were assumed in previous studies allowing simplified solutions to Equation 1.8. The factors contributing to the inability of previous *in vivo* studies to obtain reproducible results have been identified by examining the effects on the derived kinetic data of 1) fundamental signal-to-noise limitations. 2) poorly defined physical interactions. 3) unknown biochemical pathways. 4) heterogeneous metabolite compartments. and 5) non-ideal initial conditions. These factors are discussed in chapter 2.

1.6 Figure Legends

Figure 1.1: ^{31}P spectra obtained from perfused soleus at 145.6 Mhz. 16 free induction decays (FID's) were acquired following a 90° pulse and averaged to produce the spectrum. 90 degree pulse = 25usec, recycle delay = 12 seconds, 15hz of line broadening was applied to the FID prior to Fourier transformation. Rapid chemical exchange is occurring between mono- and di-hydrogen phosphate and ATP and Mg^{++}-ATP, resulting in single resonances at frequencies equal to the weighted averages of the two states. The slow ^{31}P exchange between PCr and γ-ATP can be observed by a magnetization transfer experiment.

Figure 1.2: Generalized spectrometer pulse sequence for chemical exchange experiments (top). By setting the appropriate delays to zero, sequences for specific experiments can be obtained. a) 1-3-3-1 binomial selective inversion recovery sequence. b) 1-1 binomial selective inversion recovery. In all inversion transfer and inversion recovery sequences, spectra are obtained for variable D2 delays. c) Selective saturation sequence, type A (SSA). Saturation occurs during time D1 at either one (obs) or two (obs and dec) frequencies. Magnetization of non-saturated resonances are sampled with pulse P2 as a function of variable D1. d) Type b saturation experiment (SSB). An inversion recovery sequence 180-D2-90 is performed during continuous saturation of a single resonance at the decoupler frequency. P1 and P2 are set for 90 degrees and D4 is set to zero.

Figure 1.3: Examples of transient selective inversion to monitor chemical exchange between two NMR visible sites $M_1 <--> M_2$. At time, t=0, resonance M_1 is

selectively inverted and the return to equilibrium followed by sampling the z component of magnetization, y axis, with 90° pulses at increasingly long times following inversion. Chemical flux from $M_1 \rightarrow M_2$ carries inverted spin and reduces the signal of M_2. Top: Simulated data from complete solution of the modified Bloch equations. Bottom: Data obtained from the isomerization reaction of valium (100mM in D-Chloroform, 40°C). See Chapter 2 for details.

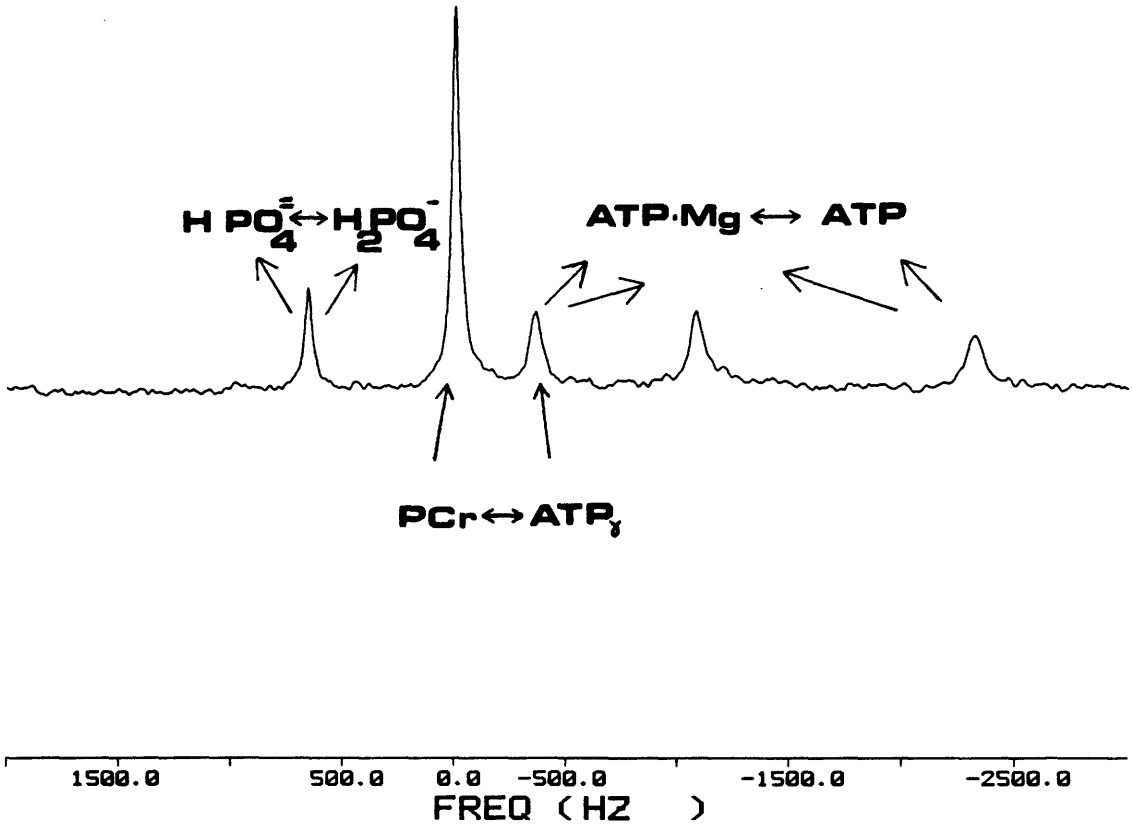
H PO4= ↔ H2PO4-
ATP·Mg ↔ ATP
PCr ↔ ATPγ
1500.0
500.0
0.0
-500.0
-1500.0
-2500.0
FREQ (HZ)

Figure 1.1

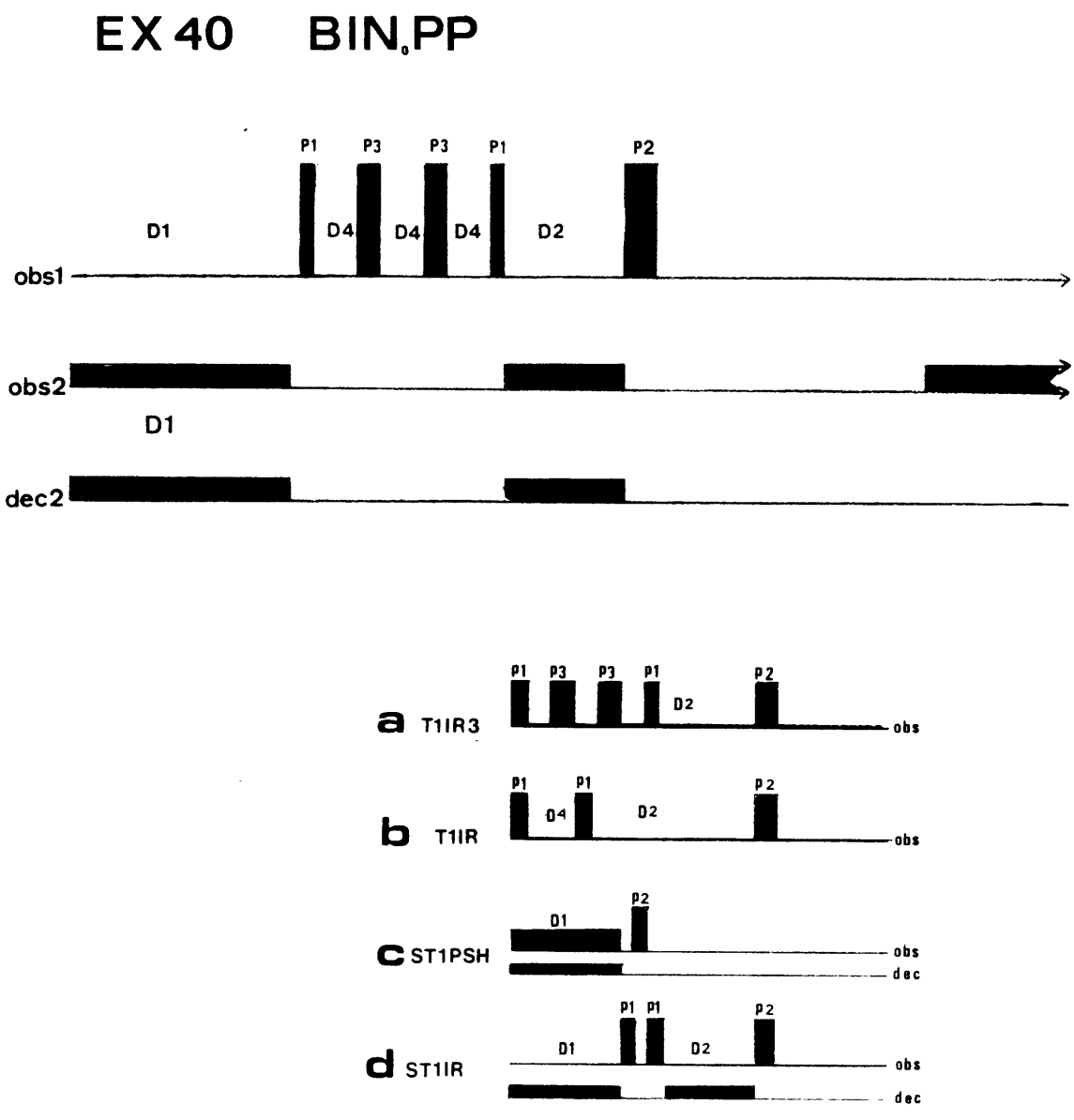
EX 40 BIN,PP
P1
P3
P3
P1
P2
D1
D4
D4
D4
D2
obs1
obs2
D1
dec2
a T1IR3
P1 P3 P3 P1 D2 P2 obs
b T1IR
P1 P1 D4 D2 P2 obs
c ST1PSH
D1 P2 obs dec
d ST1IR
P1 P1 P2 D1 D2 obs dec

Figure 1.2

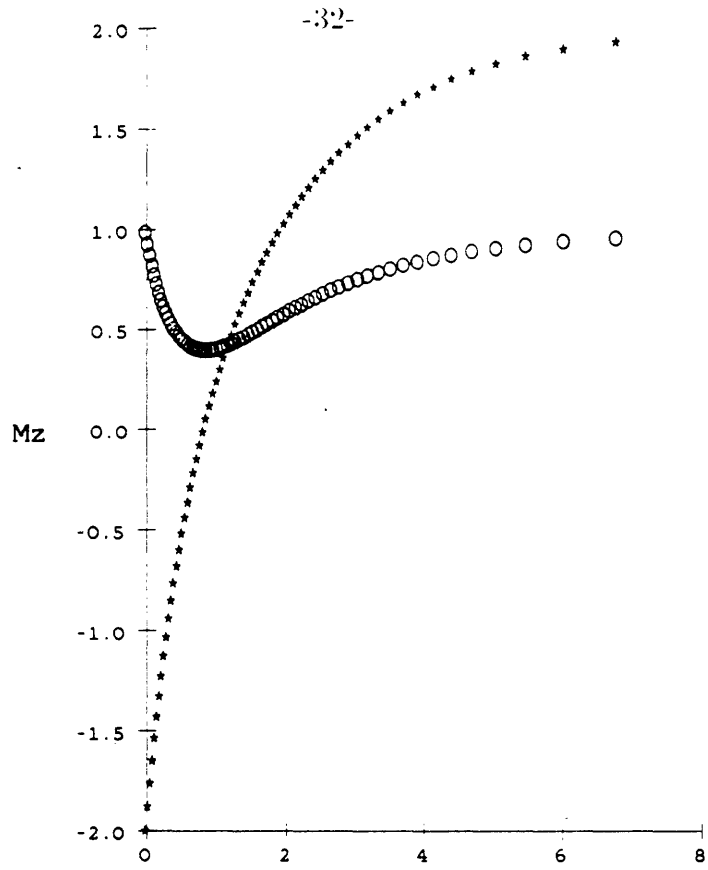
2.0
1.5
1.0
0.5
Mz
0.0
-0.5
-1.0
-1.5
-2.0
0
2
4
6
8
180-90 delay time (sec)

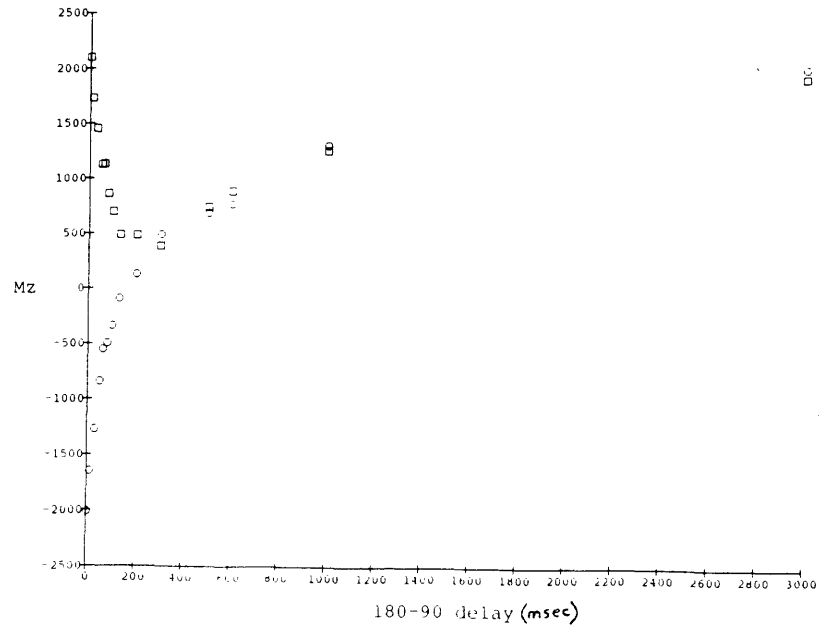
2500
2000
1500
1000
500
Mz
0
-500
-1000
-1500
-2000
-2500
0
200
400
600
800
1000
1200
1400
1600
1800
2000
2200
2400
2600
2800
3000
180-90 delay (msec)

Figure 1.3

CHAPTER 2

LIMITATIONS OF in vivo SPIN TRANSFER EXPERIMENTS

2.1 Introduction

To derive precise chemical flux information from any reacting system using NMR magnetization transfer, prior definition of all ongoing biochemical and physical processes is necessary. Only in such circumstances can the correct formulation of the modified Bloch equations be made. In living systems this precondition will almost never be fulfilled. The task is to 1) formulate testable models describing the suspected dependencies of the chemical flux and 2) experimentally attempt to exclude the models. Interpretation of the results will depend upon the sensitivity of the results to errors in the model. This in turn depends on which of the two classes of experiment are chosen.

Assuming that the exchanging system has been defined correctly and completely with the appropriately modified Bloch equations, there are several problems associated with implementation of the theory that limit the sensitivity of the method beyond fundamental limitations imposed by the signal-to-noise ratio. Though either the transient or steady-state experiment as outlined in Chapter 1 can measure two-site exchange, there are significant differences in efficiency and sensitivity to specific models. For a given acceptable error in the molecular flux it is desirable to minimize the experimental time to assure stability of the living preparation and obtain maximal temporal resolution. An analytical approach to this problem was developed and a comparison of the methods is shown below.

The two classes of experiments also differ in their required initial conditions.

It is frequently assumed that ideal initial conditions are easily established experimentally. It will be shown that this is not the case, especially *in vivo*, and that proper interpretation of data requires consideration of the method of establishing the initial spin state.

2.2 Fundamental Limits

As was stressed above, NMR measurements are inherently insensitive. The principle limitation is the intrinsic signal-to-noise ratio (SNR). At the high frequencies (60-400 Mhz) used for spectroscopy, the noise from a living sample is dominated by Johnson noise when the probe design is optimized (60). The coil-sample interaction can be modeled as an inductively coupled network as shown in Figure 2.1. An analysis for the SNR from such a system was developed for a homogeneous r.f (H_1=constant) excitation incorporating solution of Maxwell's equations in a homogeneous conducting object (72). This analysis can be generalized for the non-homogeneous field, $H_1(r)=\mu B_1(r)$, produced by r.f surface coils. The time domain SNR (peak-to-peak signal)/(rms noise) from an object of conductivity σ_ϵ becomes

$$\text{(2.1a)} \qquad SNR(t) \sim \frac{N^{1/2} H_o^{\,2} * \int_V (B/i)\,dV}{[\Delta\omega T(R'+R_c)]^{1/2}}$$

where $R' = (\omega^2/4) / \sigma_\epsilon (A/i)^2 dV$. Note that (B/i) and (A/i) are the ratios of the r.f magnetic and vector fields at r to the current in the coil and will, in general, be spatially varying.

In a homogeneous H_1 field King (72) showed that

$$(2.1b) \qquad SNR(t) \sim \frac{N^{1/2}H_o^{\,2}*V_{sample}*(B/i)}{[\Delta\omega T(R'+R_c)]^{1/2}}$$

where N is the number of signal averages and is proportional to the total experimental time, $\Delta\omega$ is the bandwidth. T is the coil and sample temperature (assumed equal), R_c and R' are the coil and the equivalent series resistance of the sample. R' can be calculated from σ and the vector potential, A/i.

In the frequency domain the approximately Lorentzian resonance peak will have a peak-height to rms noise ratio, $SNR(\omega_{rms})$, related to time domain by

$$(2.2) \quad SNR(\omega)_{p\text{-}p}=g*SNR(\omega)_{rms}=SNR(t)_{p\text{-}p}[\Delta\omega T_2^{\,*}(1-\exp(-t_a/T_2^{\,*}))]^{1/2}$$

The factor g varies between 2.5 and 5.0 (11), and t_a is the FID acquisition time. An improvement in SNR can be obtained by integrating the Fourier transformed signal over n data points between $-\omega_1$ to $+\omega_1$. The peak area will have a square root of n increase in SNR.

Figure 2.2a shows a ^{31}P time domain signal (free induction decay, FID) from a perfused muscle obtained at 145.6Mhz (Chapter 4). With N=16 averages the PCr peak height in the unfiltered spectrum has a SNR of 100. Figure 2.2b. The FID amplitude consisted of superposition of signals from all 5 ^{31}P resonances; approximately 50% of the amplitude is from the PCr resonance. The overall SNR(t) of the FID is 10 and the SNR(t) for PCr is 5. Equation 2.2 predicts that the SNR in the frequency domain, $SNR(\omega)$, will be between 150 and 300 {

5*12*(2.5 to 5)} using a T_2^* of approximately 30msec, and $t_a >> T_2^*$, Figure 2.2b. The acquisition bandwidth was 10000hz. Using a matched filter (exponential line broadening = natural linewidth) Figure 2.2c shows an optimal SNR= 160. These figures illustrate the quality of data typical of *in vivo* experiments where the SNR(ω) is typically limited to values between 75 and 200.

To approximate the SNR and insure a satisfactory coil design, the Q of the coil is measured with a network analyzer or reflectance bridge (125). Q reflects the ratio of peak energy in the coil's magnetic field to the energy dissipated per cycle. The Q of an empty coil of inductance, L, and series resistance, R_c, is given by the expression

$$(2.3) \qquad Q_o = \omega L_c / R_c$$

When the electric field is properly eliminated from the sample with a Faraday shield, dielectric losses can be neglected. With the sample inside, the coil Q will be reduced by inductive losses to

$$(2.4) \qquad Q_l = \frac{\omega L_c}{(\omega^2 \kappa L_s L_c / R_s + R_c)} = \frac{1}{(\omega \kappa L_s / R_s + 1/Q_o)} = \frac{\omega L_c}{R' + R_c}$$

L_c, R_c and L_s, R_s are the series inductances and resistances of the coil and effective inductance and resistance of the sample. The factor κ is a geometric coupling constant describing the flux linkage between L_c and L_s; κ ranges between 0 and 1; in a proper design κ is above 0.8 . The SNR can then be expressed in terms of Q's by noting that the integral of (B/i) is proportional to $(L_c/V_c)^{1/2}$,

$$(2.5) \quad SNR \sim \frac{N^{1/2}(\omega^2)V_s(L_c/V_c)^{1/2}}{[\omega L_c/Q_l]^{1/2}} \sim N^{1/2}(\omega^{3/2})[Q_l V_s * ff]^{1/2}$$

where $ff = V_s/V_c$, the coil filling factor. In this form the SNR can be seen to depend on the square root of Q_l, which is relatively insensitive to Q_o for large values of Q_o.

Maximizing SNR is always important in NMR. Equations 2.1 and 2.5 have as key parameters under the control of the experimenter the sample volume V_s, the number of signal averages N, the field strength $H_o=\omega/\gamma$, and the coil geometric factors determining (B_1/i), (A/i) and the filling factor ff. For spectroscopy of relatively homogeneous tissue V_s is limited to small samples. The number of signal averages is proportional to the duration of the experiment and will generally be dictated by the viability of the living preparation. Ideally, the mainfield strength, H_o, will be optimized at the highest value achievable; however, spectrometer magnets are limited at present to fields less than 15 T. To maximize V_s and B/i the sample of homogeneous tissue should be as large as possible and the r.f. coil wound tightly around the sample. This process will also optimize κ and ff to approximately unity. For the data of Figure 2.2, $H_o=8.5T$, $V_s=$ 6cc, N=16, T=295°K, and $\Delta\omega=10000$ hz.

Contrary to popular belief, at frequencies above approximately 25 Mhz there is little to gain in SNR by building coils with $Q_{unloaded}$ greater than approximately 200 if the sample volume is greater than approximately $1cm^3$. It is always desirable to maximize $Q_{unloaded}$; however, for a fixed Q_{loaded} equations 2.5 and 2.1

show that the dependency becomes very weak

$$(2.6) \qquad SNR(t) \sim [V_s{*}ff/(\omega\kappa L_s/R_s + 1/Q_o)]^{1/2}$$

The term representing sample noise, $\omega L_c\kappa/R_s$, is approximately 0.05 and only weakly dependent on ω. This follows from the fact that R_s increases nearly linearly with ω. Increasing Q_o from 200 to 400 (an extremely difficult task) raises the SNR only 14%.

It is always desirable to maximize Q_l. This unfortunately can only be achieved by changing the geometric coupling constant, κ at the expense of a decreased filling factor. In a coil where the sample losses are made to dominate by reducing R_c and using low loss components to achieve $Q_o \sim 200$, Q_l is set by the electrodynamical properties of the sample itself.

2.3 Relative Efficiencies of the Steady-State and Transient Experiments in the presence of noise.

Given an accurate model describing the chemical system, the efficiency with which kinetic information can be extracted will be determined by the sensitivities to noise of the experimental technique and the data analysis process to noise. The SNR per spectrum is determined by the coil-sample interactions independent of which technique is used. For a given coil and sample configuration there will be a fixed SNR per signal average, snr=SNR/N. The integrated resonance peak from a noisy spectrum is a single data point acquired in a time $N{*}t_a$ where t_a is the period of a single acquisition. The question is, what method should be used to obtain the rate constants to a given accuracy in a minimum of time?

To use the general theory to extract rate constants and fluxes, magnetization

data must be fit to the complete solutions of the modified Bloch equations. Equation 1.9 can be solved for a transient experiment, Equation 1.12, or the simplified expressions of Equations 1.16 and 1.17 used in steady state SSA or SSB experiments. The fits require nonlinear curve fitting with several parameters. Methods of efficiently performing this task have been suggested (81); however, at best these procedures are useful for *in vitro* data with high signal-to-noise-ratios (SNR's). The problem of fitting noisy data unambiguously to multiparameter models is often not possible under the best of circumstances. Fortunately, approximate values of the parameters in the nonlinear expressions can always be obtained by careful linearization. This was applied to ^{1}H NMR transient experiments *in vitro* (23).

For two-site exchange $X_1 <---> X_2$ following selective inversion of M_1, the behavior of the relaxation functions for times $t << T_1 + 1/K$ can be approximated from Equation 1.7 as:

$$(2.7a) \qquad \Delta M_1/\Delta t \approx R_1(M_{1_o} - M_1) - \Psi_{12_o}(M_1/M_{1_o}) + \Psi_{21_o}(M_2/M_{2_o})$$

$$(2.7b) \qquad \Delta M_2/\Delta t \approx \Psi_{12_o}(M_1/M_{1_o}) - \Psi_{21_o}(M_2/M_{2_o})$$

The initial condition $M_2(t=0) = M_{2_o}$ eliminates relaxation effects from 2.7b. If the reaction is assumed to be near chemical equilibrium, $\tau_{12}=\tau_{21}$, $\Psi_{12_o}=\Psi_{21_o}$, the simple forms are obtained.

$$(2.8a) \qquad \Delta M_1/\Delta t \approx (1 - M_1/M_{1_o})(M_{1_o} R_1 + \Psi_{12_o}) = (M_{1_o} - M_1)(R_1 + k_{12})$$

$$(2.8b) \qquad \Delta M_2/\Delta t \approx -(M_{1_o} - M_1)(\Psi_{12_o}/M_{1_o}) = -(M_{1_o} - M_1)k_{12}$$

Figure 2.3 illustrates how flux information can be obtained from magnetization transfer data. It is important to note that when using the initial slope of the non-inverted resonance the resulting kinetic constant is independent of T_1. This will only be true for early times when $M_2(t) \sim M_{2_o}$.

Suppose the $X_1 <--> X_2$ exchange was not near equilibrium. Equation 2.7 can be rewritten in a general form as

$$(2.9a) \qquad \Delta M_1/\Delta t \sim R_1(M_{1_o} - M_1) \quad -\sum_j \psi_{1j} + \sum_j \psi_{j1}$$

$$(2.9b) \qquad \Delta M_2/\Delta t \sim \quad -\sum_j \psi_{2j} + \sum_j \psi_{j2}$$

Since only M_2 is different from its equilibrium value, $\psi_{ij} = \psi_{ij_o}$, i not equal to 2. The steady-state assumption requires that the net flux by all paths is zero, therefore:

$$(2.10a) \qquad \Delta M_1/\Delta t \sim R_1(M_{1_o} - M_1) \quad -\sum_j \psi_{1j_o}(1 - M_i/M_{i_o})$$

$$(2.10b) \qquad \Delta M_2/\Delta t \sim \quad -\sum_j \psi_{2j_o} + \sum_{j \neq i} \psi_{j2_o} + \psi_{12} = -\psi_{12_o}(1 - M_1/M_{1_o})$$

It is important to note that only the non-inverted resonance, M_2, can be used reliably to determine flux in the absence of equilibrium. The inverted resonance will have its relaxation rate enhanced not only by exchange processes ($M_2 --> M_1$) but, in addition, any other potentially unknown exchanges ($M_j --> M_1$); relaxation of M_1 is not uniquely influenced by the single 2-->1 pathway.

To compare qualitatively the relative efficiencies of the steady-state and transient experiments, simulated magnetization transfer data was generated and fit to the ideal solutions. Random noise (Gaussian) was introduced using the conversion factor 5.0 for the ratio of peak-to-peak to rms noise (11). N points were used to fit the solutions (N=9 for transient, N=5 for steady state, N=3 for linear), where N was chosen as 2 times the number of parameters minus 1. Time intervals on the approximately exponential relaxation functions were taken as:

$$(2.11) \qquad \tau_{n+1} = T_1*[1-(1+f)\exp(\tau_n/T_1)/(2-n)] + \tau_n$$

where $f = (1 - 2e^{-4}) = .96$ was used based on an interpulse delay of $4*T_1$. The three points used in the linearized fit were equally spaced between 0 and $1/(1/k + T_1)$.

The experimental time to acquire the 9, 5, and 3 points was calculated as follows: In all experiments, relaxed spectra were obtained using an interpulse delay of $4*T_1$. The transient data were fit to the form $A + B*e^{-\lambda_1 t} + C*e^{-\lambda_2 t}$. To complete one set (9 points) of a transient experiment requires a time

$$(2.12) \qquad t_t = T_1*[9*4 - \sum_{j=1}^{8}(9-j)\ln(1+\exp(4*t_{j-1}/T_1)/9)]$$

The SSA experiment (Figure 1.2c) requires a saturation pulse, D1, of increasing duration as described in Section 1.5. The experiment is repeated for saturation of the complementary resonance to obtain both forward and reverse flux information. Data for the steady-state experiments were fit to the form $y=A*e^{-B*t} +C$. The total time for an SSA experiment is

$$(2.13) \qquad t_{ssa} = 2*T_1*[5*4 - \sum_{j=1}^{4} (5\text{-}j)\ln(1+\exp(4*t_{j-1}/T_1)/5)]$$

Similarly the SSB experiment (Figure 1.2d) uses 5 points; however, a constant saturation pulse, D1, is typically applied and the interpulse delay, D2, is varied. The time for both complementary inversions in the SSB procedure will always be longer than that for SSA and is given by:

$$(2.14) \qquad t_{ssb}=t_{ssa} + 10*(t_{presat} + 4*T_1)$$

In practice the total time for a steady-state experiment will be approximately a factor of 2 longer than predicted because of the need for a complementary set of saturation data to use as an experimental control. If saturation of M_1 occurs at a frequency, ω_1 relative to M_2, then the complementary experiment must be performed at $-\omega_1$ relative to M_1. This complementary experiment is required to correct for unavoidable distortions of the spectrum and particularly distortions in the steady-state magnitude of M_2 arising from non-ideal components of the saturating pulse power spectrum. In the calculations below an idealized saturation pulse is assumed where a complementary saturation is not required.

For the linearized transient experiment (Figure 1.2a,b) separate inversions are required for each of the exchanging species with 3 different 180-90 delays, D2's, per peak. A single broad-band pulse on the fully relaxed spectrum is also required to obtain M_{1_o} and M_{2_o}. The experimental time is,

$$(2.15) \qquad t_{lin} = [4*T_1 + .5*(1/k + T_1)]*6 + 4*T_1$$

The sensitivities of the rate constants to the fit parameters were calculated

using Equation 1.12 for the complete transient experiment, Equation 2.8 and the fit y=mX+b of the M_2 data for the linearized experiment. The SSA and SSB sensitivities were calculated Equations 1.16 and 1.17 assuming a fit to Y=A +Bexp(-CX). The simplified results in terms of the fit parameters are

(2.16a) $$\sigma_{k_t} = .5^*[\sigma_{\lambda_1}{}^2 + \sigma_{\lambda_2}{}^2]^{1/2}$$

(2.16b) $$\sigma_{k_{linear}} = k^*[(\sigma_m/m)^2 + (\sigma_M{}^2 + \sigma_b{}^2)(M_{1_o} - M_1)^{-2}]^{1/2}$$

(2.16c) $$\sigma_{k_{ssa}} = (1 + C/A)^{-1}[\sigma_b{}^2 + (B/(A+C))^2[(C/A)^2\sigma_A{}^2 + \sigma_C{}^2]]^{1/2}$$

(2.16d) $$\sigma_{k_{ssb}} = [k^2(\sigma_c/C)^2 + (C^*M_{i_{sat}}/M_{i_o})^2[(\sigma_{Mo}/M_o)^2 + \sigma_A{}^2/A^2]]^{1/2}$$

Four sets of simulated data were generated (Appendix) at each of 5 SNR values and the data fit to the exact solution forms using a Marquardt-Levenberg non-linear least squares algorithm (86). The standard errors in the fit parameters were used in Equation 2.6 to obtain Figure 2.4 which shows a plot of the average standard error in the rate constant for the 5 SNR values. The SNR is proportional to the square root of the normalized total time, plotted logarithmically on the abscissa. Clearly, the error in the fitted parameter k can be significantly higher than the noise per point would predict. More importantly, the technique with the greatest accuracy depends on how long one is willing to wait. The non-linear exact methods will eventually give the correct value to a high degree of accuracy if the

SNR is made large through time consuming signal averaging, most often limited by the sample stability.

Figure 2.4 also demonstrates that use of the initial slope as a linear approximation of the transient behavior offers a time efficient method of obtaining the kinetic data. The fixed systematic error introduced by the linearization procedure is analyzed quantitatively in Chapter 3.

It is useful to examine the sensitivity of the steady-state experiment as a function of the kinetic parameters being evaluated. Assuming that T_1 in the absence of exchange is known, Equation 1.13 gives the relationship between the measured signals before and after saturation. Figure 2.5 is a plot of the steady-state change in M_1 following saturation of M_2 (Equation 1.13) plotted as a function of k^*T_1. As the exchange rate increases M_1 approaches zero and there will be little sensitivity to small changes in k. Curve b was obtained by differentiating Equation 1.13 and illustrates the change in fractional error, σ_α/α, in k as k^*T_1 is increased. The minimum occurs for $k^*T_1 = 0.5$. Fortunately, the range of parameters found in ^{31}P studies of CK are near the optimum, T_1's are between 1 and 4 seconds, and k frequently falls between .08 and 1.0 sec^{-1}.

2.4 Practical Approximation of Initial Conditions

The comparisons made above assumed that the necessary conditions for simplification of the modified Bloch equations were ideally satisfied. For the transient experiment selective excitation of a single resonance in a time short compared to the relaxation and exchange time is required. The steady-state experiment requires saturation of a single resonance in a similarly short time. In both cases, to achieve selectivity, a low power r.f. magnetic field is applied for a

relatively long period of time. In many cases the excitation field, $B_1(r)$ will be non-homogeneous.

The power spectrum of a pulse of length T_o is given by $T_o*\text{sinc}\{ii*T_o*(\omega-\omega_o)\}$ with a width at the first zero crossing of $1/T_o$ Hz. This is not an ideal excitation function for a spin system where, *in vivo*, line broadening of resonances is due, primarily, to local main field inhomogeneities. If the spin system response was linear there would be a distribution of excitations as a function of frequency. Selective inversion may produce a 180° pulse at ω_o; however, there will be a distribution of flip angles about ω_o identical in form to the pulse power spectrum. This is equivalent to the problem of excitation with a non-homogeneous H_1 field discussed below. Similarly, if saturation is obtained at ω_o insufficient saturation will occur for all spins where local field inhomogeneities shift their resonance frequency away from the saturation frequency. Figure 2.6 is the proton spectra of water as a function of the duration of the applied excitation pulse. The amplitude of the pulse was adjusted to achieve an approximately 90° pulse in each spectrum. Clearly, the excitation band narrows as the pulse width increases, and the assumption that all nuclei are selectively excited or saturated is incorrect.

The problem of irradiation with a weak H_1 field was analyzed, in the absence of chemical exchange, by Redfield (110). Incorporating off resonance effects he showed that following application of a low power irradiation at a frequency ω, the z magnetization of nuclei with resonance frequency $\omega_o=\gamma*H_o$ approached,

$$\frac{M_{i_{sat}}}{M_{i_o}} = \frac{(H_o-\omega/\gamma)[(H_o-\omega/\gamma)^2+H_1^2]^{1/2}}{R_1(H_o-\omega/\gamma)^2 + R_bH_1^2 + R_cH_{loc}^2} \tag{2.17}$$

This result applies for long irradiation times where previous perturbation theory results broke down. Note that if the transmitter frequency corresponds to the resonance frequency of M_i, its amplitude is reduced to 0. If the transmitter frequency is not near ω_i the $H_o - \omega/\gamma$ terms dominate and $M_{i_{sat}} = M_{i_o}$, no saturation. H_1 must be increased in power to adequately saturate the entire spin distribution, yet not produce significant reduction in signal from the remaining spectrum. In a two resonance exchange system, adequate saturation of spins off resonance by one half-width (1/2 the width of the resonance peak measured at 1/2 its maximum amplitude) deposits 11% of the full saturation power at the center of a second resonance 1.5 full widths away and 4% of full saturation power at frequencies 2.5 full widths.

Use of low power pulses to achieve selectivity will cause difficulty when environmental broadening of the resonance is significant compared to the natural linewidth. At 146 Mhz T_2 values for ^{31}P containing metabolites range from 20 to 100 msec. The natural widths of these resonances [$\Delta\omega = 1/(\pi * T_2)$] are less than 20 hz. Published spectra from *in vivo* studies display linewidths in excess of 80 Hz. Therefore, environmental broadening appears to be the dominant broadening factor *in vivo* and the limitations of the frequency selective pulses must be considered.

The behavior of an exchanging spin system in the presence of a low power H_1 field was investigated further using a numerical solution of the modified Bloch equations (Appendix). A finite difference Runga-Kutta integration scheme was modified to include automatic step size scaling for efficiency in computational time. In Figure 2.7 the z magnetization components are shown as a function of time in a weak H_1 field (1 Gauss). The nucleus is taken as ^1H in a 0.1 T main field, T_2=10msec, and $T_{1\rho}=T_1$. The important observation is that even before the excited resonance reaches saturation, exchange via spin transfer begins to reduce

the magnetization of the non-excited resonance, X_2. The initial conditions of the SSA method require that M_j is instantaneously saturated and that M_i is unaffected at t=0. Figure 2.7 demonstrates that for large α (fast exchange) this will not be the case.

The limitation illustrated in Figure 2.7 will also hold for long pulses used for selective inversion. In the transient experiment as the pulse width approaches a length $\tau \sim 1/k$ significant transfer of magnetization will have occurred during the establishment of the initial state. In Figure 2.7 inversion was complete at approximately 10 msec. The condition of $M_z(t=0)=M_o$ can no longer be made for the non-inverted species, and the simplifications to Equation 2.7 are no longer justified. With resonance lines typically $>$ 0.5 ppm in width this limitation will place restrictions on k values, for accurate NMR measurement, to less than 10 sec^{-1} at approximately 100Mhz.

H_1 INHOMOGENEITIES: In the theoretical formulation of the modified Bloch equations it is assumed that the excitation due to $H_1(t)$ is uniform throughout the system. Typical *in vivo* experiments are performed using surface coils where this is not the case. In a non-exchanging system the transient experiment is identical to a T_1 measurement. Several studies have been published analyzing errors in T_1 due to H_1 inhomogeneities. Results claiming significant effects (42,66,87) and no effects (36) have been published. In an exchanging system additional factors enter the analysis which were addressed in this study both theoretically and experimentally.

In the transient experiment, a non-uniform $H_1(t,r)$ applied to a spin system at the resonance frequency for a time τ will result in a distribution of flip angles $\alpha(r)=H_1(t,r)\gamma\tau$. Note that H_1 is no longer constrained to be perpendicular to H_o, though only perpendicular components will influence the spin system. The

additional issue of resonance offset due to main field inhomogeneity can effectively be included by noting that nuclei off resonance will have a reduced flip angle about the "effective" r.f. field of $\gamma^* H_1^* \tau_p$. Phase errors can be neglected when identical coils are used for receiving and transmitting. In these cases the system can be treated as a collection of discrete spin groups each within a homogeneous $H_1(r)$. The modified Bloch equations become:

$$M_1 = \sum_j m_{1j} \tag{2.18}$$

The solutions from Equation 1.9 each have unique initial conditions for m_{1_i} due to spatial differences in $H_1(r)$. Superimposing the solutions gives:

$$M_1(t) = (\sum_j a_i)e^{-t^*\lambda_1} + (\sum_j b_i)e^{-t^*\lambda_2} + \sum_j c_i \tag{2.19}$$

The pre-exponential terms contain all spatial dependencies due to the position dependent flip angles. The exponentials, however, contain no dependence on position. The rate information contained in the pre-exponentials can be extracted by noting

$$\frac{\sum a_i}{\sum a_i + \sum b_i} = \frac{\lambda_2 - k_1}{\lambda_2 - \lambda_1} \tag{2.20}$$

$$\frac{\sum b_i}{\sum a_i + \sum b_i} = \frac{\lambda_1 - k_2}{\lambda_2 - \lambda_1} \tag{2.21}$$

In the absence of chemical exchange, $\lambda_1 = \lambda_2$ (see Equation 1.12), the system reduces

to the standard inversion recovery form. The prediction is that the exponential time constant will reflect true T_1 in the presence of excitation field inhomogeneities. A similar, though more cumbersome, separation of coefficients will occur with the multiexponential forms obtained when exchange is present.

This result was tested and verified experimentally with the probe arrangement shown in Figure 2.8. The single loop coil has a field profile that decreases in magnitude approximately as 1/r. The precise vector profile is presented in standard references (61). T_1 measurements were made using an inversion recovery sequence ($2^*\beta^o$-τ-β^o) in two experiments. ^{31}P (10% phosphoric acid) and 1-H (water) samples were placed at different spatial positions with different H_1 field characteristics and the relaxation times measured. For the ^{31}P samples, the pulse power was set to deliver a 90° pulse when the sample was positioned at the theta=180° position; power was held constant for all positions. The results, listed in Table 2.1, show that the T_1's (+/- standard error) measured at all positions agreed with the mean value. At theta = 0 the sensitivity of the measurement was extremely small due 1) to the relatively small B/i given in Equation 2.1a and 2) to the small β readout pulse.

For measurement of proton relaxation times a β^o pulse was adjusted to optimize the signal from a semi-infinite water phantom replacing, temporarily, the sample vile. This power adjustment is similar to the one performed in *in vivo* experiments with surface coils. With the pulse power fixed, the sample holder was restored and the T1's measured as a function of theta. In Figure 2.9 signal intensities are plotted for six spatial positions. Though the relative phases vary, as reflected by the sign of the data, the exponential rate constants are the same. Table 2.1 shows that again the T_1's are invariant with position. These results are in agreement with several reports in the literature and the arguments given above

(36), and allow the general statement to be made, that relaxation, or similarly transient kinetic measurements, are independent of H_1 field homogeneity.

In the steady-state experiments, $H_1(r)$ calculated from Equation 2.17 will give values of M_{sat} that are variable within the sample. Each location will require a different minimum time to reach a true steady-state saturation. Fortunately, in locations of incomplete saturation the fact that $H_1(r)$ is small means that the coil sensitivity to signal from those locations is also small. This follows from the proportionality of $H_1(r)$ and B/i. In such a case $M_{sat}(r)$ will be weighted by $H_1(r)/H_{1max}$.

2.5 Incomplete Description of Physical Processes

DIPOLAR INTERACTIONS: To extract chemical flux information from magnetization transfer data all processes contributing to the time changes in the magnetization must be accounted for. The nuclear magnetic dipole-dipole interaction (Nuclear Overhauser Effect, NOE) is a process of transferring magnetization without chemical exchange. NOE interactions between M_i and like (homonuclear) or unlike (heteronuclear) nuclei can occur and have an effective rate proportional to $(M_{jo} - M_j)^*\sigma_{ji}$, where σ_{ji} is the dipolar coupling constant between M_i and M_j, often expressed as the NOE factor, $N = \sigma/R$.

The generalized interaction matrix, Equation 1.9, was derived to include both homonuclear and heteronuclear NOE. In the transient experiment the effect is manifested by an increased effective relaxation of the inverted resonance and an apparent decrease in the transferred magnetization to the non-inverted resonance. In a saturation experiment the interaction causes a more rapid relaxation of the non-saturated resonance so it appears as if less transfer had occurred, thus an underestimate of the rate constant. To predict the magnitude of this underestimate

consider the steady-state result following saturation of M_2 in the presence of homonuclear NOE between M_1 and M_2.

$$(2.21) \qquad \dot{M}_1 = 0 = R_1(M_{1_o} - M_1) - \Psi_{12} + \sigma M_{2_o}$$

The "effective" rate constant is given by

$$(2.23) \qquad {}^*\alpha_{12} = \alpha_{12}(1 - (N/\alpha_{12})M_{2_o}/M_{1_o})/(1+NM_{2_o}/M_{1_o})$$

Figure 2.11 shows a plot of the error term in Equation 2.22 for increasing N for three different values of α.

For the frequently studied ^{31}P compounds both homonuclear (^{31}P--^{31}P) and heteronuclear (^{1}H--^{31}P) NOE's have been measured in living preparations. Homonuclear NOE's have been reported anecdotally and as incidental findings (88). In tissue extracts no significant NOE's have been measured (7). Several groups have reported heteronuclear NOE's *in vivo* for ^{31}P PCr and ATP (103.28). In a steady-state experiment, the effective rate constant (expressed as α) in the presence of the heteronuclear interaction to a species M_3 is

$$(2.23) \qquad {}^*\alpha = \alpha(1+\sigma_{13}{}^2/(R_1R_3))^{-1}$$

Using the heteronuclear NOE factors given by Nunnally (103), of 0.44 for PCr and 0.35 for ATP, and assuming $T_1(^1H) \sim T_1(^{31}P) \sim 1$ second the effective ${}^*\alpha$ measured by the steady-state technique will be less than the actual α by approximately 16% and 11% respectively.

The dependency of the transient experiment to NOE interactions differs from

that found for the steady-state technique. If initial slopes are used in a transient experiment, all dipolar terms except those from the inverted resonance drop out, Equation 1.9. Therefore, heteronuclear dipolar coupling will not effect the transient results. The initial slopes for the inverted and non-inverted resonance become will reflect the homonuclear NOE as:

$$\frac{\Delta M_1/\Delta t}{(M_{1_o} - M_1)} = R_1 + k_{12} \qquad (2.24a)$$

$$\frac{\Delta M_2/\Delta t}{(M_{1_o} - M_1)} = -(k_{12} - \sigma) \qquad (2.24b)$$

EXPERIMENTAL EXAMPLE: NMR spin transfer measurements of the slow intramolecular conformational exchange in diazepam (Valium, 7-chloro-1.3-dihydro-1- methyl-5-phenyl-2H-1,4-benzodiazepin -2-one) have been performed previously (23). The study revealed a homonuclear NOE between the exchanging resonances of the first order dipolar system. This system was used as a model to demonstrate possible complications in *in vivo* studies where first and second order NOE interactions are poorly characterized and generally neglected.

The isomerization of valium (100mM in D-chloroform) was examined by ^1H NMR at 360 MHz, Figure 2.10. The Overhauser interaction is seen to increase the effective magnetization of the non-inverted proton following a selective inversion of diazepam at 0°C, where negligible conformational chemical exchange occurs, Figure 2.9b. Equation 2.24b predicts this behavior for k_{12}=0. At higher temperatures

(40°C), Figure 2.10a, the expected transfer of magnetization can mask the competing NOE and eventually dominate. Multiparameter fits of typical inversion or saturation transfer data to analytical solutions of the modified Bloch equations based on models neglecting NOE will converge incorrectly on simple double and single exponentials respectively.

The inversion transfer studies were performed at 0, 20, and 40 °C. The NOE was determined from the initial slopes at 0° as 0.30+/-0.05. At 20°C the product k^*T_1 was calculated as 0.50 +/- 0.02 and compared to that obtained using the steady-state technique of 0.33 +/- 0.05. This error was predicted for the NOE of 0.30 by Equation 2.23. In Figure 2.11 the fractional error in the product k^*T_1 is plotted as a function of the NOE factor (σ/R) for the steady-state experiment, Equation 2.23. As α increases the error due to neglect of the dipolar interaction is reduced. Inversion transfer and saturation transfer experiments performed at 40 °C gave equivalent values of k^*T_1 to within experimental error.

SPIN-LATTICE INTERACTIONS: The steady-state experiment can be performed on two-site systems in significantly less time if the T_1's of the exchanging nuclei (in the absence of exchange) are known. Only two data points are required with and without equilibrium saturation to determine k^*T_1 from Equation 1.12. Knowledge of T_1 then allows calculation of k. This requirement, however, is difficult in practice to fulfill. It is often assumed that T_1 values measured under normal physiological conditions using a single complete SSA or SSB experiment can be used for subsequent studies following physiologic perturbations. T_1 relaxation rates are sensitive measures of the chemical environment, and they are difficult to measure accurately. ^{31}P T_1 values *in vivo* are in the range of 0.9 - 5.0 seconds at 30 °C; however, there is tremendous scatter in the published values. T_1 values for PCr in glucose perfused rat hearts at 37 °C

vary from 1.6 to 5.4 seconds at 146 Mhz (41,89); there is clearly a difficulty in obtaining accurate T_1 values. Kuhn et al (74) showed that there are significant errors in T_1 values obtained using weak r.f. saturation off-resonance in a saturation-transfer experiment and that values obtained should be corrected. In the previous heart studies T_1 was assumed constant and flux calculated directly from $k=\alpha/T_1$. Errors in the T_1 determination are probably the major cause of the tremendous variations in published steady-state magnetization transfer derived chemical fluxes measured in identical systems.

Two likely factors accounting for variability in T_1 measurements are temperature and pH. That ^{31}P relaxation times vary with pH was demonstrated over the physiological range (47). Most sensitive were the Pi and γ-ATP T_1's which varied as much as 100% following a 1 unit change in pH in the 6.5 to 7.5 range. The pH dependence is very sensitive to paramagnetic chelates and the applicability of these results to *in vivo* systems poorly understood. It is not unlikely that common experimental protocols of hypoxia, arrest, and increasing work load vary the system pH.

Temperature effects on the relaxation rate are well known and follow directly from the Solomon-Bloembergen relaxation expressions (17). Proton relaxation measurements have been used for *in vivo* thermography, which has demonstrated significant temperature gradients within normal tissue (31).

The temperature dependence of T_1 in common ^{31}P metabolites was measured in solutions containing 5mM P_i, 5mM ATP, 6mM MgCl, 20 mM PCr, 100mM KCl, 20 mM MOP's buffer at pH 7.0. The results shown in Figure 2.12 demonstrate a strong relationship between thermal energy, and relaxation, especially for the P_i resonance (- 0.2 sec/°C). Note that in the physiological temperature range the relaxation rate for the relatively small P_i molecule gets shorter with increased

thermal energy while the T_1 of the larger ATP and PCr increases as their faster tumbling rate becomes further from resonance where energy transfer to the lattice is most efficient. The T_1's γ-ATP and PCr have similar qualitative behavior to that found for water protons; however, their sensitivities are significantly higher (0.06 and 0.04 sec/°C) than that found for water protons (0.005-0.01 sec/°C). ^{31}P relaxation times for Pi, PCr, and γ-ATP obtained from the soleus at 22 and 30°C are indicated in Figure 2.12 alongside the *in vitro* data. At 30°C the measured T_1's (mean +/- standard error) for soleus are: $T_{1_{PCr}}$=3.8 +/- 0.7 sec, $T_{1_{Pi}}$=4.2 +/- 0.3 sec, $T_{1_{ATP}}$=3.0 +/- 0.5 sec, and at 22°C, $T_{1_{PCr}}$=3.4 +/- 0.8 sec, $T_{1_{Pi}}$=4.4 +/- 0.8 sec, $T_{1_{ATP}}$=1.3 +/- 0.5 sec. It is important to note that the T_1 value for the γ-ATP resonance is higher than values from previous studies (13). The above values were obtained using the transient inversion transfer method whereby it was possible to separate exchange processes from lattice relaxation. Chemical exchange with PCr will increase the apparent relaxation rate of ATP and lead to erroneous T_1's if ignored.

In spite of large standard errors the *in vivo* data demonstrates the identical qualitative temperature dependencies as that found *in vitro*. The absolute values are strongly determined by the properties of the solutions. These data suggest that 1) *in vivo* relaxation time will be a strong function of temperature and must be considered following any perturbation that may alter metabolic rate or circulation sufficiently to effect a local temperature change. 2) correction for temperature effects can be made using *in vitro* calibration curves. The unexpected behavior of P_i is probably a result of chemical exchange effects; however, the precise mechanism was not investigated. The characteristic time associated with Pi relaxation will be effected by the rapid on/off rate of the protons on the mono- and diphosphate moieties. These rates may approach resonance 145.6 x 10^6 sec^{-1} at

higher temperatures.

2.6 Improper Models

Valid interpretation of the NMR data relies on the assumption that the modified Block equations correctly describe the system. The *in vivo* reaction must be properly described both in terms of the biochemical pathway and the spatial homogeneity of the kinetic parameters or physiological compartments. Previous kinetic models have assumed simple exchanges between two or more NMR distinguishable components. For the enzyme catalyzed reaction these treatments are inadequate.

BIOCHEMICAL MODELS: For the simplest $X_1 <--> X_2$ slow exchange without dipolar coupling the modified Bloch equations can be written in terms of fluxes from Equation 1.6 as :

$$\dot{M}_1 = R_1*(M_{1o}-M_1) - \Psi_{12} + \Psi_{21} \tag{2.25}$$

Monitoring M_1 before and after saturation of M_2 ($\Psi_{21}=0$) allows calculation of α_{12} from Equation 1.14. Prior knowledge of X_1 and R_1 gives the chemical flux, τ_{12}, as

$$\tau_{12} = \alpha_{12}*X_1*R_1 = k_{12}*X_1 = [\Psi_{12_o}/M_{1_o}]*X_1 \tag{2.26}$$

Note that the assumptions made were that steady-state saturation was achieved and only $X_1 <--> X_2$ exchange existed.

In the transient experiment only the assumption that an equilibrium exists between X_1 and X_2 is required. For selective inversion in a transient experiment the behavior of the non-inverted resonance follows from Equation 2.10b as:

$$(2.27)\qquad \frac{\Delta M_2/\Delta t}{(M_{1_o} - M_1)} = \frac{\Psi_{12_o}}{M_{1_o}} = \frac{r_{12}}{X_1} = k_{12}$$

Therefore, in the simple system both the steady-state and transient experiment give an NMR derived rate constant equivalent to the chemical first order rate constant.

Enzymatic reactions typically involve multiple substrates and the formation of several intermediate activated complexes prior to formation of products. For several enzymatic reactions, including creatine kinase, the rate determining step is the interconversion of enzyme-substrate complex to enzyme-product complex. Unfortunately, even the simple enzymatic scheme X_1+C+E <--> XCE <--> XDE <--> X_2+D+E requires assumptions that complicate interpretation of magnetization transfer data. Typical Michaelis-Menton kinetic analysis fixes only the total enzyme concentration and ignores the reverse flux. In this equilibrium system all chemical species are constant in time. Perturbation of the spin system is similar to an isotope exchange where free and bound enzyme concentrations do not change. Chemical equilibrium for this reaction sequence gives:

$$(2.28a)\qquad \frac{X_1}{X_{E1}} = \frac{k_{-1}}{[E][C]k_1} = \frac{M_{1_o}}{M_{E1_o}} = \frac{k_{-1}}{k'_1}$$

$$(2.28b)\qquad \frac{X_{E2}}{X_{E1}} = \frac{k_2}{k_{-2}} = \frac{M_{E2_o}}{M_{E1_o}}$$

$$(2.28c)\qquad \frac{X_2}{X_{E2}} = \frac{k_3}{[E][D]k_{-3}} = \frac{M_{2_o}}{M_{E2_o}} = \frac{k_3}{k'_{-3}}$$

Without making assumptions about the NMR visibility of the enzyme bound substrates denoted as E1=X_1EC, E2=X_2ED and neglecting dipolar coupling, A of Equation 1.9 becomes:

$$(2.29)\quad A = \begin{vmatrix} R_1+k_1 & -k_{-1} & 0 & 0 \\ -k_1 & (R_{E1}+k_2+k_{-1}) & -k_{-2} & 0 \\ 0 & -k_2 & (R_{E2}+k_3+k_{-2}) & -k_{-3} \\ 0 & 0 & -k_3 & (R_2+k_{-3}) \end{vmatrix}$$

Saturation of M_2 does not reduce the system to the same simple forms unless additional assumptions are made. The main one is that M_{E2} from X_2 bound in the EXD complex is saturated either by having the same resonance frequency as unbound M_2 or by the process of rapid equilibrium XDE<-->X_2+D+E. Rapid equilibrium of the free substrates and the enzyme complex is commonly encountered in this form of reaction (112). Solving first for M_{E1} using Equation 2.29 and Equation 1.9 with initial conditions M_{E2}=0=M_2:

$$(2.30)\qquad M_{E1} = (M_{E1_o} R_{E1} + M_1 k_1)/(k_2+k_{-1}+R_{E1})$$

With M_{E1}, Equation 1.9 is used again with Equation 2.29 to solve for M_1,

$$(2.31) \qquad \frac{M_{1_o}}{M_1} = 1 + \frac{k_2 k_1}{R_1 k_{-1}} \times [1+(k_2(1+k_1/R_1)+R_{E1})/k_{-1}]^{-1}$$

Here the desired flux, Ψ_{2o}, can be included by assuming chemical equilibrium $\Psi_{2_o}=k_2*M_{E1}=k_2*(k_1/k_{-1})*M_{1o}$, then

$$(2.32) \qquad M_{1_o}/M_1 = 1 + (\Psi_{2_o}/(R_1 M_{1_o}))/[1 + (k_2(1+k_1/R_1)+R_{E1})/k_{-1}]$$

In many applications, the bracketed term is multiplied by $M_{1o}*R_1$ to obtain an apparent flux. The apparent flux will only reflect the true flux when the denominator is unity. However, in cases where M_1 in the complex relaxes quickly as in the case of enzymes with active paramagnetic components, R_{E1} can be quite large and even for rapid equilibrium ($k_{-1}>k_2$), R_{E1} may be $>>k_{-1}$ and the apparent flux will be an underestimate of the actual flux.

$$(2.33) \qquad (\tau_{2_{actual}} - \tau_{2_{obs}})/\tau_{2_{actual}} = [1 + (k_2(1+k_1/R_1)+R_{E1})/k_{-1}]^{-1}$$

Note that the assumption here was that only the unbound M_1 is present in sufficient quantities to be NMR visible, ($k_1/k_{-1}< .1$).

The transient experiment will also be affected by the enzymatic step if the enzyme bound M_1 is not detectable and in large quantity. In such a case

$$(2.34a) \qquad \dot{M}_1 = -\Psi_1 + \Psi_{-1}$$

$$(2.34b) \qquad \dot{M}_{E1} = \Psi_1 - \Psi_{-1} + \Psi_{-2} + \Psi_2$$

Then using chemical equilibrium

$$(2.35a)\qquad \frac{\dot{M}_1}{(1-M_{E2}/M_{E2_o})_{t=0}} \cong -\psi_{2_o}\left[1 - \frac{((1-M_{E1}/M_{E1_o})/(1-M_{E2}/M_{E2_o})] + X_{E1}/X_1}{1 + X_E/X_1}\right]$$

If the rate limiting step is XCE <--> XDE and $X_1 >> X_{E1}$
then $M_{E1} = M_{E1o}$ and

$$(2.35b)\qquad \frac{\dot{M}_1}{(1 - M_{E2}/M_{E2_o})_{t=0}} \approx -\psi_{2_o}[1- (1 + X_1/X_{E1})^{-1}] \sim -\psi_{-2_o}$$

When M_{E1} is NMR detectable, $\dot{M}_{1\ total}=\dot{M}_1 + \dot{M}_{E1}$ and the initial slope will reflect the true flux ψ_{2o} as

$$(2.35c)\qquad \frac{\dot{M}_1+\dot{M}_{E1}}{(1-M_{E2}/M_{E2_o})_{t=0}} \approx -\psi_{2_o}$$

A single NMR flux measurement does not yield information about the reaction mechanism or the specific model. For example, an $X_1+C<--->X_2+D$ system could not be distinguished from the more complicated enzyme-substrate model above in any single NMR experiment. Only by changing the chemical equilibrium and remeasuring the flux as a function of changes in the actual concentrations of the chemical species can the model be tested. Perturbations to

the chemical equilibrium of the muscle cell were used to test biochemical models *in vivo* and will be discussed in Chapter 4.

An incomplete account of all reaction pathways is potentially a serious problem when studying complex systems likely to be encountered *in vivo*. Suppose a third NMR visible species, X_3, was involved in the assumed simple two-site system $X_1 <--> X_2 <--> X_3$. Solution of Equation 1.13 for steady-state saturation of M_1 and M_2 give respectively:

$$(2.36) \qquad M_{1_o}/M_{1_{sat}} = 1 + \Psi_{12_o}/(R_1 M_{1_o}) = 1 + \alpha_{12}$$

and

$$(2.37) \qquad M_{1_o}/M_{1_{sat}} = 1 + \alpha_{21}[1 - (1/\alpha_{23} + (M_{2_o} R_2)/(M_{3_o} R_3) + 1)^{-1}]$$

Assuming accurate knowledge of the T_1's, (R_1, R_2), the apparent flux $M_1 * k_{12}$ for the forward exchange $X_1 ---> X_2$ will be the actual flux, however, the reverse flux $X_2 ---> X_1$ will be reduced by the error term in Equation 2.37. The fractional error in the flux from Equation 2.37 is

$$(2.38) \qquad (\Psi_{2o_{actual}} - \Psi_{2o_{obs}})/\Psi_{2o_{actual}} = [((1 + 1/\alpha_{32})R_2/R_3)M_{2_o}/M_{3_o} + 1]^{-1}$$

In this system a steady-state saturation transfer experiment will give apparent flux values that are in error and lead to the incorrect conclusion that the forward and reverse fluxes are not equal. Reports from ^{31}P studies of heart using steady-state saturation methods have suggested a mismatch between the forward and reverse CK flux (103,13). If the assumed two-site exchange is extended to include transfer

from γ-ATP to either P_i or other potential sites, Equation 2.37 explains this discrepancy when these pathways are significant.

Forsen suggested that a three-site system can be treated like a two-site system if the third site is continuously decoupled with a saturating r.f. field at ω_c (39). This method was implemented in rat heart studies and the forward and reverse rates were found to be equal (104). Initial slopes from a transient experiment performed on the same three-site system are not sensitive to the extra site as long as selective excitation is applied to only a single resonance. In practice it is probably useful to employ both methods. The saturation technique is easily implemented and can be used to identify all sites of significant transfer with rate-relaxation relations, k^*T_1 in the range 10 to 0.1. The transient method can then be used for quantitative determination of the flux.

COMPARTMENTATION: The heterogeneity of cell types within a tissue, and the intracellular structural divisions within cells, gives rise to the possibility and often the reality of macro and microscopic compartmentation of biochemical compounds (56,98). The NMR parameters are also spatially varying as evidenced by the spectacular contrast in NMR images which rely for contrast primarily on large variations in relaxation times within tissues. The effects on the NMR derived fluxes of physical separation of reactions has been recognized as a potential complicating factor in data interpretation (103). Quantitative predictions of the effects, however, have not been made.

In Figure 2.13 two simple compartmentalization schemes are shown. NMR visible species X_1 coexists in two non-communicating compartments while species X_2 is ubiquitous (a situation encountered in cells with selectively permeable membranes) in the top figure and separated into two pools in the lower figure.

The transient NMR experiment gives as initial slopes following inversion of M_2

$$(2.39) \qquad \frac{\Delta M_1/\Delta t}{(M_{2_o} - M_2)} = -(\psi_{21_A} + \psi_{21_B})/M_{2_o}$$

and following inversion of M_1

$$(2.40) \qquad \frac{\Delta M_2/\Delta t}{(M_{1_o} - M_1)} = -(\psi_{1_A 2} + \psi_{1_B 2})/M_{1_o}$$

In both cases the transient derived fluxes reflect correctly the actual chemical exchange.

The transient method can be generalized for the selective inversion of species j in an n compartment system. Equation 1.9 becomes:

$$(2.40b) \qquad \begin{vmatrix} \Delta M_1/\Delta t \\ \Delta M_2/\Delta t \\ \Delta M_3/\Delta t \\ \vdots \\ \Delta M_j/\Delta t \\ \vdots \\ \Delta M_n/\Delta t \end{vmatrix} \approx \overline{A} \cdot \begin{vmatrix} 0 \\ 0 \\ 0 \\ \vdots \\ M_{j_o} - M_j \\ \vdots \\ 0 \end{vmatrix}$$

All non-inverted species, M_i (i not equal to j), will have initial slopes,

(2.40c) $$\Delta M_i/\Delta t \approx (\sigma_{ij} - k_{ji})(M_{j_o} - M_j)$$

and the inverted resonance will follow

(2.40d) $$\Delta M_j/\Delta t \approx (R_j + \sum_{i \neq j} k_{ji})(M_{j_o} - M_j)$$

The important result is that observation of the non-inverted species gives information that is independent of T_1 and reflects exclusively exchange processes (chemical and, when present, dipolar) with the selectively inverted species.

In contrast, the requisite competition between relaxation and exchange complicates the steady-state solutions. Following saturation of M_1, the equilibrium transfer of magnetization from M_2 to M_{1_A} and M_{1_B} superimpose to act as a single flux channel,

(2.41) $$M_{2_o}/M_{2_{sat}} = 1 + \alpha_{21_A} + \alpha_{21_B} = 1 + k_{app}/R_2$$

The product of M_{2_o} and $k_{apparent}$ is the true total flux, Ψ_{21_o}. However, upon saturation of M_2 the apparent flux, $\Psi_{12_{app}}$ is

(2.42) $$\Psi_{12_{app}} = k_{app} * M_{2_o}$$

which differs from the true flux, Ψ_{12_o}, with a fractional error

$$(2.43) \qquad (\Psi_{12_o} - \Psi_{12_{app}})/\Psi_{12_o} = [1 - (1+\alpha_{1B}/(f_A+(1-f_A)\alpha_{1B}/\alpha_{1A}))(1 + \alpha_{1A}(1-f_A) + f_A\alpha_{1B})^{-1}]$$

Where $f_A = M_{2_o}/M_{total} = X_2/(X_1+X_2)$. The plot of fractional error in the flux versus relative pool size, f, is shown in Figure 2.14. The apparent flux is always less than the true flux, causing a perceived net flux from X_2 to X_1. Note that the error can be quite large for large differences in α's as might be expected in physiological compartmentation where R's are strongly dependent on the ionic composition and presence of paramagnetic species. Also k will depend on enzyme concentration which may vary throughout the system.

The simple model in the lower diagram of Figure 2.13 has a solution identical to the system shown in the upper diagram where X_2 was contained in a single pool, Equation 2.43. This model could easily be applied in the situation where PCr <--> γ-ATP exchange through CK was large in one region of the tissue, due to a high concentration of enzyme, while a separate type of muscle cell nearby has a low enzyme concentration.

Consider the example where two regions of equal size contain identical PCr/ATP ratios and have $k_f*T_{1a}=50$ and $k_f*T_{1b}=0$. $\Upsilon_a=50*1$ while $\Upsilon_b=0$; the actual net PCr to ATP flux is 50 if T_1's are taken as 1. Saturation of ATP, however, reduces M_{pcr_a} to approximately 0 while M_{pcr_b} is unchanged. The apparent flux is $\alpha = 1/(1/2) - 1 = 1$, a significant reduction and predicted from Equation 2.43 by using f=.5, $\alpha_{1a}=50$ and $\alpha_{1b}=0$.

2.7 Summary

The limitations of the spin transfer experiment have been examined. SNR is certainly the major concern, and it is always productive to obtain the largest SNR within the time constraints of the experiment. Nonetheless, noise will always be

present, and it was demonstrated that the non-linear curve fitting required for the most common spin transfer experiments has a relatively low efficiency compared to the linear approximations used for a transient inversion transfer experiment. If time is not an issue both, steady-state and transient magnetization transfer experiments will give reliable flux information when the correct model is known. However, if there is any doubt that all chemical and dipolar interactions have been completely accounted for, the transient experiment is the technique-of-choice exhibiting only a homonuclear dipolar sensitivity. The transient technique was also shown to be relatively insensitive to the undesirable effects of inhomogeneities in the H_1 field when a short selective inversion pulse is used. When using a steady-state saturation technique care must be exercised to insure that true steady-state is achieved in all regions contributing significantly to the total signal. For the experiments of Chapter 4 the transient method was used in the experimental protocol described in Chapter 3.

2.8 Figure Legends

Figure 2.1: Inductive coupling of receiving coil and a conductive sample. The sample can be modeled as a series circuit with a signal source, S(t), and noise source, N(t), and an effective complex impedance, Z. The probe circuit is tuned (C_t) and matched (C_m) with variable capacitors to have a total impedence equal to the input impedence of the preamplifier.

Figure 2.2: a) ^{31}P time domain signal from a perfused soleus demonstrating typical signal-to-noise obtainable from in vivo experiments (SNR(t)=10). b) Direct Fourier transformation of time domain signal (SNR(ω)=100). c) Spectra obtained following multiplication of the time domain signal by a matched exponential filter (SNR=160).

Figure 2.3: Calculation of chemical flux, A-->B, from the initial slope of magnetization response to transient inversion of M_a. The initial time derivatives of the resonance peak areas of the inverted species, (m_a), and noninverted, (m_b), species are divided by the difference between the equilibrium value of the inverted resonance $M_{a_{oo}}$ and its value immediately following inversion M_{a_o}. The NMR derived rate constant, k_a, and the relaxation time of M_a, T_{1_a} can then be calculated. k_a is the ratio of the chemical flux between A and B and the chemical concentration of A.

Figure 2.4: Comparison of three implementations of magnetization transfer experiments. Random noise was added to simulated data from ideal experiments. In two cases, an inversion was applied and the data fit 1) to the complete transient

solution, or 2) to an initial slope approximation. The third experiment was the SSA steady-state experiment. The standard error in the NMR derived rate constant is plotted versus relative experimental time. Simulated data was generated for $k_a=k_b=0.5$ sec^{-1}, $T_{1_a}=T_{1_b}=2$ seconds with added random noise (Gaussian). The magnitude of the noise was varied and data fit to the technique dependent solutions.

Figure 2.5: Characteristics of steady-state saturation transfer in an X_1-->X_2 exchange. The monotonically decreasing curve is the ratio of M_1 following steady-state saturation of M_2 to the equilibrium magnetization $M_{1_{oo}}$ plotted versus $\alpha=k^*T_1$ (Equation 1.13). The second curve indicates the fractional error in k^*T_1, (σ_α/α), as a function of α. The insert is an expansion near the origin demonstrating the minimum.

Figure 2.6: Proton lineshape for increasing pulse length from a water sample in a mainfield with inhomogeneities that dominate the line width. Power was adjusted to achieve a maximum amplitude, approximately a 90° pulse, for each duration. Power spectrum is seen to narrow with increasing pulse length.

Figure 2.7: Calculated behavior of Z magnetization during approach to saturation in an X_1<-->X_2 system. Calculated z magnetization (Appendix) is plotted versus saturation time. $[X_1]/[X_2]=2$, and a 1 gauss B_1 field is applied. Top: $k_{12}=10$ sec^{-1}. Bottom: $k_{12}=1$ sec^{-1}. This figure demonstrates that for increasing fluxes the assumption of instanteous saturation is invalid.

Figure 2.8: Schematic of probe assembly for measurements of T_1 in the presence of an inhomogeneous B_1 field. Sample holder was constructed to allow

rotation from outside the magnet. A hole was machined off-center, within the holder a radius R from the axis of rotation. Liquid samples are placed within the hole, allowing their distance, r, and axis angle phi relative to the circular current loop to be altered. These geometric variations allow measurement of relaxation in different $B_1(\emptyset)$'s.

Figure 2.9: Magnitude of Z magnetization in an inversion recovery experiment performed within an inhomogeneous receiver field. The ^1H signal amplitude from water, as measured from various sample positions (Figure 2.8), is plotted versus the time between the $2^*\beta$ and β pulses. The angle theta refers to the axial rotation of the sample holder, Figure 2.8. The pulse power was set such that for a β pulse the signal was maximum when a semi-infinite water phantom was substituted for the sample holder. Data was collected and ^1H resonance areas determined with identical phase corrections for each spectrum. (Apr298619BX).

Figure 2.10: Transfer of magnetization between valium isomers (100mM in d-chloroform). A) At 40°C the dominant exchange mechanism is chemical. B) At 0°C chemical exchange is essentially eliminated and an INCREASE in magnetization is noted due to homonuclear NOE between the two isomeric forms.

Figure 2.11: Estimated fractional error in $\alpha = k^*T_1$, (σ_α/α), for an, $X_1 \rightarrow X_2$, exchange in the presence of homonuclear NOE (Equation 2.22). In all cases an underestimate of the flux results from neglect of the dipolar exchange mechanism. NOE factor $= \sigma^*T_1$, $[X_1]=[X_2]$.

Figure 2.12: Temperature dependence of ^{31}P relaxation times measured *in*

vitro. Also indicated are data obtained *in vivo* at 23°C and 30°C from the cat soleus. Solutions contained 5mM Pi, 5mM ATP, 6mM MgCl, 20mM PCr, 100mM KCl, 20mM MOP's buffer at pH 7.0. (jun0886,jun0886).

Figure 2.13: Two simple forms of compartmentalization of a reaction $X_1 <--> X_2$. Top: large central pool of X_1 communicating with two pools of X_2 through independent pathways. Bottom: two physically isolated reacting systems.

Figure 2.14: Calculated fractional error in the experimentally determined chemical flux, $X_1 --> X_2$, in a two compartment model (Figure 2.13, top) using the SSA steady-state saturation method. The calculated error is plotted versus the relative size of compartment A for 3 different values of α.

Table 2.1

T1 by inversion recovery in presence of H1 distortions

31P 90 degree pulse set with at the 180 degree position

Angle(theta)	Relative Intensity	T1 (std. error)
180	1	0.64 (.06)
120	0.73	0.61 (.08)
-120	0.73	0.51 (.08)
60	0.12	0.52 (.50)
-60	0.12	0.50 (.50)
0	0.08	0.12 (.79)
weighted mean		0.57 +/-.10

1H 90 deg pulse set for optimum signal in semi-infinite plane, all phase corrections identical.

Angle(theta)	Relative Intensity	T1 (std error)
180	1.0	3.60 (.65)
135	0.74	3.34 (.49)
90	0.55	3.15 (.03)
45	0.60	3.11 (.16)
-45	0.18	3.29 (.48)
0	0.09	1.42 (.67)
weighted mean		3.29 (.89)
T1 from semi-infinite sample		3.40 (.26)

Experiment #Apr2919

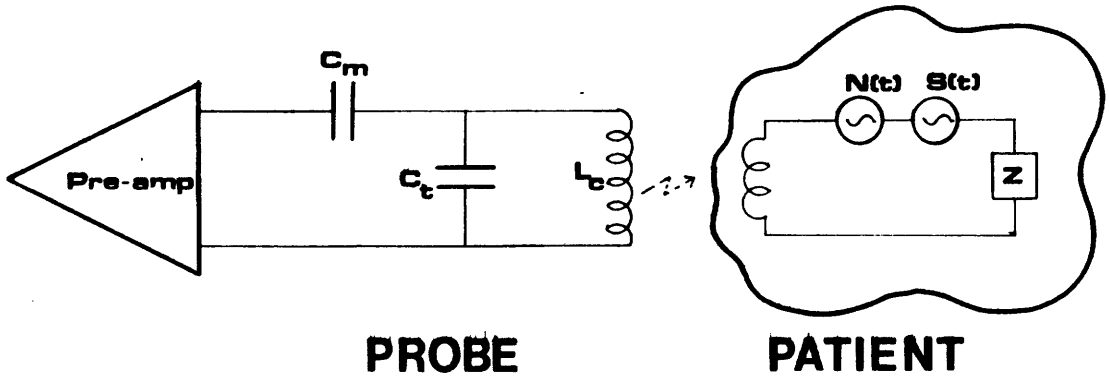

Figure 2.1

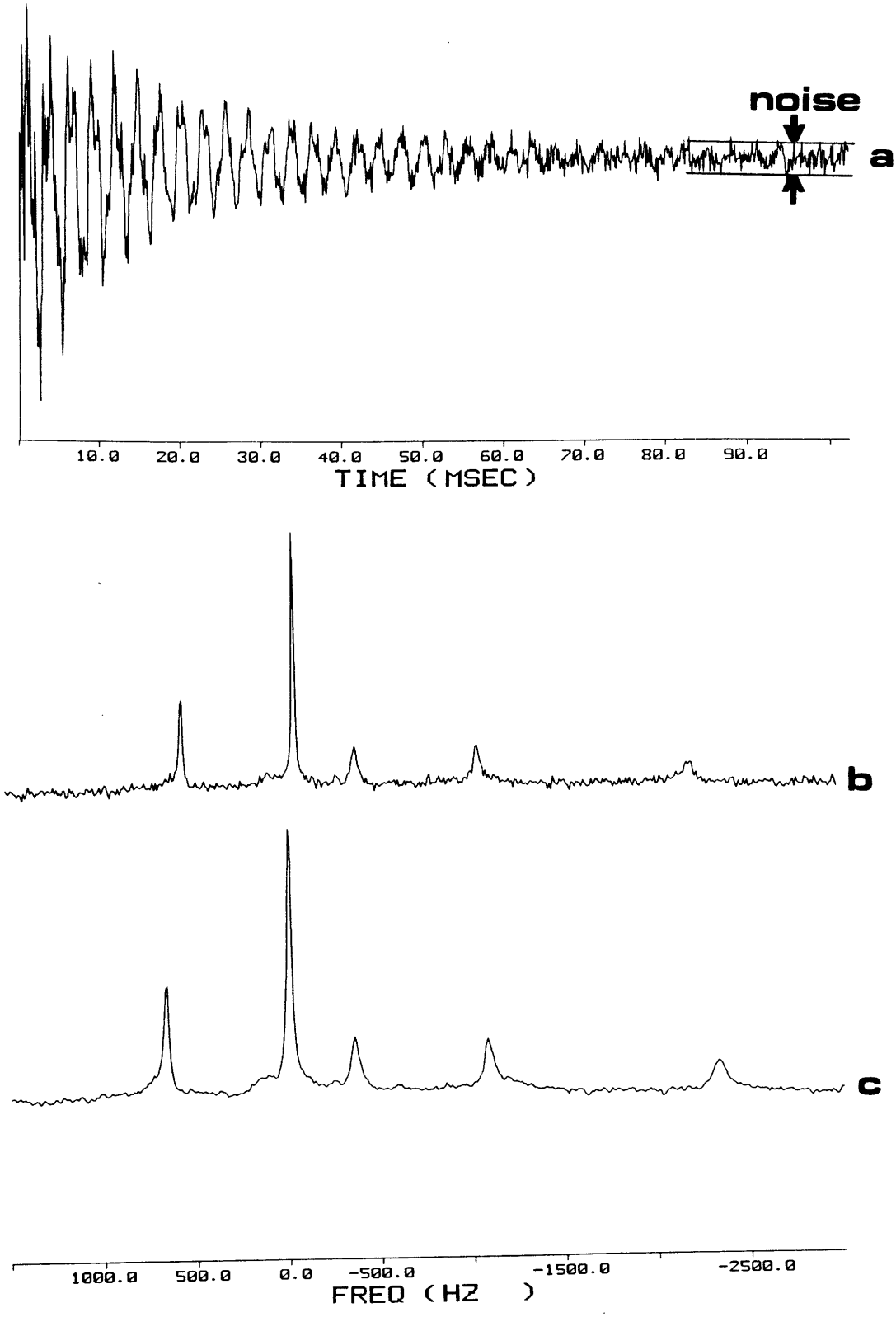
noise
a
10.0
20.0
30.0
40.0
50.0
60.0
70.0
80.0
90.0
TIME (MSEC)
b
c
1000.0
500.0
0.0
-500.0
-1500.0
-2500.0
FREQ (HZ)

Figure 2.2

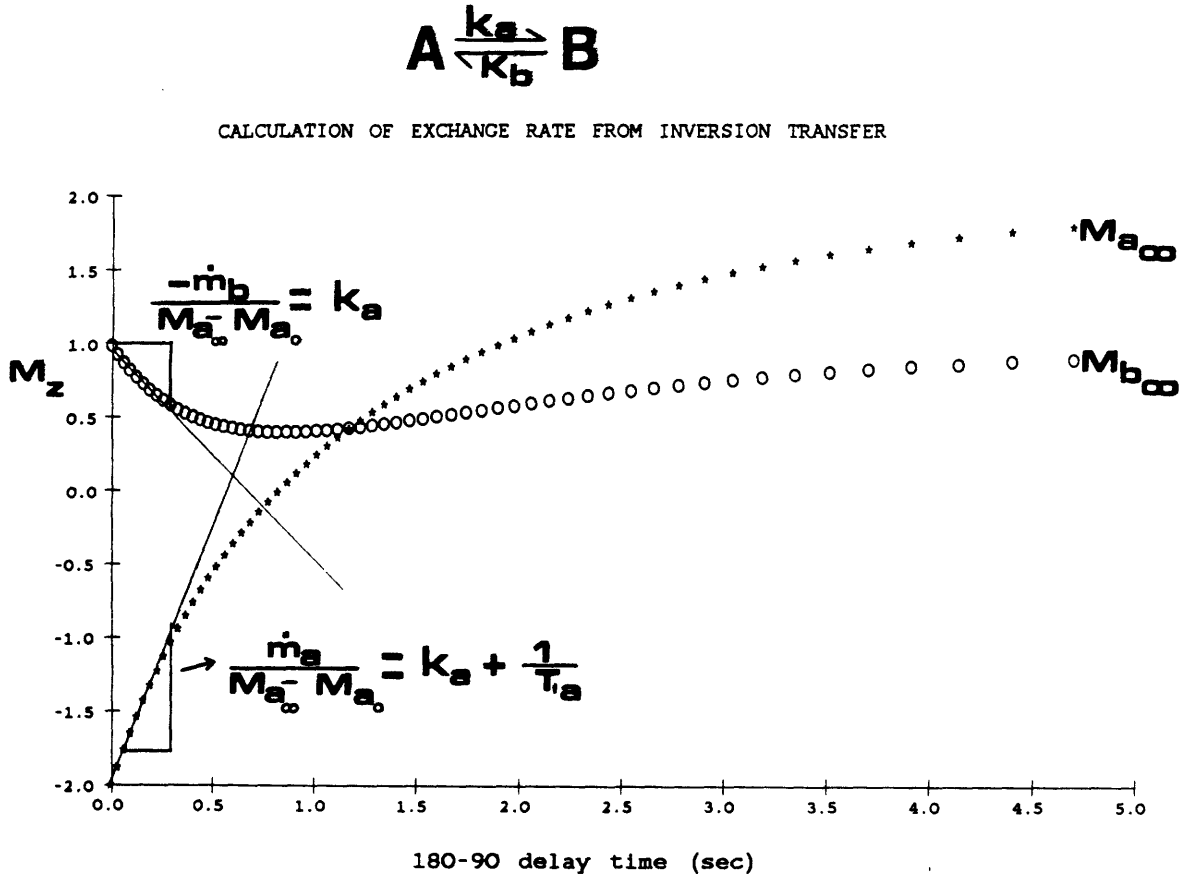
A ⇌ B
CALCULATION OF EXCHANGE RATE FROM INVERSION TRANSFER
$\frac{-\dot{m}_b}{M_{a_\infty} - M_{a_o}} = k_a$
$\frac{\dot{m}_a}{M_{a_\infty} - M_{a_o}} = k_a + \frac{1}{T_{1a}}$
M_z
$*M_{a_\infty}$
oM_{b_∞}
2.0
1.5
1.0
0.5
0.0
-0.5
-1.0
-1.5
-2.0
0.0
0.5
1.0
1.5
2.0
2.5
3.0
3.5
4.0
4.5
5.0
180-90 delay time (sec)

Figure 2.3

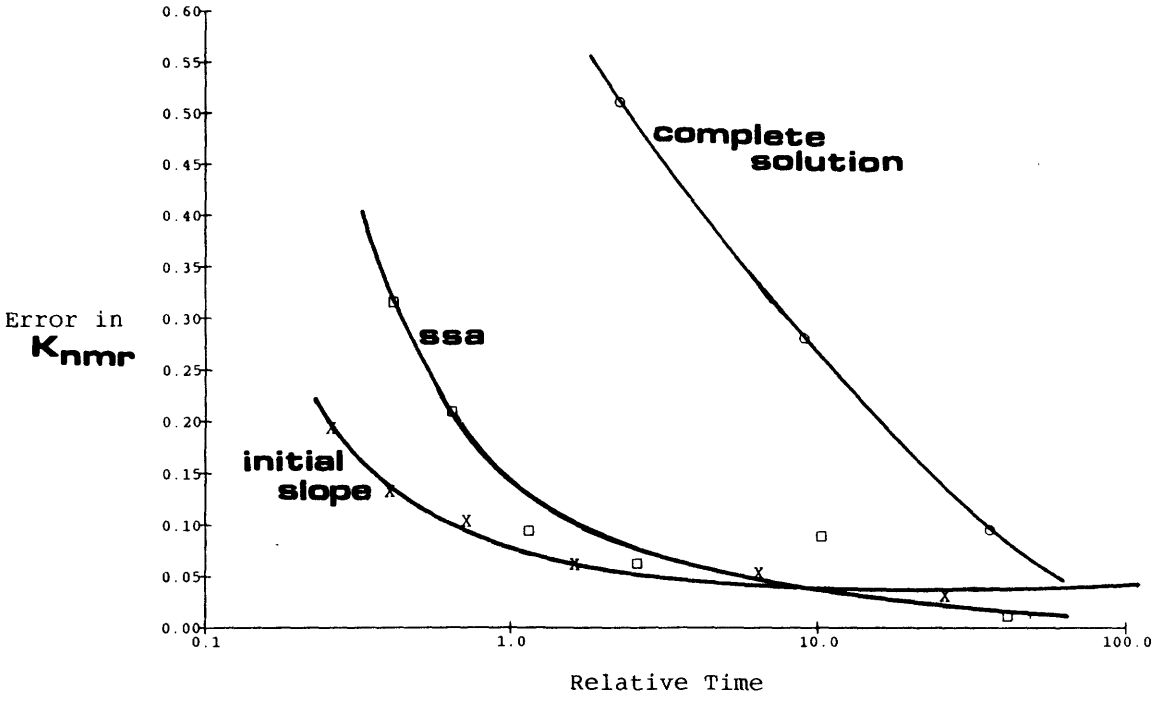
Error in
K_{nmr}
0.60
0.55
0.50
0.45
0.40
0.35
0.30
0.25
0.20
0.15
0.10
0.05
0.00
0.1
1.0
10.0
100.0
Relative Time
complete solution
ssa
initial slope

Figure 2.4

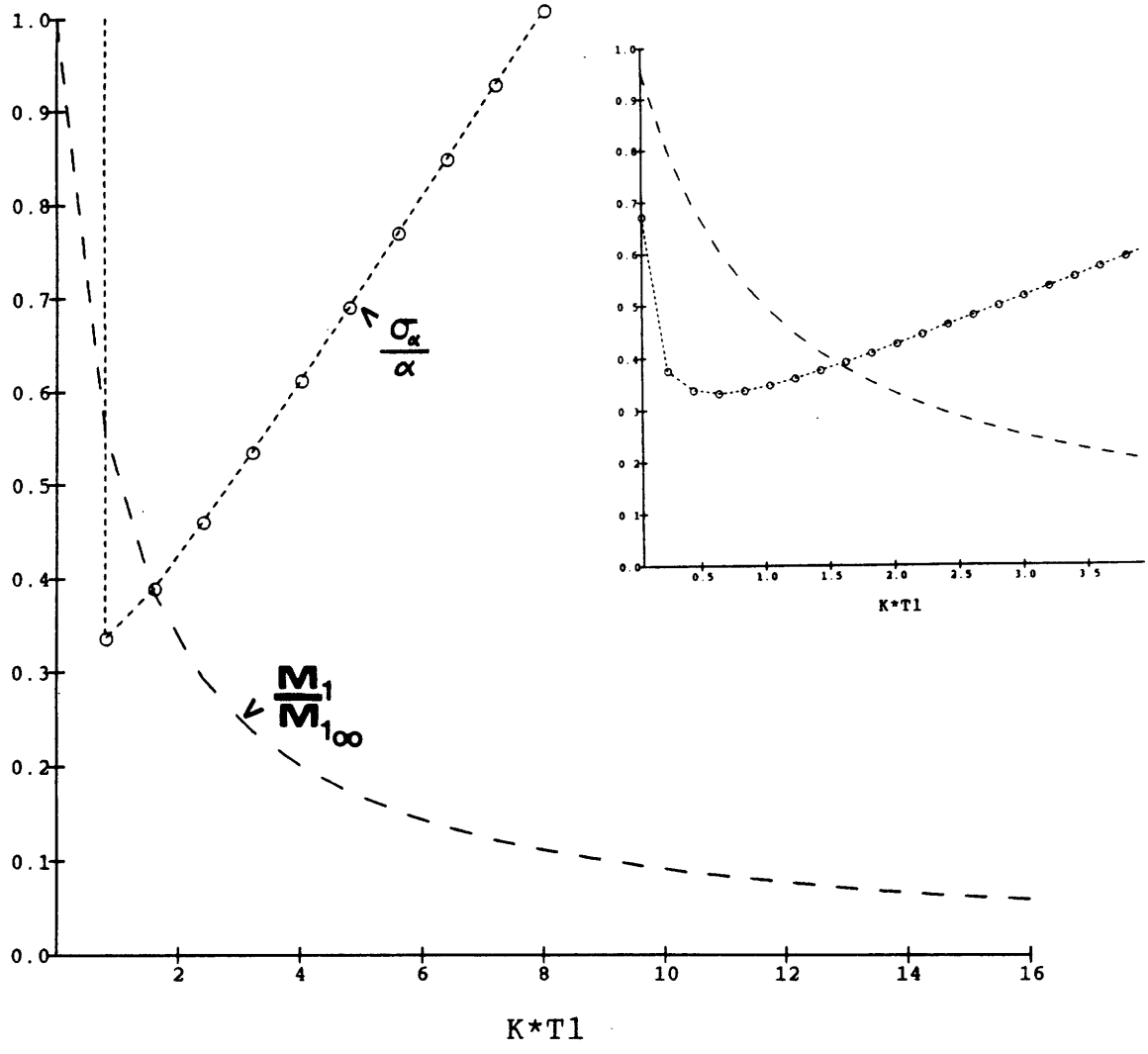
1.0
0.9
0.8
0.7
0.6
0.5
0.4
0.3
0.2
0.1
0.0
2
4
6
8
10
12
14
16
K*T1
$\frac{\sigma_\alpha}{\alpha}$
$\frac{M_1}{M_{1\infty}}$
K*T1

Figure 2.5

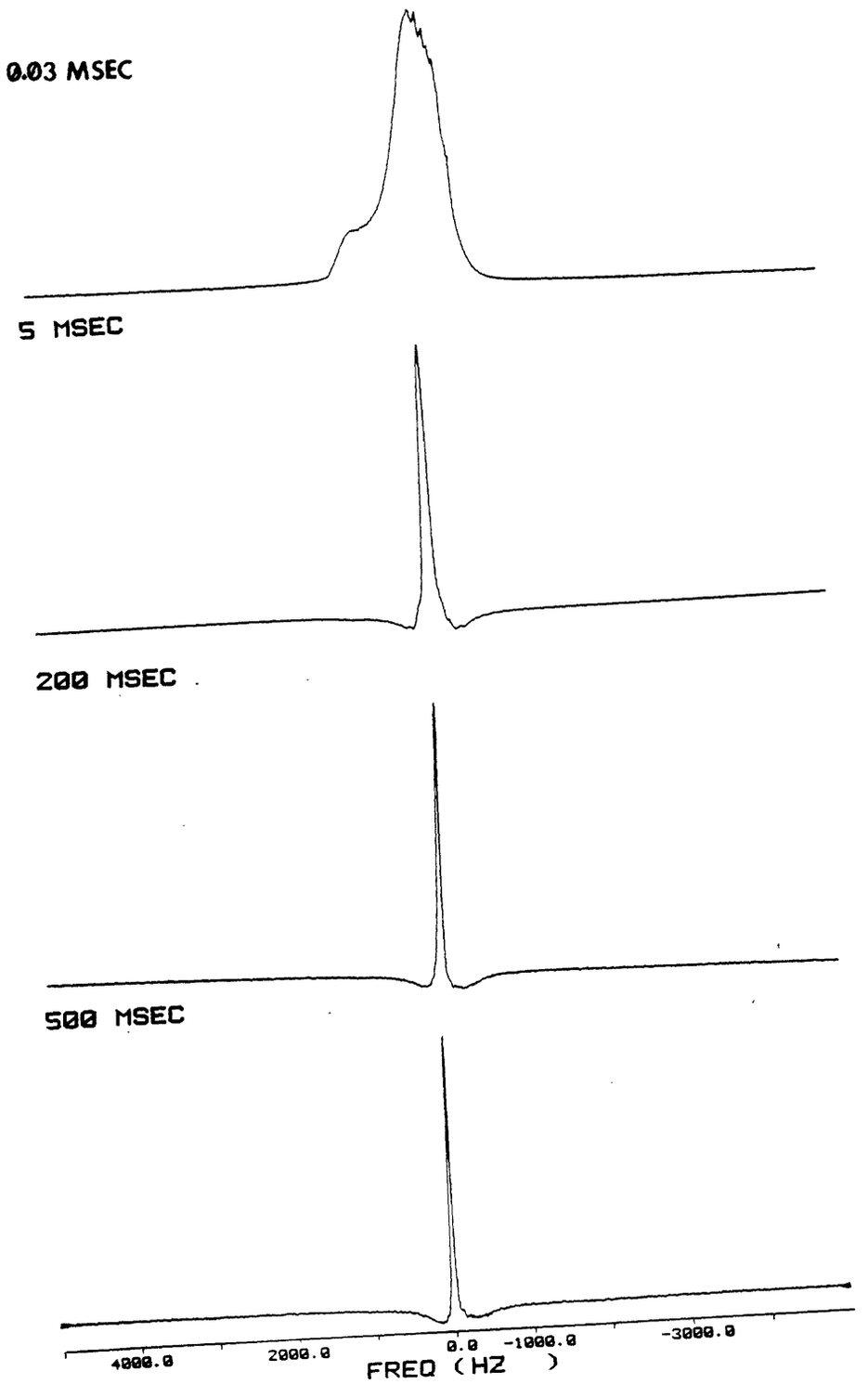
0.03 MSEC
5 MSEC
200 MSEC
500 MSEC
4000.0
2000.0
0.0
-1000.0
-3000.0
FREQ (HZ)

Figure 2.6

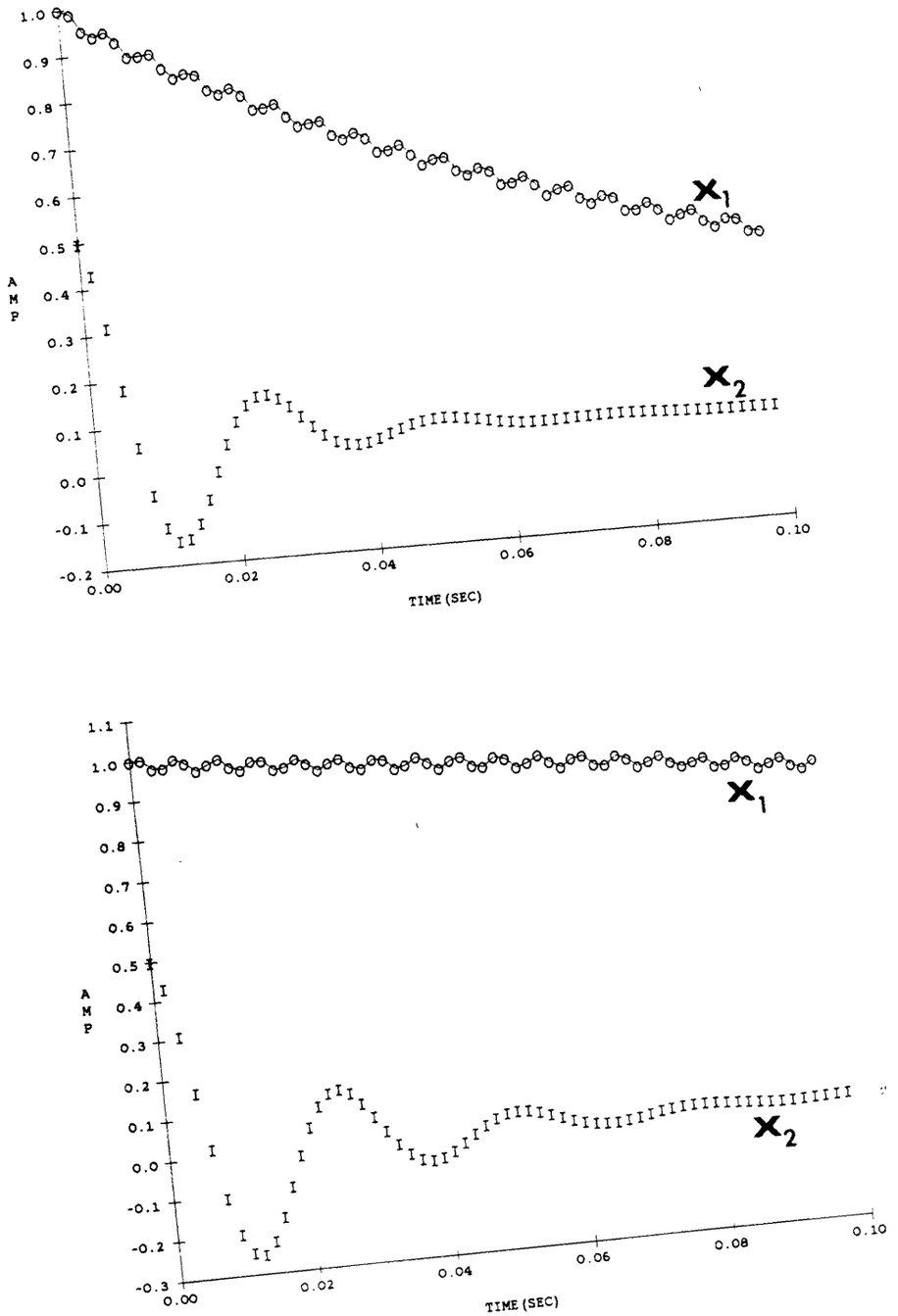
1.0
0.9
0.8
0.7
0.6
0.5
0.4
0.3
0.2
0.1
0.0
-0.1
-0.2
AMP
0.00
0.02
0.04
0.06
0.08
0.10
TIME (SEC)
X1
X2
1.1
1.0
0.9
0.8
0.7
0.6
0.5
0.4
0.3
0.2
0.1
0.0
-0.1
-0.2
-0.3
AMP
0.00
0.02
0.04
0.06
0.08
0.10
TIME (SEC)
X1
X2

Figure 2.7

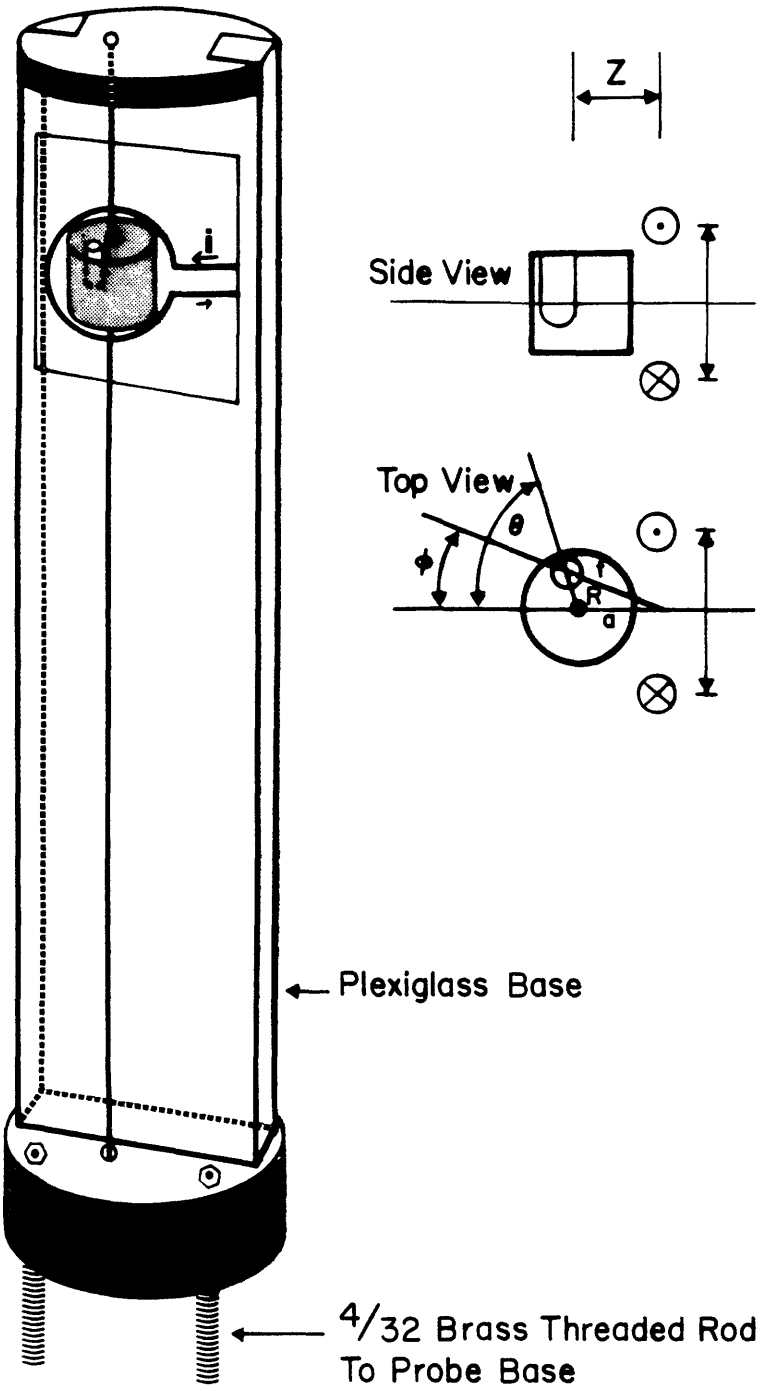
Z
Side View
Top View
θ
φ
r
R
a
Plexiglass Base
4/32 Brass Threaded Rod
To Probe Base

Figure 2.8

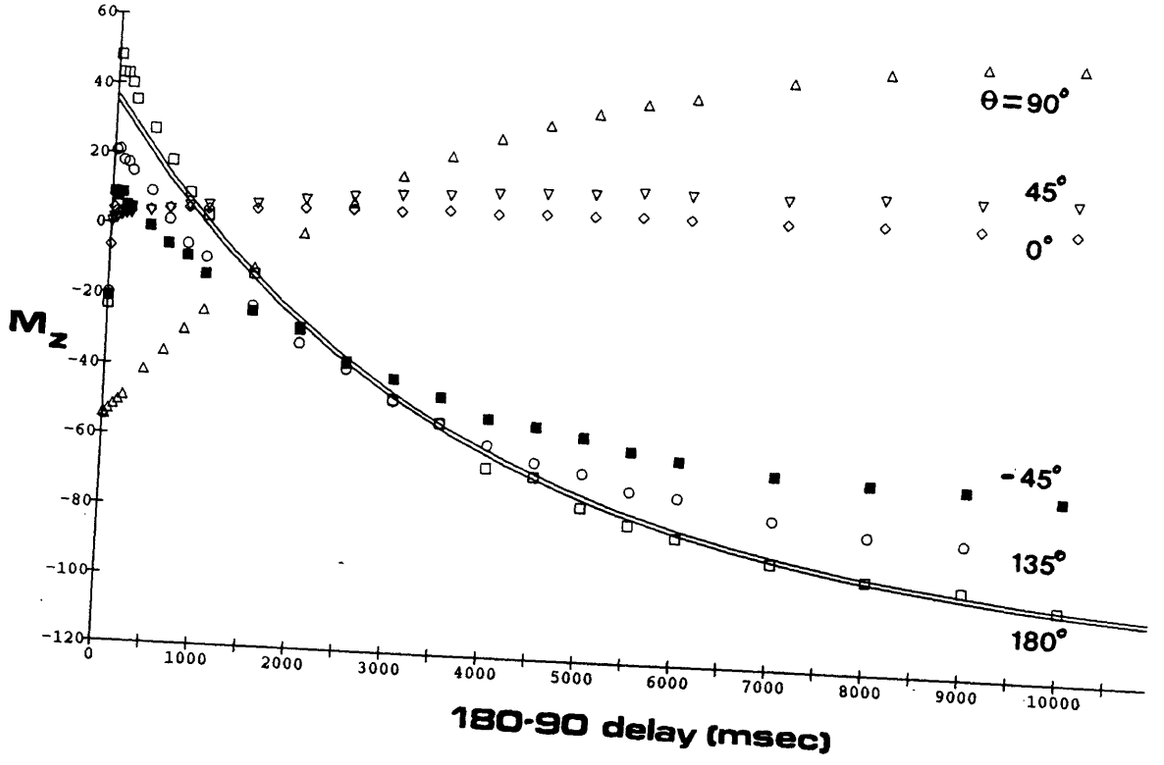
60
40
20
0
-20
-40
-60
-80
-100
-120
M_z
θ=90°
45°
0°
-45°
135°
180°
0
1000
2000
3000
4000
5000
6000
7000
8000
9000
10000
180-90 delay (msec)

Figure 2.9

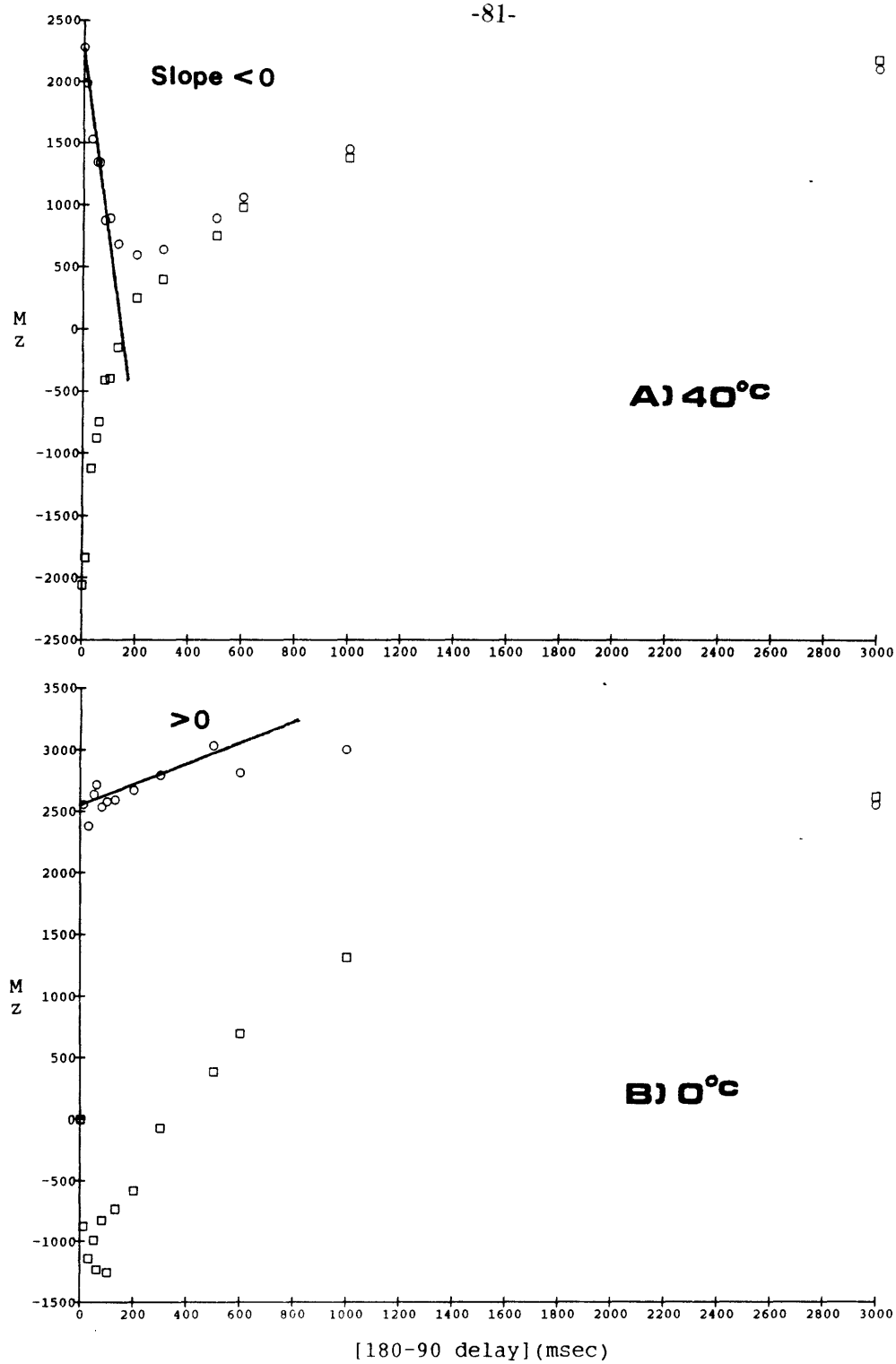

Figure 2.10

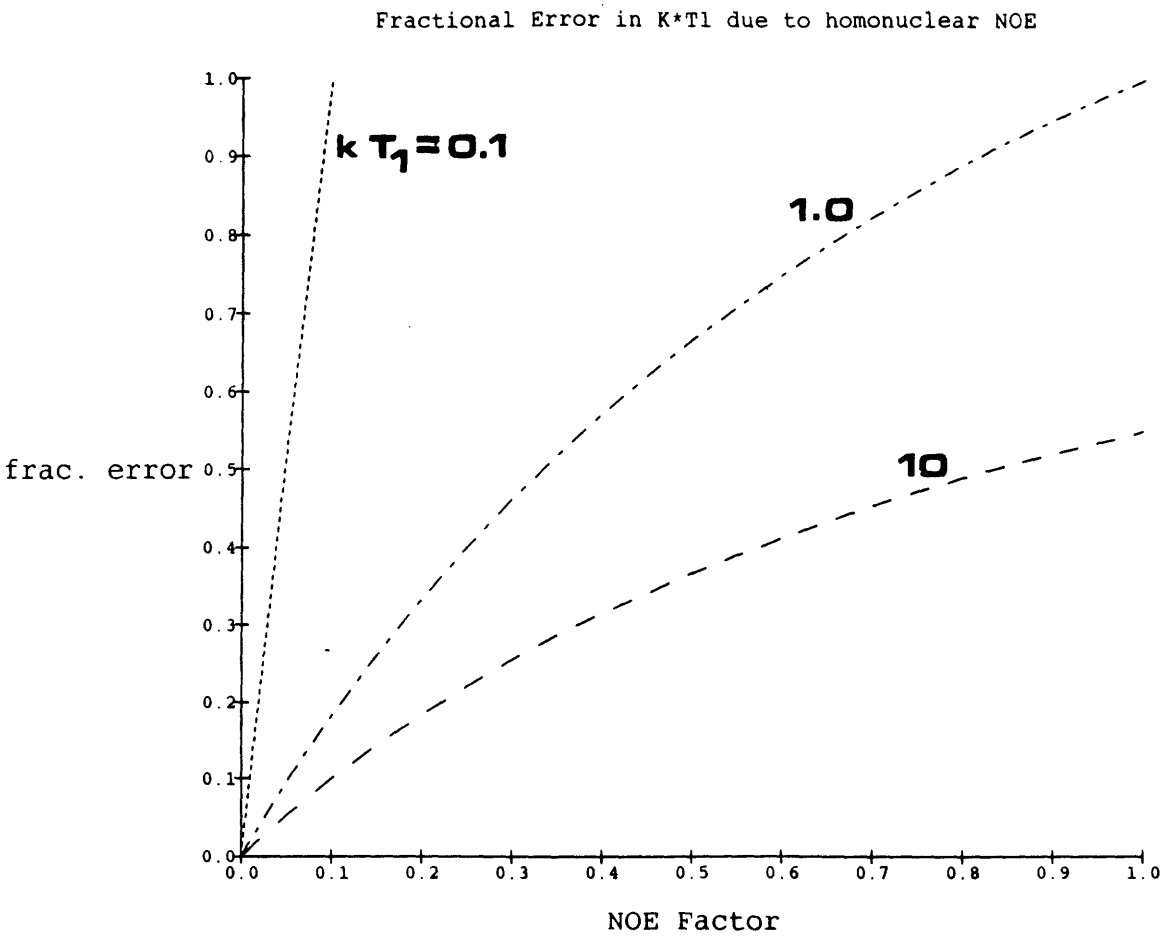
Fractional Error in K*T1 due to homonuclear NOE
frac. error
k T1 = 0.1
1.0
10
NOE Factor
0.0
0.1
0.2
0.3
0.4
0.5
0.6
0.7
0.8
0.9
1.0

Figure 2.11

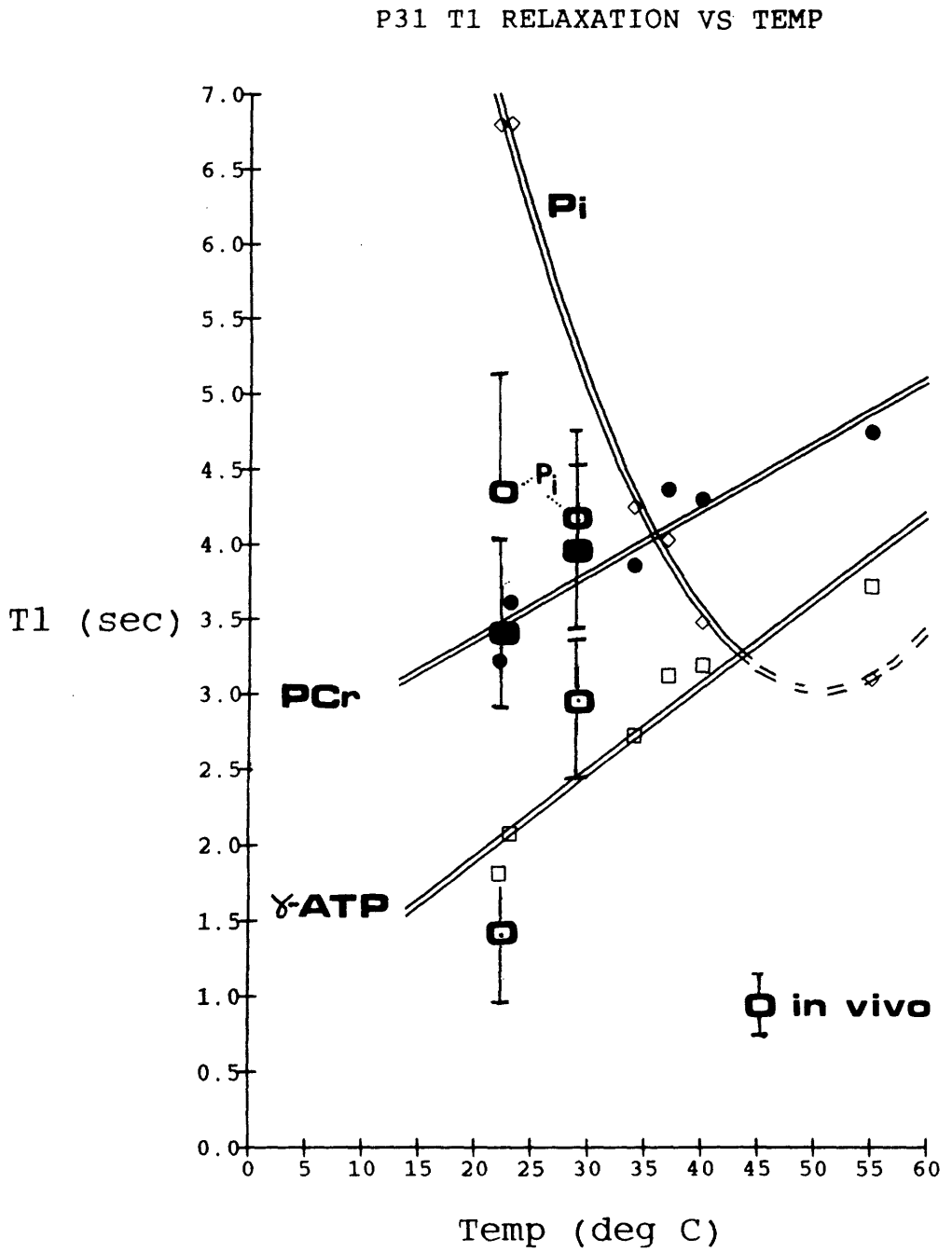
P31 T1 RELAXATION VS TEMP
T1 (sec)
Temp (deg C)
Pi
PCr
γ-ATP
in vivo
7.0
6.5
6.0
5.5
5.0
4.5
4.0
3.5
3.0
2.5
2.0
1.5
1.0
0.5
0.0
0
5
10
15
20
25
30
35
40
45
50
55
60

Figure 2.12

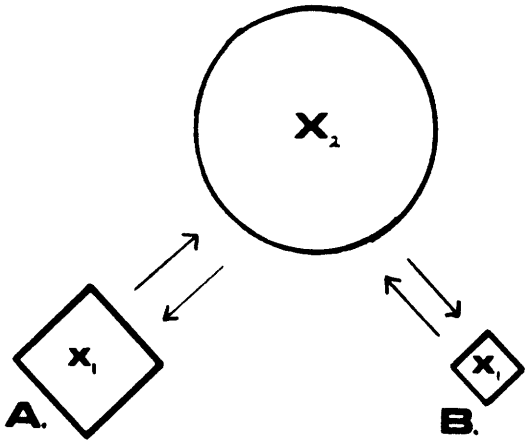

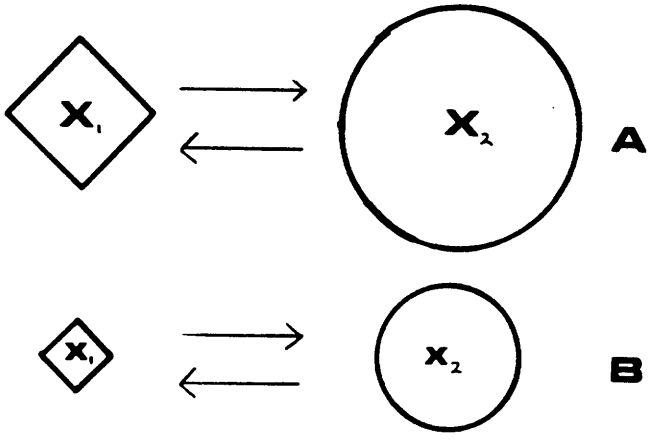

Figure 2.13

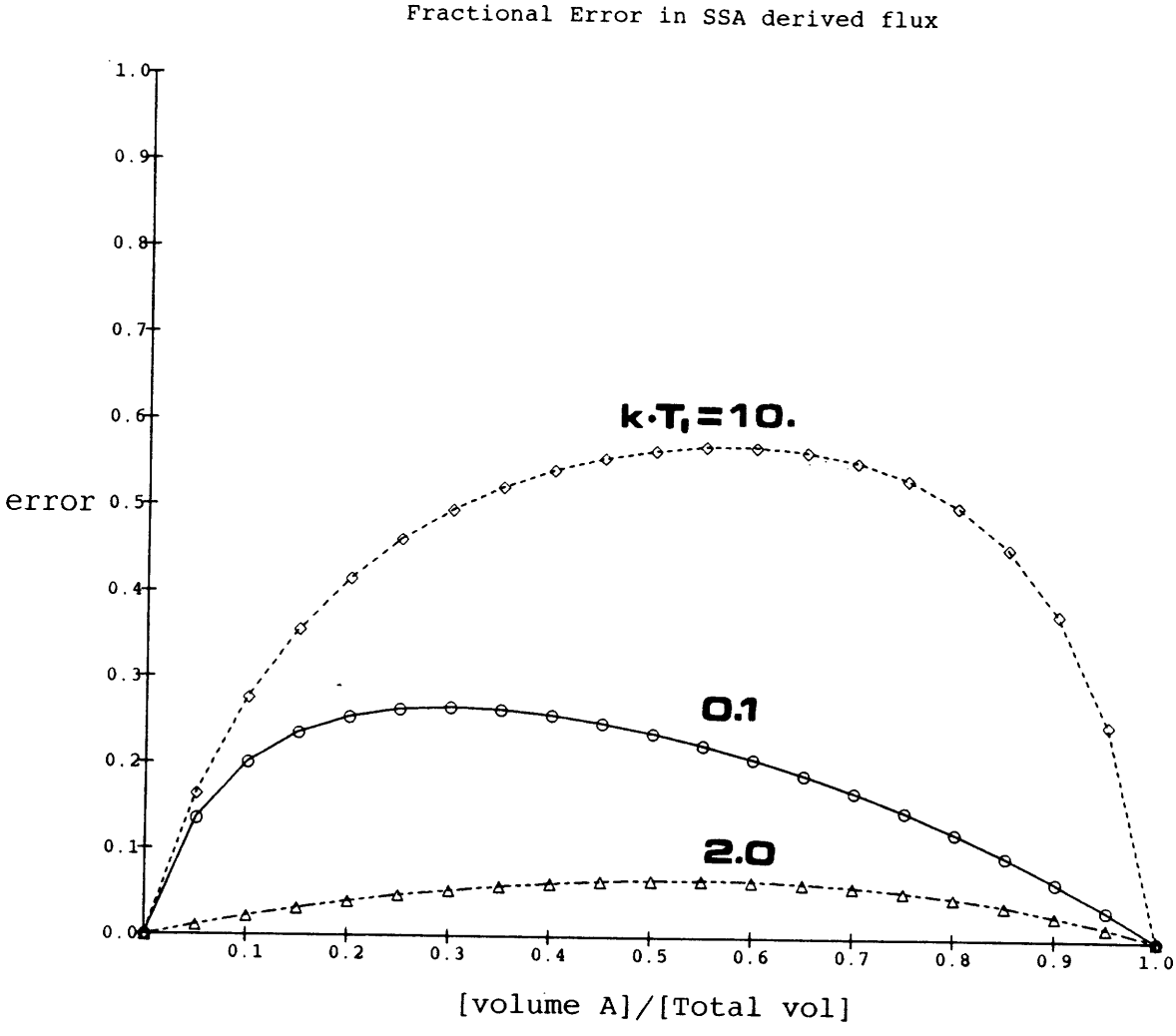
Fractional Error in SSA derived flux
error
1.0
0.9
0.8
0.7
0.6
0.5
0.4
0.3
0.2
0.1
0.0
k·T₁=10.
0.1
2.0
0.1
0.2
0.3
0.4
0.5
0.6
0.7
0.8
0.9
1.0
[volume A]/[Total vol]

Figure 2.14

CHAPTER 3:
OPTIMIZED PROTOCOL FOR MOLECULAR FLUX DETERMINATION

Several theoretical descriptions of NMR magnetization transfer have been published (90,116). Unfortunately, a practical, calibrated, experimental implementation of the technique is lacking. As described in Chapter 2, the susceptability to misinterpretation of all steady-state saturation methods precludes their reliable application *in vivo*. A transient spin-transfer technique is the optimum choice for ill-defined physiological systems, as explained in Chapter 2. The transient inversion transfer method prescribed by Dahlquist et al (30) was implemented by Brown and Ogawa to study the adenylate kinase reaction in E. Coli (21). A limited number of relatively slow reactions can be studied using the long pulse selective inversion methods described. With more rapid exchanges, the long low power pulses used for selective inversion will introduce significant errors (23). An improved experimental technique was developed and calibrated for use in living tissue to give quantitative molecular flux data in a minimum time from samples characterized by low signal-to-noise ratios.

3.1 The Transient Experiment

A transient technique was developed to avoid the theoretical and practical problems associated with the steady state spin transfer experiment. Essential to the transient kinetic experiment is establishment of the initial conditions in a time short compared to the characteristic time of exchange. Traditionally, this was

accomplished with a frequency selective inversion of a single resonance using an approximately 50-200 msec low power pulse (23,4).

Frequency selectivity can also be achieved using a series of short high power ("hard") pulses. Several pulse sequences, including the Dante sequence, have used long trains of hard pulses for selective solvent suppression. Recently, these schemes have been proposed for use in magnetization transfer experiments(113). These sequences are similarly long in duration (38), they are thus undesirable for the study of moderately rapid exchange where significant transfer of magnetization will occur during the establishment of the initial spin state.

Recently, a simple selective excitation sequence was proposed for suppression of unwanted water signals in proton spectroscopy (57). The "binomial pulse" consists of a series of short high power pulses where the flip angle of each element of the series is proportional to coefficients in the binomial series (1-1, 1-3-3-1, ...). An excitation power spectrum of the form (cos(2π*d*f)**n) can be obtained where; d is the delay between the pulses, f is the frequency offset relative to the r.f. transmitter frequency, and n is the number of terms used in the expansion. Nuclei that resonate at the transmitter frequency receive total flips equal to the sum of the individual pulses. For example, a 90-τ-90 pulse is an n=2 pulse producing a 180° pulse in nuclei at the transmitter frequency. The frequency response of a n=4 1-3-3-1 pulse is shown in Figure 3.1b. For selective inversion transfer, the delay d between each hard pulse element is determined by the frequency difference between the two exchanging resonances. For example, the PCr-ATP separation is 360 Hz at 8.5 T. A 90-d-90 pulse centered on PCr with d $=(2*360)^{-1}$ $=.0014$ seconds will invert the PCr resonance and have no effect on the ATP resonance that sits on a null of the sinc power spectrum.

Binomial pulses were incorporated into a transient spin transfer sequence,

Figure 3.2. These and other hard pulse based sequences do not have restrictive timing or waveform requirements and are relatively simple to implement on commercial spectrometers and imagers. In addition to their simplicity, the duration of the binomial sequence is $((n-1))/(2*\Delta\omega)$ where n is the number of binomial coefficients and $\Delta\omega$ is the chemical shift difference between the two exchanging resonances. In the example above the 1-1 selective inversion of PCr required only 1.4 milliseconds and can be reliably applied for reaction rate constants as high as 500 sec^{-1} without allowing significant transfer during the inversion. Achieving inversion essentially instantaneously is critical if the assumed initial conditions of the McConnell equations are to be adequately approximated and use of the simplified initial slope calculations justified.

3.2 Analysis Using the Complete Solutions.

A complete description of the time dependency of the perturbed equilibrium magnetization in any NMR experiment generally requires exponential analysis. In all but the most simple cases, this quickly becomes an intractable problem as combinations of relaxation and chemical exchange add multiple exponential behavior to the evolution of magnetization described by Equation 1.9. Even under the most ideal circumstances fitting transient or steady-state NMR spin transfer data to complicated analytical forms is unreliable. Analytical techniques for fitting *in vitro* exchange data have been presented and methods for optimizing the fits suggested (45). In living systems where signal-to-noise ratios are typically quite low (10-100 in the frequency domain), the exchange system is often ill-defined, and compartmentation of metabolites and non-exchange interactions may be present. For *in vivo* applications an optimized analysis of transient inversion transfer data was investigated which minimizes these effects.

The transient spin transfer data for two-site exchange can be "fit" to the complete solution, Equation 1.12 of the system Equation 1.9 assuming that all exchanges are included and that all sites are NMR observable. To fit the data requires nonlinear curve fitting with a minimum of 5 parameters. Methods of efficiently performing this task have been suggested (81); however, at best, these procedures are useful for *in vitro* data with high SNR's. The problem of fitting noisy data unambiguously to multiparameter models is difficult and easily misinterpreted.

The problem of non-linear least squares fitting of multiexponentials has been examined as a fundamental problem in multivariant analysis. A voluminous literature base exists. Unfortunately, the practical questions, such as how accurate are the best fit parameters, and how many points for a given noise level are necessary to obtain parameters with an error less than ϵ, are answered only indirectly. The difficulty arises in the formation and inversion of the error matrix. In all but the simplest cases, it is not possible.

As in all maximum likelihood or least-squares problems, the analysis begins with the expression for the sum of the squares of the differences between the best model and the data, Y_i. For two-site exchange we have from Equation 1.12:

$$(3.1) \qquad \Delta = \sum_i (\Delta Y_i/\sigma_i)^2 = \sigma^{-2} \sum_{i=1}^{N} (Y_i - A - B\exp(-CX_i) - D\exp(-FX_i))^2$$

Minimizing differences of squares and maximizing likelihood requires formation of the hyperspace Δ in the 5 parameters A,B,C,D,F. The curvature matrix, $d\Delta$, formed from the partial derivatives of the hyperplane, gives the sensitivity of the square deviation to the parameters, a_1=A, a_2=B, a_3=C, a_4=D, a_5=F.

(3.2) $\quad d\Delta = .5(\delta^2\Delta/\delta a_j \delta a_k)$

Table 3.1 is the matrix $d\Delta$ obtained after tedious manipulation of Equation 3.1. Inversion of $d\Delta$ is the fundamental problem of non-linear least squares analysis. In many applications this symmetric matrix can be diagonalized. However, the dependencies of the NMR model equations do not provide independence of $d\Delta/da_j$. Thus, derivation of simplified analytical expressions for the error dependencies is thwarted by a non-invertible matrix.

The problem can be recast and simplified as a linear least squares analysis by making the assumption that, around the minimum, the deviation between the approximation and the true function are small and that an expansion of the exponentials in their Taylor series is justifiable (32).

$$(3.3) \qquad Y(x) = Y_o(x) + \sum (\delta Y_o/\delta a_j)(a_{j_o} - a_j)$$

Now linear in the parameters, Equation 3.3 will have an invertible linear least squares error matrix that depends on the values of a_j's. These are "best" guesses of the parameters around which the expansion took place and would most likely be taken from the non-linear convergence. Their dependencies can only be determined by inversion of $d\Delta$. Thus, linearization allows calculation of errors for a particular fit, giving error estimates of the parameters. However, derivation of explicit analytical expressions for the variance of the coefficients in terms of experimental variables is not possible for the complete inversion transfer dynamical equations.

3.3 SIMULATIONS

To empirically examine the problem of non-linear least squares fitting to NMR derived data, an algorithm was developed to simulate inversion transfer data (Appendix). Random noise was introduced using the conversion factor 5.0 for the ratio of peak-to-peak noise to rms noise. The data was fit to the exact solutions using a non-linear Marquardt-Levenberg combined Gauss-Newton/Steepest Descent routine (86). Initial values were taken as +/-10% of the exact solutions. The parameters were chosen to approximate those found in typical ^{31}P NMR *in vivo* spectroscopy with T_1=2.0 sec, k=0.5 sec^{-1}. The ratio of species was chosen as 1.0 to normalize the ideal coefficients. Table 3.2a shows the results of the fit to the exact double exponential solution for the non-inverted resonance at different levels of noise. The parameter value at convergence is given with its standard error. The inverted magnetization data were fit to the correct model, Equation 1.12, and the incorrect model, Y= G+H*exp(-R*t), and the results given in Tables 3.2b and 3.2c respectively. Clearly, the standard errors in all the fit parameters are often greater when fitting the correct model. Minimization of the standard errors of the fit does not in itself guarantee correctness of the model. These standard errors are often used, improperly, as the standard error in the rate constants. The significance levels listed are the maximum of any single parameter. Large values (> 0.05) reflect a fit that was insensitive to changes in at least one parameter. Additionally, at least for the mono-exponential fits, an approximate relationship between the standard error (SE) in the coefficients and the number of data points appears to exist following, not unexpectedly, as $SE \sim (N)^{-1/2}$. N is directly proportional to the experimental time. This relation only holds for N>2*(number of coefficients). Unfortunately, convergence on double exponential solutions, for SNR_{p-p} values below 10, was not possible when there were less than 8 points; this is the regime

where *in vivo* data often fall.

3.4 AUTOCORRELATION

Since the minimum standard error can be obtained for the fit to an improper model, it is necessary to have further criteria with which to judge model validity. In non-NMR applications where noisy data is used for confirmation of multiexponential models, autocorrelation of the model to the data has been used to analyze goodness-of-fit, (48). The applicability of this method for distinguishing NMR models was investigated using the simulated data. The autocorrelation function, C(t), can be written for n experimental points, $Y(t_i)_{exp}$, as

$$(3.4) \qquad C(t_j) = (n\sum^{m} d(t_i)d(t_{i+j}))[m\sum^{n}(d(t_i))^2]^{-1}$$

where $d(t_i) = Y_{exp}(t_i) - Y_{model}(t_i)$

Figure 3.3 shows C(t) for noiseless data fit to 1) an incorrect model, Figure 3.3a and 2) the exact solution, Figure 3.3b. The random variation in Figure 3.3b arises from division of small numbers (10^{-14}) by numbers of the same magnitude. This is the expected behavior of data subject solely to stochastic fluctuations. Non-random deviations of data from the model produce autocorrelation functions exhibiting non-random behavior as in Figure 3.3a.

Data simulating inversion transfer with a peak-to-peak SNR of 10 was generated and fit to both double and single exponential solutions, (n=64 points). Both fits converged, however, the standard errors in the fits were lower by a factor of 20 for the incorrect single exponential than those for the correct fit. Autocorrelation of the two best fits to the actual data, however, shows that there is

clearly a non-random trend in the incorrect single exponential model, Figure 3.4a. Figure 3.4b shows the expected stochastic fluctuations about the accurate model. The autocorrelation has provided evidence that the single exponential model is inappropriate, in spite of the smaller standard parameter errors. Autocorrelation analysis also confirms, that the deviation of the experimental data from the actual model is consistent with random fluctuations in the data due to experimental noise. Unfortunately, the fit to the true model has significant errors associated with each of the coefficients, especially, when less than 18 points are used with low SNR's. This situation is typical of *in vivo* spectroscopy. Primarily due to limited tissue viability, data accumulation time is short and the number of signal averages limited. Though autocorrelation has shown the "better" model is indeed the biexponential a method of improving the accuracy of the kinetic parameters is still needed.

3.5 Initial Slope Approximations

From the discussion above and the practical limits on SNR for *in vivo* studies the complete solutions are clearly of limited value in determining quantitative *in vivo* kinetic information. Linearization of systems of non-homogeneous differential equations is often used to obtain estimates of coefficients. Campbell et al suggested NMR magnetization transfer data can be analyzed in this way, (23). The question is, does it make sense to even try to use the exact solution forms or, given a fixed data collection time, will the errors due to linearization be small compared to the errors associated with a multiparameter fit? The results of Chapter 2 indicated that three point linearization gives kinetic parameters with the minimum error for short acquisition times. It is desirable to further optimize the linearization to improve the necessary finite error without sacrificing efficiency.

The analysis relies on linearization of the time derivative for "early" points. The systematic error introduced by the linearization procedure was analyzed quantitatively. In Chapter 1, the initial slopes of the inverted and non-inverted resonance were shown to be approximated by

$$(3.5) \qquad \Delta M_i/\Delta t \sim (M_{i_o} - M_i)(k_{ij} + R_i)$$

for the inverted peak, and

$$(3.6) \qquad \Delta M_j/\Delta t \sim -(M_{i_o} - M_i)k_{ij}$$

for the non-inverted exchange partner. Selective inversion of resonance M_i with boundary conditions $M_i(t=0) = M_i$ and $M_j(t=0) = M_{j_o}$ was assumed. $\Delta M/\Delta t$ are the slopes of the linear least squares fit of the transfer data for early points, and $M_{i_o} - M_i$ is the difference between M_i in the relaxed spectrum ($t > 4*T_1$) and the y intercept of the linear least squares fit of the $M_i(t)$ magnetization. Note that k_{nmr} (the ratio of the flux, $M_i \dashrightarrow M_j$, to the equilibrium magnetization, M_{io}) is completely determined (independent of relaxation!) by the initial slope of the non-inverted resonance and $M_{i_o} - M_i$.

The error, ϵ, associated with linearization over the finite time interval, Δt, can be obtained by calculating k from the slope of the magnetization relation determined from the exact solutions at times t_o and t_1, $M(t=t_o)$ and $M(t=t_1)$. The calculated initial slope is obtained by expanding the exponential terms for M(t) in the appropriate Taylor series.

the systematic error due to linearization can be reduced by assuming a model for the exchange system. k' is always smaller than k and can be corrected using a factor calculated by substituting k', T_1', and $k_1'=k'+1/T_1'$ in the linearized solution of the assumed model, calculating k'' and k_1'' from these solutions, and finally calculating the errors, $\epsilon(k',k_1')$ as (k'-k'')/k' and $\epsilon 1(k',k_1')$ as $(k_1'-k_1'')/k_1'$. It is assumed that these errors are approximately equal to (k-k')/k and $(k_1-k_1')/k_1$. The final error after correction of k' by (k'-k'')/k' is

$$(3.10) \qquad \epsilon_{final} = [k - k'/(1-\epsilon(k',k'_1))]/k$$
$$=.(\epsilon(k,k_1).-.\epsilon(k(1-\epsilon),k_1(1-\epsilon_1))(1-\epsilon(k(1-\epsilon),k_1(1-\epsilon_1))^{-1}$$

Figure 3.7 shows simulated data (SNR=5) for k=0.5 sec^{-1} and T_1=2 sec. The initial slopes calculated from points t_o=0.05sec and t_1=0.5 sec are 1.45 and -0.575 for the inverted and non-inverted resonances respectively. The rate constants k' and $k_1' = k'+1/T_1'$ are calculated by dividing the slopes by the change in the inverted peak (1-(-1) = 2), which gives values of k_1' = 0.724 and k' = 0.288. These are underestimates by approximately 28% and 42% of the actual values of 1. and 0.5 respectively. Using these experimental rate constants the fractional errors are calculated from Equations 3.8 and 3.9 as 0.195 and 0.322. The experimental values are corrected by dividing by (1-ϵ), giving k_1=0.90 and k=0.42. These values only differ by 10% and 15% deviations from the true values. Further improvement can be obtained by iteration. Using k_1=0.90 and k=.42 in Equations 3.8 and 3.9 gives second iteration values to within 3% and 8%. Iteration quickly reduces the linearization error to negligible values.

In the presence of noise the error in the slope determination must also be considered. When a simple Y=mX+b linear least-squares fit is used for calculating

$$(3.7)\qquad dM_i/dt \sim (M_i(t_1)-M_i(t_0))/(t_1-t_0) = (t_1-t_0)^{-1}[B[(1-Ct_1+C^2t_1^2/2! + \ldots) -(1-Ct_0+C^2t_0^2/2! + \ldots)] +D[(1-Ft_1+F^2t_1^2/2! + \ldots) -(1-Ft_0+F^2t_0^2/2! + \ldots)]]$$

A similar expression is obtained for M_j. Equation 3.7 can be simplified by writing it in terms of normalized units, $\alpha=k^*T_1$, $\tau=t_1/t_o$, and making the simplification that $\alpha_i \sim \alpha_j$

$$(3.8)\qquad [(k+R) - (k+R)_{exp}]/(k+R) = \epsilon_1 \sim .25(t_o/T_1)(\tau+1)(1 +(2\alpha+1)^2)(\alpha+1)^{-1} -(1/12)(t_o/T_1)^2(\tau^3 -1)/(\tau-1)(1+(2\alpha+1)^3)(\alpha+1)^{-1} + \ldots\ldots$$

$$(3.9)\qquad [k -k_{exp}]/k = \epsilon \sim .25(t_o/T_1)(\tau +1)((2\alpha+1)^2-1)\alpha^{-1} -(1/12)(t_o/T_1)^2(\tau^3 -1)/(\tau-1)((2\alpha+1)^3-1)\alpha^{-1} + \ldots.$$

The error is plotted in Figure 3.5 for a fixed t_o. As expected the error increases with larger linearization intervals and with increased time between the inversion and the first data point. Error is reduced if t_o is taken earlier. The limitation on t_o is largely due to the necessary delay following the inversion pulse within which transverse magnetization must be allowed to diminish prior to application of the 90° readout pulse. This delay can be minimized to approximately 2-4 msec's by use of a homospoil gradient pulse applied immediately after the inversion. The error increases approximately linearly in k, and decreases inversely with T_1, Figure 3.6. Molecular reactions with small exchange fluxes and long T_1's will have the lowest linearization error.

Once the experimental $k = k'$ and $T_1 = T_1'$ are obtained from the linear fit,

the initial slope, the standard error in m is

$$(3.11) \qquad \sigma \sim \sigma_y\left(\sum (X_i\text{-}X)^2\right)^{-1/2}$$

and the standard error for b is

$$(3.12) \qquad \sigma \sim \sigma_y\left[\sum X_i^2/(n \cdot \sum (X_i\text{-}X)^2)\right]^{1/2}$$

where σ_y is the noise per point. Clearly, the lowest errors result from the largest point spacing and the largest SNR. For n measurements we want n/2 at each of the extreme ends of the interval, not equally spaced! If n/2 points are located at t_o and n/2 points at t_1 the standard error from Equation 3.12 is

$$(3.13) \qquad \sigma_m \sim 2\sigma_y * N^{-1/2} * (t_1 - t_o)^{-1}$$

The error in k can be computed from the expression for k, Equation 2.8. For SNR > 10, $\sigma_k \sim \sigma_m/(2*Y_o)$ where Y_o is the equilibrium peak height or area value. Error estimates for k can thus be made using the standard errors in the fits.

To estimate the total error in terms of parameters under the control of the experimenter the standard propagation expression is used

$$(3.14) \qquad \sigma_{k_{total}}{}^2 \sim \sigma_{k_{exp}}{}^2(1\text{-}\epsilon)^{-2} + k_{exp}{}^2(1\text{-}\epsilon)^{-4}[(\sigma_k \delta\epsilon/\delta k)^2 + (\sigma_k \delta\epsilon/\delta k)^2]$$

with $k_1 = 1/T_1 + k$. Using only the first term of Equation 3.9 the total error is

$$(3.15)\quad \sigma_{k_{total}}^{2} \sim \sigma_{Y_i}^{2}[((t_1+t_0)/2 - t_0)^{-2}((1-\epsilon)^{-2} + .(1-\epsilon)^{-4}((k_1(t_1+t_o)-\epsilon)^2 + ((t_1+t_0)(k_1+2k)-\epsilon))^2)]/4N$$

This expression can be optimized to give the conditions for minimum error. Figure 3.8 shows an estimate of the total error for T_1=2 sec and k=.5 and 1.0 sec-1. In both cases t_o= 50 msec. Clearly, different optimum values of the point spacing are found for the two different k values. An increased reaction rate requires a shorter linearization interval for optimal accuracy. For small linearization intervals the error in the slope determination dominates the total error while longer intervals are poorer approximations of the non-linear equations and the linearization error dominates.

3.6 Calibration

Validation of chemical flux values measured by any NMR method must be performed *in vitro* before meaning can be ascribed to measurements made in living systems. Unlike lineshape analysis, where numerous reports comparing NMR derived exchange rates to non-NMR methods have been published (85,64,52), the saturation and inversion transfer techniques have not had adequate calibration. Following the early theoretical formulations of the magnetization transfer, phenomena biomedical investigators have applied the method without the requisite controls. The principle reason for this neglect is the paucity of suitable reactions. NMR methods were developed to measure rates that were difficult to measure by other methods.

For calibration the familiar carbon dioxide hydration reaction was chosen as

the "gold standard" with which to confirm the accuracy of the NMR spin transfer technique, Figure 3.9. In aqueous solution CO_2 reacts to form HCO_3^- directly or by way of the short-lived intermediate H_2CO_3. Most studies have measured rate constants only for the direct conversion, k_{31}. This reaction has been frequently studied by non-NMR techniques, and the published rates appear to be in reasonable agreement (115,71,34). Interestingly, other procedures used to study the carbon dioxide reaction have difficulty in determining individually the rate constants k_{13}, k_{31}, k_{23}, and k_{32} (34). In the course of the calibration measurements, it was discovered, quite unintentionally, that in addition to the desired overall rate of carbon dioxide formation and disappearance, the NMR method could give separately the values of k_{13} and k_{31} and the sum of $k_{32} + k_{31}$ and $k_{13} + k_{12}$. Further work on determining the activation energies of these important steps could be pursued.

Measurements were obtained in solutions near pH 6.5 where the concentrations of bicarbonate and carbon dioxide are approximately equal. The precise pH was calculated from the measured ratios of the CO_2 and HCO_3^- resonances and the temperature corrected equilibrium relationship $[HCO_3^-][H^+/[CO_2] = 5 \times 10^{-7}$ at 37°C and 2.6×10^{-7} at 0°C (54). Figure 3.9 shows ^{13}C spectra of solutions prepared by bubbling ^{13}C CO_2 into 25 mM NaOH, previously purged of oxygen. ^{13}C NMR selective inversion transfer experiments were performed over a range of temperatures (8°C to 55°C) and the rate constants obtained from the initial slopes of the magnetization curves.

The extremely long T_1's of ^{13}C in carbon dioxide and bicarbonate (14 and 25 seconds respectively) allow linearization of the data to approximately 1 second with a negligible systematic error, described in the previous section. In Figure 3.10 an Arrhenius plot of the NMR derived rate constants is shown together with a linear

fit of well accepted data taken from Sanyal and Maren (115) who used stopped flow spectrophotometric techniques. The data was obtained for k_{31} following inversion of the CO_2 resonance. At higher temperatures the decreased solubility of CO_2 reduces the SNR and increases the measurement error. Nonetheless, the NMR derived rate constants are quantitatively in good agreement with the accepted values. Additionally, the activation energy of the reaction CO_2-->HCO_3 determined from the slope of the linear least-squares fit of the data in Figure 3.10 is 63 +/- 8 KJ/mole, which compares to within 16% of the frequently sited value 74.9 KJ/mole (17.9 kcal/mole) (115). From this data it can be concluded that the NMR derived rate constant obtained using a binomial selective inversion in a transient experiment reflects quantitatively the true molecular kinetics.

The rate constant, k_{12}, was also derived from the NMR data, Figure 3.9. This reaction is difficult to observe by non-NMR methods, and the rate is poorly characterized. Following inversion, the HCO_3^- resonance relaxes due to T_1, k_{13}, and k_{12} exchange. k_{13} is calculated from the reduction in the CO_2 resonance. Using a T_1 (from initial slope data) of 24.6 seconds, a value for k_{12} of 1.2×10^{12} $M^{-1}sec^{-1}$ was obtained at 20°C, $^{HCO_3}/_{CO_2} = 0.72$. This preliminary result is approximately 100 times larger than the single unconfirmed value located in the literature (35).

3.7 Applications to Multiple-Site Exchange

The question of multiple-site exchange often arises in poorly defined systems. Binomial selective inversion transfer can be further extended to allow quantitative monitoring of such exchanges. Several methods for studying three-site exchange have been proposed; however, all rely on selective saturation (120,121,104,39). These methods require multi-channel transmission or amplitude modulation of a low power excitation pulse to achieve multi-site irradiations, thereby suffering from

the limitations described in Chapter 2. A transient selective inversion can provide multi-site exchange information with a single excitation. For the three-site exchange of acetlyacetone, Figure 3.1, a single species, M_i, can be inverted. The z magnetization of all non-inverted sites, M_j, follows from Equation 2.10 as

$$\Delta M_j/\Delta t = -(M_{i_o} - M_i)k_{ij} \tag{3.16}$$

Each non-inverted resonance will be reduced in magnitude solely from the exchange processes with M_i. Figure 3.11 shows experiments performed with catalytic amounts of triethylamine added to acetylacetone demonstrating the behavior of the three-site system. From the initial slopes of both non-inverted resonances the fluxes from the inverted resonance to each of the other two sites can be calculated independently. The catalyzed rate constants were found to be k_{ab}=.04+/-.03 sec^{-1}, k_{ac}=.21 +/-.03 sec^{-1} at 23°C. This reaction was studied previously by Forsen et al using saturation techniques (6). It was reported that the direct exchange between the olefinic proton (b) and the enolic form (a) was undetectable (k_{ab}=0) and that all exchange must occur via the keto form. The transient method can similarly be applied to other three or n-site systems.

3.8 Summary

A numerical fit of spin transfer data to the complete solutions of the modified Bloch equations is desirable. However, in experimental situations where noise is the principle limitation, a multiparameter non-linear fit is not practical. Additionally, the proper model of the reacting system is frequently inadequately defined. Often one is approaching a relatively unknown system where the investigation begins with the proposition of a biochemical model. If NMR is to be used to test the

model, autocorrelation of the inversion transfer data with the best fit of the model may support the hypothesis or detect non-random deviations from the best fit parameters, suggesting an error in the description. Once the system model is verified and the form of the modified Bloch equations determined, inversion transfer is the preferred method to quantitatively characterize the kinetics. Data can be obtained optimally by linearizing the equations for early periods following inversion. It is prior knowledge of the model equations that allows this simplification and optimization in data collection. In view of the low sensitivity of the *in vivo* NMR experiment the simpler linear approximations can often give a meaningful, albeit limited, result when insufficient sampling and signal-to-noise is present for convergence on exact solution forms. Fewer data points are required for use of the initial slope technique which provides economy in total experimental time and, under certain circumstances, gives more accurate rate constant values.

In both two and three-site exchange the initial time derivatives will be preferable to the theoretically more precise, though practically difficult, multiparameter fits of the complete analytic solutions. Data obtained *in vivo* rarely have accuracy to better than 20%, and the systematic error introduced by linearization is certainly of acceptable magnitude. If necessary, the data can be further corrected for the predictable deviation using the assumed chemical model.

3.9 Figure Legends

Figure 3.1: Binomial selective 1331 pulse applied to the 3-site exchange of acetylacetone. a) Fully relaxed ^1H control spectrum, (NA=4, LB=1 hz, 360 Mhz). b) Pulse power spectrum for the binomial pulse generated at a frequency centered 2400 hz upfield from resonance B. The location of the center frequency was chosen to optimally invert only resonance B. c) Selective inversion of B is accomplished without perturbation of other exchanging resonances.

Figure 3.2: Generalized pulse sequence for frequency selective magnetization transfer experiments (see also Figure 1.2). RF pulse power can be delivered at two independently controlled frequencies, obs and dec. Selective saturation can be accomplished using low power obs2 or dec2 channels to saturate at the hard pulse (obs1) frequency or an independently selected frequency. a) 1331 binomial pulse inversion recovery sequence without saturation. D_4 is set for $(2*(\omega_1 - \omega_2))^{-1}$ seconds for a $X_1 <--> X_2$ exchange. P_1=22.5° pulse width. $P_3=3*P_1$. D_2 is the variable delay time between the 180° and 90° pulses. P_2 is the 90° readout pulse, $= 4*P_1$. b) 11 binomial pulse sequence without saturation.

Figure 3.3: Autocorrelation of simulated noise-free NMR kinetic data. a) Autocorrelation function, c(t), of simulated inversion transfer data to an incorrect model. Non-random behavior of c(t) is indicative of deviations between the data and the model not attributable to noise. b) Random behavior of c(t) is observed when the correct model is correlated to the data.

Figure 3.4: Autocorrelation of simulated NMR kinetic data (identical to that used in Figure 3.3) with the addition of random noise. a) Gaussian noise (SNR_{p-p}=8) is added to the ideal simulated data and c(t) determined for an

incorrect model. Non-random behavior of c(t) is observed. b) Autocorrelation to the correct model exhibits random fluctuations.

Figure 3.5: Error in NMR derived rate constant due to linearization over a finite period (t_o,t_1). Error (Equation 3.9) is plotted versus t_1/t_o for a fixed t_o set to $T_1/100$. With increasing reaction rates, $\alpha=k*T_1$, the error increases dramatically as the linearization becomes a poorer approximation of the rapidly varying function.

Figure 3.6: Fractional error in k (Equation 3.9) and $k+1/T_1$ (Equation 3.8) as a function of $k*T_1$ for a fixed linearization interval, $t_1/t_o = 5$ with $t_o/T_1=0.01$.

Figure 3.7: Correction of calculated rate constants for linearization errors. Simulated data was generated with SNR=5, k=0.5 sec^{-1}, T_1=2.0 sec. Using the linearization interval t_o=.05 sec and t_1=.5 sec, the calculated k is .29 sec^{-1} and T_1 is 2.3 sec. After iterative correction the final values are 0.42 sec^{-1} and 2.1 sec respectively.

Figure 3.8: Error in the calculated rate constant, k, due to the combined effects of both linearization and random noise. Curves are the error (independent of the number of averages, N, and SNR per point, σ_M) as a function of the length of the linearization interval. Total error is calculated by multiplication of the factor by ($\sigma_M^2/4N$) and taking the square root. For short linearization intervals the error is dominated by large errors in fitting a linear function to a closely grouped set of noisy data. It is assumed that half the points are taken at each end of the interval. As the point spacing is increased, the linear fit is an inadequate approximation to the true relaxation function and the error increases significantly. A clear minimum

exists for optimal point selection. Decreased reaction rates allow larger linearization intervals.

Figure 3.9: Hydration of CO_2 by ^{13}C NMR. In water, CO_2 is in slow exchange with bicarbonate. Carbonic acid is present in only negligible quantities. The rate constant k_{31} can be determined using NMR spin transfer by inversion of the CO_2 resonance and observing the initial slope of the HCO_3^- resonance. Bottom: ^{13}C spectra of an aqueous solution of CO_2 and HCO_3^- obtained at 20°C. pH was determined from the ratio of the peak areas and adjusted with HCl. Shown are spectra from solutions at two different pH values. Insert: The modified Bloch equations for the CO_2 hydration.

Figure 3.10: Arrhenius plot of NMR derived rate constant k_{31}. Data is plotted and compared to the well accepted data from Sanyal et al (3.8), which was determined photometrically (solid line). Activation energy, E_a, for the CO_2 hydration is calculated from the least squares fit of the plot to be =63 +/- 8 KJ/mole. (jan1886,2886,3086,3186,jun0786,0886)

Figure 3.11: Three-site ^1H exchange in acetylacetone at 20°C. Binomial selective inversion transfer data following addition of catalytic amounts of triethylamine. Inversion of resonance A (figure 3.1) was accomplished with a 1331 binomial pulse set 2000 hz upfield from resonance B. From the initial slopes of the magnetization recovery plots, the values for k_{AB}=.04+/-.03 sec^{-1} and k_{AC}=.21+/-.03 sec^{-1} were obtained. (jan288663*.dat).

Table 3.1
Curvature Matrix for Complete Transient Spin Transfer Solution

N	$-\sum \exp[-a_3X_i]$	$\sum a_2X_i\exp[-a_3X_i]$	$-\sum \exp[-a_5X_i]$	$\sum a_4X_i\exp[-a_5X_i]$
$-\sum \exp[a_3X_i]$	$\sum \exp[-2a_3X_i]$	$-\sum (Y_i-a_1+a_4e^{-a_5X_i}+2a_2e^{-a_3X_i})X_i\exp[-a_3X_i]$	$\sum \exp[-X_i(a_3+a_5)]$	$-\sum a_4X_i\exp[-(a_3+a_5)X_i]$
$\sum a_2X_i\exp[-a_3X_i]$	$-\sum (Y_i-a_1+a_4e^{-a_5X_i}+2a_2e^{-a_3X_i})X_i\exp[-a_3X_i]$	$\sum (Y_i-a_1+a_4e^{-a_5X_i}+a_2e^{-a_3X_i})a_2X_i^2\exp[-a_3X_i]$	$-\sum a_2X_i\exp[-X_i(a_3+a_5)]$	$\sum a_4a_2X_i^2\exp[-X_i(a_3+a_5)]$
$-\sum \exp[-X_ia_5]$	$\sum \exp[-X_i(a_3+a_5)]$	$-\sum a_2X_i\exp[-X_i(a_3+a_5)]$	$\sum \exp[-2X_ia_5]$	$-\sum (Y_i-a_1+a_2e^{-a_3X_i}+2a_4e^{-a_5X_i})X_i\exp[-a_5X_i]$
$\sum a_4X_i\exp[-X_ia_5]$	$\sum a_4X_i\exp[-X_i(a_3+a_5)]$	$\sum a_2a_4X_i^2\exp[-X_i(a_3+a_5)]$	$-\sum (Y_i-a_1+a_2e^{-a_3X_i}+2a_4e^{-a_5X_i})X_i\exp[-a_5X_i]$	$-\sum (Y_i-a_1+a_2e^{-a_3X_i}+2a_4e^{-a_5X_i})a_4X_i^2\exp[-a_5X_i]$

$$d\Delta = [\text{above}] \times \sigma^2/2$$

TABLE 3.2A Best Fit Coefficients and Standard Error of
Y= A + B*EXP(-C*X) + D*EXP(-F*X)

SNRpp	n	A(SE)	B(SE)	C(SE)	D(SE)	F(SE)
inf	20	1.00(1e-7)	-1.00(7e-6)	0.50(3e-6)	1.00(8e-6)	1.50(6e-6)
	10	1.00(1e-7)	-1.00(7e-6)	0.50(3e-6)	1.00(7e-6)	1.50(6e-6)
	5	1.00(1e-10)	-1.00(8e-9)	0.50(3e-9)	1.00(1e-9)	1.50(1e-9)
28	32	0.98(.01)	-1.04(.16)	0.53(.06)	1.05(.17)	1.48(.12)
	18	1.02(.03)	-0.95(.12)	0.45(.07)	0.93(.14)	1.54(.14)
	14	1.01(.04)	-0.97(.21)	0.48(.11)	0.96(.24)	1.53(.20)
	12	1.11(.06)	-0.85(.03)	0.31(.07)	0.73(.08)	1.76(.14)
	10	0.95(.03)	-1.25(.68)	0.63(.19)	1.29(.71)	1.38(.26)
	8	1.11(.06)	-0.82(.02)	0.30(.05)	0.71(.05)	1.84(.09)
	6	0.98(.07)	-1.03(.38)	0.54(.21)	1.04(.44)	1.52(.27)
17	32	0.97(.02)	-1.07(.30)	0.56(.11)	1.09(.32)	1.46(.20)
	20	0.97(.03)	-1.37(.74)	0.63(.18)	1.39(.76)	1.32(.28)
	16	1.01(.05)	-0.95(.26)	0.47(.15)	0.93(.30)	1.55(.28)
	10	0.97(.04)	-1.26(1.1)	0.62(.29)	1.28(1.1)	1.39(.52)
	8	0.98(.07)	-1.39(2.1)	0.61(.48)	1.39(2.1)	1.30(.79)
8	32	0.95(.04)	-1.18(.94)	0.62(.27)	1.22(.96)	1.42(.45)
	16	1.02(.11)	-0.91(.39)	0.43(.27)	0.88(.48)	1.60(.53)
	8	0.98(.13)	-1.90(12.)	0.69(1.4)	1.89(12.)	1.18(2.0)
3	32	0.89(.08)	-1.74(12.)	0.85(1.6)	1.82(12.)	1.37(2.2)
	16	1.09(.54)	-0.84(.31)	0.31(.62)	0.72(.72)	1.79(1.4)
	8	1.00(.40)	-1.80(22.)	0.67(3.4)	1.73(23.)	1.22(5.5)

TABLE 3.2B Best Fit Coefficients and (Standard Error) of Fit to
Y= A + B*EXP(-C*X) + D*EXP(-F*X)

SNR	n(sig lev)	A	B	C	D	F
inf	20	1.00(1e-6)	-1.00(1e-5)	0.50(1e-5)	-1.00(1e-5)	1.50(1e-5)
	10	1.00(2e-6)	-1.00(2e-5)	0.50(1e-5)	-1.00(2e-5)	1.50(2e-5)
	5	1.00(e-17)	-1.00(e-16)	0.50(e-16)	-1.00(e-16)	1.50(e-16)
	all to sig lev < .0001					
28	32(.0001)	0.98(.01)	-1.04(.14)	0.53(.06)	-0.95(.15)	1.52(.12)
	18(.001)	1.02(.03)	-0.95(.15)	0.45(.08)	-1.08(.17)	1.46(.13)
	14(.004)	1.01(.04)	-0.97(.24)	0.48(.12)	-1.04(.27)	1.48(.19)
	12(.10)	1.16(.15)	-0.78(.04)	0.25(.13)	-1.37(.16)	1.29(.09)
	10(.06)	0.96(.03)	-1.14(.31)	0.60(.13)	-0.82(.34)	1.59(.29)
	8(.32)	1.31(.36)	-0.82(.26)	0.16(.13)	-1.49(.11)	1.22(.05)
	6(.30	0.98(.07)	-1.03(.42)	0.54(.23)	-0.95(.49)	1.48(.31)
17	32(.001)	0.97(.02)	-1.06(.25)	0.56(.10)	-0.92(.26)	1.54(.22)
	20 (.02)	0.97(.02)	-1.30(.23)	0.63(.09)	-0.68(.25)	1.80(.35)
	16 (.02)	1.01(.05)	-0.94(.32)	0.46(.17)	-1.08(.37)	1.45(.26)
	14 (.05)	1.01(.07)	-0.95(.38)	0.46(.21)	-1.07(.44)	1.46(.31)
	10 (.16)	0.95(.02)	-1.50(.28)	0.71(.10)	-0.47(.29)	2.22(.95)
	8 (.22)	0.97(.03)	-1.47(.34)	0.67(.13)	-0.53(.35)	2.25(1.1)
	7 (.33)	0.98(.05)	-1.41(.47)	0.63(.19)	-0.61(.48)	2.16(1.3)
	5 (1.)	1.16(ncv)	-0.88(ncv)	0.26(ncv)	-1.30(.46)	1.42(ncv)
	5 (1.)	1.06(ncv)	-0.49(ncv)	0.22(ncv)	-1.57(ncv)	1.14(ncv)
8	32 (.17)	0.95(.03)	-1.14(.58)	0.61(.20)	-0.83(.60)	1.58(.55)
	16 (.27)	1.02(.14)	-0.88(.58)	0.42(.36)	-1.16(.70)	1.40(.46)
	8 (.42)	0.97(.05)	-1.62(.37)	0.72(.17)	-0.41(.35)	3.03(3.2)
3	32 (.87)	0.89(.06)	-1.58(2.1)	0.84(.56)	-0.34(2.1)	1.99(4.9)
	16 (.87)	1.31(3.7)	-0.84(2.5)	0.15(1.3)	-1.51(1.2)	1.22(.70)
	14 (.84)	1.13(1.3)	-0.83(.70)	0.27(1.3)	-1.34(1.9)	1.32(1.3)
	8 (.76)	0.99(.13)	-1.76(.57)	0.72(.32)	-0.42(.46)	4.62(14.)

TABLE 3.2C Fit of Spin Transfer to Y= G + H*exp(-R*x)
Best-Fit Parameters (Std. Error)

SNR	n(sig. lev)	G	H	R
inf	20	0.90(.013)	-1.86(.017)	0.93(.022)
	10	0.92(.020)	-1.86(.027)	0.90(.034)
	5	0.94(.030)	-1.83(.050)	0.84(.060)
	all to sig lev < .0001			
28	32(.0001)	0.90(.01)	-1.87(.01)	0.92(.02)
	18(.0001)	0.90(.02)	-1.87(.02)	0.92(.03)
	14(.0001)	0.89(.02)	-1.87(.02)	0.94(.03)
	12(.0001)	0.89(.02)	-1.87(.02)	0.94(.03)
	10(.0001)	0.88(.02)	-1.86(.02)	0.96(.03)
	8(.0001)	0.87(.02)	-1.86(.02)	0.96(.03)
	6(.001)	0.87(.02)	-1.86(.03)	0.98(.04)
17	32(.0001)	0.90(.01)	-1.87(.01)	0.93(.02)
	20(.0001)	0.90(.01)	-1.87(.02)	0.92(.02)
	16(.0001)	0.89(.02)	-1.87(.02)	0.93(.03)
	14(.0001)	0.89(.02)	-1.87(.02)	0.93(.03)
	10(.0001)	0.91(.02)	-1.87(.03)	0.91(.03)
	8(.0001)	0.92(.03)	-1.87(.03)	0.89(.04)
	5(.0001)	0.92(.05)	-1.88(.06)	0.89(.08)
8	32(.0001)	0.89(.01)	-1.87(.02)	0.94(.02)
	16(.0001)	0.89(.02)	-1.87(.03)	0.93(.03)
	8(.0001)	0.92(.03)	-1.89(.04)	0.89(.05)
3	32(.0001)	0.87(.03)	-1.88(.04)	0.97(.05)
	16(.0001)	0.88(.04)	-1.89(.05)	0.92(.07)
	8(.0001)	0.94(.07)	-1.96(.09)	0.87(.11)

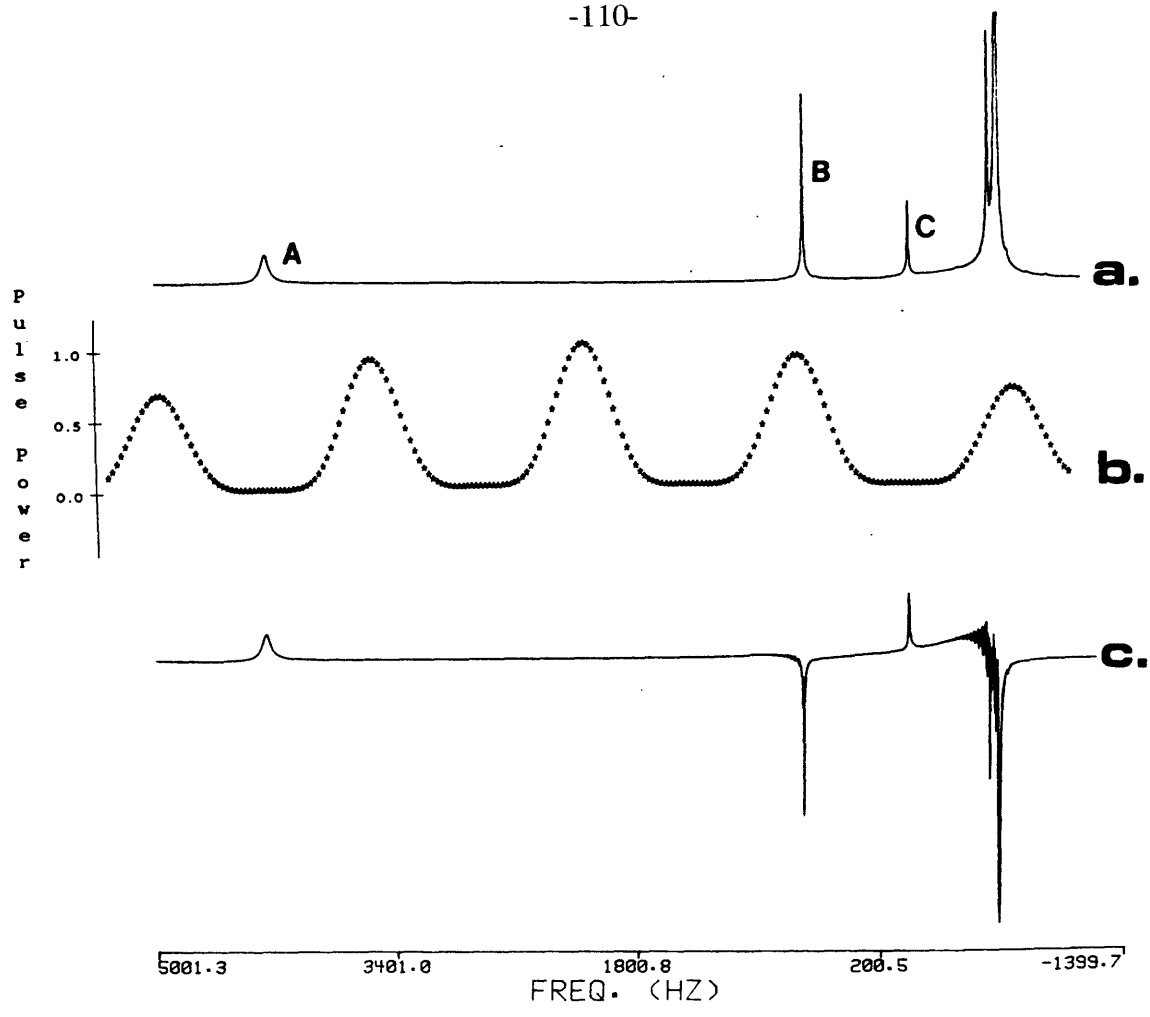
A
B
C
a.
b.
c.
Pulse power
1.0
0.5
0.0
5001.3
3401.0
1800.8
200.5
-1399.7
FREQ. (HZ)

Figure 3.1

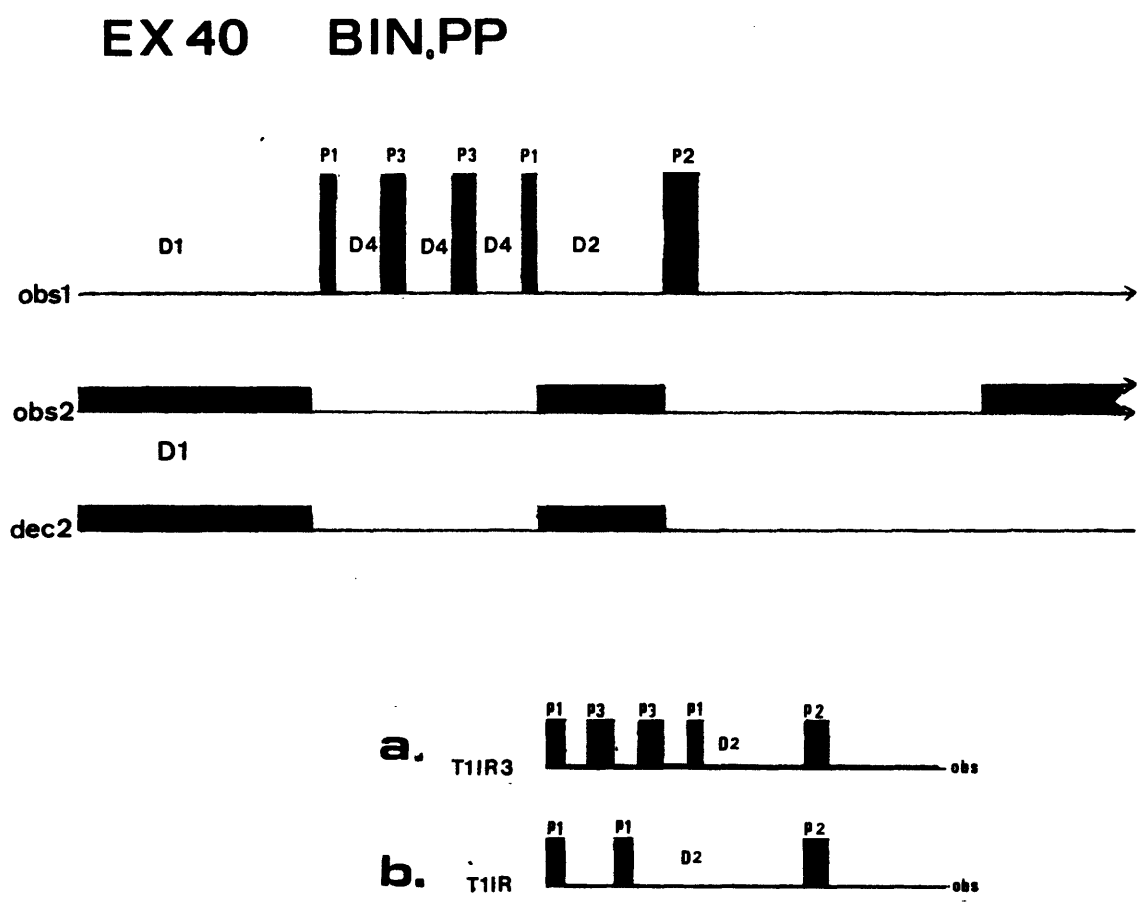
EX 40 BIN.PP
P1
P3
P3
P1
P2
D1
D4
D4
D4
D2
obs1
obs2
D1
dec2
a.
T1IR3
P1
P3
P3
P1
D2
P2
obs
b.
T1IR
P1
P1
D2
P2
obs

Figure 3.2

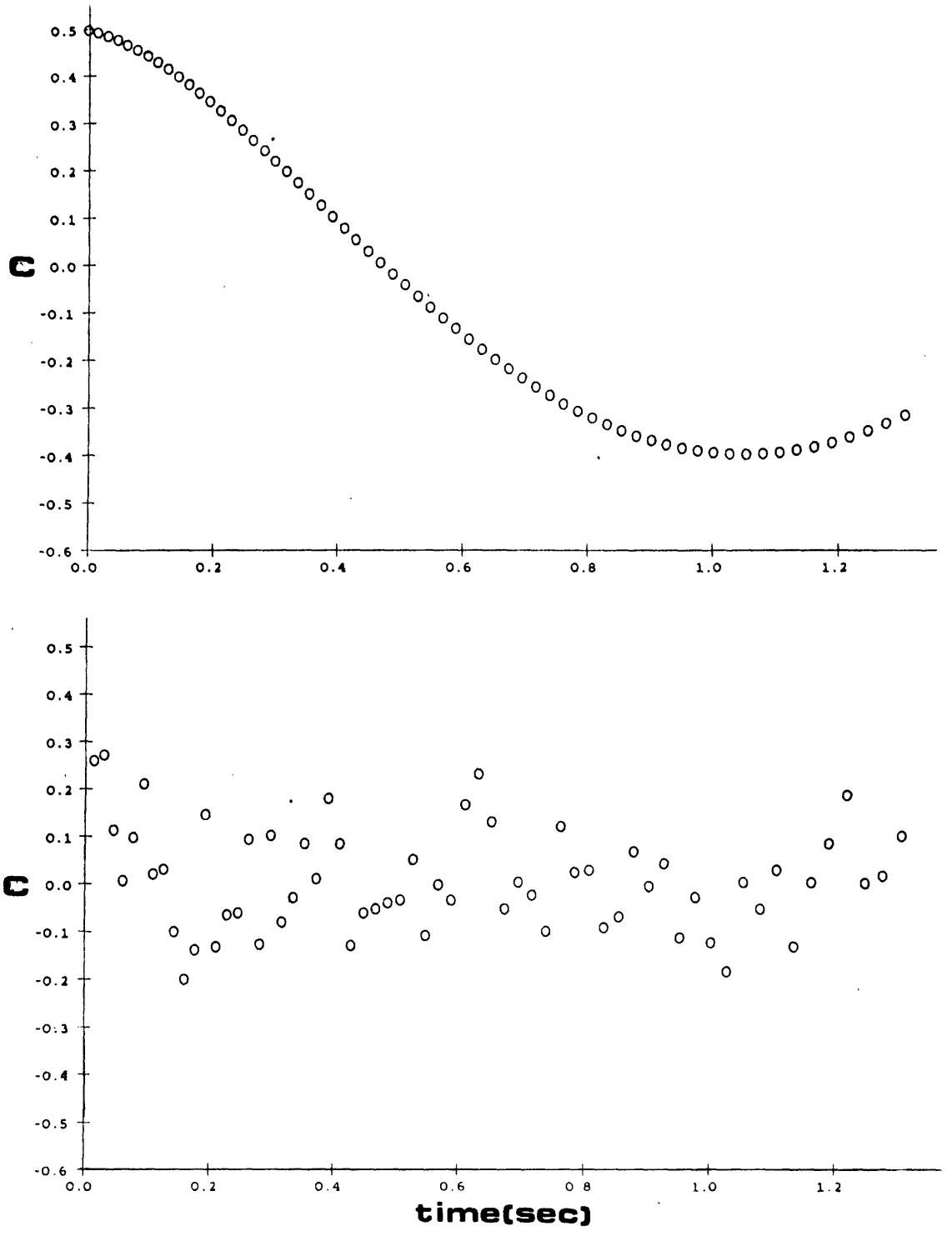

Figure 3.3

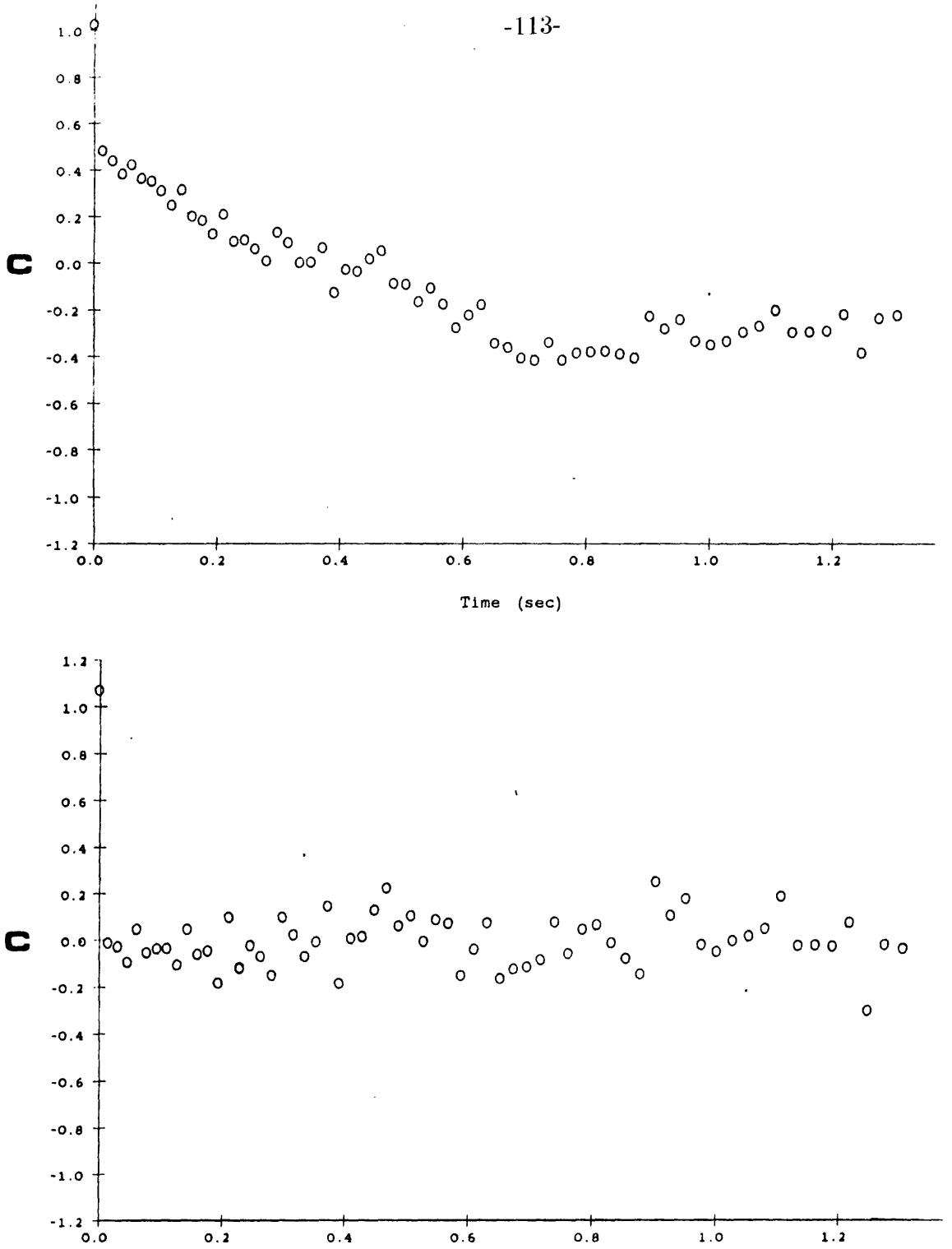
C
1.0
0.8
0.6
0.4
0.2
0.0
-0.2
-0.4
-0.6
-0.8
-1.0
-1.2
0.0
0.2
0.4
0.6
0.8
1.0
1.2
Time (sec)
C
1.2
1.0
0.8
0.6
0.4
0.2
0.0
-0.2
-0.4
-0.6
-0.8
-1.0
-1.2
0.0
0.2
0.4
0.6
0.8
1.0
1.2

Figure 3.4

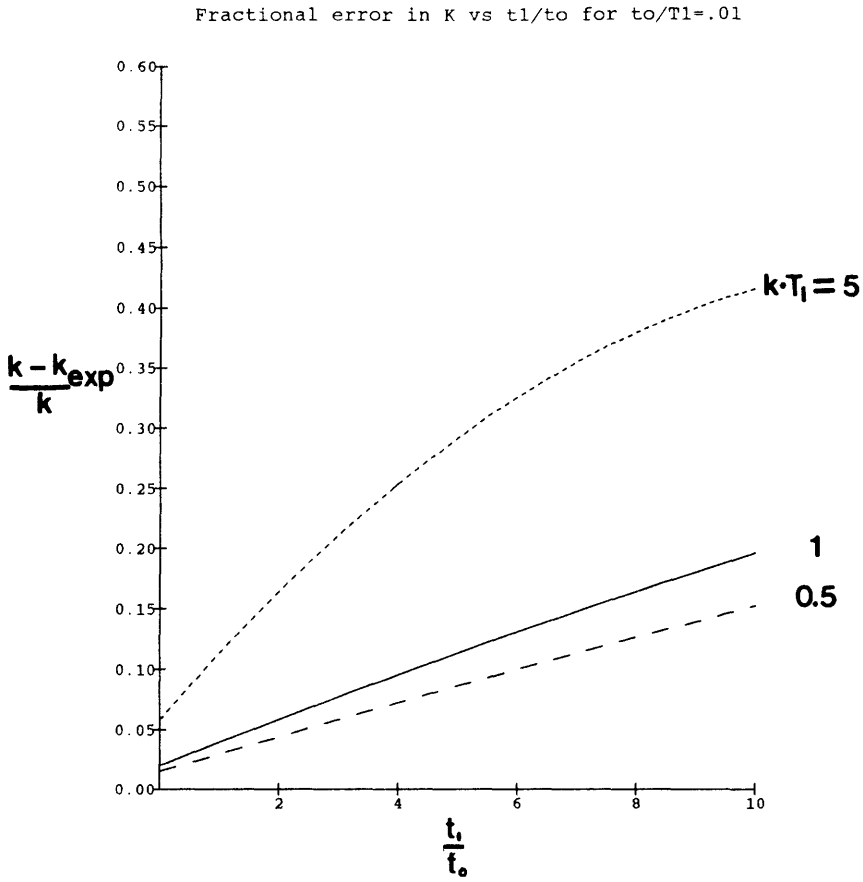
Fractional error in K vs t1/to for to/T1=.01
0.60
0.55
0.50
0.45
0.40
0.35
0.30
0.25
0.20
0.15
0.10
0.05
0.00
2
4
6
8
10
k·T1 = 5
1
0.5
k − kexp / k
t1 / to

Figure 3.5

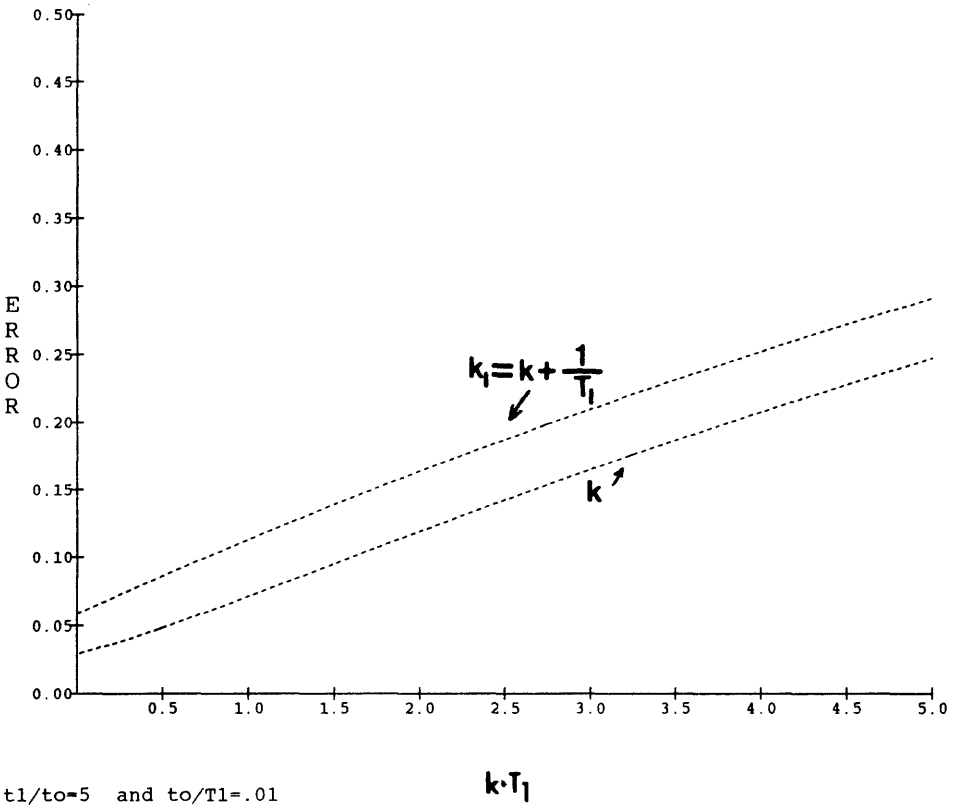
0.50
0.45
0.40
0.35
0.30
0.25
0.20
0.15
0.10
0.05
0.00
ERROR
$k_1 = k + \frac{1}{T_1}$
k
0.5
1.0
1.5
2.0
2.5
3.0
3.5
4.0
4.5
5.0
$k \cdot T_1$
t1/to=5 and to/T1=.01

Figure 3.6

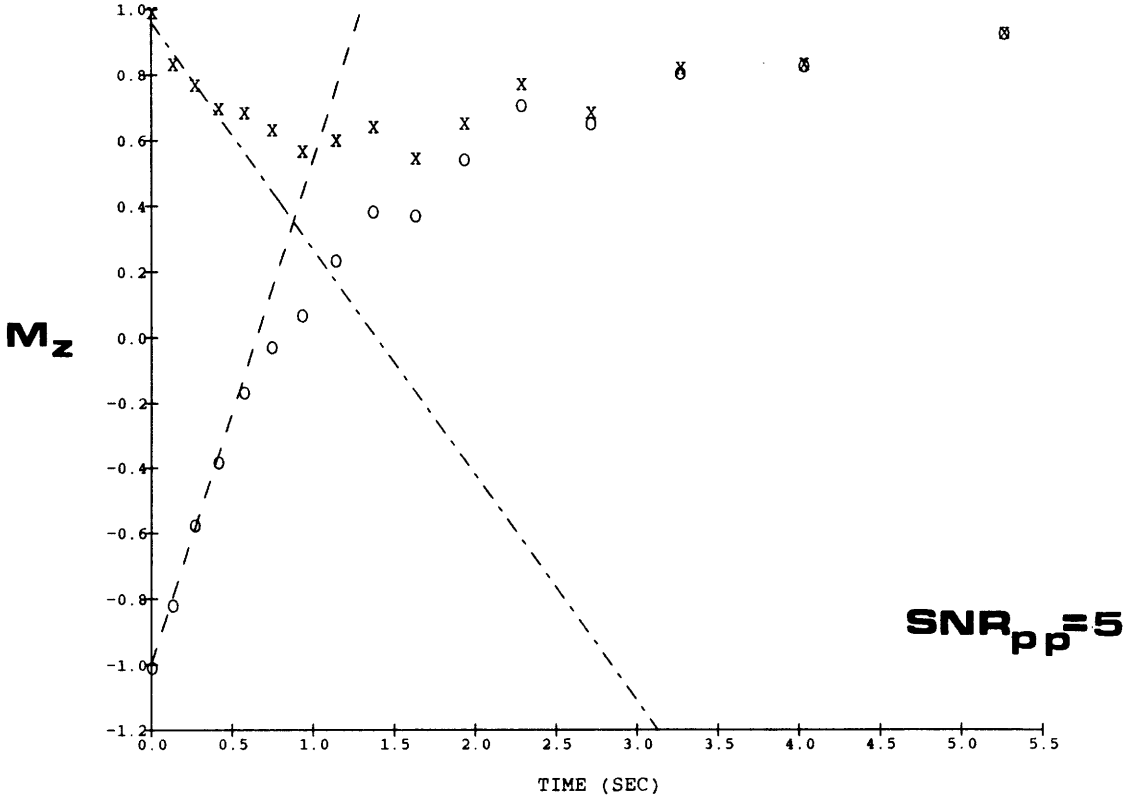
M_z
$SNR_{pp}=5$
TIME (SEC)
1.0
0.8
0.6
0.4
0.2
0.0
-0.2
-0.4
-0.6
-0.8
-1.0
-1.2
0.0
0.5
1.0
1.5
2.0
2.5
3.0
3.5
4.0
4.5
5.0
5.5

Figure 3.7

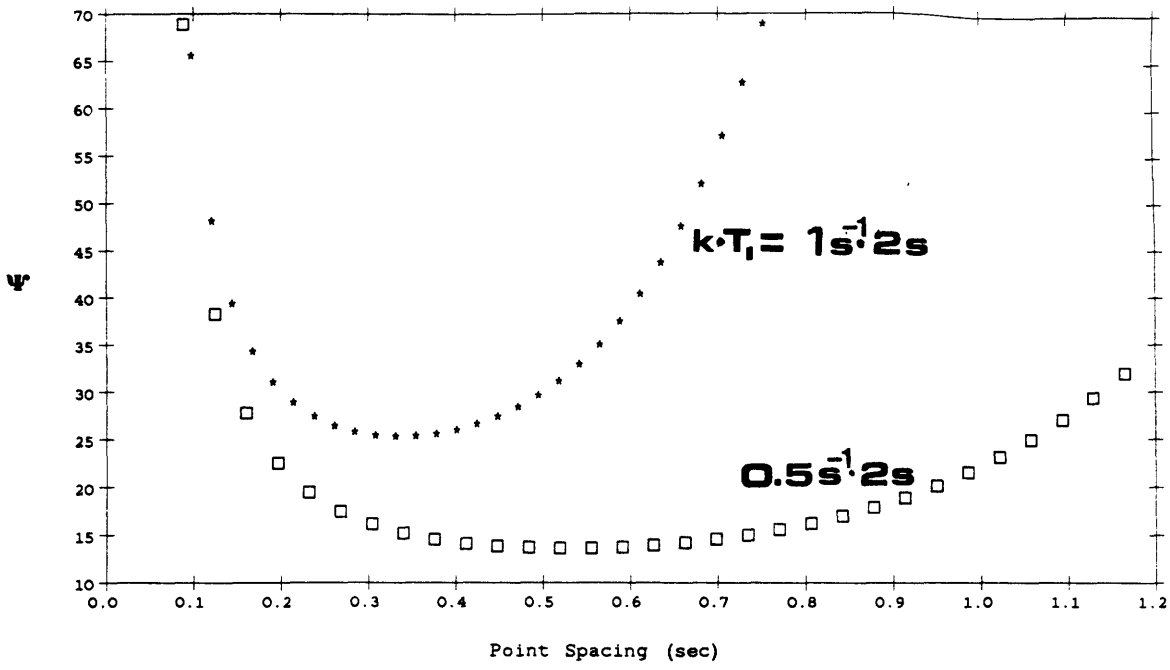

$$\sigma^2_{total} = \Psi * \frac{\sigma^2_M}{4*N}$$

Figure 3.8

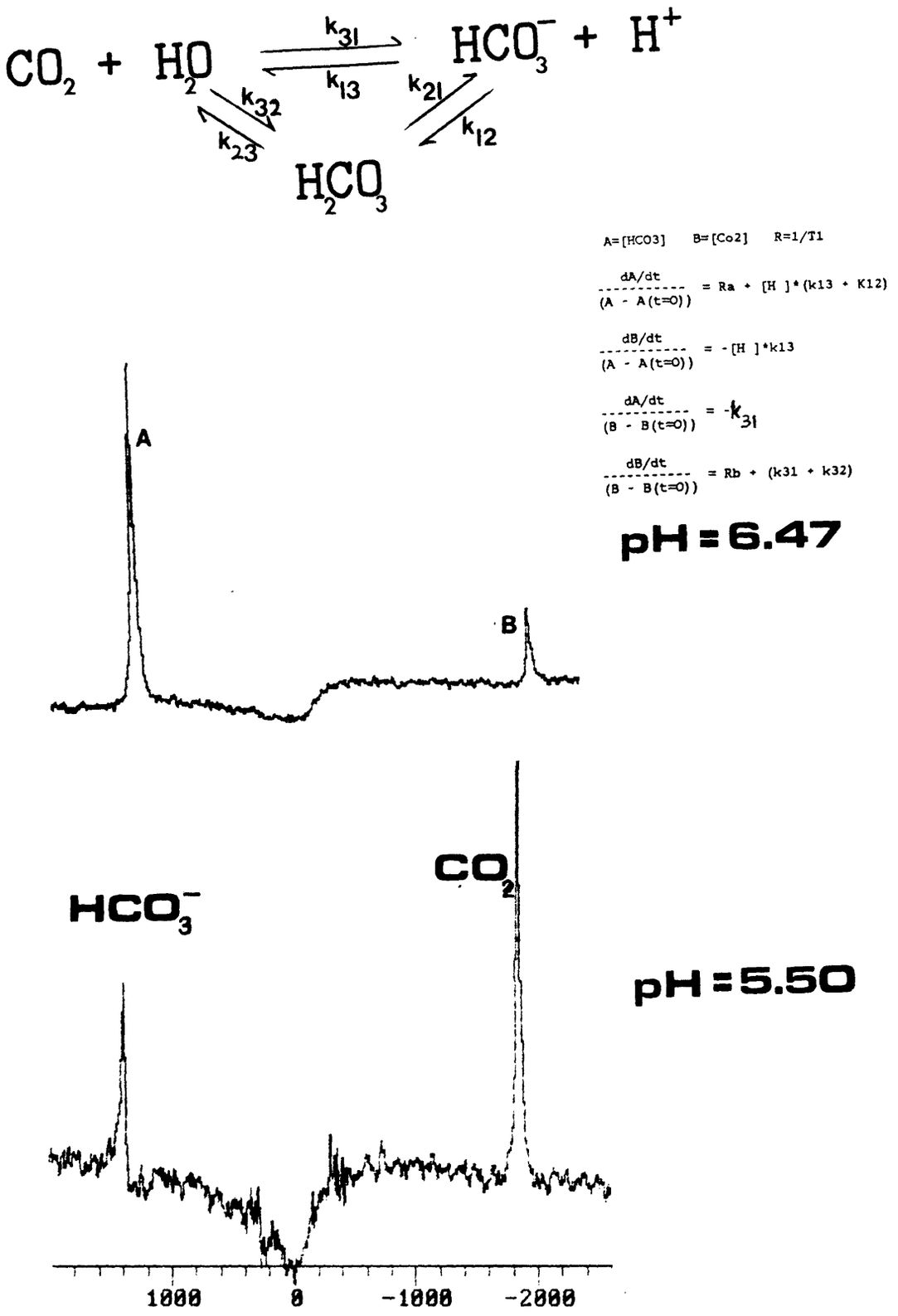
$CO_2 + H_2O$
k_{31}
k_{13}
$HCO_3^- + H^+$
k_{32}
k_{23}
k_{21}
k_{12}
H_2CO_3
A=[HCO3] B=[Co2] R=1/T1
dA/dt / (A - A(t=0)) = Ra + [H]*(k13 + K12)
dB/dt / (A - A(t=0)) = -[H]*k13
dA/dt / (B - B(t=0)) = -k31
dB/dt / (B - B(t=0)) = Rb + (k31 + k32)
pH = 6.47
A
B
HCO_3^-
CO_2
pH = 5.50
1000
0
-1000
-2000

Figure 3.9

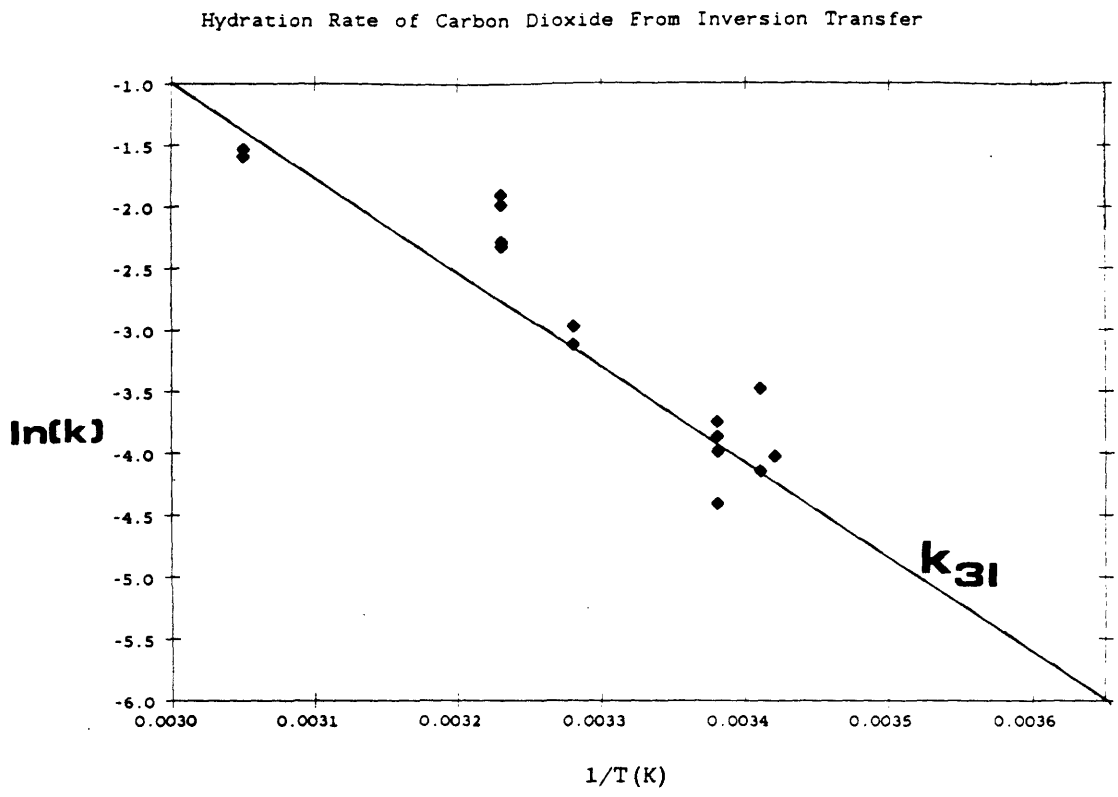
Hydration Rate of Carbon Dioxide From Inversion Transfer
ln(k)
-1.0
-1.5
-2.0
-2.5
-3.0
-3.5
-4.0
-4.5
-5.0
-5.5
-6.0
0.0030
0.0031
0.0032
0.0033
0.0034
0.0035
0.0036
1/T(K)
k31

Figure 3.10

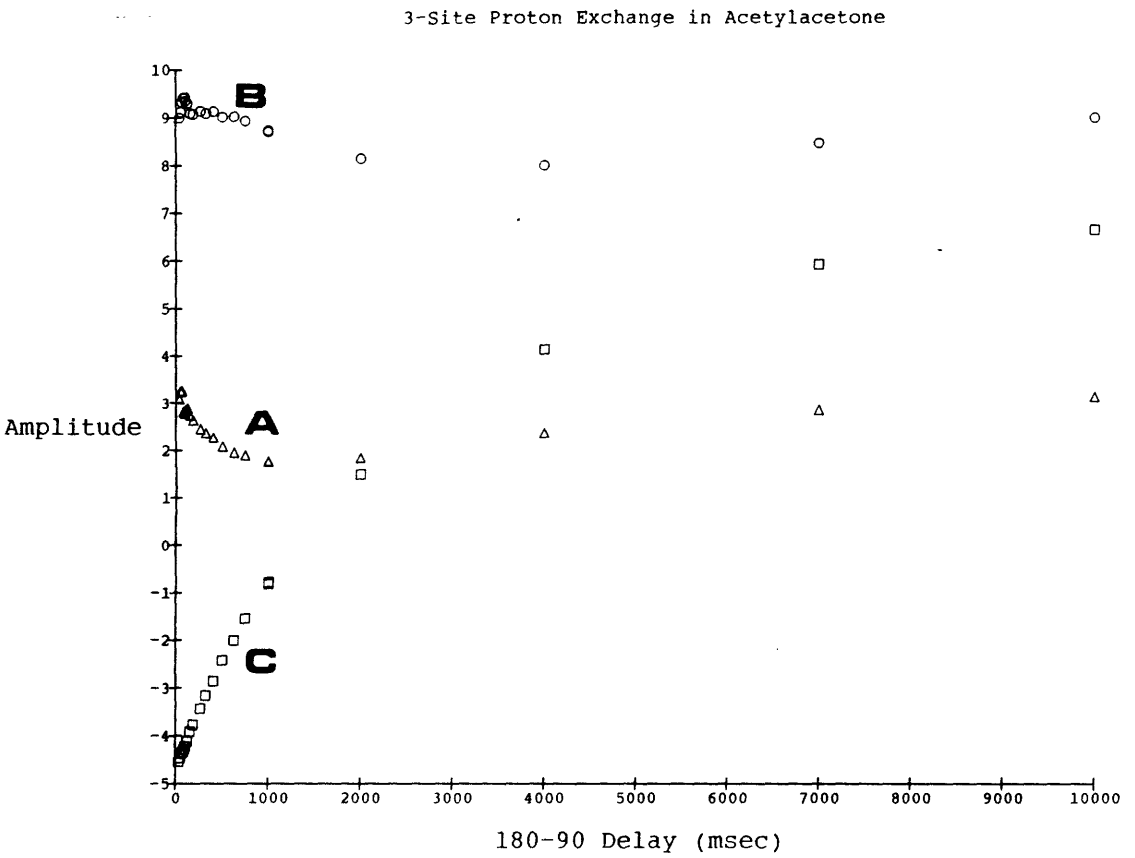
3-Site Proton Exchange in Acetylacetone
Amplitude
B
A
C
10
9
8
7
6
5
4
3
2
1
0
-1
-2
-3
-4
-5
0
1000
2000
3000
4000
5000
6000
7000
8000
9000
10000
180-90 Delay (msec)

Figure 3.11

CHAPTER 4:
[ADP] AND THE ROLE OF CREATINE KINASE IN SLOW-TWITCH MAMMALIAN MUSCLE

4.1 ADP Determination and the Controversial Role of Creatine Kinase in Muscle

^{31}P NMR has made possible the direct quantitative determination of the millimolar concentrations of intracellular ATP, PCr, and Pi, *in vivo*. Previously, labile phosphate compounds were assayed by rapid freezing methods which over-estimated [Pi] and [ADP] and under-estimated [PCr] in living tissue (111). The acid extraction processes utilized for ADP assays are thought to release the nucleotide from actin binding sites and are unable to instantaneously halt ATP hydrolysis (82). Intracellular ADP concentrations greater than 0.6mM were measured by these methods (111). Direct ^{31}P NMR determination of [ADP] is not practical *in vivo* because the two ADP resonances are of negligible magnitude in comparison to the γ and α ATP peaks which overlap them. However, [ADP] can be indirectly determined using the NMR measured quantities of other ^{31}P metabolites.

Muscle contains the enzyme creatine kinase, (CK), catalyzing the ^{31}P transfer reaction PCr + ADP + H^+ <--> ATP + Cr. At equilibrium, the concentration of intracellular [ADP] may be estimated using the relationship:

$$(4.1) \qquad K_{ck} = \frac{[ATP]*[Cr_{total} - PCr]}{[H^+]*[PCr]*[ADP]}$$

It is assumed that total tissue creatine remains constant and $[Cr_{free}]=[Cr_{total} - PCr]$. The equilibrium constant, K_{ck}, of the purified enzyme has been shown to be strongly dependent on pH and $[Mg^{++}]$ and falls in the range of 1.0-3.0 x $10^9 M^{-1}$ in skeletal, smooth, and cardiac muscle (80).

Estimates of intracellular [ADP] levels determined using Equation 4.1 and the ^{31}P NMR measured [ATP], [PCr], and pH are considerably lower than previously established. NMR studies in resting skeletal muscle (93,43) and normoxic heart (14,88) have determined [ADP] to be in the range of 5-50uM. Such low concentrations have important regulatory implications for glycolysis, oxidative phosphorylation, and other pathways of intermediate metabolism. The validity of these estimates relies on the applicability of Equation 4.1 to the *in vivo* system; the necessary conditions for use of the equation will be discussed below.

ADP is thought to be a key regulator of the glycolytic enzyme pyruvate dehydrogenase, 3-phosphoglycerate kinase, and the Kreb's cycle enzyme isocitrate dehydrogenase (8,101). Assuming that the myokinase (adenylate kinase, AK) reaction is near equilibrium, [AMP] can be calculated from the ADP level and the equilibrium constant for AK. It is thought that, together with ADP, AMP regulates glycogenphosphorylase and phosphofructokinase (101). The regulatory functions of ADP and AMP were determined largely from *in vitro* studies of purified enzymes that are of unproven relevance in the living cell.

In isolated mitochondria, the K_m for ADP in oxidative metabolism was found to be approximately 20um (27). The notion that cellular respiratory control is based on [ADP] is convenient for matching ATPase activity and ATP synthesis (24). Others have suggested the more important variable in oxygen consumption is

redox state as determined by NAD/NADH (70). Several factors probably contribute as discussed by Groen (49) and Chance (26).

Essential to precise definition of the relationship between [ADP] and the mechanism of control is an accurate method for determining intracellular [ADP] as a function of ATPase activity or oxygen consumption, Vo_2. If the ATP to PCr phosphate transfer can be shown to be an equilibrium, dead end reaction, and if CK is freely accessible to all the substrates, then [ADP] can be determined from the NMR-determined pH, [ATP], [Mg^{++}], and [PCr] using Equation 4.1.

[PCr] in resting muscle is higher than that of any other phosphate containing compound, yet its role in muscle function continues to be controversial. Following the discovery in 1927 of the rapid conversion of PCr to Cr in muscle (37), two different functional roles have been postulated for PCr in muscle and other excitable tissue. The traditional view is that PCr acts through the Lohmann reaction (Equation 4.1) as an energy storage molecule necessary for maintenance of constant levels of ATP (83) and, perhaps more important, the micromolar concentration of ADP.

The high rate of phosphoryl group transfer is due to catalysis by creatine kinase (adenosine 5'-Triphosphate-creatine phosphotransferase, CK, EC 2.7.3.2). The properties of CK have been carefully studied *in vitro* (124). Enzyme assays and ^{31}P NMR measurements of CK flux in resting fast-twitch muscle have shown that this flux is several times the rate of maximum ATP utilization, supporting the energy buffer function of PCr (94). Use of PCr analogues that replace PCr in muscle without major changes in function have led some to believe that the storage role is non-essential for adequate muscle function (95). Recent data, however, has shown that the presence of these analogues is associated with adaptive changes that will complicate the interpretation of these studies (106).

Recently another view of PCr has been put forth, based on studies in isolated mitochondria (12,63) and on preliminary ^{31}P NMR data from heart (97,13). According to this view PCr may be an essential link between the sites of production and use of ATP. This model of functional coupling between mitochondrial produced ATP and the myofibrillar ATPases through a PCr "shuttle" was inspired by the identification of localized distinguishable isozymes of creatine kinase in the mitochondria membrane, on the myofibrils, and in the sarcoplasm (62,119,9). The three isoforms are distributed primarily in the cytosol (80%) and approximately 20% distributed in the mitochondrial inner membrane and the myofilaments. Together with the results from microstructural studies this compartmentalization of CK has been used as evidence to support elaborate CK shuttle models (122).

The two current views of CK function in muscle described above are schematically illustrated in Figure 4.1. In the classical view, 4.1a, PCr exists in rapid equilibrium with ATP, maintaining an approximately constant [ATP] following transient changes in ATP production or utilization. Such an "energy buffer" assures adequate chemical potential for cellular homeostasis. In this model the CK flux is independent of ATP utilization or production and depends only upon the steady-state kinetics of CK and its substrates as if contained in a well-mixed solution. Substrate and product concentrations will assume their equilibrium values in the steady-state. The CK shuttle notion as illustrated in 4.1b attaches an obligatory transport role to PCr, thereby linking CK flux to ATP utilization.

A necessary property of muscle employing a PCr shuttle, as pictured in Figure 4.1, is that flux through the enzyme would vary with myofibrillar ATPase activity. This behavior can be tested directly in living tissue using ^{31}P NMR spin transfer techniques. *in vivo* spin transfer studies of heart and skeletal muscle CK

flux have been reported by a number of investigators. The focus has been on two issues 1) Near equilibrium of the CK catalyzed transfer as measured by the equality of the forward and reverse fluxes and 2) Dependence of the flux on ATPase activity. Conflicting results have led to significant disagreement in both areas. Studies in cardiac and skeletal muscle have appeared a) supporting equality of the fluxes (44), b) showing no link between CK flux and ATPase activity (117), c) showing no difference in the forward and reverse fluxes, however, demonstrating a relationship between CK flux and ATPase activity (89,120), and d)showing both an imbalance in the fluxes and a link between ATPase and flux (103,43,13,14,97). Without established equilibrium in the CK catalyzed reaction, the calculated [ADP] must be questioned together with any subsequent connections between [ADP] and control of oxidative metabolism.

The specific aims of this ^{31}P NMR study of stimulated mammalian muscle were: 1) To determine the intracellular pH and quantify the levels of the NMR detectable ^{31}P-containing compounds PCr, ATP, and Pi over large steady-state changes in ATPase activity within the normal physiological range. 2) To use a transient spin transfer technique to measure the CK flux and test the hypothesis that *in vivo* CK kinetics are predictable from the well-known properties of enzymes in homogeneous solutions. These results allow confirmation of CK equilibrium and examination of dependencies of CK flux on the ATPase activity. 3) From the measured metabolite levels, and prior knowledge of total creatine, calculate [ADP] at rest and during steady-state stimulations and compare these values and the other NMR derived quantities to tissue oxygen consumption measured independently.

4.2 Model System

The isolated perfused cat soleus muscle was chosen as a model system for its viability over long periods of chronic stimulation and for its unique cellular homogeneity. Whereas most mammalian skeletal muscles are composed of mixed fiber types, the feline soleus has been characterized histochemically as consisting of over 95% slow oxidative fibers (18,94). Using electrical stimulation the muscle oxygen consumption can be increased over 20-fold and maintained at a constant rate for several hours. This allows a range of ATPase activities to be studied that is from two to ten times greater than those used in previous studies of heart (105). The soleus has the additional attractive feature that the mitochondrial density (10-15%) is somewhat less than that of heart (34-42%), (68,69). A greater diffusion distance from sites of ATP production to the sites of utilization emphasizes physiological conditions whereby a requisite energy shuttle would be most useful. Thus, if a functional relationship between CK flux and ATPase rate were to be important, the feline soleus would allow large excursions in ATPase activity to be maintained for significant periods of time during which the flux can be accurately quantified.

4.3 Methods

ENZYME ASSAYS: CK activity was measured using a standard assay kit (Sigma Co. St. Louis, MO.) for comparison with the NMR results. Activity, determined by the magnitude of change in the NADPH absorbance (extinction coefficient 6.22 cm^2/umole), was determined in standard enzyme units (U). 1 U is defined as the quantity of enzyme that will transfer one umole of phosphate from PCr to ADP per minute. Assays were performed on soleus from two animals on the same day as the NMR experiment. Muscle was stored at 0°C prior to

homogenization [4°C, 50 mM Na-PIPES(pH 7 at 20°), 50mM Na-acetate, 4mM DTT, 10uM EDTA, 1mg/ml BSA]. Both samples had similar mass adjusted activities with a mean of 1271 +/-25 umoles/gm wet wt/min. This is a V_{max} activity corresponding to approximately 1694 Units/ml intracellular water. Conversion factors used to calculate intracellular water from wet weight are given in Figure 4.1.

NMR DATA ACQUISITION AND ANALYSIS: Experiments were performed on a homebuilt NMR spectrometer interfaced to a VAX 750 computer (MIT Francis Bitter National Magnet Laboratory). The ^{31}P resonance frequency was 145.6 Mhz in the 8.5 T superconducting magnet used for the studies. Prior to each experiment the mainfield was shimmed for maximum homogeneity. The water proton FID from soleus was sufficiently intense from the ^{31}P tuned probe to be used for shimming. Typically ^{1}H linewidths of 50 hz were achieved.

Control spectra were obtained from 16 or 32 averaged single pulse experiments using a 90 degree pulse and an interpulse delay of 12 seconds. The CK flux was measured using the NMR transient spin transfer technique as described in Chapter 3 and illustrated in Figure 2.3. The ratio of the chemical flux to the NMR measurable reactant concentration is defined as a pseudo first-order rate constant, k_{nmr}. Reaction mechanisms should not be inferred from this ratio alone. Selective inversion of either the γ-ATP or the PCr resonance was accomplished using a 1-τ-1 binomial pulse where $\tau = 0.5/\sigma = 1.4$msec. σ is the chemical shift difference between γ-ATP and PCr (361 Hz at pH=7). Eight inversion-readout delays, D2, were chosen. Twelve seconds were allowed between averages for relaxation to occur. This delay is sufficient for the ATP ($T_1 = 2.97$ sec.) and PCr ($T_1 = 3.84$ sec.) resonances to have negligible saturation effects. Each data set consisted of a relaxed control inversions at D2=12000 msecs followed

by six inversions at alternating values of D2 (355-45-360-55-350-50 msecs) subsequently followed by a second D2=12000 control. At each of eight D2 values a spectrum of either 16 or 32 averages was obtained. One complete data set consisting of eight spectra required 32 or 64 minutes to obtain. Stability was insured by comparing the first and last spectra of each set.

For selective saturation transfer studies a second synthesizer channel and r.f. amplifier were used (Figure 4.5). This allowed separate control over the saturation and receiver reference frequencies. By attenuating the saturating pulse after it passes through the isolation diodes, there is minimal distortion of low power frequency selective signals. The diodes are driven well above their cutoff levels, preventing significant non-linear attenuation effects.

The time domain signal was detected in quadrature and 1024 points digitized at 10kHz. The digitized signal was multiplied by a matched exponential filter and zero-filled to 4096 points prior to Fourier transformation. Integrals of the phase corrected spectra were obtained and used as measures of the relative metabolite concentrations. Typically, direct integration of the resonances was used; however, in several data sets correction for baseline offsets was necessary. Offsets were calculated from the integrals over spectral regions eight half-widths away from the resonance center on both sides of the peak. The frequency spans of the regions varied from 50 to 150 hz depending upon adjacent peaks and the condition of the baseline. The offset integrals were added together and scaled to represent equivalent integration limits by multiplication by the ratio of the resonance peak integration span to the sum of the two offset spans. The scaled offset was subtracted from the original peak integral to obtain the corrected resonance area.

For data analysis, the initial slopes were obtained by a least-squares fit of the plots of the resonance peak areas versus D2. The initial slope from the non-

inverted resonance was used in Equation 2.27. The y-intercept of the plot of the inverted species was used as M_1 in Equation 2.27; M_{1o} was obtained from the average of the two D2 = 12000 msec values. The error in k_{nmr} was estimated from the standard error in the fit which was always the dominant factor in the complete error expression. The k_{nmr} determined from Equation 2.27 was used to obtain the flux as the product of k_{nmr} and the metabolite concentration. Figure 4.7 shows a typical data set and the linearization of the magnetization for short D2 values.

in vitro SPECTROSCOPY: NMR spin transfer studies were performed on purified CK (Sigma Co. St. Louis, MO., Rabbit Muscle,160 Units/mg, cat# c-3755) for comparison with results obtained from intact tissue. CK flux was measured as a function of substrate and enzyme concentrations. 6000 Units/ml of purified enzyme was added to stock solution containing 25mM PCr, 5mM Na-ATP, 8.3mM KPi, 6mM MgCl, 12mM KCl, 10 mM Creatine, and 1% bovine serum albumin. The buffer capacity and ionic conditions of the solution were designed to mimic intracellular conditions. The pH increased following addition of the enzyme and was adjusted to 6.8 with HCl. The enzyme concentration was varied by sequential dilutions with stock solution. CK flux was monitored at 30°C for enzyme concentrations of 6000, 4000, 2000, and 1000 Units/ml.

To examine the substrate limited kinetics of CK at low concentrations of PCr, a solution was prepared as above without Cr and with 6.7mM PCr. Following addition of CK the [PCr] fell to an equilibrium value less than 2mM. The PCr-->ATP flux was measured as a function of [PCr]. [PCr] was determined by comparing the resonance area of the PCr peak to that of the Pi which had a known concentration of 8.3mM.

Intracellular pH can be calculated from the chemical shift of the Pi resonance (99). A plot of the resonance frequency versus $[H^+]$ is a sigmoidal titration curve;

however, at low pH the PCr resonance also shifts. The relative PCr-Pi chemical shift is a convenient *in vivo* measure of pH; however, since both compounds have titratable protons the difference frequency will not follow a simple sigmoidal relationship. A calibration curve was constructed using solutions of PCr (10 mM) and Pi (10mM as KH_2PO_4) of known pH. The ionic strength of the solutions was fixed with added KCl (140mM) and $MgSO_4$ (1 mM). Measurements were performed of the relative PCr-Pi shift at 145.6 Mhz (145.6hz=1ppm) and the curve in Figure 4.2 obtained. Figure 4.2 was used for intracellular pH determinations in the soleus.

In vivo NMR PROBE: For *in vivo* spectroscopy of perfused muscles a probe was designed and constructed for use in an 8.5T, 89 mm bore superconducting magnet, Figure 4.3. The nominal outside diameter is 8 cm with an aluminum r.f. shield covering the entire probe body. The probe temperature is controlled by circulating humidified room air through a glass 0.8 cm ID conduit with a resistive heating element inline. Temperature is monitored with a copper-constantan thermocouple located at the base of the muscle. Force was measured with a cantilever beam strain gauge (BLH model SP83-06-12) to which the proximal end of the muscle was fastened. Electrical stimulation (0 to 160 twitches per minute, tpm) was achieved using platinum electrodes wrapped securely around the insertion and origin of the mounted muscle. The thermocouple, stimulating, and force transducer leads were individually filtered to prevent noise transmission using series inductors (100uH) and capacitors (10000uF) to ground.

The r.f. coil was connected in a balanced configuration, Figure 4.4, to minimize dielectric losses (100). The variable capacitors, C_1, C_2, and C_3, were adjustable over a range 1-30pF (Johannson Corp. New Jersy, #5641). The fixed non-magnetic capacitor, unlabeled, was 33pF (Am. Tech. Ceramics, New York, ATC330K). The r.f. coil was wound in a saddle configuration using 10 gauge high

purity copper wire. The coil had a length of 3 cm's and a diameter of 1.3 cm's. The unloaded Q of the coil at 145 Mhz was approximately 200 and with the muscle in place, the loaded Q was less than 100. For ^{31}P the 90 degree pulse width was 23-30 usec at approximately 50 watts.

ANIMAL PREPARATION: Soleus muscles (4-6 gms) were removed from adult cats (2-3Kg) under general anesthesia with sodium pentobarbital (30 mg/Kg, IP for induction, supplemental doses for maintenance). To expose the soleus, the Achilles tendon was severed and the gastrocnemius-plantaris muscle group retracted toward the popliteal space. The popliteal artery into the soleus was canulated following ligation of all other branches. During cannulation the muscle is unavoidably ischemic for approximately two minutes.

The soleus was removed by cutting the proximal heads of the fibula and tibia, leaving the insertions intact. The muscle was perfused with a 15% v/v suspension of washed human red cells in Kreb's bicarbonate Ringer (pH 7.3) containing 4.4% w/v bovine serum albumin, 5mM glucose, 0.15mM pyruvate, 30ug/L papaverine HCL, 10 ug/ml gentamicin sulfate and 1-4mM lactate from erythrocyte glycolysis. A peristaltic pump delivered the perfusate at a constant flow rate (0.2-1.0 ml/min) that produced a perfusion pressure ranging from 30-100 torr. The perfusate was equilibrated with 95% O_2:5% CO_2 v/v. Further details of the preparation and its use have been published (94). A total of 13 preparations were studied, four were immediately unstable and not used for analysis. Six preparations were sufficiently viable for stimulation studies.

in vivo SPECTROSCOPY: The isolated muscle was suspended inside the r.f. coil, Figure 4.3, which was matched to 50 ohms and tuned to the proper NMR frequency (145.6 Mhz ^{31}P). Prior to data collection the tissue was allowed to reach thermal equilibrium and metabolic steady-state for approximately 30 minutes.

Control spectra and magnetization transfer data were obtained under resting conditions. Stimulations with 5-8 volts for 2 msec durations were started at rates between 15 and 120 twitches per minute. Data was collected after allowing for steady-state to be achieved as determined by constant force generation and constant PCr/ATP (Figure 4.6). The initial reduction of force stabilizes after approximately 5 minutes tracking the decrease in PCr/Pi ratio. Tissue perfusion pressure was observed to increase over the course of several hours, often dropping back to original values following stimulation as previously observed (94). Under steady-state conditions spectra and magnetization transfer data were obtained.

Saturation transfer studies were performed to investigate the possibility of an observable ATPase flux between γ-ATP and Pi. The saturation power was adjusted for complete suppression of the saturated resonance in 300msec. For steady-state to be achieved in the exchanging system, the low power pulse must be applied for $t > T_1 + 1/k$. A 12 second saturation pulse was used based on the measured T_1 of Pi >4 seconds and $1/k > 6$ seconds. Following saturation of the γ-ATP resonance (at -2.49 ppm relative to PCr), a control spectrum was obtained by setting the saturation frequency to +2.49 to correct for any significant power deposition in the PCr resonance due to the finite width of the saturating pulse. These experiments gave the values of M_{1sat} and M_{1o} in Equation 2.36 from which $k*T_1$ was calculated.

Metabolite concentrations were calculated using data for intracellular ATP and total creatine obtained by Meyer et al (94) from extracts of resting cat soleus. Total creatine was assumed constant at 22.4 mM (17.8 uMole/gm wet wt. +/- 0.9) and [ATP] = 5.03 mM (3.67 umole/gm wet wt +/- .26). It was assumed that 1 gm wet wt = .73 gm intracellar water (94). CK equilibrium constants were corrected for pH and Mg^{++} using the data of Lawson and Veech (80).

4.4 in vitro Results

CK FLUX: The NMR derived rate constant, k_{nmr}, was measured over a range of enzyme concentrations. The results of two independent experiments are shown in Figure 4.8 together with the best linear fit. Both solutions contained 25mM PCr and 5mM ATP. The solutions were studied at 30°C for comparison with the intact muscle results. The CK flux was calculated from the expression, $\Psi_{PCr\text{-}ATP}=k_{nmr}*[PCr]$. Over the range of enzyme concentrations studied, (1000 to 6000 Units/ml), the CK flux was found to vary approximately in proportion to the enzyme concentration. A decrease in T_1 for PCr from 3.2 seconds to 2.1 seconds was observed with increasing enzyme concentration.

The NMR-determined CK flux as a function of [PCr] is shown in Figure 4.9 at 30°C and 4000 Units CK/ml. PCr was added directly to the solutions to effect the changes, and therefore the substrate concentrations did not remain constant. [PCr] was determined from the ratio of the PCr and Pi resonance areas. Buffer solution was used with a calibrated Pi concentration of 8.3mM; the PCr/Pi value times 8.3mM gave the PCr concentration. Least-squares analysis (86) of the data gave a value of K_m =8.3+/-4.2 mM and V_{max} = 3.7+/-1.4 mM/sec. This compares well to the K_m of 8.6 mM given by Watts (124).

4.5 in vivo RESULTS

STABILITY: In Figure 4.10 the relative concentrations of the ^{31}P metabolites are plotted versus time for two soleus preparations. These experiments are representative of good (Figure 4.10a) and poor (Figure 4.10b) extremes of temporal stability for the soleus preparations. In Figure 4.10a metabolite levels are normalized to the area of an external standard, phenylphosphonic acid (PPA),

contained within a capillary tube alongside the muscle. The ATP resonance is seen to remain constant over a wide range of metabolic excursions. In the absence of a PPA reference, PCr and Pi levels in Figure 4.10b were normalized to the ATP resonance area. The abscissa of both plots is the data record number. The data record number is not strictly linear in time; however, records 5-150 were acquired sequentially in both cases over approximately 16 hours. Poor preparations have a gradual increase in Pi and decrease in PCr in time; however, most preparations had sufficient stability over the acquisition period (approximately 60 minutes) that the metabolite levels were constant to within 15%. In all preparations stimulation decreased the PCr resonance and increased, approximately stoichiometrically, the Pi resonance. Recovery to baseline following 30 minutes of stimulation required from 10 to 30 minutes, a period which was found to increase as the muscle degraded. In several preparations, a slight irreversible acidification of approximately 0.1 pH units was observed.

NMR SPECTRA: ^{31}P spectra were obtained from resting soleus at 22 and 30°C. Figure 4.11 shows typical spectra from control and stimulated soleus. In contrast to heart, bladder, and amphibian muscle there are no resolvable resonances in the phosphodiester (0-1ppm) region. The soleus spectra have significant resonances only for α,β, and γ ^{31}P's of ATP, PCr and Pi. Intracellular concentrations of the ^{31}P metabolites are listed in Table 4.1. Resting pH was found to average 6.8 units and 7.0 units at the high and low temperatures respectively. Generally, the pH remained constant throughout the experiment. The narrow linewidth of Pi in single spectra is evidence for homogeneity in intracellular pH. The PCr ^{31}P linewidth depends primarily on the shimming and varied between .1 and .3 ppm (20 - 50 Hz at 8.5T). The Pi linewidth was typically equal to that of the PCr resonance to within +/- .03 ppm. Free [Mg^{++}] was estimated at 2.0mM

at 30°C and 0.74mM at 22°C using the β-ATP chemical shift calibration curves published by Kushmerick et al (75).

Graded electrical stimulation of the soleus caused a reduction in the PCr peak area and corresponding increase in the Pi area. Figure 4.11 shows typical effects on the ^{31}P spectrum of an increasing stimulation rate. Under steady-state conditions the intracellular pH, as measured by the Pi chemical shift, was unchanged with stimulation rates as high as 90 twitches/min.

BI-DIRECTIONAL CK FLUXES: In n=5 preparations data was collected from stable preparations to specifically examine the forward and reverse CK fluxes. In one preparation data was acquired over approximately 5 hours in resting muscle at 30°C. Table 4.2 lists the results of spin transfer in both the forward and reverse direction. The mean and standard deviation of the ratio of the forward to reverse flux from Table 4.2 is 1.01 +/-0.8. The resting flux between PCr and γ-ATP was found to be 1.8 +/0.4 umole/gm/sec.

Steady-state saturation of γ-ATP was performed to investigate the possibility of measurable ATP <--> Pi exchange through ATPase and ATP synthetase activity. Figure 4.12 shows spectra before and after saturation. No detectable transfer of magnetization was found to occur between the ATP and Pi resonances. ATP -->Pi transfer would be reflected in a positive Pi peak in the difference spectrum.

GRADED STIMULATION: In Figure 4.13 the stimulation rate is denoted on the ordinate with the observed ATP/PCr ratio plotted as the abscissa. An approximately linear relationship exists over the range of rates studied. This plot allows a qualitative comparison to be made between oxygen consumption and the ATP/PCr ratio. Oxygen consumption data from Meyer (77) demonstrate that in an

identical soleus preparation at 30°C, the Vo_2 also varies nearly linearly with stimulation rate at 1.2 umoles/min/100gm/twitch/min over this range of stimulations. Vo_2 is indicated qualitatively on the right hand y-axis. Together these results suggest that oxygen consumption, and thus ATPase activity vary nearly linearly with PCr/ATP. The O_2 consumption data was used in constructing Figure 4.14, illustrating the variation in ATPase ^{31}P flux with increasing ATP/PCr (increasing stimulation). Using a P/O ratio (phosphate atoms/oxygen atoms) of 3 and 2 grams wet tissue weight to 1 gram intracellular water, the resting soleus O_2 consumption (0.07 uMoles/gm-min) is equivalent to a resting ^{31}P flux of 0.014 mM/sec increasing to greater than .3 mM/sec at high stimulation rates.

With increased stimulation PCr is utilized to maintain nearly constant ATP levels. The ^{31}P from PCr is conserved in the Pi resonance as a product of ATP hydrolysis. The stoichiometric variation of Pi as a function of the PCr/ATP ratio is demonstrated in Figure 4.15 where Pi/ATP is plotted versus PCr/ATP. The slope obtained from a least-squares fit of the data from all 9 stable preparations is -.8 +/- .2. Clearly, the deviation from the ideal value of -1.0 is strongly influenced by the variable amounts of Pi in any non-viable tissue within each of the various preparations. Data from a single experiment are shown; Figure 4.15 (upper right) shows nearly ideal behavior. The [ATP] as monitored by the resonance area was observed to be constant over the range of stimulations and is assumed to be numerically equal to the assayed concentration of 5.03 mM obtained by Meyer et al (94).

In Figure 4.16 k_{nmr} (the ratio of CK flux to [PCr]) is plotted versus ATP/PCr following graded stimulations over the range 0 to 60 twitches/min. The increase in k_{nmr} reflects the decrease in [PCr]. Data from a single preparation at two temperatures are shown in Figure 4.20. At both 22 and 30°C k_{nmr} varies

approximately linearly with ATP/PCr, which for constant [ATP] is consistent with a constant PCr -->ATP flux.

The CK flux, $\gamma_{PCr-->ATP}$, was calculated from $\gamma = k_{nmr}*(PCr/ATP)*[ATP]$ using [ATP]=5.03 mM. The results from n=9 viable preparations are shown in the upper right of Figure 4.17. The center plot shows data from 6 of the more stable preparations. The majority of the data were obtained at rest and at low stimulation rates (low ATP/PCr), and only the most stable preparations were stimulated above 30 twitches/min. Both sets of data have a least-squares slope of -.26 mM/sec; however, the errors are +/- .34 and .50 mM/sec for the n=6 and n=9 sets respectively. There is no evidence for an increase in the CK flux at even the highest ATPase rate.

Activation Energy: An Arrhenius plot of $\ln(k_{nmr})$ vs $1/T(^{o}K)$ is shown in Figure 4.18 for both the soleus *in vivo* and purified enzyme (2.3 KU/ml) in solution (Pi =5mM, ATP =5mM, $MgSO_4$= 6mM, PCr= 20mM, KCl= 100mM, MOP's buffer = 20mM, pH=7). The data obtained from the soleus at 22°C and 30°C are well below the knee ($1/T \sim .0032\ ^{o}K^{-1}$), demonstrated *in vitro* where protein denaturation reduces the catalytic activity and hence the value of k_{nmr}. An apparent activation energy, E_a, can be calculated from the plots. For temperatures below 37°C the value of E_a for the *in vitro* enzyme is 35 +/- 7 KJ/mole and 76 +/- 26 in intact soleus.

ADP: Using the value of total creatine for soleus of 24.4 +/- 1.4 mM from Meyer et al (94), the free [ADP] can be calculated from the CK equilibrium as a function of ATP/PCr. Values of $K_{ck}*[H^+]$ = 177 and 203 were obtained from Veech (80) for use at 30°C (pH=6.8) and 20°C (pH=7.0) respectively. Figure 4.19 is a plot of [ADP] calculated from the CK equilibrium using Equation 4.1. Over the range of stimulations used, the [ADP] is seen to vary (Figure 4.19) between

approximately 15 uM at rest to over 140 uM at high ATPase activity. A slightly lower value was obtained from the 20°C preparations, 5uM.

4.6 Discussion

To draw conclusions valid at the cellular level from studies of whole tissue preparations, homogeneity of cell type is essential. The arterial perfused cat soleus is an ideal preparation for study by NMR spectroscopy because of its unique composition of slow-twitch fibers. Heart (13,103) and rat hindlimb (117), used commonly for the study of phosphate metabolism and CK flux, are mixtures of cell types. In these models changes in metabolic performance following chronic changes of physiological conditions or training must be separated from fiber type transformation (84). Smith et al found significant differences in CK flux in two avian skeletal muscle fiber types with nearly identical NMR visible ^{31}P metabolite levels and nearly identical assayed enzyme activities; [ADP] differences between the types was sited as an explanation (118). Problems of tissue heterogeneity were effectively eliminated by use of the soleus preparation, and the following conclusions are specifically applicable to slow-twitch mammalian muscle.

1) In the resting soleus at 30°C the measured ^{31}P metabolite levels allow ΔG_{ATP} to be calculated from Equation 1.1 as -59 KJ/mol. This value is in excellent agreement with the value of -58 given by Meyer et al (94) for soleus. From Matthews et al (88) ΔG_{ATP} can be calculated for KCl arrested heart as -62 KJ/mol. at 37°C which is comparable to the soleus value. The slow oxidative soleus must, like the heart, perform work for long periods without fatigue. The maximum rate of ATP hydrolysis, and thus force production, by the contractile protein ATPases will be limited by ΔG_{ATP}. The relatively high mitochondrial densities of the heart and soleus allow ΔG_{ATP} to be maintained at these modest levels and

provide constant force generation. The significantly higher ΔG_{ATP} reported for the fast-twitch biceps, -72 KJ/mole, is consistent with its relatively higher force generating potential. Without a sufficient mitochondrial reserve the Pi and ADP levels in stimulated biceps quickly rise, saturating the mitochondrial adenine nucleotide translocase and generating constant force only as long as glycolysis and glycogenolysis (stimulated by Pi and ADP) can provide ATP. Mitochondria in the slow-twitch soleus and heart are able to balance ATP production with utilization at modest stimulation rates, thus avoiding fatigue.

2) An estimate of the effective CK activity for soleus can be made by plotting the k_{nmr} obtained in the resting soleus at 30°C to Figure 4.8 obtained from purified enzyme. A value of 3.2 +/- 1.1 Kunits/ml is obtained from Figure 4.8. This activity is comparable, but higher than the value derived from soleus extracts, 1.7 Kunits/ml (73). Estimates by NMR for CK activity in fast-twitch muscle, with higher measured CK fluxes, are significantly larger, 5.0 KUnits/ml (93). The CK flux in bladder smooth muscle is lower than either type of skeletal muscle by nearly a factor of 10 (73). These findings are consistent with CK assays of muscle extracts where the specific activity has been shown to decrease in the order a) fast-twitch muscle b) slow-twitch muscle c) heart muscle d) smooth muscle (73). Only NMR determined fluxes obtained from cardiac preparations are inconsistent with the extract data (13,14).

3) During ATP synthesis and utilization a ^{31}P exchange between Pi and ATP occurs. Several investigators have thought this exchange to be an important component of the observed magnetization transfer (121). In this study significant Pi <--> ATP was not detected. Additionally, the forward and reverse CK fluxes, as measured using a transient spin transfer method were found to be equal, further eliminating an ATP --> Pi exchange as a significant ^{31}P transfer pathway. That

the ATPase flux is not detectable is consistent with its relative magnitude compared to that of CK exchange, Figure 4.14. Oxygen consumption data from soleus at rest and during high rates of stimulation allow calculation of ATPase ^{31}P flux ranging from 0.01 to 0.30 mM/sec. This flux is negligably small compared to the measured CK flux of 2.7 +/- 1.0 mM/sec. It is unlikely that sufficient accuracy in the CK flux determination can be achieved *in vivo* to allow separation of the two fluxes or accurate characterization of the ATPase exchange. For a T_1 of Pi of approximately 4.2 sec and [Pi] = 8.5 mM, $\alpha = T_1$*(ATPase flux)/[Pi] = 0.005. Figure 2.5 showed that the fractional error for such a small α is extremely high.

Interpretation of the data as evidence for CK equilibrium and independence of the CK flux from ATP production and utilization is in conflict with previous results from heart where a difference in the forward and reverse fluxes was reported and a significant ATP --> Pi exchange postulated. The dominance of the CK flux, however, should hold true not only for soleus , but for all mammalian muscle types, based on the same argument. In Table 4.3 the data from this study are compiled along with data from the literature for the CK fluxes determined by NMR and ATPase ^{31}P fluxes calculated from tissue oxygen consumption. Compared to the CK flux, relatively small ATPase fluxes are found for fast-twitch biceps, slow-twitch soleus, and bladder smooth muscle. The magnitudes of the CK fluxes drop from biceps to bladder in agreement with relative decreases in the CK activity as determined by assay (73). In the fast-twitch biceps a large reserve against rapid, short-term reductions in [ATP] is provided by the large ratio of CK flux to ATPase flux. Less dramatic physiological reductions in [ATP] would be expected in the soleus, which requires less of an "energy buffer" and has a correspondingly lower flux ratio. Finally, bladder faces only mild physiological

[ATP] challenges and requires less of an energy reserve; its flux ratio is predictably small.

In skeletal and smooth muscles the observed kinetics are consistent with the classical role of PCr as an energy storage molecule. Its essential role is to maintain relatively constant [ATP] levels and the ΔG necessary for ATP hydrolysis during large transient changes in ATP utilization prior to stimulation of oxidative metabolism. Figure 4.21 is the calculated Gibb's function for variations in the PCr/ATP ratio in soleus and biceps using the metabolite concentrations determined in this study and data from Meyer et al for biceps (94). Over the physiological range of stimulations PCr/ATP falls from 3.2 at rest for the soleus to approximately 0.5. The presence of PCr allows for large changes in PCr/ATP without significant changes in ΔG.

The results from NMR studies of CK and ATPase fluxes in cardiac muscle vary considerably and report several unexplained inconsistencies with previous results from non-NMR sources. In particular, enzymatic assays of CK from cardiac muscle estimate the CK activity as less than that for soleus (73) as mentioned above. Oxygen consumption data from cardiac muscle, used to estimate ATPase activities, vary by a factor of approximately tenfold in reports made by several groups not involved in NMR (6). Nevertheless, the upper end of these data still support a factor of 10 greater CK flux than ATPase flux in agreement with the classical view. Compilations of physiological data from muscle of all types show little variation between skeletal and cardiac muscle (6). Oxygen consumption data reported in conjunction with NMR studies of CK flux tend to be factors of 10 to 50 times higher than the highest values obtained in non-NMR studies (89,120,13). It remains to be explained why such a large difference between cardiac muscle oxygen consumption and skeletal muscle might exist. If such large ATP utilization rates

did exist, one possible mechanism to support the energy transport might be the parallel diffusion interpretation of the PCr shuttle (96).

4) In the soleus, the measured equality in fluxes together with the observation of resonance area stability in time confirm that the reaction is in steady-state. Reports denying steady-state were all based on data obtained using the model-dependent steady-state magnetization transfer technique. Though large ATPase exchanges may be neglected based on the arguments presented above, there are several reports of homonuclear and heteronuclear NOE's existing for the PCr and ATP resonances (103,89). The effects described in Chapter 2 show that such effects can lead to incorrect conclusions regarding the ratio of forward to reverse flux.

5) In the stimulated muscle, [ATP] was found to remain constant with respect to an external standard (phenylphosphonic acid). The value of 5.03 mM was assigned based on chemical assay (94). The observed increase in ATP/PCr and decrease in ATP/Pi found to accompany the stimulation are well-known and in agreement with reports in other muscle preparations during increased energy demand (76).

6) With increasing stimulation the NMR measured magnetization transfer rate constant (k_{nmr}) for PCr to gamma-ATP exchange was found to increase, tracking the increased ATPase activity (as measured by Vo_2) and the observed decrease in PCr content. However, the ^{31}P flux between PCr and ATP, k_{nmr}*[PCr], was constant over a greater than tenfold increase in ATPase activity, Figure 4.17. The CK flux is clearly not dependent on the rate of ATP utilization or on the concentrations of substrates which were found to vary considerably over the range of stimulation rates. At the highest stimulation rates (90-120 hz), [PCr] falls to nearly 5 mM, a level where a reduction of CK flux might be expected due to substrate limitations. With improved signal-to-noise a decrease in the flux

might be expected as PCr falls below its K_m for CK. This finding agrees with results obtained from an intact rat leg model using steady-state saturation methods (117). However, these results are contrary to data obtained in heart where the CK flux was found to vary significantly with changes in heart work rate of only twofold. The latter finding excludes a requisite "PCr Shuttle" linking mitochondrial ATP production to utilization. If a "PCr Shuttle" existed as originally described, a variation in CK flux would be observed following such a large change in ATPase activity. The findings from this study do not exclude a possible role for PCr in energy transport, as described by Meyer et al (96), whereby a minimal PCr flux participates in energy transport independent from its primary function as an energy storage molecule.

The results from studies in heart have two important limitations. First, the majority of the work has been performed in preparations over relatively small ranges of ATPase activity. KCl arrested hearts have been used in several studies to achieve a larger oxygen consumption range. Interpretation of a KCl induced physiological state is poorly investigated. Intact heart is an inhomogeneous mixture of cell types that is difficult to control metabolically and has ill-defined intrinsic endocrine properties. Second, in all studies where CK exchange was found to be in apparent non-equilibrium, and in studies where an apparent link between ATPase activity and CK flux was identified, a steady-state magnetization transfer technique was used that is sensitive to incomplete biochemical models and to physiological compartmentation as shown in chapter 2. The results from such studies are quantitatively incorrect, and conclusions regarding qualitative connections between flux and ATPase activity are invalid.

7) The large reduction in [PCr] and large increase in [ADP] following significant increases in ATPase activity produced no change in flux. This suggests

that for CK both ADP and PCr are above their K_m's or that the relationships between reaction velocity and $K_{mADP}/[ADP]$ and $K_{mPCr}/[PCr]$ achieve a balance and maintain a constant enzyme catalyzed flux. The more likely explanation is that both PCr and ADP are above their *in vivo* K_m's, thereby setting their values *in vivo* below approximately 3mM and 17 uM respectively.

8) The calculated ADP concentrations at rest and for moderate changes in ATPase activity are lower than previously measured and in the range of the K_m for mitochondrial adenylate transport, Figure 4.19. At these ADP levels, the important conclusion is that mitochondrial transport limited oxidative metabolism is entirely consistent with the near linear relationship between ATP/PCr and both Vo_2 and [ADP]. The validity of the calculation rests on the homogeneity of the tissue, the absence of significant intracellular concentration gradients, and accurate knowledge of K_{ck}. The presence of intracellular compartmentation of the adenosines has recently been suggested and mitochondrial [ADP] reported as approximately two times higher than the extramitochondrial space (56,98). An NMR imaging method for investigating physical compartmentation is described in chapter 5; however, at present the resolution of such methods is insufficient to address this intracellular issue.

The value of K_{ck} depends on calculated levels of free Mg^{++}, pH, and [ADP]. [ADP] calculated from Equation 4.1 is the total ADP content including both free ADP and ADP bound to Mg^{++}. Other studies have shown intracellular $[Mg^{++}]$ in skeletal muscle to be in the range of $10^{-2.6}$ to 10^{-3}M (75). Though greater than 97% of the intracellular ATP will be Mg^{++} bound, the Mg^{++} binding constant for ADP is lower than that for ATP by a factor of 10 (1320 M^{-1} for 37°C). The bound/free ADP ratio will near unity which will serve to further reduce the ADP availability for reactions requiring Mg-ADP, such as CK and several ATPases, and

further support adenylate transport control of oxidative metabolism.

The concentration of AMP can be estimated if the adenylate kinase reaction is assumed to be near equilibrium (92). The equilibrium constant is approximately unity, thereby setting [AMP] at the exceptionally low value of 0.057 uM in the resting soleus. Figure 4.22 shows the [ADP] and [AMP] changes over the range of stimulations studied. As the [ADP] changes between 15uM and 140uM, the AMP ranges non-linearly between 0.057uM and 2.4uM. The levels of both [ADP] and [AMP] are well below the K_m of several key enzymatic reactions (92).

9) Variations in temperature produced changes in the internal environment predictable from *in vitro* enzymology. At the lower temperature the pH was found to be 0.2 units higher and the Mg ++, determined from the β-ATP chemical shift, decreased. Both changes reflect increased proton and Mg^{++} binding constants. These values were independent of steady-state stimulation. The reduced slope of Figure 4.20 at 22°C and the resting fluxes plotted on Figure 4.18 are expected from a Q_{10} of 2.1 calculated from the data of Table 4.1.

Variations of muscle temperature provided a means for changing the metabolite concentrations and ATPase activity without stimulation. In contrast to previous studies in heart (88) which suggested that PCr/ATP levels remain constant with temperature, the results in soleus, together with preliminary studies in fish fast-twitch muscle, show a decrease in PCr (and increase in Pi) with increased temperature while [ATP] remains constant. The necessary ADP concentration increase with decreased [PCr]/[ATP] was approximately a factor of 3, Table 4.1. Note that this increase correlates with, though is not necessarily related to, the increased oxygen consumption at increased temperatures.

4.7 Summary

Transient NMR spin transfer methods described in chapter 3 were applied to resting and stimulated slow-twitch soleus muscle to verify that the creatine kinase catalyzed molecular flux between PCr and ATP was in equilibrium and independent of ATPase activity *in vivo*. The observed equilibrium behavior is identical to that expected from an enzyme in a homogeneous solution and consistent with the classical model of PCr as an energy storage molecule. Total intracellular [ADP] was determined from the known equilibrium constant for CK and found to increase from a resting value of 15 uM to approximately 140uM at maximum stimulation. Free [ADP], which will be the important determinate for adenylate transport in the mitochondria, is lower and, over moderate rates of stimulation, near the K_m for mitochondrial ADP transport. This finding is consistent with ADP control of cellular respiration.

4.8 Figure Legends

Figure 4.1: Schematic representations of PCr's role in muscle. a) Classical energy buffer model. b) The "Phosphocreatine Shuttle" model whereby PCr acts to couple the mitochondrial sites of ATP production to ATPase sites of utilization at the myofibrils. ATP synthesized in the mitochondria transfers phosphoryl bond energy to PCr at mitochondrial (mit) CK sites. PCr transports energy to myofibrillar (mf) CK sites, where it is converted back to ATP.

Figure 4.2: pH calibration curve for determining intracellular pH. The chemical shift difference between PCr and Pi resonances is plotted as a function of solution pH. Calibration was performed at 30°C in solutions of 20mM PCr, 10mM Pi, 140mM KCl, and 1mM $MgSO_4$. Chemical shift in Hz determined at 8.5 Tesla (resonance frequency of ^{31}P=145.6Mhz, 1ppm = 145.6hz). Solid line is the least-squares fit of the measured chemical shifts.

Figure 4.3: Probe Assembly for *in vivo* spectroscopy of perfused muscle.

Figure 4.4: *In vivo* probe circuit. The coil, L, is connected in a balanced configuration to minimize dielectric coupling to ground. A single turn saddle geometry was used for L (length= 3 cm, diameter= 1.3 cm). All tunable capacitors were 1-30pF, and the unlabeled fixed capacitor was 33pF.

Figure 4.5: RF transmit/receive probe interface to spectrometer for *in vivo* spectroscopy. The 360 Mhz spectrometer is a prototype system designed and constructed at the Francis Bitter National Magnet Laboratory.

Figure 4.6: Transient response of stimulated soleus. Prior to acquisition of

kinetic data, steady-state was determined by constant force generation, below, and stable ^{31}P-NMR resonance amplitudes, above. Approximately 10 minutes were required to reach steady-state once stimulation began. Spectra are sequential acquisitions (NA=32) following stimulation at 15 twitches/minute. Twitch force was monitored by strain gauge and bridge network, Figure 4.3 (exp. May26).

Figure 4.7: Two sets of data representing the range of data quality. Plots are of the PCr and γ-ATP resonance areas at early times (x-axis) following inversion of the PCr peak. From the linear fit of these initial points the flux is determined. Both sets were 32 signal averages from two different soleus preparations. On the right the linear fits are in good agreement with all the data points. On the left less agreement was found between the individual points and the fit due in part to the reduced size, and thus signal, of the second preparation. Tables list the parameters from the least-squares fit of the data.

Figure 4.8: Rate constant, k, for creatine kinase versus enzyme concentration measured *in vitro* at 30°C. (25mM PCr, 5 mM NaATP, 1.2mM KPi, 6mM MgCl, 12mM KCl, 1% BSA, 7.5mM KHPO4, 10mM Cr). The value obtained for resting soleus is shown on the plot setting an approximate *in vivo* activity of 3.2 KU/ml, pH=6.8. (experiments oct1736E(filled) ,oct1936BE(open))

Figure 4.9: Creatine Kinase Flux versus [PCr] measured *in vitro*. Data was obtained at 30°C. Initial solution contained 6.7mM PCr, 5mM ATP, 8.3mM Pi, 6mM MgCl, 12mM KCl, .025mg/ml BSA. PCr was added to vary [PCr]. Concentration was determined from Pi resonance area which remained constant. The pH, determined from the Pi -- PCr chemical shift was constant 7.2 +/-0.1 (exp. Oct1937e).

Figure 4.10: NMR determined metabolite concentrations over the course of two experiments representative of a highly stable preparation and a minimally stable preparation. a) Data are normalized to an external reference phenylphosphonic acid (PPA) to correct for any change in the probe sensitivity. ATP is seen, as in all preparations, to remain remarkably constant (exp. may26). b) A less viable preparation with data normalized to [ATP] which was observed to remain constant (exp. oct03).

Figure 4.11: Changes in the ^{31}P spectrum following steady-state electrical stimulation. Metabolite concentrations are taken as proportional to the resonance areas. [ATP] is found to remain constant while [PCR] decreases and [Pi] increases.

Figure 4.12: Steady-state saturation of γ-ATP phosphate demonstrating absence of significant ATP-->Pi exchange. Shown are control spectra from resting soleus (a), spectra obtained following γ-ATP saturation (b), and the spectra obtained by subtracting the saturated from the unsaturated data, (a-b). The difference spectrum demonstrates magnetization transfer. The difference spectrum from a stimulated soleus (30 twitches/min) is also shown (a'-b'); gain is increased to emphasize the absence of exchange to Pi.

Figure 4.13: Soleus data from a single preparation demonstrating a dependence of ATP/PCr ratio on stimulation rate. Also plotted are data from Meyer et al (94) for oxygen consumption versus stimulation rate. These independent relationships suggest a connection between ATP/PCr and oxygen consumption in the soleus (exp. may2686.dat).

Figure 4.14: Estimated ^{31}P flux through soleus ATPase versus ATP/PCr ratio. ATPase flux was calculated from oxygen consumption data of Meyer with P:O taken as 3. Note the CK flux as measured by NMR is greater than 10 times higher at all ATP/PCr values.

Figure 4.15: Stoichiometric relationship between Pi and PCr during steady-state stimulation in the soleus. Pi/ATP is plotted versus PCr/ATP for the perfused soleus at 30°C at rest and during steady-state stimulation up to 120 twitches/min. Data for 9 preparations is shown. Scatter is due to the preparation-to-preparation viability differences whereby small regions of non-viable tissue contribute a constant Pi signal. Top Right: Data from a single preparation (exp. oct03), demonstrating nearly ideal conservation. The linear least-squares fits are shown.

Figure 4.16: NMR derived rate constant in N=6 soleus preparations determined by transient selective inversion transfer, PCr-->ATP, k= (chemical flux/chemical concentration). Data were obtained at rest and following graded electrical stimulation in the soleus to 60 twitches/minute. Muscles were maintained at 30°C.

Figure 4.17: Creatine kinase flux (mM/sec) versus ATP/PCr in cat soleus at 30°C following graded electrical stimulation. At rest the average ATP/PCr ratio was approximately 0.3 increasing to nearly 1.6 at stimulation rates as high as 60 twitches per minute. 24 data sets from 6 stable soleus preparations are shown. Best linear least-squares fit gives a slope of -0.26 +/- (0.34) mM/sec. Upper Right: Data from all 9 preparations (including those with limited stablity). Slope = -0.26 +/- (0.50).

Figure 4.18: Arrhenius plot of the logarithm of the NMR derived rate constant, k, versus 1/T(°K) for the creatine kinase catalyzed ^{31}P exchange PCr-->ATP. Indicated are data obtained *in vitro* from purified enzyme, open circles, and data obtained *in vivo* from resting soleus muscle, Table 4.1. Linear least-squares fit to the *in vitro* data for T<38°C gives a slope of -4172 +/- 818 °K, which reflects an equivalent activation energy of 35 KJ/mole.

Figure 4.19: [ADP] as calculated from the creatine kinase equilibrium based on data obtained *in vivo* from the perfused soleus at 20°C and 30°C, Table 4.1. The dashed line represents the K_m for adenylate transport in mitochondria (24).

Figure 4.20: NMR derived rate constant, k, versus stimulation rate from a single soleus preparation. k is the ratio of the chemical flux PCr-->ATP to the PCr concentration. The slope change reflects the Arrhenius relationship, Figure 4.18. (exp. May26).

Figure 4.21: Calculated Gibb's function for ATP hydrolysis in muscle. The creatine kinase equilibrium maintains ΔG over large fluctuations in [PCr]/[ATP], thereby allowing large metabolic perturbations to occur without dramatically altering the free energy required for maintainance of ATPase activity. Curves were calculated from Equation 1.1 using the creatine kinase equilibrium, Equation 4.1, to obtain ADP. The sum of PCr and Pi was assumed constant.

Figure 4.22: Calculated [AMP] and [ADP] for soleus at rest and stimulated up to 90 twitches-per-minute. Equation 4.1 was used for ADP, and the adenylate

kinase equilibrium was assumed with $[AMP]=.4[ADP]^2/[ATP]$ (4.9). NMR derived [ADP] and [AMP] are significantly less than those measured by other, invasive, techniques. The adenylate levels are well below their K_m's for several enzymes in key metabolic pathways. Indicated on the figure are the Km's of ADP for mitochondrial adenine transport, nucleoside diphosphate kinase, and pyruvate dehydrogenase. ADP levels are well below the K_m of phosphoglycerol kinase (0.26 mM). ADP has a dominant inhibitory effect on isocitrate dehydrogenase at approximately 140 mM. AMP will not have inhibitory effects on fructose diphosphatase in concentrations less than approximately 0.03mM and is not thought to stimulate phosphofructokinase at concentrations less than 0.1 mM.

TABLE 4.1

Summary of Results in Resting Soleus

	30 C	22 C	
*** [ATP]	5.03 +/- .04	5.03 +/- .04	mM
T1(ATP)	3.0 +/- 0.5	1.3 +/- 0.5	sec
[PCr]/[ATP]	3.2 +/- 0.6	4.0 +/- 0.3	
[PCr] cal.	16 +/- 3	20 +/- 2	mM
T1 (PCr)	3.8 +/- 0.7	3.4 +/- 0.8	sec
[Pi]/[ATP]	1.7 +/- 1.1	1.2 +/- 0.2	
[Pi] cal.	8.5 +/- 5.5	6.0 +/- 1.0	mM
T1 (Pi)	4.2 +/- 0.3	4.4 +/- 0.8	sec
pH	6.8 +/- 0.1	7.0 +/- 0.1	units
[Mg++]	2.0 +/- 0.3	0.7 +/- 0.3	mM
** Keq=$\frac{ATP*Cr}{ADP*PCr}$	177	203	
*** [ADP](cal)	15 +/- 9	5 +/- 2	uM
k(PCr->ATP)	0.17 +/- 0.06	0.08 +/- 0.02	sec-1
Flux (PCr->ATP)	2.7 +/- 1.1	1.6 +/- 0.4	mM/sec

** corrected for temperature by ΔG=-9.4 KJ/mole (80).
*** ATP = 5.03 +/- .04 mM, Total Creatine = (PCr + Cr)= 24.4 mM
From Meyer et al (94)

Table 4.2 : Balance of Creatine Kinase Flux

	PCr/ATP	Kr/Kf	(PCr/ATP)/(Kr/Kf)
T-30 degrees C			
May02	4.9	5.1	.96
	3.9	3.7	1.05
Jul21	2.7	2.2	1.21
	1.2	1.7	0.71
Sep19	2.9	2.5	1.16
Oct03	3.1	3.2	0.95
		mean +/- sd	1.01 +/- 0.18

$$\frac{\text{FLUX FORWARD}}{\text{FLUX REVERSE}} \approx 1$$

TABLE 4.3

Comparison of ATPase Flux and CK Flux for Different Muscle Types

Muscle	PCr ATP	[ATP]mM	CK Flux(mM/sec) low work(lw)	CK Flux(mM/sec) high work(hw)	ATPase(mM/sec) lw	ATPase(mM/sec) hw	CK flux ATPase flux lw	CK flux ATPase flux hw
Bicep	3.9	8.9	7.3	7.3	0.01	0.08	660	100
Soleus	3.3	5.0	2.7	2.7	0.01	0.12	240	20
Heart(d)	2.1	9-25	2-20		8.	16.	0.25-2.5	
Heart(a)			non-NMR studies		.05		40-400	
(b)					.08		25-250	
(c)					.22		9-90	
Bladder	1.7	0.94	.32		.01		32	

Note: Heart data is for rats perfused with:
a) Phosphate buffer, Angelova,Gateva P.(1969)Exp.Geron. 4:177-187
b) Glucose, Barker,SB. Klitgaard (1952)AM.J.Physiol.170:81-86
and Field J.(1948) Methods Med. Res. 1:289-307
c) Glucose, van Bertalanfty L. Estwick RR.(1954)Am.Jou.Physio 177:16-18
d) Values vary +/- >100% taken from estimate of literature mean
see for eg Ugurbil,K. Biochem.(1986)
Note: Assumed cell wet weight to dry weight ratio is 4.0.
Assumed Intracellular space is 75% of total.
Assumed 6 moles of ATP are produced for each molecule of oxygen consumed.

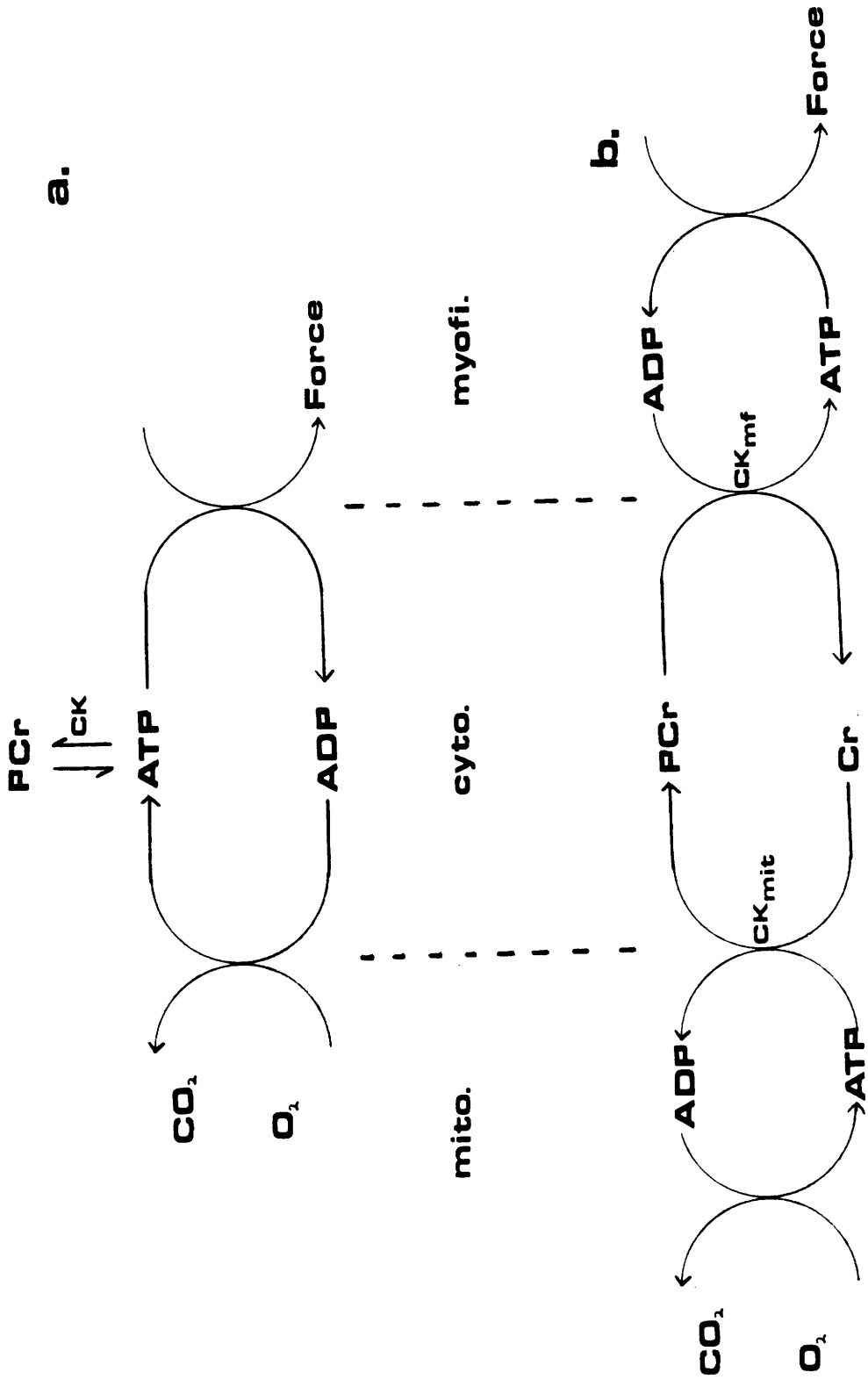
a.
PCr
CK
ATP
ADP
Force
myofi.
cyto.
mito.
CO2
O2
b.
Force
ADP
ATP
CKmf
PCr
Cr
CKmit
ADP
ATP
CO2
O2

Figure 4.1

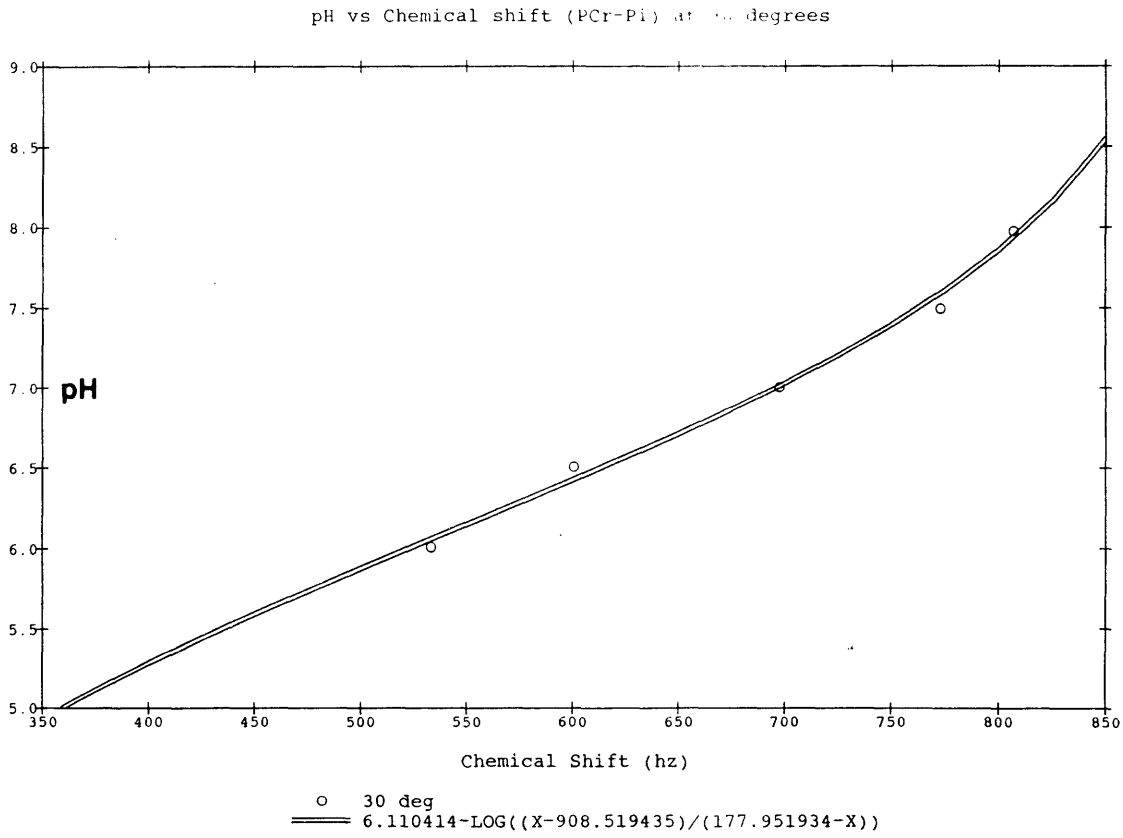
pH vs Chemical shift (PCr-Pi) at ... degrees
9.0
8.5
8.0
7.5
7.0
6.5
6.0
5.5
5.0
pH
350
400
450
500
550
600
650
700
750
800
850
Chemical Shift (hz)
30 deg
6.110414-LOG((X-908.519435)/(177.951934-X))

Figure 4.2

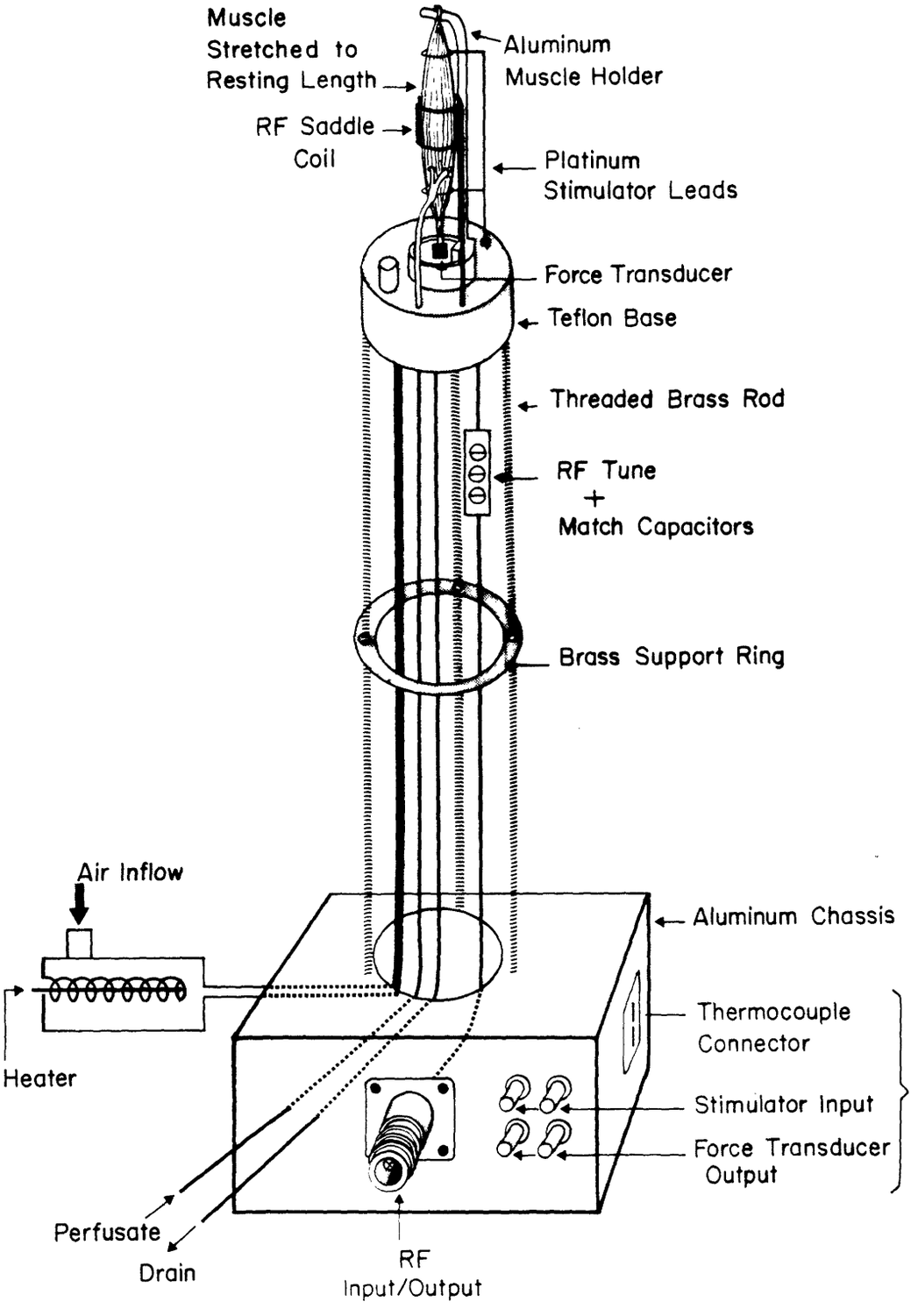
Muscle
Stretched to
Resting Length
RF Saddle
Coil
Aluminum
Muscle Holder
Platinum
Stimulator Leads
Force Transducer
Teflon Base
Threaded Brass Rod
RF Tune
+
Match Capacitors
Brass Support Ring
Air Inflow
Aluminum Chassis
Thermocouple
Connector
Heater
Stimulator Input
Force Transducer
Output
Perfusate
Drain
RF
Input/Output

Figure 4.3

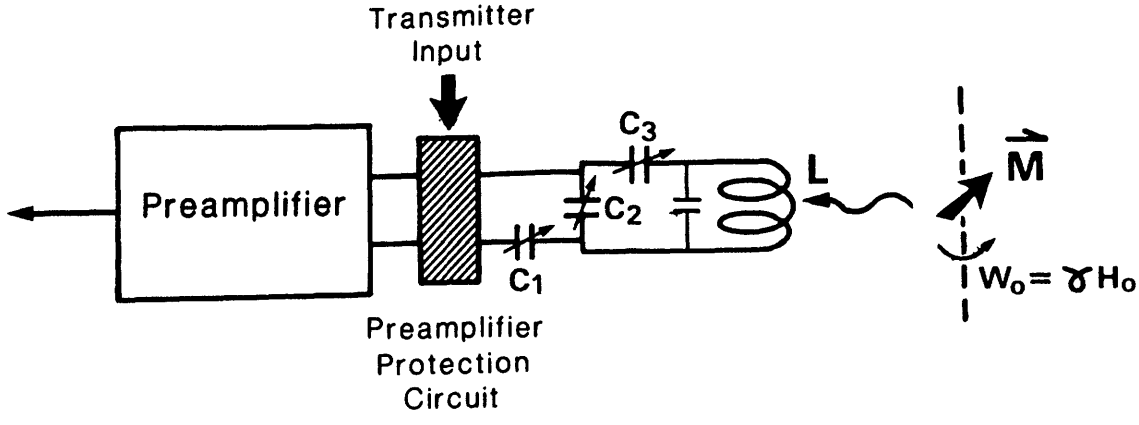
Transmitter
Input
Preamplifier
C3
C2
C1
L
M
Wo= γ Ho
Preamplifier
Protection
Circuit

Figure 4.4

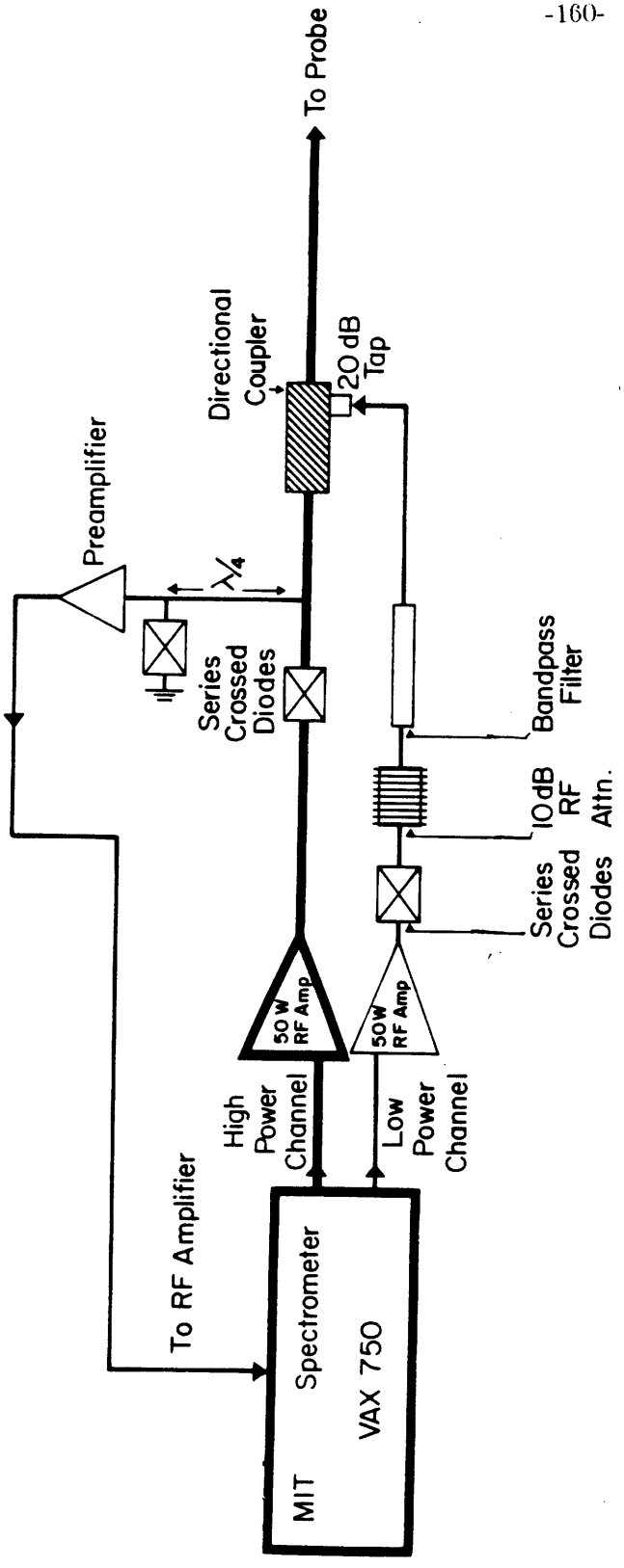
To Probe
Directional Coupler
20 dB Tap
Preamplifier
λ/4
Series Crossed Diodes
Bandpass Filter
10dB RF Attn.
Series Crossed Diodes
50 W RF Amp
50W RF Amp
High Power Channel
Low Power Channel
To RF Amplifier
MIT Spectrometer VAX 750

Figure 4.5

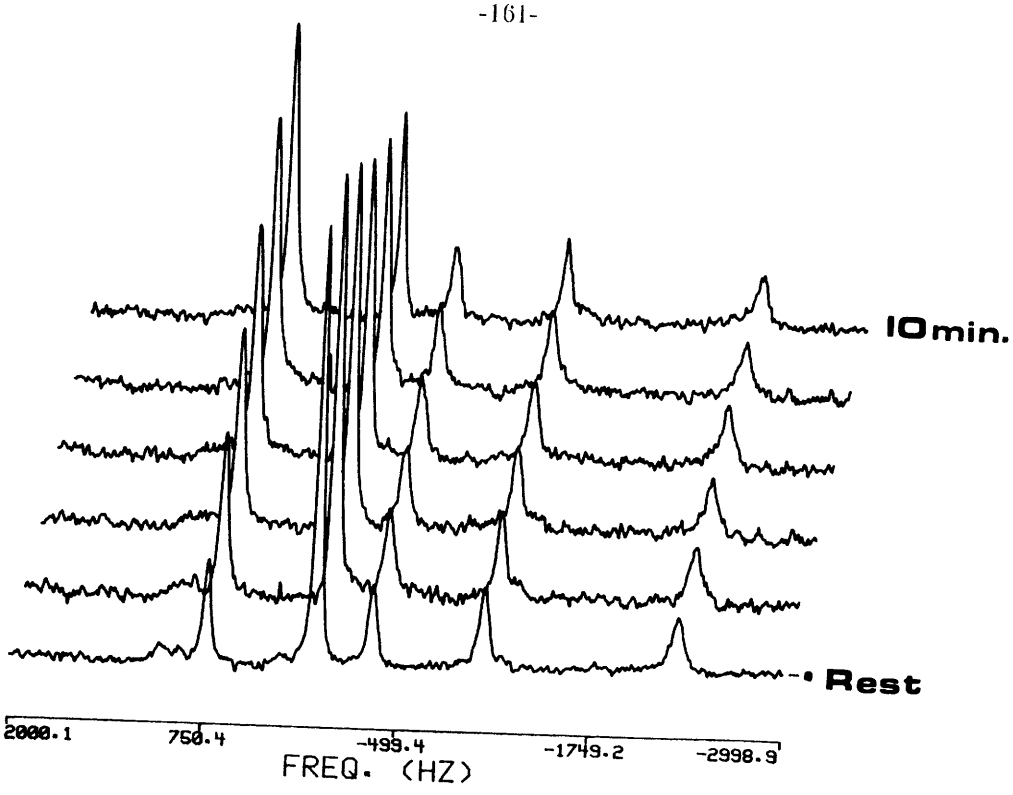
10min.
Rest
2000.1
750.4
-499.4
-1749.2
-2998.9
FREQ. (HZ)

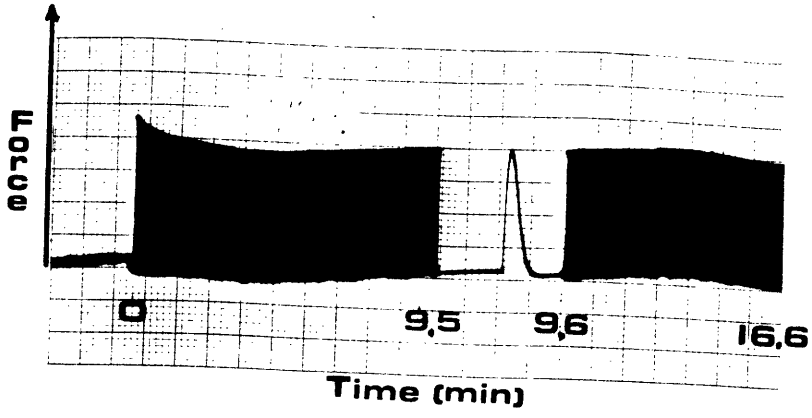
Force
0
9,5
9,6
16,6
Time (min)

Figure 4.6

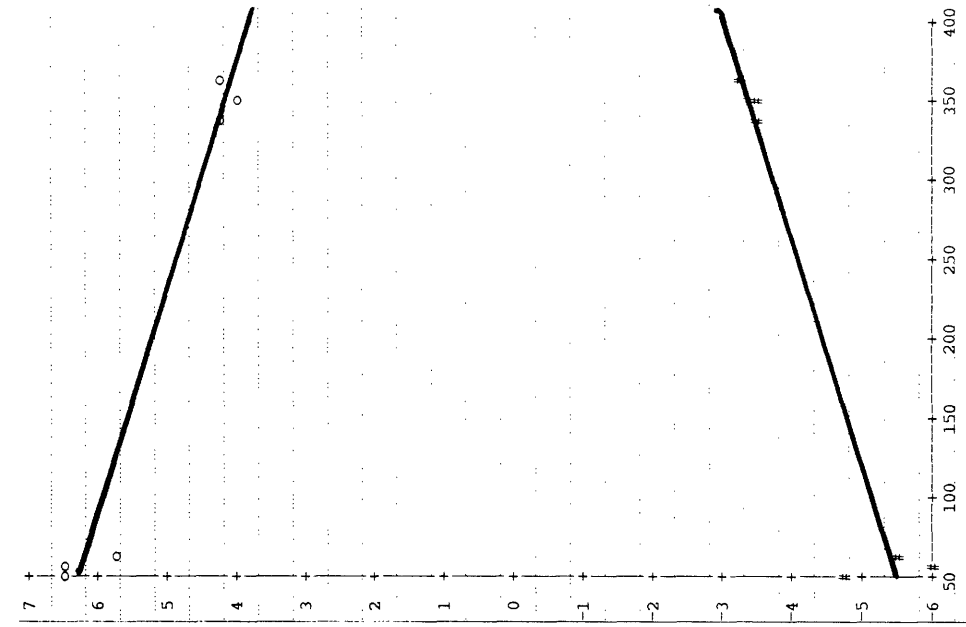

PARAM.	FINAL VALUES	STD ERRORS	T VALUE	SIG. LEV.
M	0.006579	0.001390	4.732	0.009091
B	-5.665502	0.348434	-16.260	0.001000
M	-0.007078	0.000727	-9.731	0.001000
B	6.711723	0.182296	36.820	0.000100

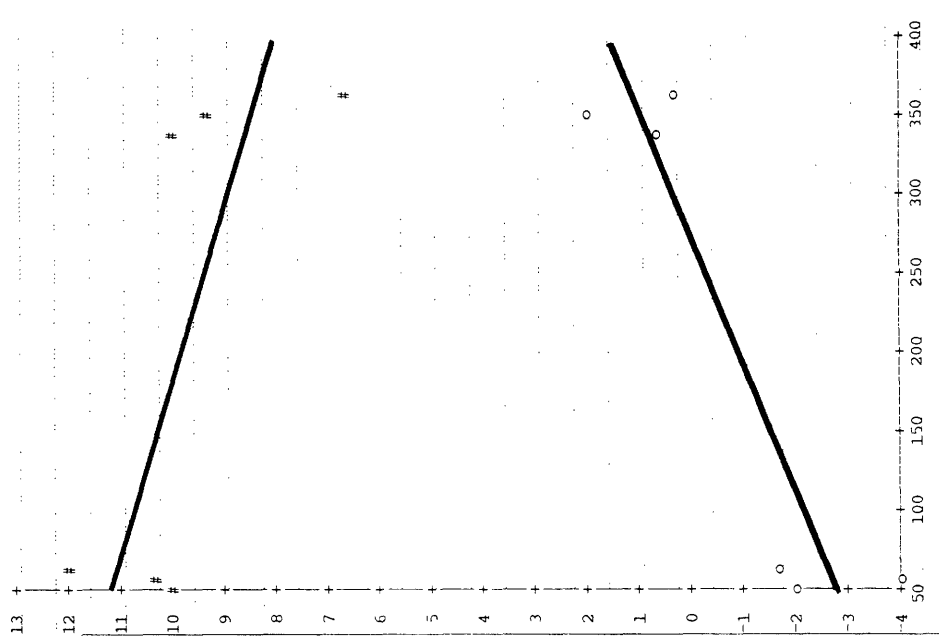

PARAM.	FINAL VALUES	STD ERRORS	T VALUE	SIG. LEV.
M	-0.007173	0.003898	-1.840	0.13960
B	11.230767	0.976855	11.500	0.00100
M	0.011862	0.003052	3.886	0.01775
B	-3.193681	0.764964	-4.175	0.01397

Figure 4.7

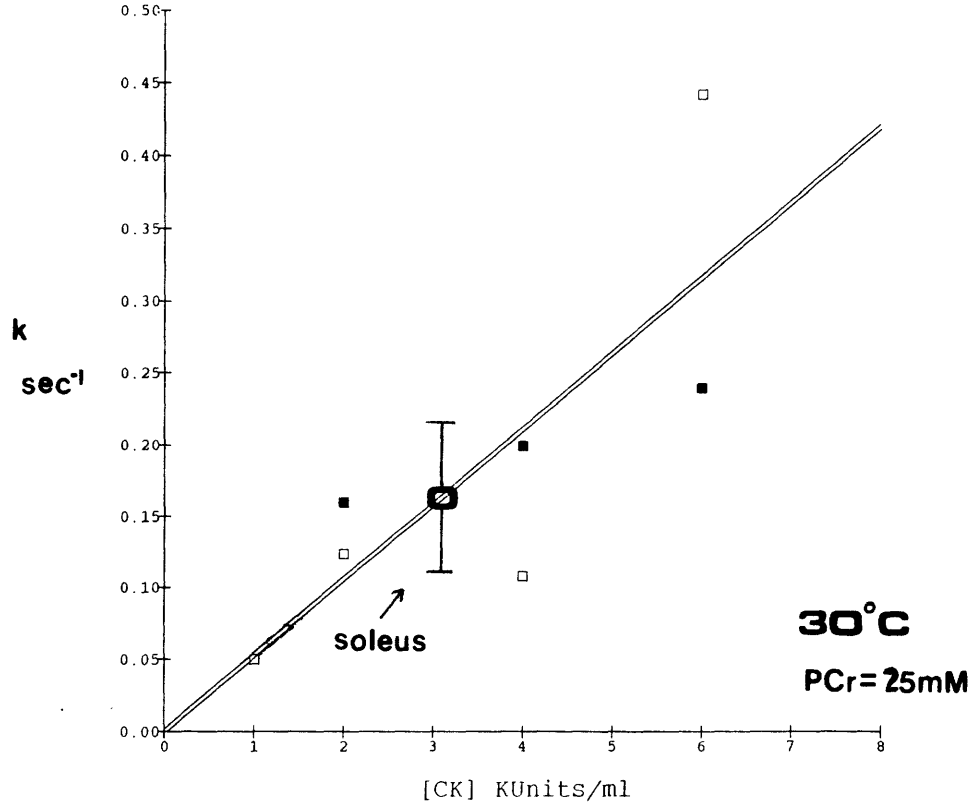
k
sec-1
0.50
0.45
0.40
0.35
0.30
0.25
0.20
0.15
0.10
0.05
0.00
0
1
2
3
4
5
6
7
8
soleus
30°C
PCr= 25mM
[CK] KUnits/ml

Figure 4.8

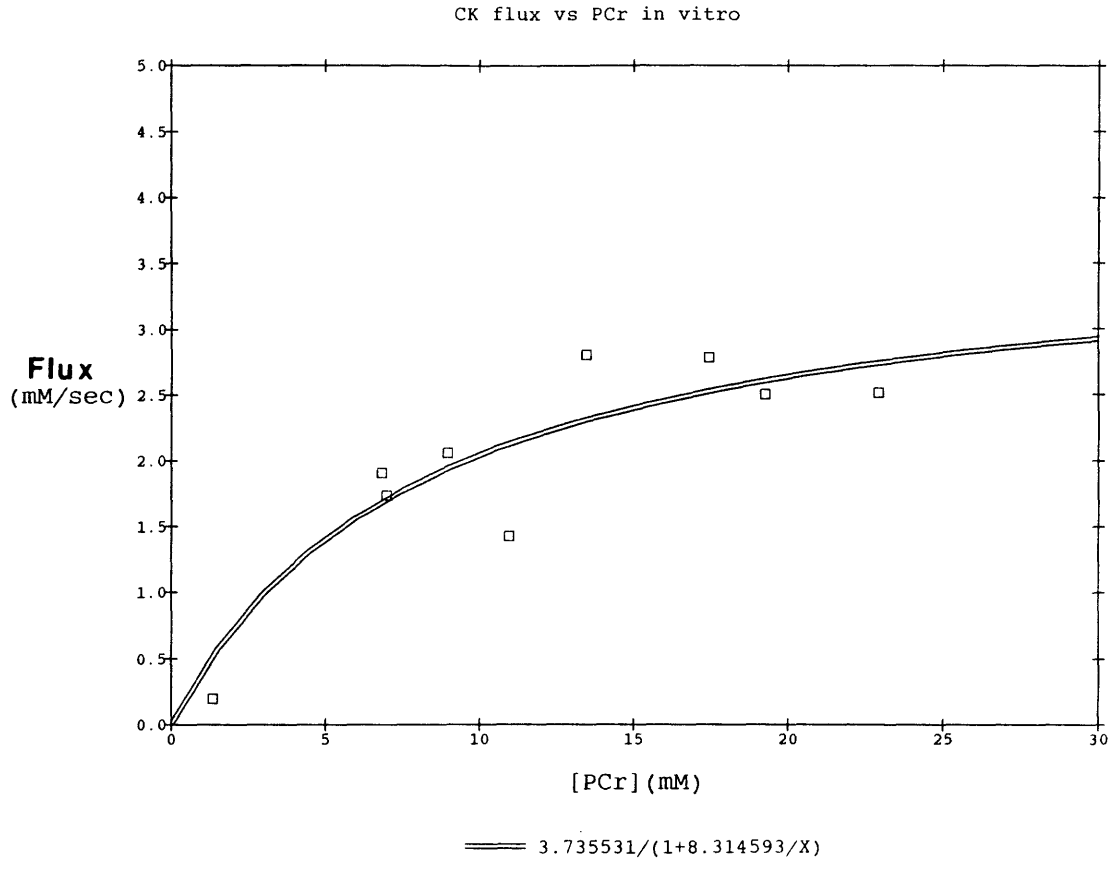
CK flux vs PCr in vitro
Flux
(mM/sec)
5.0
4.5
4.0
3.5
3.0
2.5
2.0
1.5
1.0
0.5
0.0
0
5
10
15
20
25
30
[PCr](mM)
3.735531/(1+8.314593/X)

Figure 4.9

Temporal Stability of Single Soleus

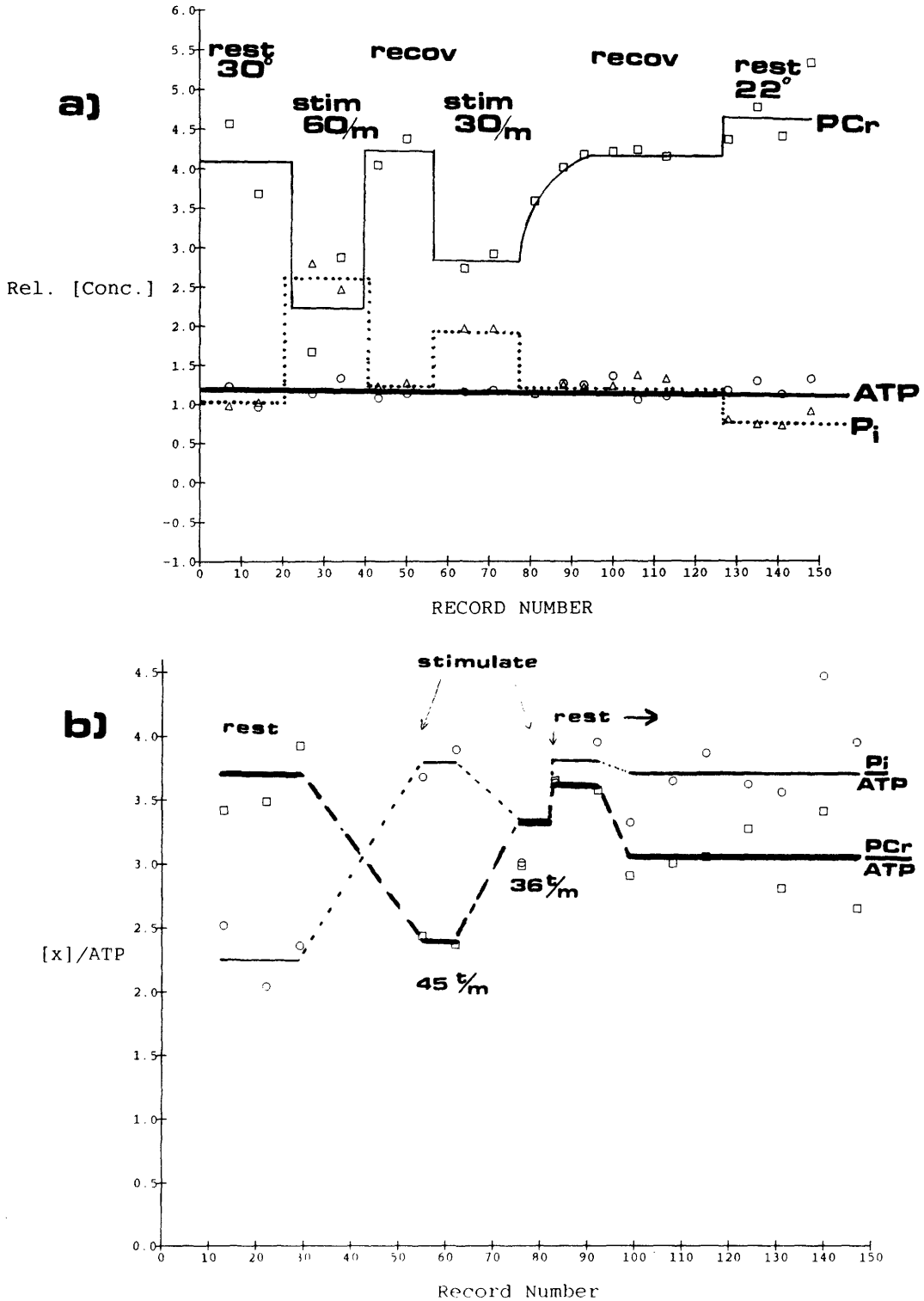

Figure 4.10

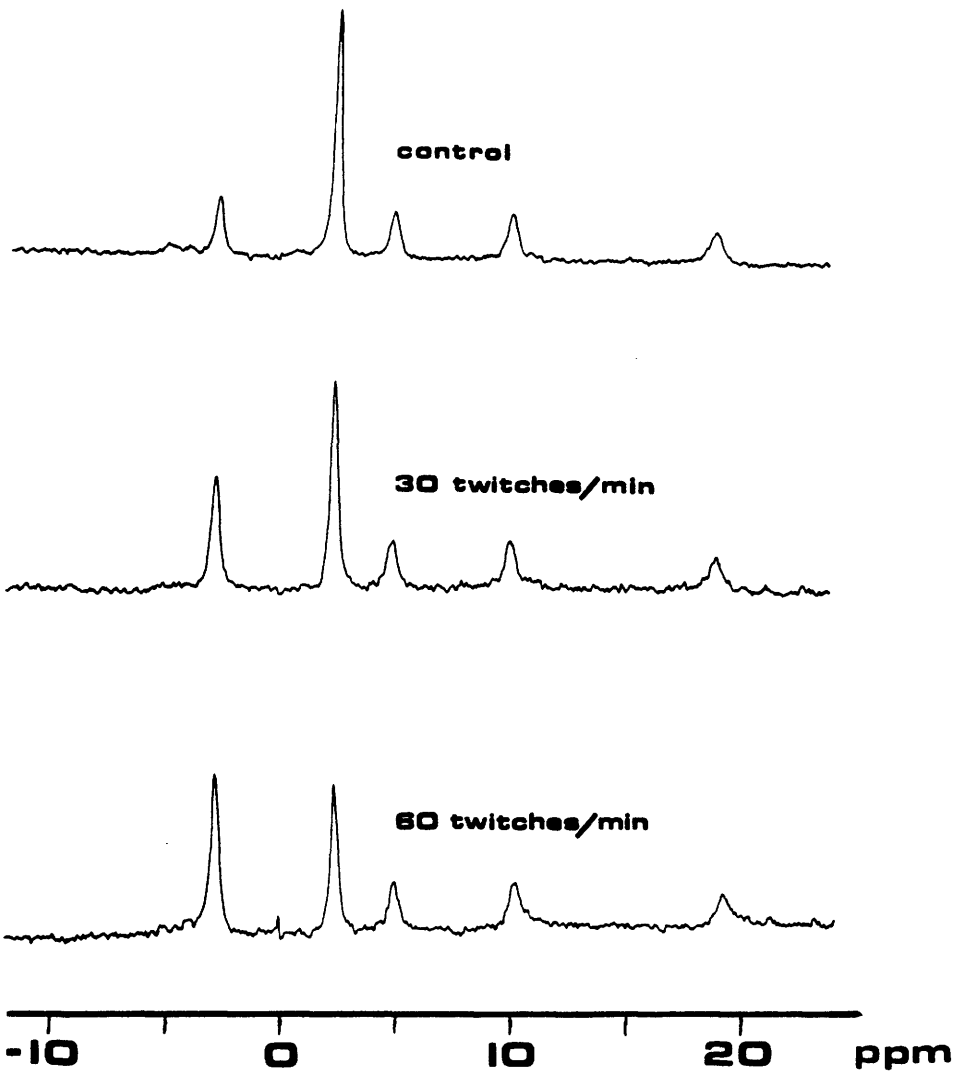

Figure 4.11

Figure 4.12

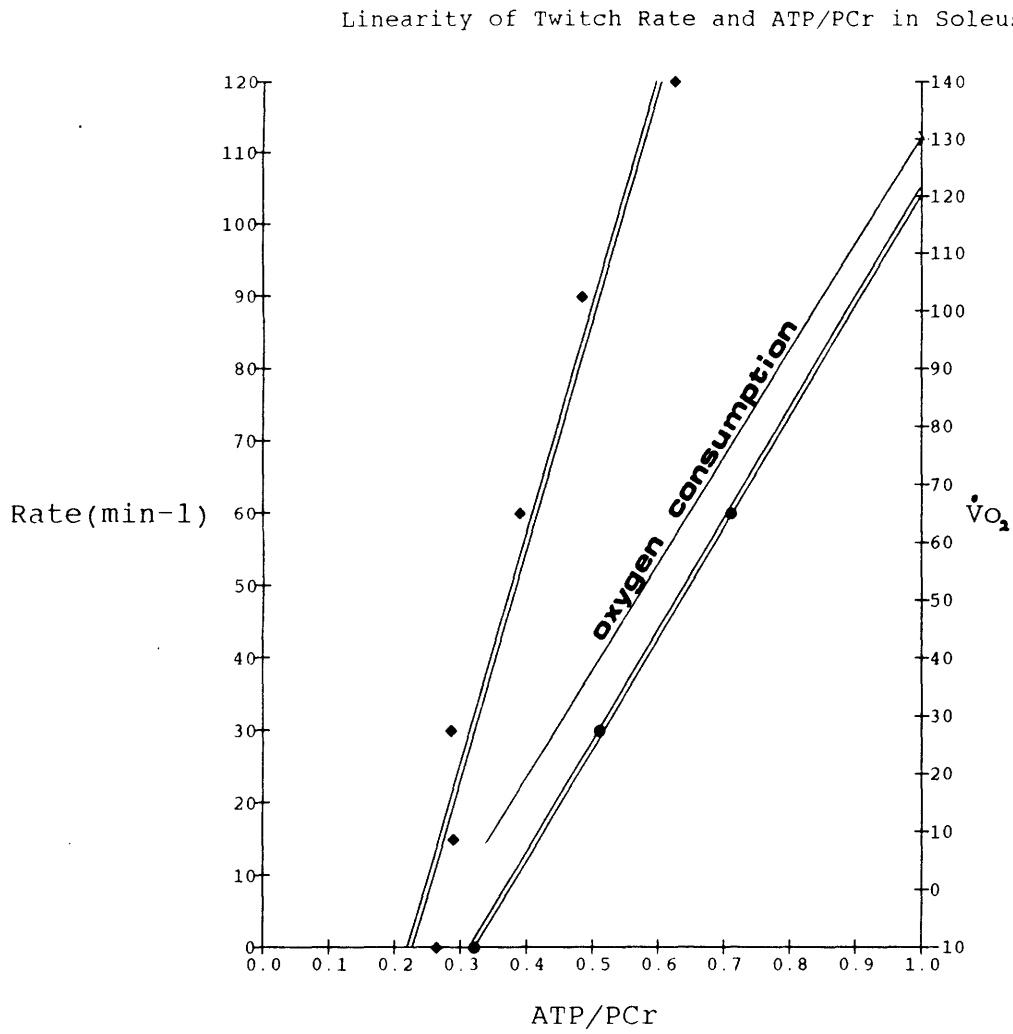
Linearity of Twitch Rate and ATP/PCr in Soleus
Rate(min-1)
$\dot{V}O_2$
oxygen consumption
ATP/PCr
0.0
0.1
0.2
0.3
0.4
0.5
0.6
0.7
0.8
0.9
1.0
0
10
20
30
40
50
60
70
80
90
100
110
120
130
140

Figure 4.13

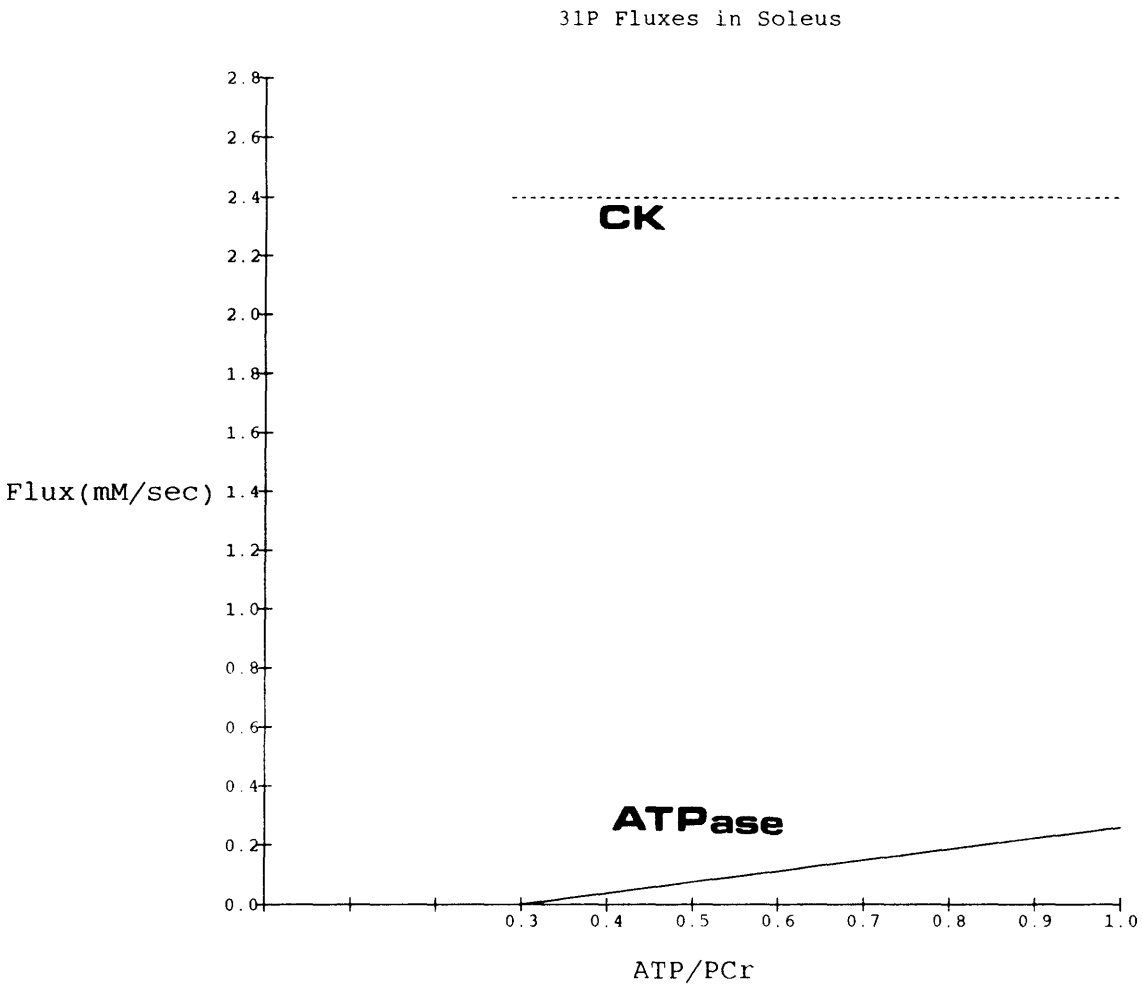
31P Fluxes in Soleus
Flux(mM/sec)
2.8
2.6
2.4
2.2
2.0
1.8
1.6
1.4
1.2
1.0
0.8
0.6
0.4
0.2
0.0
CK
ATPase
0.3
0.4
0.5
0.6
0.7
0.8
0.9
1.0
ATP/PCr

Figure 4.14

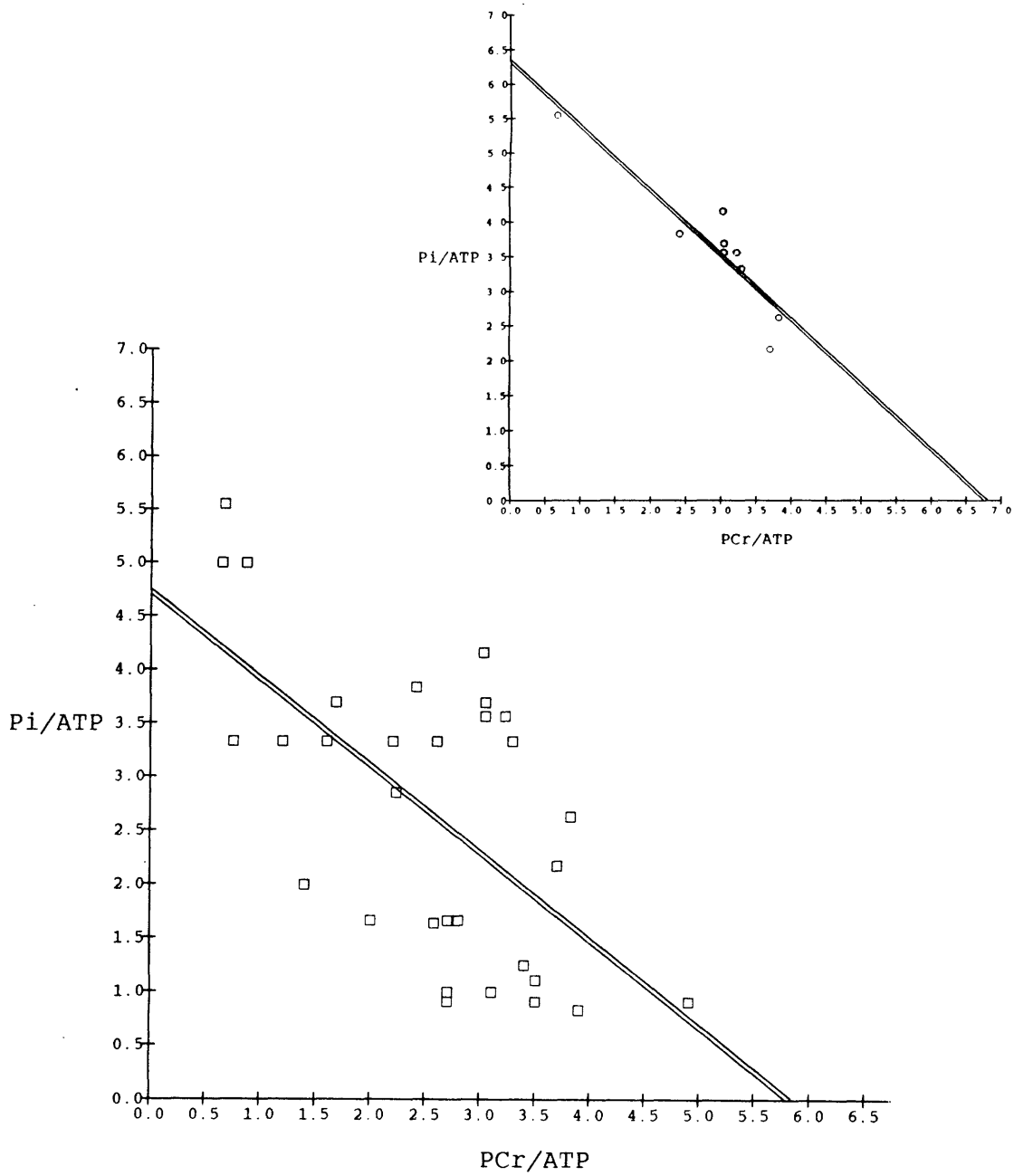

Figure 4.15

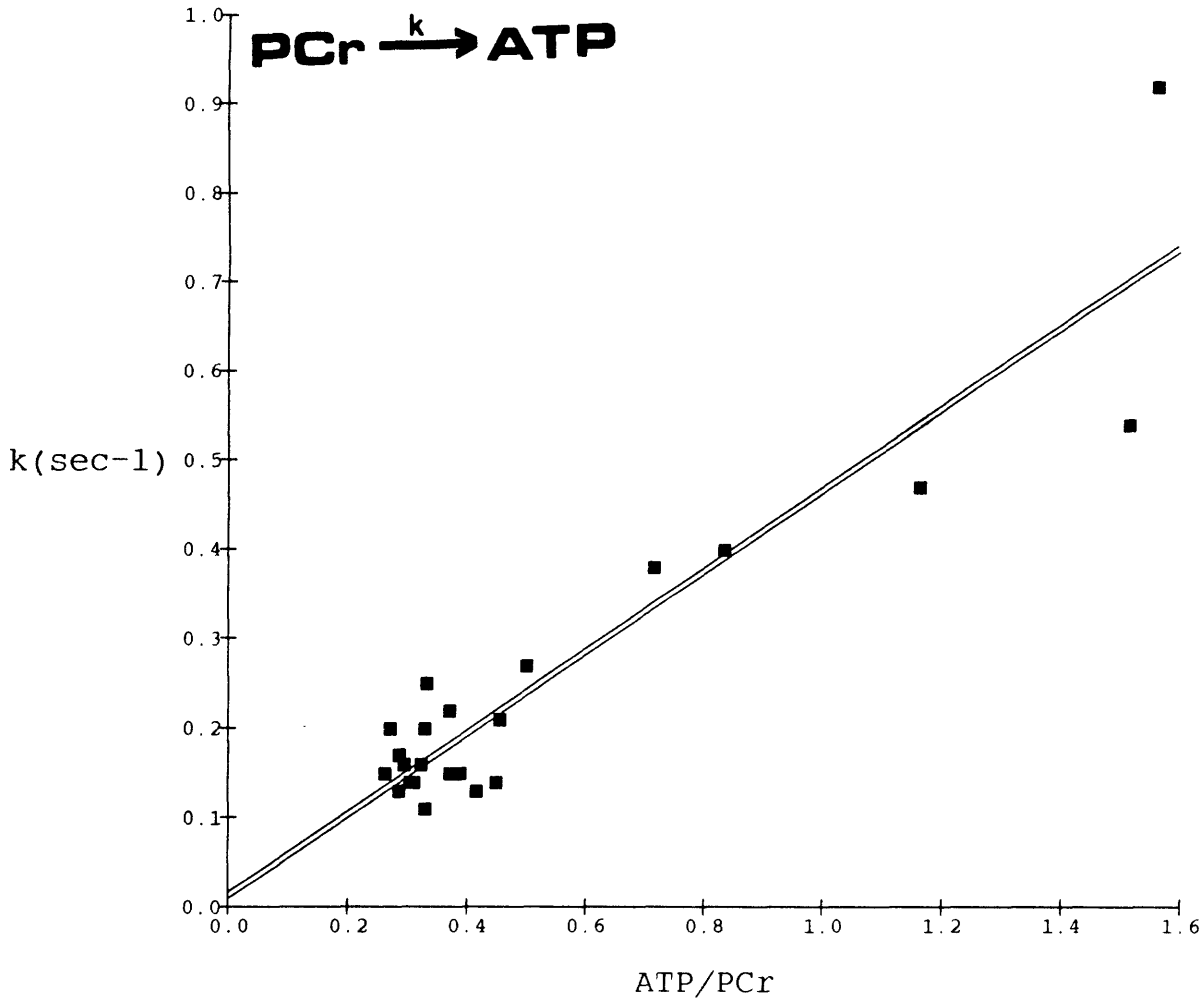
PCr k ATP
k(sec-1)
ATP/PCr
1.0
0.9
0.8
0.7
0.6
0.5
0.4
0.3
0.2
0.1
0.0
0.0
0.2
0.4
0.6
0.8
1.0
1.2
1.4
1.6

Figure 4.16

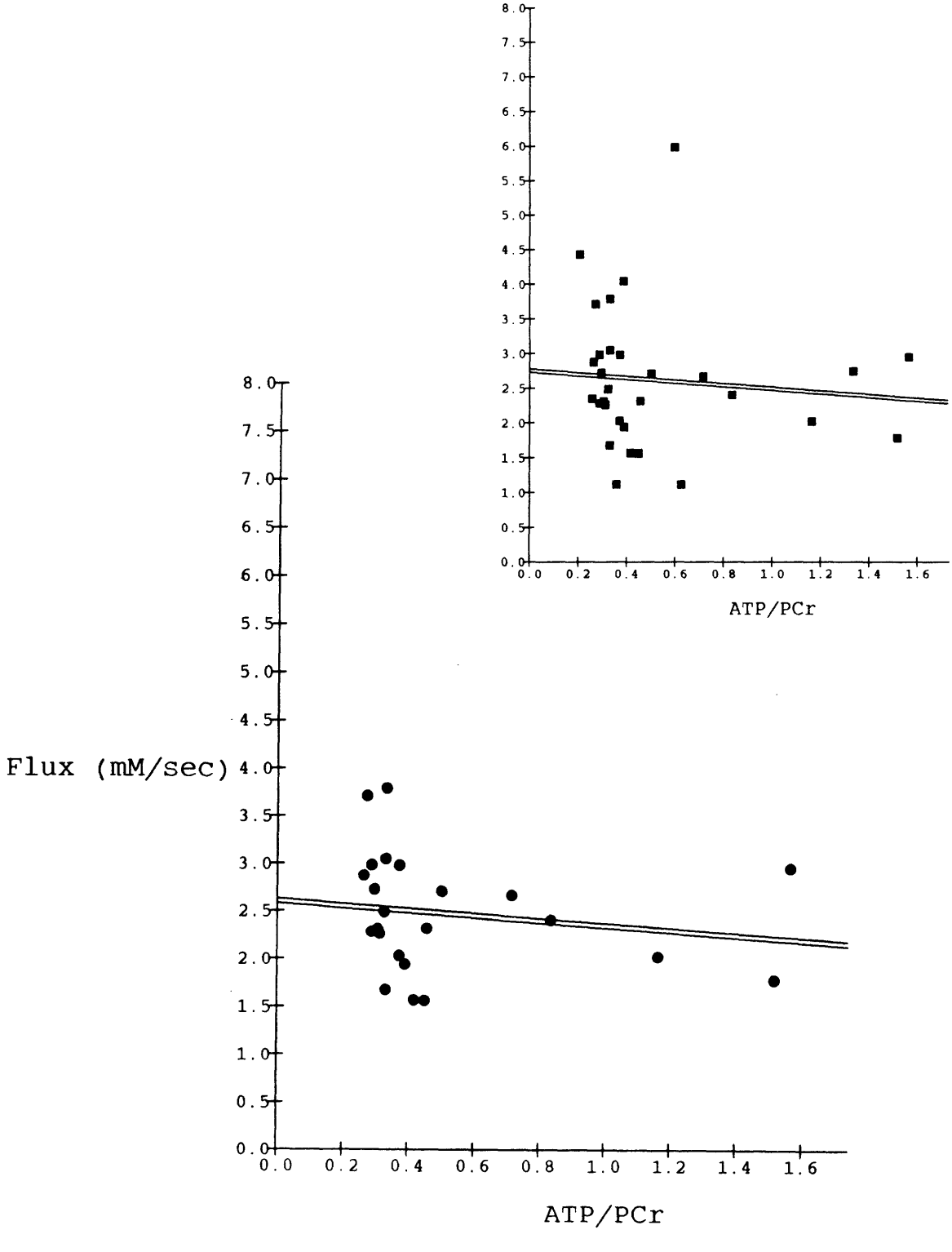
Flux (mM/sec)
8.0
7.5
7.0
6.5
6.0
5.5
5.0
4.5
4.0
3.5
3.0
2.5
2.0
1.5
1.0
0.5
0.0
0.0 0.2 0.4 0.6 0.8 1.0 1.2 1.4 1.6
ATP/PCr

Figure 4.17

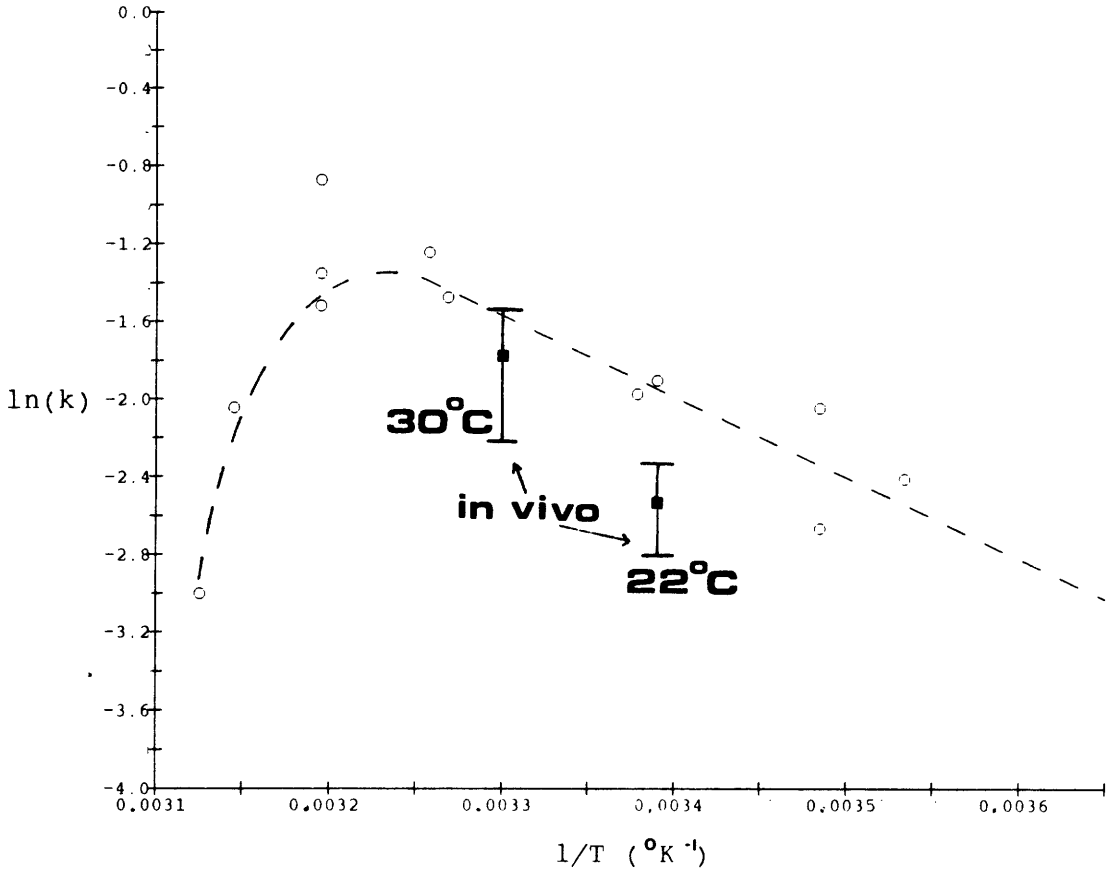
0.0
-0.4
-0.8
-1.2
-1.6
-2.0
-2.4
-2.8
-3.2
-3.6
-4.0
ln(k)
0.0031
0.0032
0.0033
0.0034
0.0035
0.0036
1/T (°K⁻¹)
30°C
in vivo
22°C

Figure 4.18

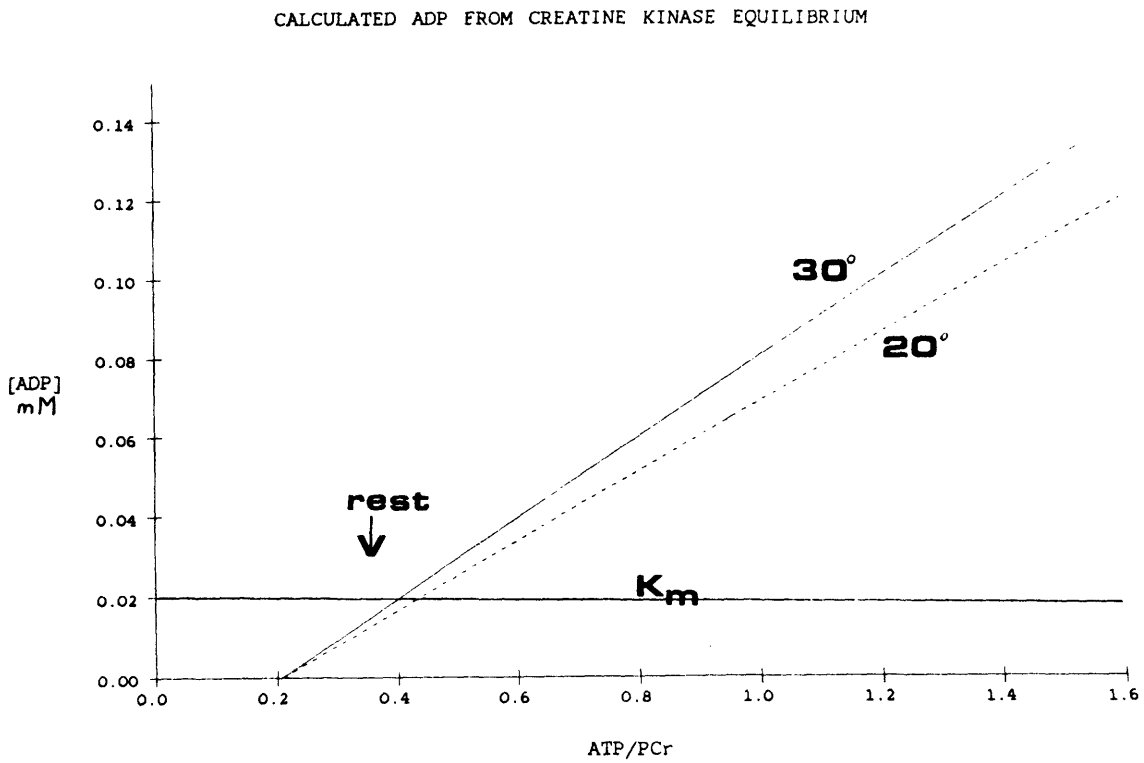
CALCULATED ADP FROM CREATINE KINASE EQUILIBRIUM
[ADP]
mM
0.14
0.12
0.10
0.08
0.06
0.04
0.02
0.00
0.0
0.2
0.4
0.6
0.8
1.0
1.2
1.4
1.6
ATP/PCr
30°
20°
rest
Km

Figure 4.19

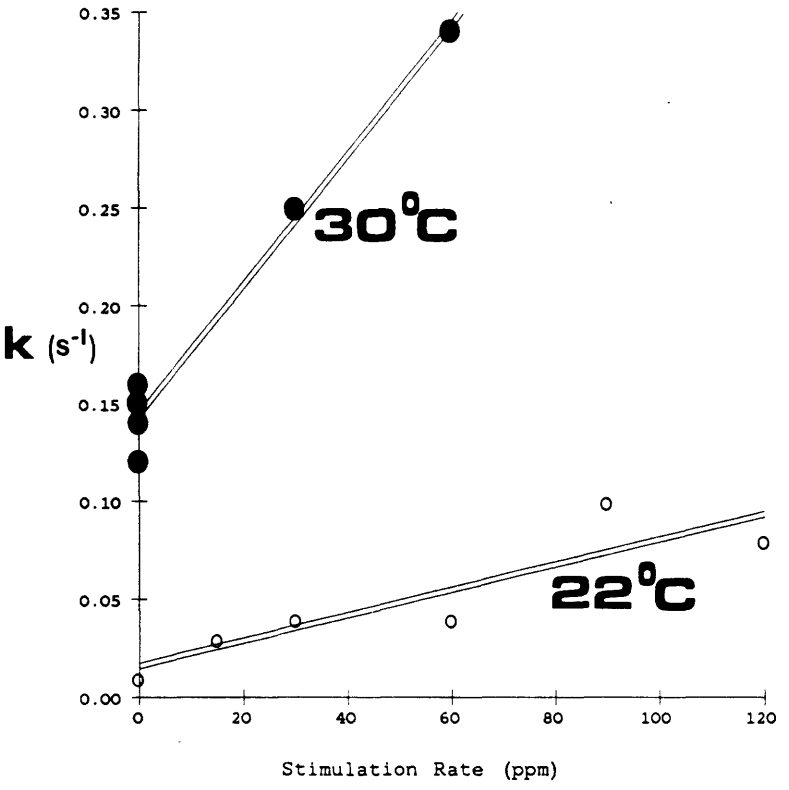
0.35
0.30
0.25
0.20
0.15
0.10
0.05
0.00
k (s-1)
30°C
22°C
0
20
40
60
80
100
120
Stimulation Rate (ppm)

Figure 4.20

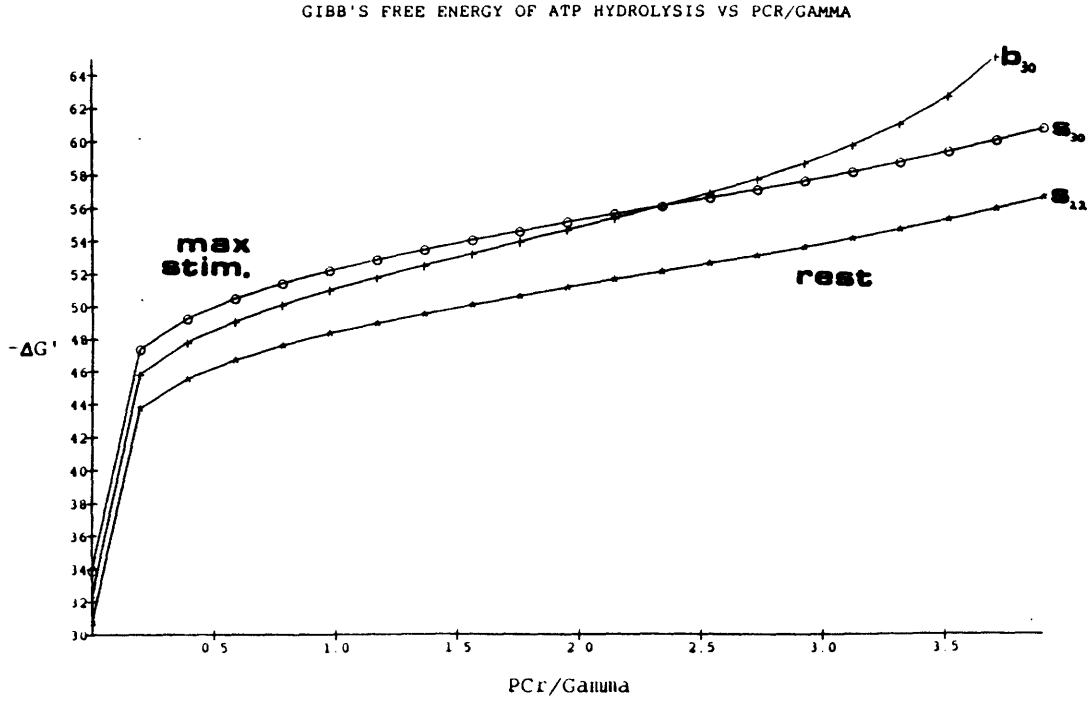
GIBB'S FREE ENERGY OF ATP HYDROLYSIS VS PCR/GAMMA
-ΔG'
PCr/Gamma
max stim.
rest
b30
s30
s22

Figure 4.21

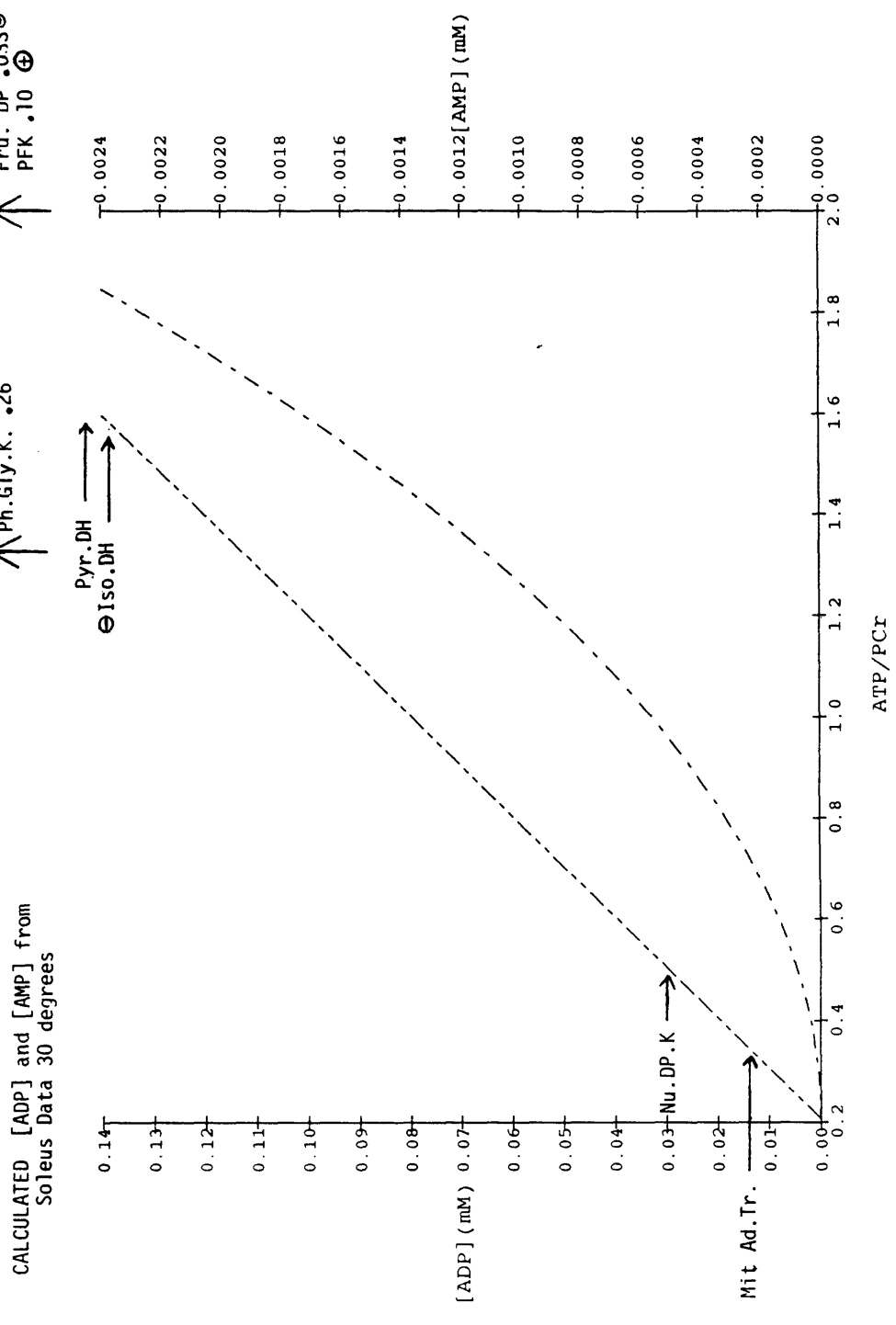
CALCULATED [ADP] and [AMP] from
Soleus Data 30 degrees
Cit.Syn .60 ⊖
Ph.Gly.K. .26
Pyr.DH
⊖Iso.DH
Cit.Syn 2.00 ⊖
Fru. DP .033 ⊖
PFK .10 ⊕
[ADP](mM)
[AMP](mM)
ATP/PCr
Nu.DP.K
Mit Ad.Tr.
0.14
0.13
0.12
0.11
0.10
0.09
0.08
0.07
0.06
0.05
0.04
0.03
0.02
0.01
0.00
0.0024
0.0022
0.0020
0.0018
0.0016
0.0014
0.0012
0.0010
0.0008
0.0006
0.0004
0.0002
0.0000
0.2
0.4
0.6
0.8
1.0
1.2
1.4
1.6
1.8
2.0

Figure 4.22

CHAPTER 5: MICROSCOPIC MAPPING OF CHEMICAL EXCHANGE-INDUCED MAGNETIZATION TRANSFER

5.1 Introduction

NMR spectroscopy provides nuclear spin information averaged over the entire sample volume. In many applications, especially biological ones, the sample is spatially heterogeneous with respect to chemical composition, chemical reaction velocities, and other properties influencing magnetic resonance parameters (67). Compartmentalization of chemical reactions will complicate understanding of NMR data representing globally averaged behavior in terms of quantitative reaction processes. Spatially localized flux information is necessary if these reaction dynamics are to be accurately characterized.

Using high-field magnets and strong gradients, several investigators have demonstrated submillimeter spatial resolution in proton magnetic resonance images (78,55,53,33,3,65). Signal-to-noise and diffusion considerations are the practical and ultimate limiting factors, respectively. The ability to resolve volumes on the scale of single living cells (typical diameters of $\sim$50 um) allows the possibility of NMR studies of microscopic heterogeneity in non-living and living systems. This chapter describes the use of an NMR microscope to 1) investigate the limits of detectability of tissue heterogeneity, and 2) implement an NMR method for spatially encoding chemical flux information.

5.2 Chemical Exchange Magnetic Resonance Imaging (CHEMI)

CHEMICAL EXCHANGE MAPPING: As described in chapters 1 and 2 the magnetization dynamics of an exchanging system of NMR visible nuclei can be characterized by transfer of longitudinal magnetization via physical mechanisms (lattice relaxation, R_i, and dipolar coupling, σ_{ij}) and chemical mechanisms (intra- and inter-molecular exchanges, k_{ij}). For an $X_i <-> X_j$ chemical exchange, with z components of magnetization M_i and M_j, a pseudo-first order unidirectional rate constant, k_{ij}, is often defined as the ratio of the spin flux, Ψ_{ij}, to the substrate magnetization at equilibrium, M_{io}, which is taken as a measure of the true chemical flux, Υ, per unit of substrate concentration:

$$(5.1) \qquad k_{ij} = \Psi_{ij}/M_{i_o} = \Upsilon_{ij}/[X_i]$$

The unidirectional magnetization flux from M_i to M_j is given by $\Psi_{ij}=M_i{}^*k_{ij}$. In the case of slow exchange ($k_{ij} << (\omega_i-\omega_j)$), the longitudinal magnetization can be used to monitor transfer of magnetization via chemical exchange.

The modified Bloch equations were extended in chapter 2 to include heteronuclear and homonuclear dipolar coupling with nucleus M_k and M_j respectively and rewritten in terms of flux. In a steady-state magnetization transfer experiment, saturation of M_j (with the assumption of complete saturation, $M_j=0$) reduces the system of equations 1.7 to

$$(5.2) \qquad dM_i/dt = 0 = R_i(M_{i_o} - M_{i_{sat}}) - k_{ij}M_{i_{sat}} + \sigma_{ji}M_{j_o} + \sum_{k \neq i,j} \sigma_{ki}(M_{k_o} - M_{k_{sat}})$$

If all dipolar interactions can be neglected, $\sigma=0$, this expression reduces to the familiar steady-state result (40):

$$(5.3) \qquad M_{i_o}/M_{i_{sat}} = 1 + \alpha_{ij}$$

Use of this equation in spectroscopy assumes that k^*T_1 is constant throughout the sample. In non-uniform samples relaxation and/or exchange vary spatially and α becomes $\alpha(r)$. The errors in the NMR derived flux from a multicompartment system were described in chapter 2. These errors will invalidate chemical flux determinations obtained from bulk samples. To characterize accurately the kinetics of the system, it is necessary to determine the function $\alpha(r)$ at every position within the sample.

It is possible to measure the spatially dependent chemical flux accurately by combining an NMR imaging technique with the steady-state magnetization transfer experiment. This approach allows separation of the entire sample into individual physical compartments limited in size by the spatial resolution of the image. Chemical flux information can be preserved for each resolvable image element, voxel.

An image sensitive to chemical exchange can be produced by preceding a spin density imaging sequence with a spin preparation period during which chemical exchange can be selectively encoded, Figure 5.1. To image $\alpha(r)$ quantitatively in a $X_i <--> X_j$ system existing as a simple spectrum with two resonances at ω_i and ω_j, the following procedure is followed. First, a chemical shift selective image (114) of M_i is obtained, Figure 5.1a. During the spin preparation period any one of several methods can be used to suppress M_j to eliminate the chemical shift artifact. A M_j selective 90° pulse is sufficient. M_j must not be saturated for this first image.

Spatial encoding can be accomplished using a spin echo imaging sequence with a short echo time ($T_E << T_2$) and a long recycle time ($RD > 3*T_1$) to minimize relaxation effects and produce primarily a spin density image. Second, slow exchange is encoded into the spin density distribution by application of a presaturation pulse for a time t_{sat} followed by spatial encoding using switched gradients (figure 5.1). Following steady-state saturation ($t_{sat} > \{T_1 + 1/k\}$) of resonance M_j in the $X_i <-> X_j$ system, the effective image spin density at each voxel, $D_{sat}(r)$, is reduced relative to the value obtained in the absence of saturation, $D_o(r)$ by the amount given by:

$$(5.4) \qquad D_o(r)/D_{sat} = 1 + \alpha_{ij}(r)$$

which is identical in form to the one dimensional expression 5.3. $\alpha_{ij}(r)$ represents the product of $k_{ij}*T_1$ within a specific voxel element of the image.

In practice two images are acquired with and without selective saturation and stored as arrays containing the spin distributions $D_o(r)$ and $D_{sat}(r)$. $\alpha(r)$ is calculated directly at every r using equation 5.4 and the values of $D_{sat}(r)$ and $D_o(r)$. A CHEMI image can be displayed as the difference between the saturated and unsaturated images, or by displaying the $\alpha_i(r)$ magnitudes values directly.

Without knowledge of $R_i(r)$, quantitative values of the molecular flux cannot be obtained. The assumption that R is constant throughout the system can be tested using a T_1 sensitive image (short T_E and a short pulse repeat time, RD). In systems where R varies, one of several imaging methods proposed to calculate R directly from the relaxation sensitive image can be used (107). The images displaying $\alpha(r)$ alone, however, will themselves be informative even in the absence of the relaxation data.

The steady-state saturation method of flux determination suffers from the limitations described in chapter 2, namely sensitivity to NOE and compartmentation. By use of the CHEMI the compartmentation related errors will be reduced to dimensions equal to the spatial resolution of the image. As will be shown, this dimension can be made microscopic. The steady-state saturation image will be sensitive to both homonuclear and heteronuclear dipolar coupling when present. This non-chemical route of magnetization transfer can be similarly mapped to produce an NOE image.

IMAGE SIGNAL-TO-NOISE: Quantification of $\alpha(r)$ from a CHEMI image is limited by SNR and a correct description of the exchanging system. In a CHEMI image the SNR in the difference image is a function of k^*T_1 and is reduced from the value in the unsaturated image to give a fractional error in $\alpha=k^*T_1$ of:

$$(5.5) \qquad \sigma_\alpha/\alpha = SNR_o^{-1}[\alpha+2(\alpha^3+\alpha^2+\alpha+\alpha^{-1}+1)]$$

where SNR_o is the image SNR per pixel. Note that the reduction in signal intensity due to exchange described by equation 5.4 will have the minimum fractional error for α approximately equal to 0.5. Both very large and very small α's will not be efficiently measured by steady-state CHEMI.

The (SNR) is a limitation of NMR in any imaging regime, microscopic or otherwise. At frequencies greater than approximately 100Mhz, studies of biological tissue and other conductive objects of approximately 1 cm^3 will be limited by the sample noise as described by Hoult et al (60). There is no need for sophisticated r.f. hardware designs (e.g. cooled r.f. coils and preamplifiers). What is required is a low noise preamplifier (noise figure $<$ 0.7 dB) and a coil producing a uniform H_1 field for transmit with a high filling factor, (coil radius)/(sample radius) $>$ 0.8 for

the receiving coil. When imaging conductive samples of radius r_o in a coil of radius r_c, the image SNR at a pixel ΔX by ΔY from a slice thickness of ΔZ will be proportional to:

$$(5.6) \qquad SNR_o \sim [H_o{}^p(\Delta X \Delta Y \Delta Z)\rho]*[r_c(\emptyset + \beta(H_o\gamma)^{3/2}(r_o{}^5/r_c{}^{1/2}))^{1/2}]^{-1}$$

The quantities $\emptyset$ and β are factors given by Hoult and Lauterbur with magnitudes on the order of 10**-2 and 10 respectively, and ρ is the spin density per unit volume, (60). Considerable debate surrounds the value of p. The value, however, certainly depends on frequency and probably lies between 0.5 and 1.5 at frequencies of 100-400Mhz. As the sample size is reduced, coil losses will predominate and coil unloaded Q will be an important design parameter. For small sample volumes super-cooled r.f. coils and preamplifiers will provide improvements in SNR.

For multinuclear microscopic imaging of small samples it is useful to include gradient strength, G, and the gyromagnetic ratio, γ, in the SNR expression. From equation 2.1b the SNR can be rewritten as

$$(5.7) \qquad SNR_o \sim [\omega^p(\Delta X \Delta Y \Delta Z)\rho(B/i)\gamma] *[\Delta\omega(R_c+R')]^{-1/2}$$

The bandwidth, $\Delta\omega$, will be dependent on the strength of the frequency encoding gradient, G, and the size of the object in the frequency encoding direction, d_f. If the number of points in the frequency encoding dimension is n_f and ΔX is the pixel size, $d_f = n_f * \Delta X$ and $\Delta\omega = n_f * \Delta X * \gamma * G$. Ideally the minimum gradient is chosen based upon the criteria that the gradient is larger than any main field inhomogeneities, ΔH_o.

$$(5.8) \qquad G_f > [T_2{}^* \gamma \Delta X]^{-1} \approx (\pi\gamma\Delta X)^{-1}[1/T_2 + \Delta H_o\gamma/2]$$

The gradient strength and object dimension, d_f, will then set the minimum bandwidth ($\Delta\omega = n_f{*}\Delta X{*}\gamma{*}G$) as

(5.9) $\Delta\omega \geq n_f(1/T_2 + \Delta H_o\gamma/2)/\pi$

Thus, the optimal bandwidth is taken as the linewidth in the absence of gradients times the number of frequency encoding points.

It is important to note that the finite length of the sampling window sets a practical limit on the minimum gradient strength in homogeneous magnets. For efficient data collection the repetition rate for signal averaging, RD, will be approximately T_1. The data sampling time, t_s, must be less than RD, $t_s = n_f/\Delta\omega = (1/d_f){*}(1/G\gamma)$

(5.10) $\Delta\omega > n_f/(\pi T_1)$

Truncation of signal in the acquisition window effectively convolves the image point function with a sinc function of half-width $1/t_s$ and will limit the resolution to 100hz for a 10 msec value of t_s. The sampling time restriction will be most applicable to nuclei with extremely short T_1's (notably ^{23}Na) and in multi-slice imaging where $\Delta\omega_{multislice} = n_{slices}{*}\Delta\omega_{min,1\ slice}$

More frequently ΔH_o and $1/T_2$ will determine the minimum bandwidth for a single slice, $\Delta\omega_{min}$. A gradient chosen from Equation 5.9 will be optimal for SNR; however, the rectilinear image array will not necessarily have a scaler relationship with the actual object; the image will be geometrically distorted. The problem of transforming the distorted image from a curvilinear coordinate system to an

undistorted rectilinear grid has been solved by Lai (79) who showed that a generalized transformation matrix can be constructed from a precise map of the main field inhomogeneities. This scheme should be used to allow the use of the minimum gradients.

With the optimal bandwidth and the recognition that for a fixed object size, d_f, the pixel dimension will be $\Delta x = d_f/n_f$, with $\omega = \gamma H_o$ the SNR becomes:

$$(5.11) \quad SNR \sim [H_o^{p}(\Delta X^{3/2}\Delta Y \Delta Z)\rho(B/i)\gamma^{p+1}] * [(1/T_2 + \Delta H_o \gamma/2)(R_c + R')d_f/\pi]^{-1/2}$$

It is important to realize that the SNR will be higher, at the same spatial resolution, in a small sample compared to a large one.

In comparing the SNR for the same sample at different spatial resolutions in different field strengths, assume that ΔH_o dominates the linewidth. Expressing ΔH_o as $f * H_o$ the SNR, Equation 5.11, can be reduced to

$$(5.12) \quad SNR \sim [H_o^{3/2}(\Delta X^{3/2}\Delta Y \Delta Z)\rho\gamma^{5/2}] * [f(R_c + R')]^{-1/2}$$

or

$$(5.13) \quad [SNR_1/SNR_2] = [H_{o_1}/H_{o_2}]^{3/2} \times [\Delta X_1/\Delta X_2]^{3/2} \times [\Delta Y_1 \Delta Z_1/\Delta Y_2 \Delta Z_2] \times [\rho_1/\rho_2] \times [\gamma_1/\gamma_2]^{5/2}] \times [f_2/f_1]^{1/2} \times [(R_c + R')_2/(R_c + R')_1]^{1/2}$$

Equations 5.12 and 5.13 are only valid when the optimal gradient (bandwidth) is used as prescribed by Equation 5.8. Several expressions have been published that neglect the bandwidth advantage that can be achieved by optimizing the gradient for different nuclei. The factor f will be dependent upon

the magnet design. The coil and sample resistances, R_c and R_s, will both increase nearly linearly with field strength. Together with the linearity of ΔH_o with H_o, the effective probe resistance will limit the increase in SNR with field to approximately the first power unless coil and preamplifier cooling is implemented.

5.3 Materials and Methods

An 8.5 Tesla high-resolution spectrometer was adapted for microscopic imaging by adding current switches and a probe equipped with magnetic field gradients (Figure 5.2). The gradients were designed to produce maximum slice-selection fields greater than 80 Gauss/cm and generated fields of approximately 0.8, 1.0, and 0.6 G/cm-amp for the X, Y, and Z orientations respectively. Standard Helmholtz and Golay geometries were wound with #16 copper wire around a 4.5-cm diameter cylinder (59). The gradients could be switched at a rate of 0.4 Gauss/(cm-msec) at 5 V. The imaging volume was approximately ellipsoidal, with a major axis of 25 mm and a minor axis of 20 mm. A copper gradient eddy current shield was tested in early versions of the probe, with the aim of reducing gradient interactions with the Oxford room temperature shim coils, and found to be unnecessary.

The spectrometer system instrument consists of an 8.5 T Oxford magnet (bore 89 mm) and a broadband, multinuclear spectrometer designed and assembled by the staff at the Francis Bitter National Magnet Laboratory, Massachusetts Institute of Technology (Figure 5.3). The software system (RNMR) was designed and written by Dr. David Rubin in FORTRAN and is installed on a VAX 750.

The pulse sequence shown in Figure 5.1 was designed to employ phase encoding before and after the 180° pulse to achieve full +/-180° of phase.

Gradient current was switched by high current power transistors in a Darlington configuration (Figure 5.4), driven by TTL pulses generated in the pulse programmer. Gradients used for frequency and phase encoding were unipolar pulses of variable duration and constant magnitude and sign. Waveform generators were not available, so bipolar or shaped gradient waveforms and gradient refocused echoes were not possible. Precision resistors in line with the gradient coils provided a measure of gradient strength. Calibration curves for the x,y, and z gradients are shown in Figure 5.5.

The r.f. sub-assembly consisted of a solenoidal r.f. coil surrounding a glass sample tube (5 mm for ^{31}P, 2 or 10 mm for ^{1}H). The coil is connected in a standard balanced configuration, Figure 4.4, and tuned to 360 MHz for ^{1}H or 146 MHz for ^{31}P imaging. The r.f. sub-assembly is sealed in an aluminum shield (0.4 mm thick) prior to installation within the gradient coils. For biological samples in the 5 and 10 mm solenoids, the ratio of Q loaded to unloaded was approximately 0.5, indicating that the noise is dominated by the sample itself. In the smaller coils, sample loading was less than 15%. In the absence of gradients, the 2 mm proton sample could be shimmed to a linewidth of 10 Hz (0.03 ppm).

5.4 Results

High Resolution Proton Imaging: Standard spin echo images were obtained to demonstrate that the system used here was capable of achieving microscopic resolution. An image of a phantom consisting of five tubes is shown in Figure 5.6. The phantom was made from a water-filled 4.6 mm I.D. tube with four water-filled pipettes, 1.4 mm I.D.; the fifth tube was air-filled. Slice thickness was approximately 500 um. A smaller phantom was imaged to demonstrate thin slice selection, Figure 5.7. The contour plot shows two water-filled capillary tubes inside

a glass cylinder of 2.5 mm I.D. 16 averages were used, with 128 phase-encoding steps, in a spin echo sequence with RD = 500 msec, T_E = 30 msec. 256 points were acquired in the time domain to give an approximate spatial resolution of 50um x 50um x 40um.

Figure 5.8 shows a higher resolution image of several *Rana pipiens* egg cells. The cells, in normal amphibian saline, were placed inside a 2.5 mm I.D. tube. The slice thickness was approximately 50 uM. Note that in the contour plots (Figures 5.8a,b), as used for two dimensional spectroscopy, the lines are drawn for logarithmic changes in intensity set within an arbitrary limiting range. Significant improvement in apparent image quality is gained by displaying the image with a gray scale, Figure 5.8c. The contour maps may be difficult to interpret and accentuate fluctuations in peak signal because of the relatively large number of contours drawn at high signal levels. In Figure 5.9 the contour plot of a single *Rana pipiens* egg cell in D_2O is displayed. Image resolution is approximately 25um x 25 um x 40 um. 64 signal averages were acquired.

To predict the image quality expected in dilute samples, signal-to-noise ratio (SNR) analysis was performed on images obtained from a 4.6 mm I.D. phantom containing 110 M [^{1}H] (pure water), 2.4 M [^{1}H] and 0.4 M ^{1}H], prepared by adding appropriate amounts of 99.8% D_2O. All images were obtained with identical image parameters (1 average, RD = 6 sec, T_E = 14 msec). The spatial resolution was 36 um x 50 um x 7.9 mm. The thick slice was used to reduce complications from non-ideal slice selection, performed at present with square r.f. waveforms. The SNR values used were chosen to reflect the ratio of the average pixel intensity within the phantom to the RMS deviation of the pixel intensities in image regions outside the phantom. A minimum of 20 values in the image array were used in the SNR calculation. The experiment was repeated four times for each image. The SNR

values for the images were 476 +/- 50 (S.D.), 100 +/- 25 (S.D.), and 54 +/- 25 (S.D.) respectively, at [^{1}H] concentrations of 110 M, 2.4 M and 0.4 M, Table 5.1. Normalization of these values to concentrations of [^{1}H] with the approximation that SNR is linear in concentration indicates that SNR is approximately equal to 22 times the molar concentration of [^{1}H]. These estimates were used to generate Table 5.2 for several concentrations of [^{1}H] and [^{31}P] predictions of the approximate imaging times for high resolution ^{1}H and ^{31}P images.

Imaging of Intermolecular Exchange: [^{1}H] CHEMI was first used to study a well-defined chemical exchange in a capillary tube phantom. Three tubes containing acetylacetone were used, 1.4 mm I.D. The proton spectra of the phantom in the absence of gradients is shown in Figure 5.10a. This compound (see Chapter 3) has three proton resonances linked by chemical exchange, (A, B, and C), and a non-exchanging resonance (D). Acetylacetone undergoes a base-catalyzed proton exchange between an olefinic [^{1}H] in the enol configuration, B, to a hydroxylic proton, A. The exchange requires formation of the keto form of acetylacetone, C (39). The transfer of magnetization proceeds as (B-->C-->A). The uncatalyzed reaction rate is negligible. Triethylamine was added as a catalyst to two of the tubes.

The objective was to make a chemical shift-selective image of resonance B CHEMI. First, the large non-exchanging peak, D, was suppressed with a low power homonuclear decoupling pulse at the frequency of the non-exchanging resonance (Figure 5.10b). Using a spin echo (TE = 10 msec), the resonance from A was eliminated by taking advantage of its short T_2 (Figure 5.10c). Finally, to eliminate any residual signal from C, a binomial-selective 90° pulse (45_x-t-45_{-x}) was used with the synthesizer frequency set on ω_c (Figure 5.10d).

The pulse sequence of Figure 5.1 was applied (SE 6000/50/1) and images

obtained with and without saturation at ω_C (Figures 5.11b and a respectively). The difference image (unsaturated image array - saturated array) can easily be obtained and $k^*T_1(r)$ determined at each pixel using Equation 5.4. Note that in this particular three-site chemical exchange system, the CHEMI-derived value of k^*T_1 reflects only the flux from B --> C because of the absence of significant B--> A transfer. In general, three-site systems will not be correctly described by the two-site relations given above. Quantitative results can be obtained, however, by using a multi-site saturation prior to spatial encoding, analogous to the one-dimensional steady-state experiment (39).

Imaging of Intramolecular Exchange: A two-site ^{31}P exchange was studied by CHEMI in solutions containing dilute concentrations of the biologically important ^{31}P metabolites phosphocreatine (PCr) and adenosine triphosphate (ATP), (80 mM PCr, 20 mM ATP). Figure 5.12 is a chemical shift-selective image for PCr in a concentric tube phantom. In the central tube, slow ^{31}P exchange between PCr and the γ-ATP was catalyzed by adding the enzyme creatine kinase (CK). CHEMI images were obtained with or without saturation of γ-ATP. In Figure 5.12, profiles through the images with and without saturation clearly show the region of enzyme-catalyzed exchange as a reduction in signal. The value of k^*T_1 for [^{31}P] flux from PCr to ATP was calculated to be 0.9 from the difference image by the use of Equation 4. Prior to imaging, the enzyme-containing solution alone was found to have a $k^*T_1 = 1.6$ by one-dimensional saturation transfer using Equation 5.3. We attribute the difference in values to random experimental error and some loss of activity during the long experimental time. For $T_1 = 3.2$ sec, the fluxes were calculated as 22 and 40 mM/sec, respectively. This CHEMI image required approximately 4 hours to obtain and had an image SNR of approximately 25. Note that the substrate and enzyme concentrations are within a factor of 2-3 of

those found in many living systems.

5.5 Discussion

The determination of molecular flux by NMR measurements of saturation transfer rely on accurate determination of relaxation rates, and assume (for enzyme-catalyzed reactions) uniform concentrations of reactant and catalyst over the sample being analyzed. In most tissues, organ function relies on local cell type differences, and many of these differences will include effective enzyme activity variations. That the T_1 values in many objects are not homogeneous is evident from the spectacular contrast demonstrated in MRI, which relies primarily on spatial differences in relaxation times for its discriminatory power. This limitation is especially serious for heterogeneous biological tissues, but the same kind of limitation holds for chemical reactions in any spatially heterogeneous sample.

The spatial heterogeneity over a typical volume of human or animal tissue presents special difficulties for interpreting metabolite content and NMR-measured values of magnetization transfer in terms of the kinetics of chemical reactions. Actual cellular metabolic performance will not necessarily be reflected in a measurement made on bulk tissue. Moreover, since the relationships between metabolite concentration and enzyme activity are generally non-linear, conclusions based on analyses of heterogeneous samples may well be misleading if homogeneity of composition is assumed when it in fact does not exist. To begin to evaluate this kind of problem, magnetization transfer techniques were combined with microscopic chemical shift imaging to provide another dimension to NMR imaging that reflects chemical exchange. The principles and methods used above apply to any size volume elements; however, only those on the submillimeter or even micrometer scale will have biological relevance. The SNR is the ultimate limitation

of NMR in any imaging regime, microscopic or otherwise. At frequencies greater than approximately 100 MHz, thermal noise in biological tissue and other conductive objects of approximately 1 cm^3 will be the dominant limitation, as described by Hoult and Lauterbur (60). For smaller samples, coil losses will become important and coil unloaded Q will be an important design parameter.

Every effort must be made to maximize SNR in microscopic scale imaging. The signal amplitude from different nuclei, at constant field strength, increases as the cube of their gyromagnetic ratios; ^{31}P (γ=1.72 kHz/G) will have only 7% of the signal of [^1H] (γ=4.26 kHz/G) at the same concentration. Noise, however, also depends on the square root of the bandwidth, $\omega^{1/2}$. For large instruments, ω is often limited by the main field homogeneity. Ideally, the gradient strength will be set approximately 10% greater than the maximum gradient of the static main field inhomogeneities within the region of interest. This requirement will ensure that every point in space will be uniquely spatially encoded. The bandwidth in turn is proportional to the gyromagnetic ratio; thus, the overall image SNR will vary in proportion to the gyromagnetic to the 5/2 power. At a fixed main field strength and homogeneity, the SNR of ^{31}P image will be 10% of the [^1H] image.

The limits of resolution under the optimal exchange conditions will approximate those of the microscopic nuclear density image. Table 1 gives estimated imaging times required to attain a SNR of 10 in images with different spatial resolutions. These times were estimated based on the SNR obtained with our present system, as described above. The ^{31}P exchange through CK and the [^1H] exchange of pyruvate and lactate through lactate dehydrogenase are the most practical reactions for study with CHEMI. The imagable substrates are in concentrations of less than 0.10 M, and the flux and relaxation parameters, k^*T_1, are in the range of unity. For both reactions, a limit of 100 um in plane and 1 mm

slices is an optimistic limit with the present technology. Note that the reduction in signal intensity, due to exchange described by Equation 5.4 will have minimum functional error, σ_α/α, for k^*T_1 near 0.5. Neither very large nor very small k^*T_1 values will be efficiently measured by steady-state CHEMI. Clearly, CHEMI will be most applicable for characterization of kinetic heterogeneity on scales greater than the dimension of most single cells; however, intercellular and regional heterogeneity are accessible spatial domains. These methods may also have wider application in non-living systems.

5.6 Summary

An NMR microscope was developed that demonstrated spatial resolution of less than 25 uM in phantoms and biological samples. A novel technique for encoding chemical flux information was devised and implemented with the microscope. Images mapping chemical exchange processes were produced, demonstrating that a new dimension can be added to NMR images in systems with a significant chemical flux.

5.7 Figure Legends

FIGURE 5.1: Pulse sequences used for chemical exchange-encoded imaging were divided into three segments: spin preparation, spatial encoding and acquisition. During the preparation period, complex spectra were simplified by selective saturation of unwanted resonances, leaving only resonances from the exchanging X <--> Y system; two data sets were obtained. The first contained information from X in the absence of exchange obtained by suppressing signal from Y. The second data set, containing information from X in the presence of exchange width Y, was acquired following steady-state saturation of Y. Chemical exchange between X and Y reduced the magnetization of X with respect to that in the first data set. Spatial encoding in frequency was accomplished by gradient application during the acquisition of the spin echo. Frequency gradient phase compensation was applied prior to the 180° pulse such that there was no net change phase at the center of the spin echo. Symmetrical (+/-180°) phase encoding was accomplished by the combination of a gradient of fixed duration applied prior to the 180° pulse and a gradient of variable duration applied after the 180° pulse. Selection of plane slices was achieved with a third orthogonal gradient during the 90° and 180° pulses. Acquisition of a spin echo completed the sequence. A CHEMI image was displayed as the difference between the two data sets. Alternatively, display of the second data set alone only gave an image of the non-exchanging species, X.

FIGURE 5.2: Diagram of the r.f. probe used.

FIGURE 5.3: Diagram of high-resolution spectrometer adapted for microscopic imaging.

FIGURE 5.4: Schematic of one of the three identical gradient switches. TTL outputs from the pulse programmer are attenuated and directly drive the base of the Darlington.

FIGURE 5.5: top) X, Y, and Z gradient calibration curves relating the voltage measured across the sensing resistor, Figure 5.4, to the gradient field strength. Field value in G/cm is obtained by dividing the value on the ordinate by γ for ^1H, (4.26 kHz/G). Below: Selection of thin slices. Using a calibration pulse sequence that turns the slice selection gradient on during signal acquisition, a profile of a 1400 uM capillary tube is displayed in the absence of slice selection. With the slice selection on a spike representing the plane slice is displayed.

FIGURE 5.6. Proton image on a microscopic scale. Contour plot of one air-filled and four water-filled capillary tubes inside a glass cylinder of 4.6 mm I.D. Four averages were used, with 128 phase-encoding steps, in a spin echo sequence with T_R = 500 msec, T_E = 30 msec [500/30]. 256 points were acquired in the time domain to give an approximate spatial resolution of 100um x 100 um x 5000 um.

FIGURE 5.7: Thin Slice Phantom. Contour plot of two water-filled capillary tubes inside a glass cylinder of 2.5 mm I.D. 16 averages were used, with 128 phase-encoding steps, in a spin echo sequence with T_R = 500 msec, T_E = 30 msec [500/30]. 256 points were acquired in the time domain to give an approximate spatial resolution of 50um x 50um x 40um.

FIGURE 5.8: Proton image of two *Rana pipiens* egg cells in amphibian saline contained within a 2.5 mm I.D. capillary tube. a) and b) are contour maps of the same data with two different contour ranges. c) Ectachrome 400 photograph of image displayed on 16 bit grayscale monitor. 32 averages were used with T_R = 3

seconds and T_E = 80 msec; slice thickness was approximately 200 um. The edge of a third cell is also visible in the center of the field. In plane resolution is approximately 50um x 50um.

FIGURE 5.9: Contour plot of a single *Rana pipiens* egg cell in D_2O. Image resolution is approximately 25um x 25 um x 40 um. 64 signal averages were acquired.

FIGURE 5.10: Preparation of a complex spectrum for CHEMI imaging. (a) High resolution spectra of acetylacetone following a non-selective 90° pulse. Base catalyzed exchange occurs between resonances B<-->C<-->A (b) Spectra after presaturation of non-exchanging resonance, D, using the low power spectrometer channel, Figure 5.3. (c) 10 msec spin echo suppresses resonance A. (d) Binomial 1-3-3-1 selective for resonance B, with the primary r.f. transmitter set at the frequency of resonance C to provide selective supression/saturation of C while signal is acquired exclusively from resonance B.

FIGURE 5.11: CHEMI chemical shift-selective image of acetylacetone in 2.5 mm capillary tubes. Triethylamine was added as a catalyst to the two rightmost tubes. (A) Image without saturation of resonance 3 (defined in FIGURE 5 6). (B) Image obtained following saturation of resonance 3. The catalyzed chemical flux can be resolved and spatially quantified from the difference of these two images. Identical contour intensities are used in plots (A) and (B).

FIGURE 5.12: ^{31}P CHEMI image of exchange between PCr and ATP catalyzed by CK. (A) Chemical shift-selective ^{31}P image of PCr in a phantom containing 80 mM PCr, 20 mM ATP, and 5 mM Pi. Center tube contains CK (1400 U/ml). (B) Profile through the image in (A), and through the image obtained following saturation of the γ-ATP resonance. Reduction in the signal is

due to enzyme-catalyzed spin transfer. Addition of the enzyme allowed equilibrium between the reactants and products of the CK reaction to be established in the center tube, resulting in a lower concentration of PCr.

Table 5.1

[1-H]	Image SNR freq	Time actual	Time optimal
110 M	476 +/-50	10 min	5.6 min
2.4 M	100 +/-25	10 min	5.6 min
0.4 M	54 +/-25	10 min	5.6 min

Normalizing all SNR's to 110M gives an average SNR = 22*[x]
[x] in M

Noise calculated from RMS deviation of pixel data over image regions without sample

Gain changes and other machine adjustments were made for each image to optimize SNR.

Water sample was diluted sequentially with D2O (99.8%). D2O impurity assumed to be H2O contributing .2M.

In plane resolution (freqxphase) 36uM x 50 uM
Sample Volume (ID=4.5mm, 7.9mM slice) 125 mm3
Equivalent Cubic Voxel size (242um)x(242um)x(242um)

Optimal time calculated based on TR=T1

Table 5.2

Comparison of imaging times to achieve SNR=10 based on 1986 experimental data obtained at 8.5 Tesla (SNR = 22*[x]).

[X]	100u x 100u x 1000u	50u x 50u x 500u	25u x 25u x 250u
H 110 M	< 1 min	< 1 min	1.4 mins
H 1 M	4 mins	267 mins	12 days
H 0.1 M	7 hours	18 days	
P 0.1 M	42 hours	109 days	
H 0.05 M	1.2 days	74 days	
P 0.05 M	7.3 days	1.2 Years	

assumes SNR**2 ~ (time)*([x]**2)*(vol**2)*(gamma)**1.5

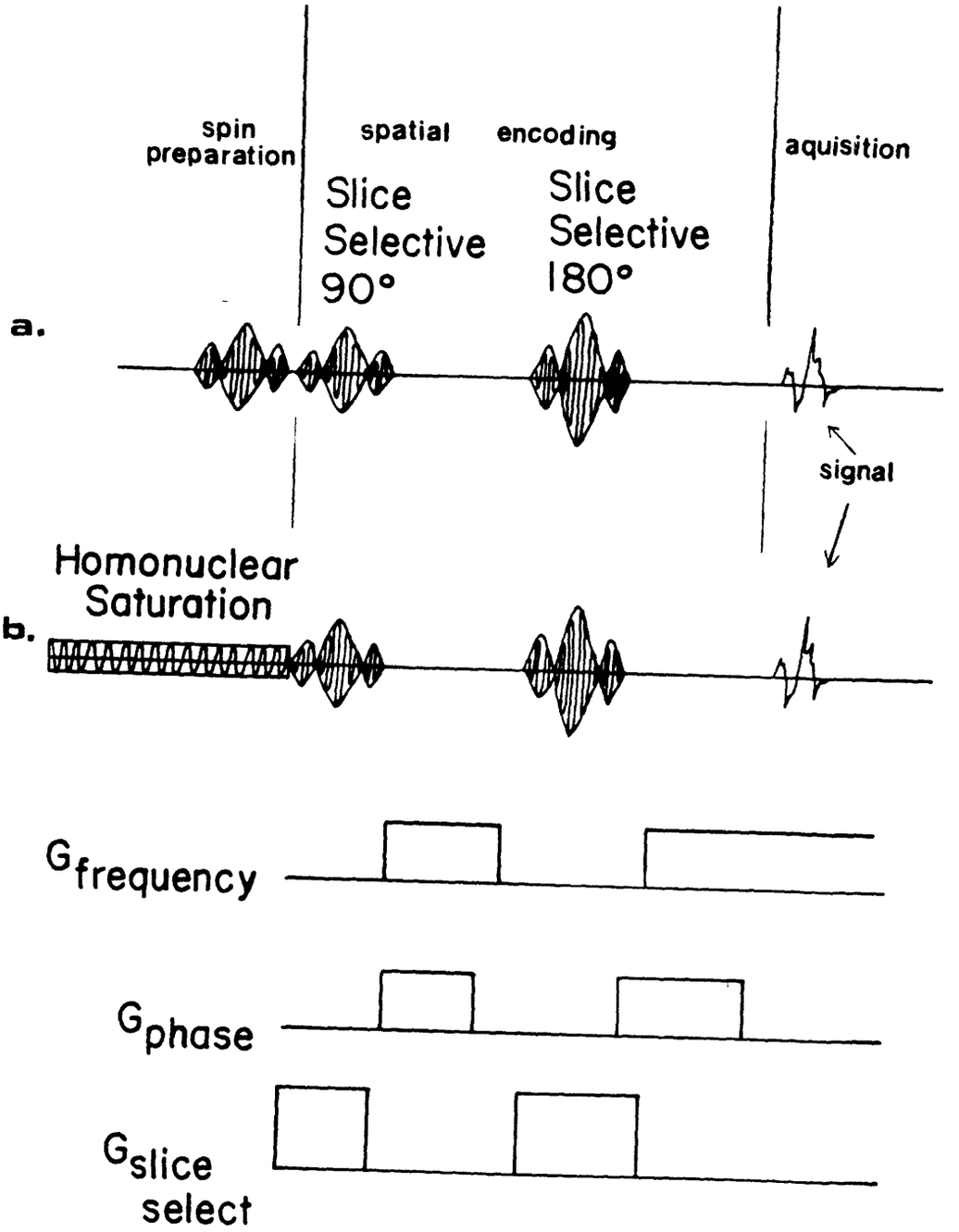
spin
preparation
spatial
encoding
aquisition
Slice
Selective
90°
Slice
Selective
180°
a.
signal
Homonuclear
Saturation
b.
$G_{frequency}$
G_{phase}
G_{slice}
select

Figure 5.1

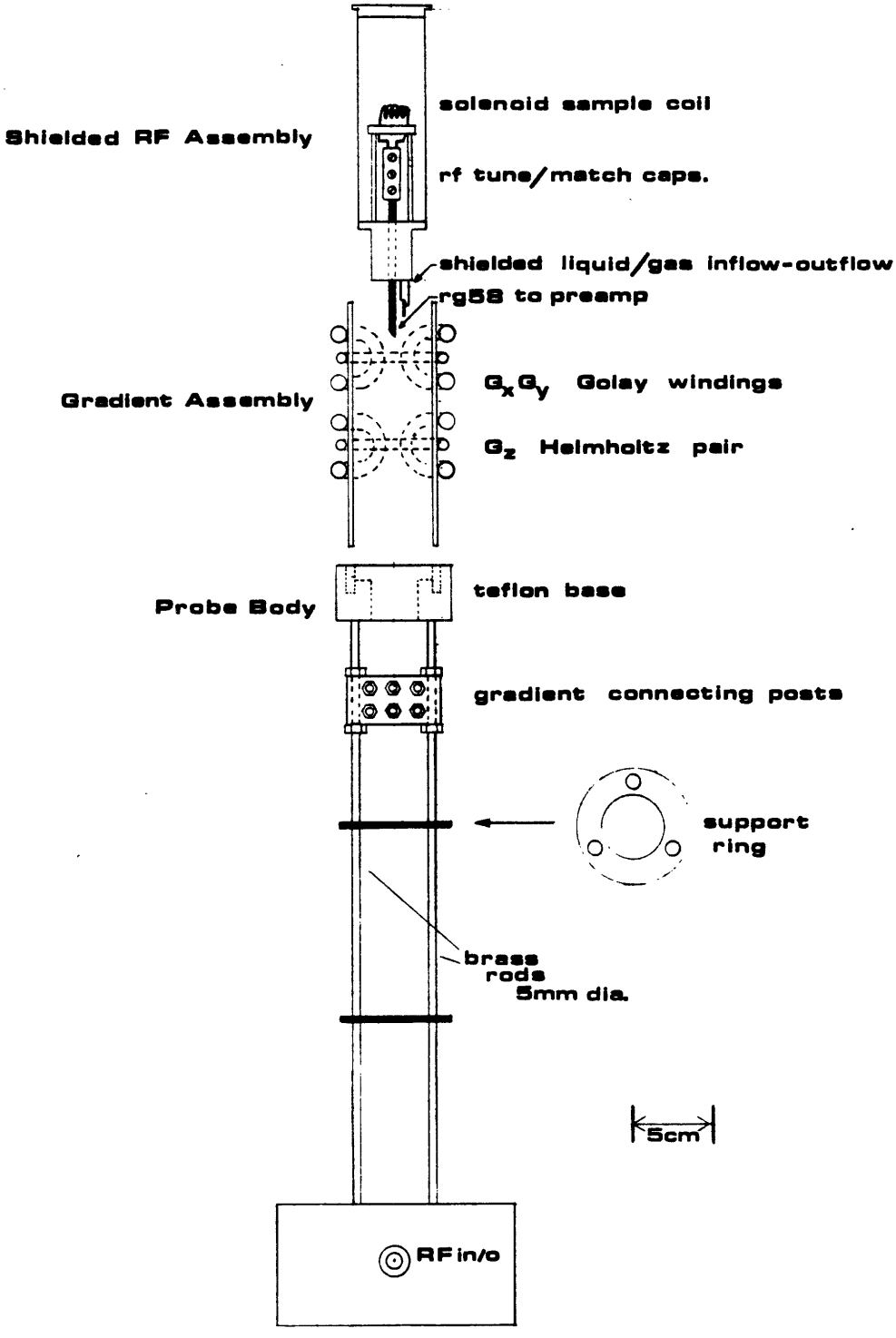
Shielded RF Assembly
solenoid sample coil
rf tune/match caps.
shielded liquid/gas inflow-outflow
rg58 to preamp
Gradient Assembly
$G_x G_y$ Golay windings
G_z Helmholtz pair
Probe Body
teflon base
gradient connecting posts
support ring
brass rods 5mm dia.
5cm
RF in/o

Figure 5.2

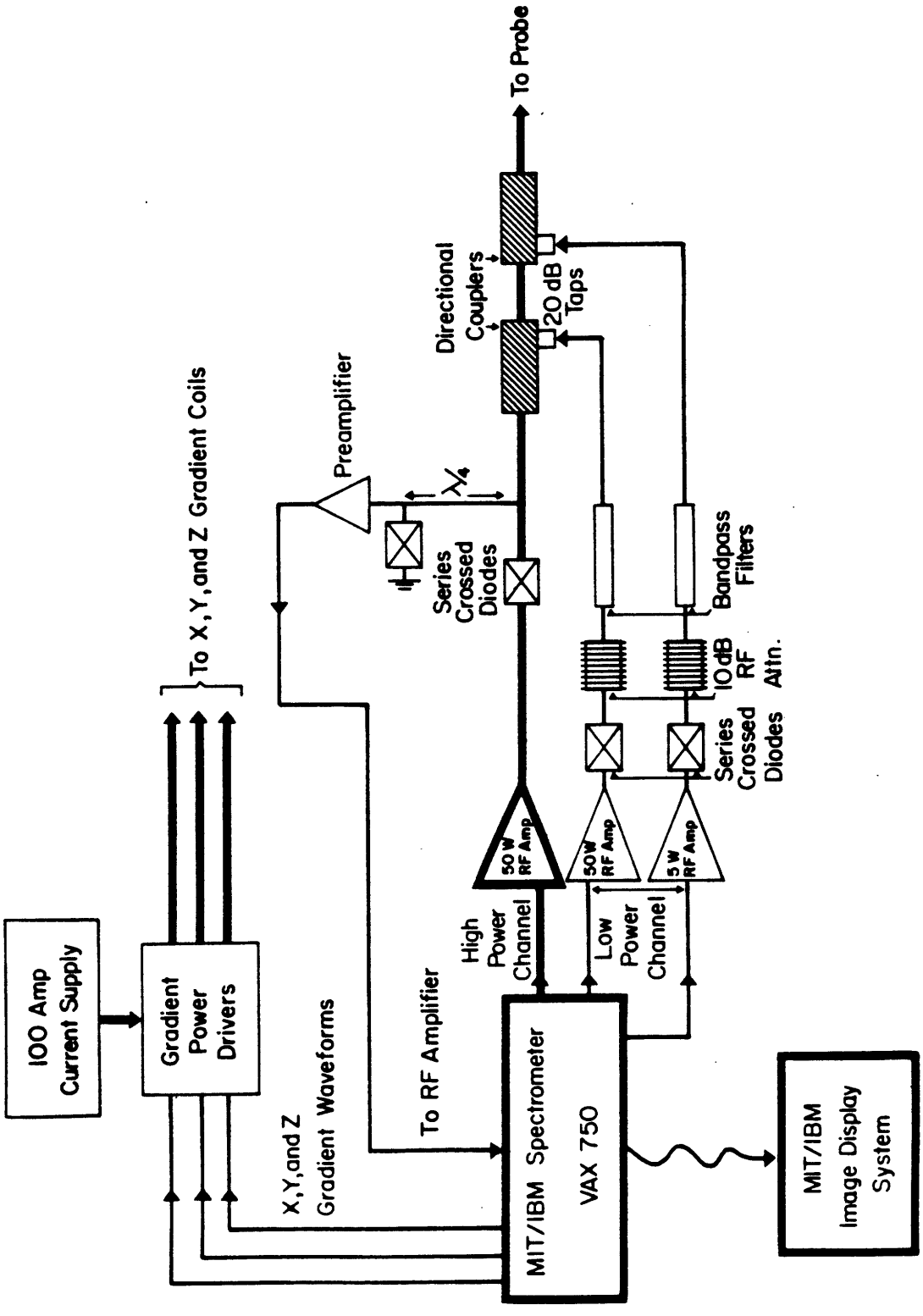
100 Amp Current Supply
Gradient Power Drivers
To X, Y, and Z Gradient Coils
X, Y, and Z Gradient Waveforms
To RF Amplifier
MIT/IBM Spectrometer
VAX 750
MIT/IBM Image Display System
Preamplifier
λ/4
Series Crossed Diodes
Directional Couplers
20 dB Taps
To Probe
Bandpass Filters
10dB RF Attn.
Series Crossed Diodes
50 W RF Amp
50W RF Amp
5 W RF Amp
High Power Channel
Low Power Channel

Figure 5.3

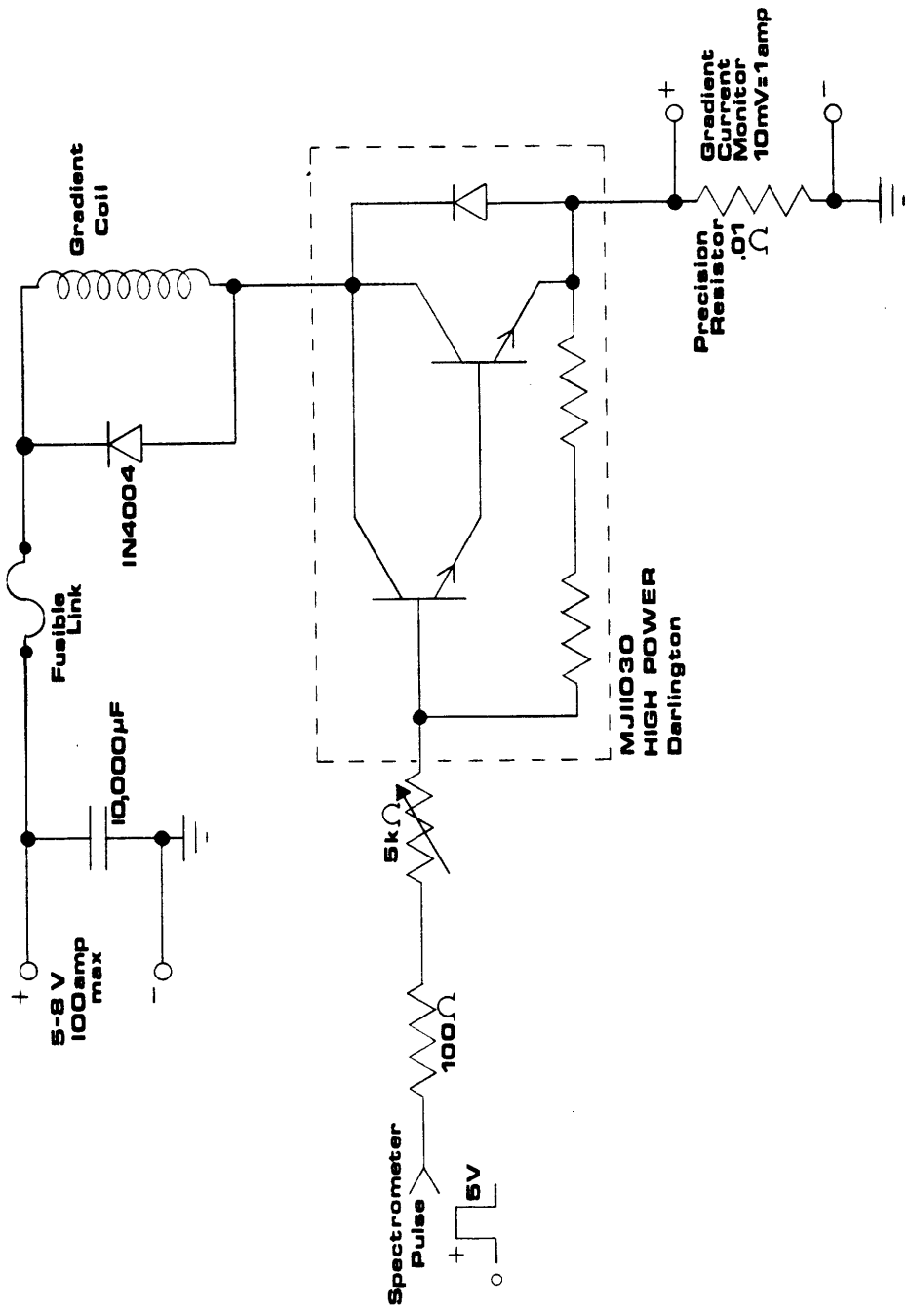
Gradient Coil
IN4004
Fusible Link
10,000μF
5-8 V 100amp max
5kΩ
100Ω
Spectrometer Pulse
5V
MJ11030 HIGH POWER Darlington
Precision Resistor .01Ω
Gradient Current Monitor 10mV=1 amp

Figure 5.4

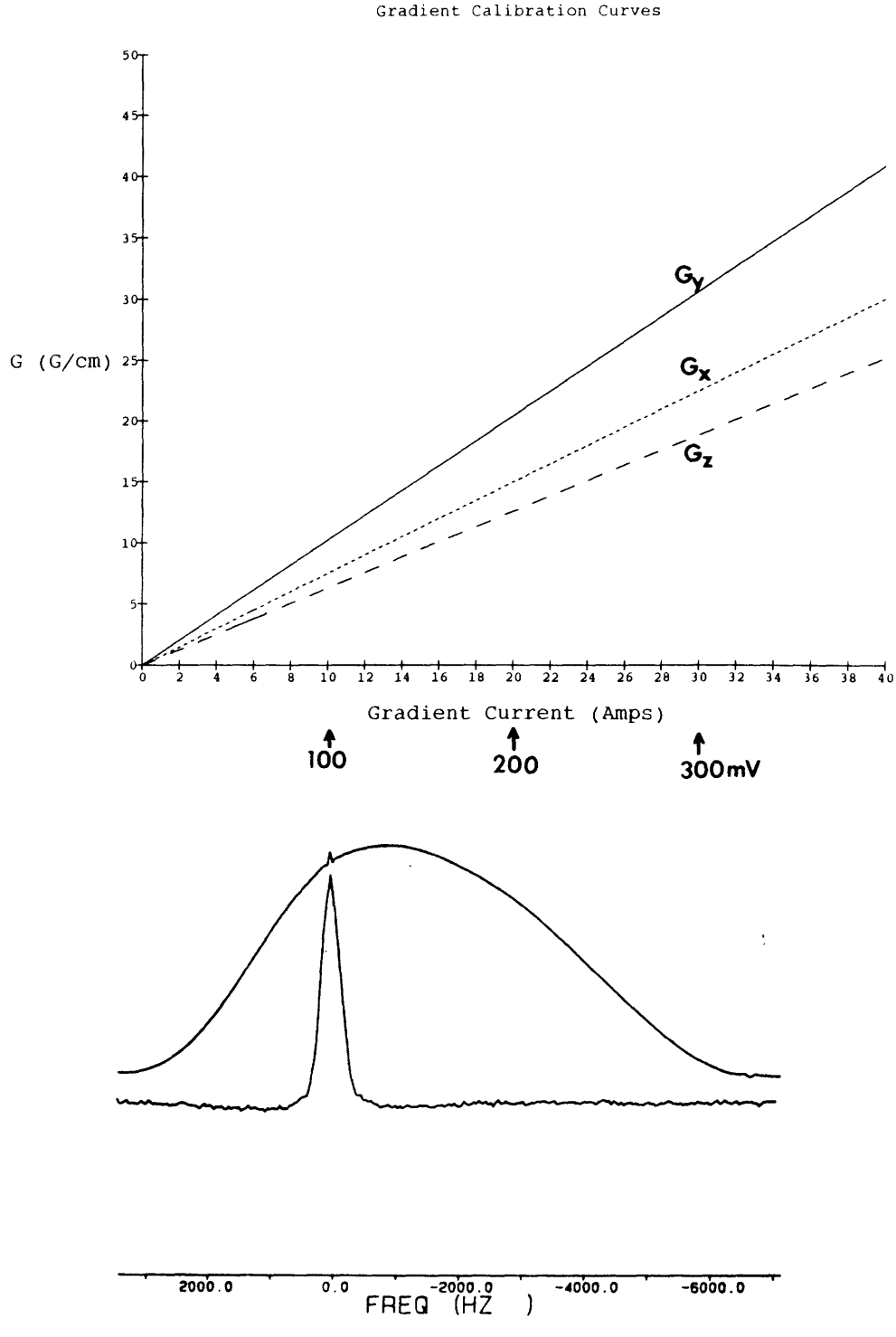
Gradient Calibration Curves
G (G/cm)
50
45
40
35
30
25
20
15
10
5
0
0 2 4 6 8 10 12 14 16 18 20 22 24 26 28 30 32 34 36 38 40
G_y
G_x
G_z
Gradient Current (Amps)
100
200
300mV
2000.0
0.0
-2000.0
-4000.0
-6000.0
FREQ (HZ)

Figure 5.5

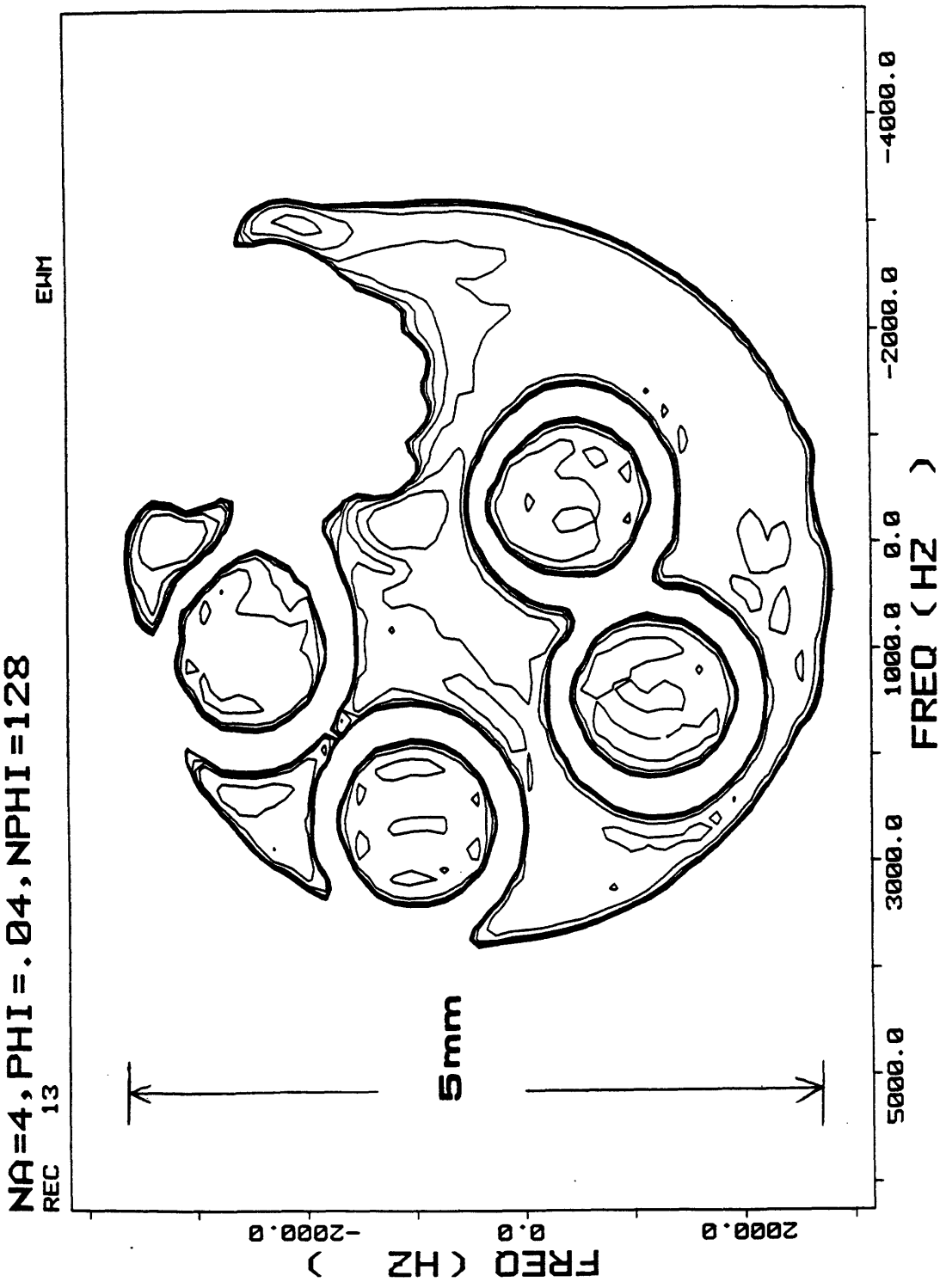
NA=4, PHI=.04, NPHI=128
REC 13
EWM
5mm
FREQ (HZ)
2000.0
0.0
-2000.0
5000.0
3000.0
1000.0
0.0
-2000.0
-4000.0

Figure 5.6

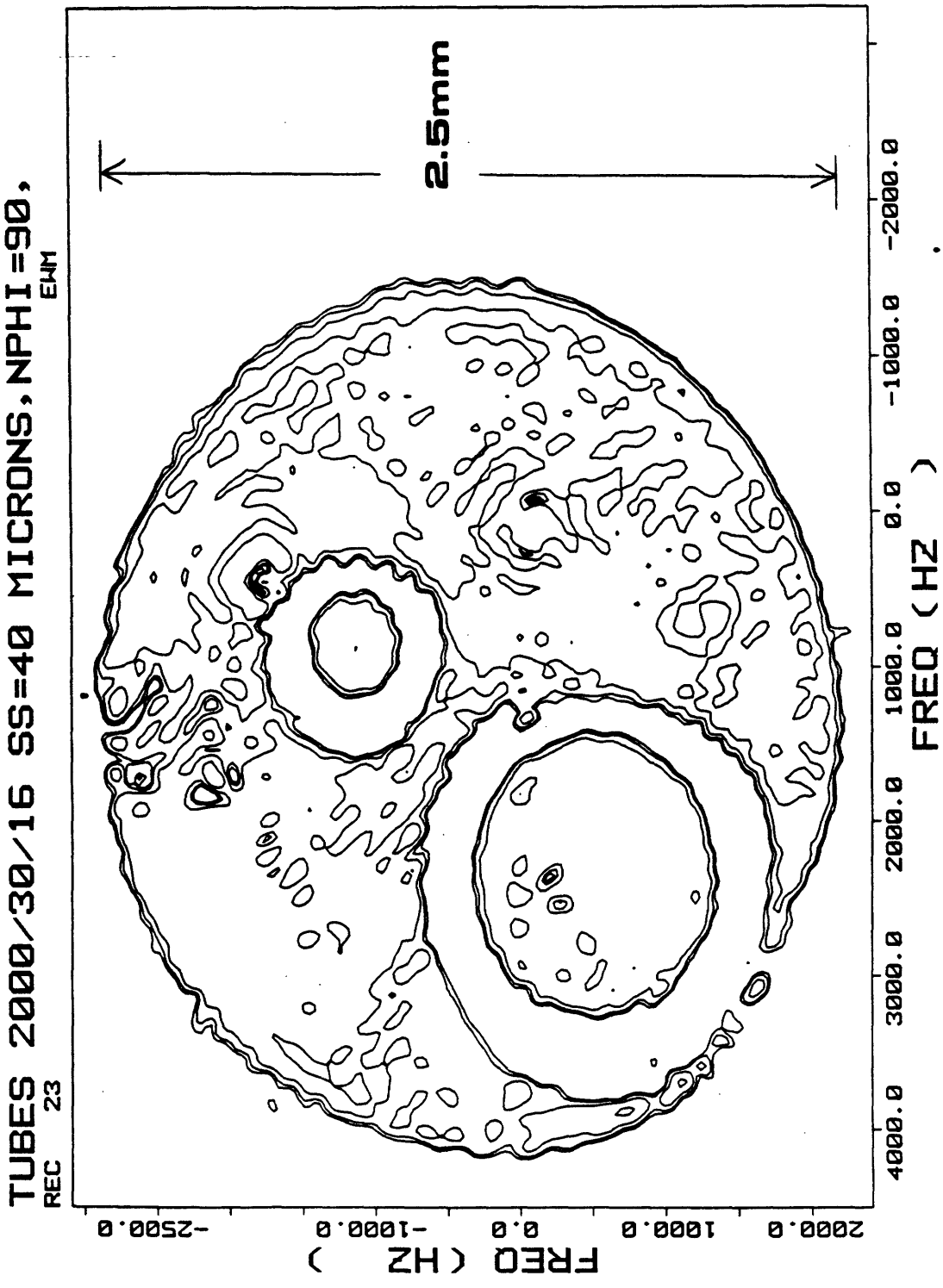
TUBES 2000/30/16 SS=40 MICRONS, NPHI=90,
REC 23
EWM
2.5mm
FREQ (HZ)
-2500.0
-1000.0
0.0
1000.0
2000.0
4000.0
3000.0
2000.0
1000.0
0.0
-1000.0
-2000.0
FREQ (HZ)

Figure 5.7

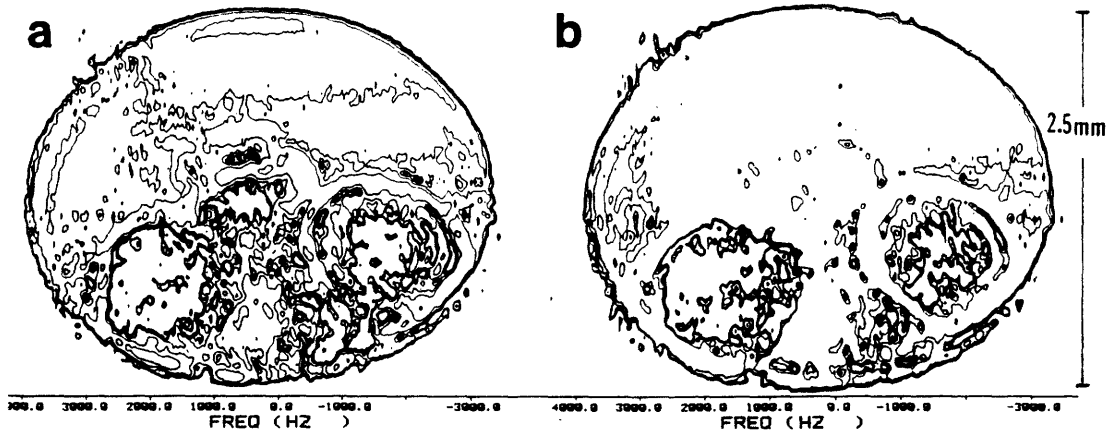

Figure 5.8

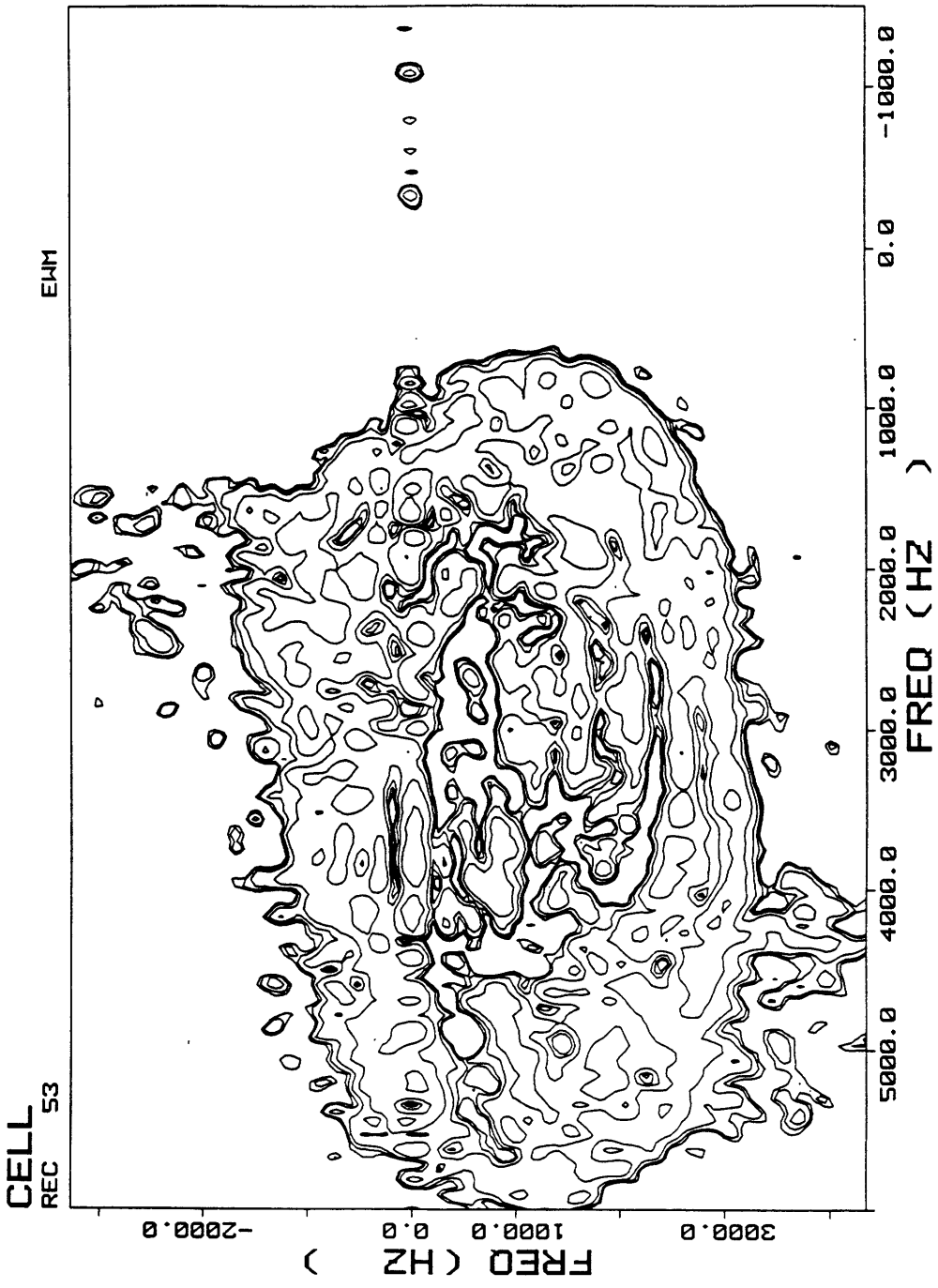
CELL
REC 53
EWM
FREQ (HZ)
-2000.0
0.0
1000.0
3000.0
-1000.0
0.0
1000.0
2000.0
3000.0
4000.0
5000.0
FREQ (HZ)

Figure 5.9

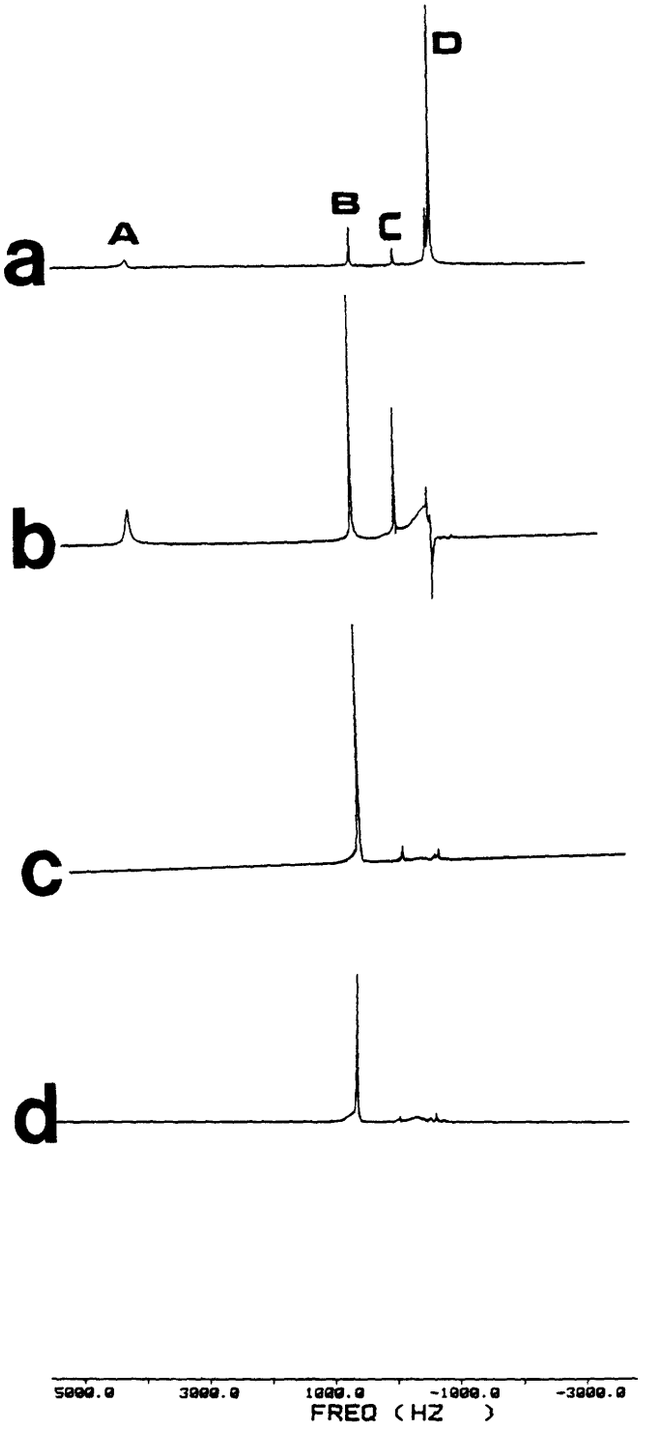

Figure 5.10

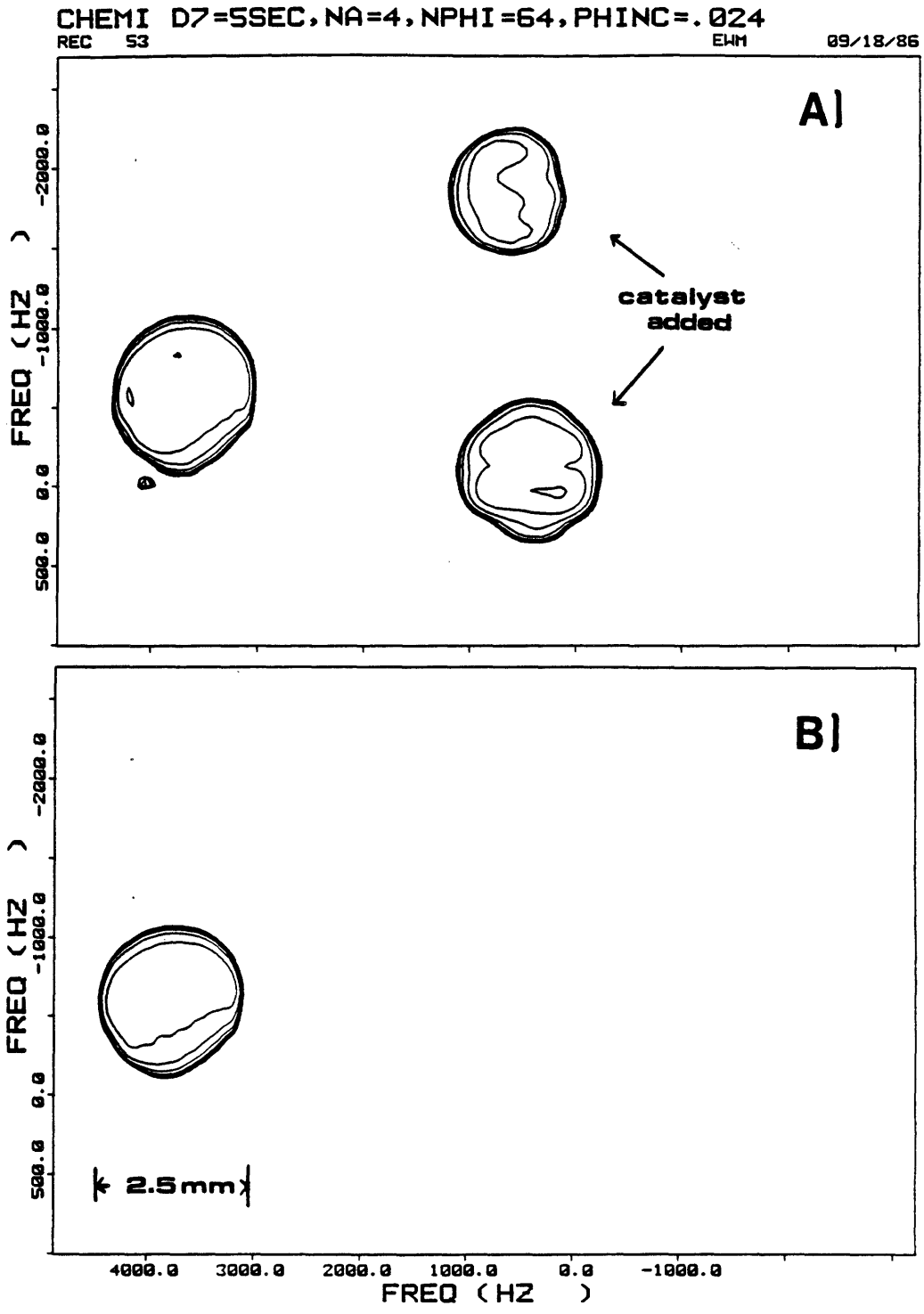
CHEMI D7=5SEC,NA=4,NPHI=64,PHINC=.024
REC 53
EWM
09/18/86
A)
catalyst added
FREQ (HZ)
-2000.0
-1000.0
0.0
500.0
B)
2.5mm
4000.0
3000.0
2000.0
1000.0
0.0
-1000.0
FREQ (HZ)

Figure 5.11

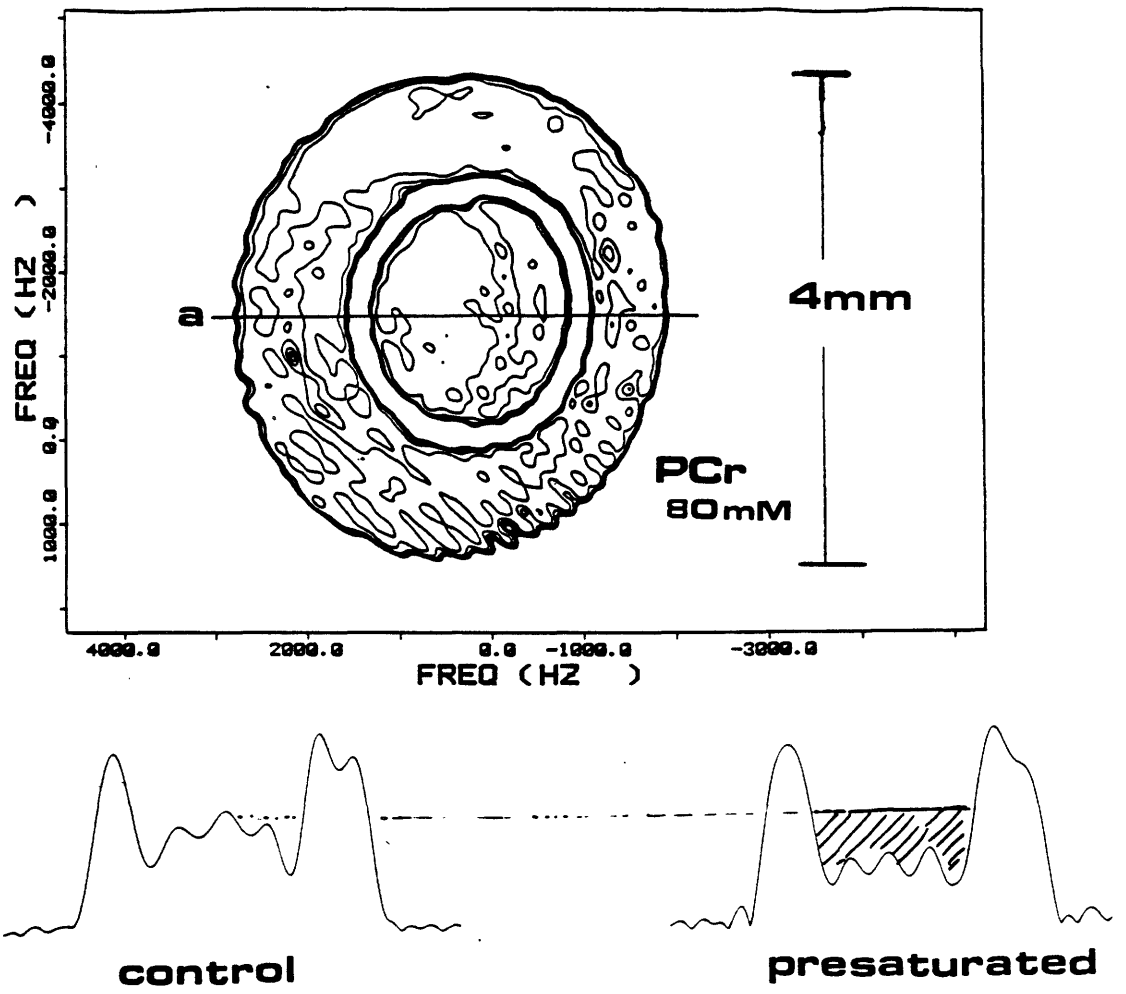
FREQ (HZ)
-4000.0
-2000.0
0.0
2000.0
a
4mm
PCr
80mM
4000.0
2000.0
0.0
-1000.0
-3000.0
FREQ (HZ)
control
presaturated

Figure 5.12

References

1) Ackerman, J.J.H., T.H. Grove, G.G. Wong, D.G. Gadian, and G.K. Radda. 1980, Mapping of metabolites in whole animals by 31P-NMR using surface coils. Nature 283:167-170.

2) Ackerman,J.J.H., Bore,P.J.,Gadian,D.G.,Grove,T.H., and Radda,G.K. 1980. NMR studies of metabolism in perfused organs. Phil.Trans.R.Soc.Lond.B 289, 425-436.

3) Aguayo, J.B., S.J.Blackband, J.Schoeniger, M.A.Mattingly, and M.Hintermann Nuclear magnetic resonance imaging of a single cell. Nature 322: 190-191, 1986.

4) Alger J.R. and Prestegard, J.H. 1977. Investigation of peptide bond isomerization by magnetization transfer NMR. J.Magn.Reson. 27:137-141.

5) Alger J.R. and Shulman R.G. 1984. NMR studies of enzymatic rates in vitro and in vivo by magnetization transfer. Quart. Rev. Biophys. 17:83-124.

6) Altman P.L. and Katz D.D. 1976. Cell Biology. Biological Handbooks, Fed. of Am. Soc. for Exp.Biol.

7) Barany M.,and Glonek T. 1984. Identification of diseased states by phosphorus-31 NMR. In Phosphorus-31 NMR (Gorenstein D.G. ed.). Academic Press.

8) Barman T.E. 1969. Enzyme Handbook. Springer-Verlag, New York.

9) Baskin, R.J., and Deamer, D.W. 1970. A membrane-bound creatine phosphokinase in fragmented sarcoplasmic reticulum, J.Biol.Chem.245:1345-1347.

10) Bax A. and Lerner L. 1986. Two-dimensional nuclear magnetic resonance spectroscopy. Science 232:960-967.

11) Becker E.D., Ferretti J.A., and Gambhir P.N. 1979. Selection of optimum parameters for pulse Fourier transform nuclear magnetic resonance. Anal.Chem. 51:1413-1420.

12) Bessman, S.P. and Geiger P.J. 1981. Transport of energy in muscle:the phosphocreatine shuttle. Science 211:448-452.

13) Bittl, J.A., and Ingwall J.S. 1985. Reaction rates of creatine kinase and ATP synthesis in the isolated rat heart. J.Biol.Chem. 260:3512-3517.

14) Bittl, J.A., Balschi J.A., and Ingwall J.S. 1986. Physiologic control of the creatine kinase reaction in the heart of living rat: effects of nor- epinephrine, halothane and hypoxemia. in Abstracts Soc. Magn. Reson. Medicine. 289-290.

15) Bloch, F. 1946. Nuclear Induction. Phys. Rev. 70,460-474.

16) Bloch, F., Hansen,W.W.,and Packard,M. 1946. Nuclear induction experiment. Phys.Rev. 70,474-485.

17) Bloembergen N.,Purcell E.M., and Pound R.V. 1948. Relaxation effects in

nuclear magnetic resonance absorption. Phys.Rev. 73:679-712.

18) Bockman E.L., McKenzie J.E., and Ferguson J.L. 1980. Resting blood flow and oxygen consumption in soleus a

nd gracilis muscles of cats. Am. J. Physiol. 239(Heart Circ.Physiol. 8):H516-H524.

19) Boyd J., Brindle K.M., Campbell I.D., and Radda G.K. 1984. A comparison of one-dimensional and two-dimensional NMR methods for measuring enzyme-catalyzed exchange. J. Magn. Reson. 60:149-155.

20) Briggs R.W., Radda G.K. and Thulborn K.R. 1985. 31-P NMR saturation transfer study of the in vivo kinetics of arginine kinase in carcinus crab leg muscle. Bioch. Biophys.Acta. 845:343-348.

21) Brown TR, Ogawa S. 31P nuclear magnetic resonance kinetic measurements on adenylate measurements. Proc Natl Acad Sci USA. 1977; 74:3627-31.

22) Burt, C.T., T. Glonek, AND M. Barany. 1977. Analysis of living tissue by phosphorus-31 magnetic resonance. Science 195: 145-149.

23) Campbell I.D. ,C.M. Dobson, R.G. Ratcliffe, and R.J.P. Williams, "Fourier Transform NMR Pulse Methods for the Measurement of Slow- Exchange Rates", J.Magn.Resonance 29,397-417(1978)

24) Chance, B. 1965. Reaction of oxygen with the respiratory chain in cells and tissues. J.Gen. Physiol. 49,Suppl:163-188

25) Chance, B., Eleff S., Leigh J.S., Sokolow D., and Sapega A. 1981. Mitochondrial regulation of phosphocreatine/inorganic phosphate ratios in exercising human muscle: A gated 31P NMR study. Proc. Natl. Acad. Sci. USA 78: 6714-6718.

26) Chance B., Leigh J.S., Kent J., McCully K., Nioka S., Clark B.J., Maris J.M., and Graham T. 1986. Multiple controls of oxidative metabolism in living tissues as studied by phosphorus magnetic resonance. Proc. Natl. Acad. Sc. 83:9458-9462.

27) Chance, B., and Williams C.R. 1956. The respiratory chain and oxidative phosphorylation. Adv.Enzymol.Relat.Areas Mol.Biol.17:65-134.

28) Cohen S.M., and Burt C.T. 1977. 31-P nuclear magnetic relaxation studies of phosphocreatine in intact muscle:determination of intracellular free magnesium. Proc.Natl.Acad.Sci.USA 74:4271-4275.

29) Cooke R. and Pate E. 1985. The effects of ADP and phosphate on the contraction of muscle fibers. Biophys. J. 48:789-798.

30) Dahlquist F.W., Longmuir K.J., and DuVemet R.B. 1975. Direct observation of chemical exchange by a selective pulse NMR technique. J.Magn.Reson. 17:406-410.

31) Dickinson R.J.,Hall A.S.,Hind A.J., and Young I.R. 1986. Measurement of changes in tissue temperature using MR imaging. J.Comp.Ass.Tomog. 10(3):468-472.

32) Draper N.R. and Smith H. 1966. Applied Regression Analysis Wiley Press.

33) Eccles, C.D. and P.T. Callaghan. 1986. High-Resolution Imaging. The NMR Microscope. J.Magn.Reson. 68: 393-398.

34) Edsall J.T. 1969. Carbon dioxide, carbonic acid, and bicarbonate ion: Physical properties and kinetics of interconversion. NASA SP-188.

35) Eigen M., Kustin K., and Maass G., 1961. Die Geschwindigkeit der hydration von SO_2 in waBringer losung. Zeit. Physik. Chemie. 30:130-136.

36) Evelhoch J.L. and Ackerman J.J.H. 1983. NMR T1 measurements in inhomogeneous B1 with surface coils. J.Magn.Reson. 53:52-64.

37) Fiske, C.H. and Subbarow Y. 1927. The nature of inorganic phosphate in voluntary muscle. Science 65:401-403.

38) Ford W.T., Periyasamy M., Spivey H.D., and Chandler J.P. 1985. Magnetization-transfer NMR determination of rates of exchange of solvent in and out of gel polymer beads. J.Magn.Reson. 63:298-305.

39) Forsen S. and Hoffman R.A. 1964. Exchange Rates by Nuclear Magnetic Multiple Resonance. III. exchange reactions in systems with several nonequivalent sites. J.Chem.Phys 40:1189-1196.

40) Forsen S. and Hoffman R.A. 1963. Study of moderately rapid chemical exchange reactions by means of nuclear magnetic double resonance. J.Chem.Phys 39,2892-2901.

41) Fossel E.T., Morgan H.E., and Ingwall J.S. 1980. Measurement of chnages in

high-energy phosphates in the cardiac cycle by using gated 31-P nuclear magnetic resonance. PNAS 77:3654-3658.

42) Freeman R.,and Hill H.D.W. 1971. Fourier transform study of NMR spin-lattice relaxation by progressive saturation. J.Chem.Phys. 54:3367-3377.

43) Gadian D.G., Radda G.K., Brown T.R., Chance E.M., Dawson M.J., and Wilkie D.R. 1981. The activity of creatine kinase in frog skeletal muscle studied by saturation-transfer nuclear magnetic resonance. Biochem.J. 194:215-228.

44) Garlick, P.B. and Turner, C.J. 1986. Investigation of creatine kinase kinetics in the isolated heart by phosphorus two-dimensional NMR. Abstract 1986 Society of Magnetic Resonance in Medicine Meeting. pg127.

45) Gesmar H., and Led J.J. 1986. Optimizing the multisite magnetization- transfer experiment. J.Magn.Reson. 68:95-101.

46) Gorter C.J., and Broer L.J.F. 1942. Negative result of an attempt to observe nuclear magnetic resonance in solids. Physica 9:591-596.

47) Granot J., Elgavish G.A., and Cohen J.S., 1979. Phosphorus-31 relaxation times of inorganic phosphate and nucleotides in aqueous solution. J.Magn.Reson. 33:569-575.

48) Grinvald A. and Steinberg I. 1974. On the analysis of fluorescence decay kinetics with the method of least squares. Anal. Bioch. 59:583-598.

49) Groen A.K., Wanders J.J.A., Westerhoff H.V., van der Meer R., and Tager

J.M. 1982. Quantification of the contribution of various steps to the control of mitochondrial respiration. J.Biol.Chem. 257:2754-2757.

50) Gutowsky H.S., Saika A. 1953. Dissociation, chemical exchange, and the proton magnetic resonance in some aqueous electrolytes. J.Chem.Phys. 21,1688-1694.

51) Gutowsky H.S., McCall D.W., Slichter C.P. 1953. Nuclear magnetic resonace multiplets in liquids. J.Chem.Phys. 21,279.

52) Gutowsky H.S., Jonas J. and Siddall T.H. 1967. Comparison of chemical exchange rates determined by nuclear magnetic resonance line shape and equilibrium methods. Internal rotation of N-methyl-N-benzylformamide. J.Am.Chem.Soc. 89:4300-4304.

53) Hall, L.D., S.Luck, and V.Rajanayagam. 1986. Construction of a high-resolution NMR probe for imaging with submillimeter spatial resolution. J.Magn.Reson. 66:349-351.

54) Harned H.S., and Davis, R. 1943. J. Am. Chem. Soc. 65: 2030-2037.

55) Hinshaw, W.S. 1976. Image formation by nuclear magnetic resonance: The sensitive-point method. J.Appl.Physics. 47: 3709-3721.

56) Hebisch, S.,Soboll S., Schwenen M.,and Sies H. 1984. Compartmentation of high-energy phosphates in resting and working rat skeletal muscle. Biochim.et. Biophys.Acta 764:117-124.

57) Hore P.J. 1983. A new method for water suppression in the proton nmr spectra

of aqueous solutions. J. Magn. Reson. 54:539-542.

58) Hoult, D.I., Busby, J.W., Gadian, D.G., Radda G.K., Richards, R.E., and Seeley, P.J. 1974. Observation of tissue metabolites using 31P nuclear magnetic resonance. Nature (London) 252, 285.

59) Hoult D.E. and Richards R.E., 1976. The signal-to-noise ratio of the nuclear magnetic resonance experiment. J.Magn.Reson. 24, 71-85.

60) Hoult D.E. and Lauterbur P.C., 1979. The sensitivity of the zeugmatographic experiment involving human samples. J.Magn.Reson. 34,425-433.

61) Jackson J.D. 1978ed. Classical electrodynamics. Wiley and Sons.

62) Jacobs, M.,Heldt, H.W., and Klingenberg, M. 1964. High activity of CK in mitochondria from muscle and brain. Evidence for a separate mitochondrial isoenzyme of CK, Biochem. Biophys.Res. Commum. 16:516-521.

63) Jacobus W.E. 1985. Respiratory control and the integration of heart high-energy phosphate metabolism by mitochondrial creatine kinase. Ann. Rev. Physiol. 1985. 47:707-725.

64) Jaeschke A., Muensch H., Schmid H.G., Friebolin H., and Mannschreck A., 1969. The conformation of a nitrosamine and a carboxamide: comparison of NMR line shape and equilibration methods. J.Mol.Spec. 31,14-31.

65) Johnson, G.A., Thompson M.B., Gewalt S.L., and Hayes C.E. 1986. Nuclear Magnetic Resonance Imaging at Microscopic Resolution. J.Magn.Reson. 68:129-137.

66) Jones D.E. 1972. Fourier transform NMR III. spin-lattice relaxation times. J.Magn.Reson. 6:191-196.

67) Jones, D.P. 1986. Intracellular diffusion gradients of O2 and ATP. Am.J.Physiol. 250(cell physiol. 19): C663-C675.

68) Kayar S.R., Conley K.E., Claasen H., and Hoppler H. 1986. Capillarity and mitochondrial distribution in rat myocardium following exercise training. J.Exp.Biol. 120:189-199.

69) Kayar S.R., Claasen H., Hoppler H., and Weibel E.R. 1986. Mitochondrial density relationship to changes in muscle metabolism in rat soleus. Respir. Physiol. 64:1-11.

70) Katz L.A., Koretsky A.P., and Balaban R.S. 1986. The effects of increased work on high energy phosphates and NADH levels in the perfused heart: A 31P NMR and fluor escence study. Abstract pg 291, Soc. Mag. Reson. in Med. Montreal Meeting.

71) Khalifah R.G. 1971. The carbon dioxide hydration activity of carbonic anhydrase. J.Biol.Chem. 216:2561-2573.

72) King K.F. 1983. Signal-to-noise ratios in nuclear magnetic resonance. Ph.D. thesis, Univ. of Wisconsin.

73) Krisanda J.M., McFarland E.W., Moerland T.S. and Kushmerick M.J. 1986. The use of one-dimensional inversion recovery spectroscopy and two- dimensional

NOESY to study the creatine kinase reaction in smooth muscle. SMRM Montreal meeting Page 337.

74) Kuhn W., Offermann W., and Leibfritz D. 1986. Influence of off-resonance irradiation upon T1 in in vivo saturation transfer. J. Magn. Reson. 68:193-197.

75) Kushmerick M.J., Dillion P.F., Meyer R.A., Brown T.R., Krisanda J.M., and Sweeney H.L. 1986. 31-P NMR spectroscopy, chemical analysis and free Mg of rabbit bladder and uterine smooth muscle. J.Biol.Chem. 261:14420-14429.

76) Kushmerick M.J. 1985. Patterns in mammalian muscle energetics. J.Exp. Biol. 115:165-177.

77) Kushmerick M.J., Meyer R.A., and Brown T.R. 1983. Phosphorus NMR spectroscopy of cat biceps and soleus muscles. in Oxygen transport to tissue-IV (Bicher H.I. and Bruley D.F. ed) Plenum Corp.

78) Lauterbur, P.C. 1974. Magnetic resonance zeugmatography. Pure Appl. Chem. 40: 149-157.

79) Lai, C.M. 1982. Reconstructing NMR images under magnetic fields with large inhomogeneities. J. Phys.E. Sci. Instru. 15:1093-1100.

80) Lawson R.W., Veech R.L. 1979. Effects of pH and free Mg on the Keq of the creatine kinase reaction and other phosphate hydrolyses and phosphate transfer reactions. J.Biol.Chem. 254:6528-6537.

81) Led J.J.,and Gesmar H. 1982. The applicability of the magnetization- transfer

NMR technique to determine chemical exchange rates in extreme cases. J.Magn.Reson. 49,444-463.

82) Lowry, O.H., Passonneau J.V., Hesselberger F.X. and Schulz D.W. 1964. Effects of ischemia on known substrates and cofactors of the glycolytic pathway in brain. J.Biol. Chem. 239:18-30.

83) Lundsgaard, E. 1950. The ATP control of resting and active muscle. Proc. R. Soc. London. Ser.B. 137:73-76.

84) Mabuchi K., Szvetko D., Pinter K. and Sreter F.A. 1982. Type IIB to IIA fiber transformation in intermittently stimulated rabbit muscles Am. J. Physiol. 242 (Cell physiol. 11):C373-C381.

85) Mannschreck A., Mattheus A., and Rissmann G. 1967. Comparison of kinetic results obtained by NMR line shapes and equilibration methods. J.Mol. Spec. 23,15-31.

86) Marquardt D.W., 1963. An algorithm for least-squares estimation of non-linear parameters. J.Soc. Ind. App. Math. 11:431-441.

87) Matson G.B., Schleich T., Serdahl C., Acosta G., and Willis J.A. 1984. Measurement of longitudinal relaxation times using surface coils. J.Magn.Reson. 56:200-206.

88) Matthews, P.M., Bland, J.L., and Radda G.K. 1983. The temperature dependence of creatine kinase fluxes in the rat heart. Bioch. Biophys.Acta. 763:140-146.

89) Matthews, P.M., Bland, J.L., Gadian, D.G., and Radda, G.K. 1982. A 31-P NMR saturation transfer study of the regulation of creatine kinase in the rat heart. Biochim.Biophys.Acta 721:312-320.

90) McConnell H.M. 1958. Reaction rates by nuclear magnetic resonance. J.Chem.Phys. 28,3.

91) McConnell H.M. and Thompson D.D., 1957. Molecular transfer of nonequilibrium nuclear spin magnetization. J.Chem.Phys 26,958.

92) McGilvery R.W. and Murray T.W. 1974. Calculated equilibria of phosphocreatine and adenosine phosphates during utiization of high energy phosphate by muscle. J. Biol. Chem. 249:5845-5850.

93) Meyer R.A., Kushmerick M.J., and Brown T.R. 1982. Application of 31-P NMR spectroscopy to the study of striated muscle metabolism. Am.J.Physiol. 242 (Cell Physiol. 11):C1-C11.

94) Meyer R.A., Brown T.R., and Kushmerick M.J. 1985. Phosphorus nuclear magnetic resonance of fast- and slow-twitch muscle. Am. J. Phsiol. 248 (Cell Physiol. 17):C279-287.

95) Meyer R.A., Brown T.R., Krilowicz B.L. and Kushmerick M.J. 1986. Phosphagen and intracellular pH changes during contraction of creatine-depleted rat muscle. Am. J. Physiol. 250 (cell physiol. 19) C264-C274.

96) Meyer R.A., Sweeney L.H., and Kushmerick M.J. 1984. A simple analysis of the

"phosphocreatine shuttle". Am.J.Phsiol. 246 (Cell Physiol. 15):C365- C377.

97) Miceli,M.V., Hoerter, J.A. and Jacobus, W.E. 1983. Evidence supporting the phosphocreatine-ATP energy transport shuttle in perfused rabbit hearts: a 31-P NMR saturation transfer study. Circulation 68:III-65.

98) Miller D.S.,and Horowitz S.B. 1986. Intracellular compartmentation of adenosine triphosphate. J.Biol.Chem. 261:13911-13915.

99) Moon RB, Richards JH. Determination of intracellular pH by 31P nuclear magnetic resonance. J Biol Chem. 1973; 248:7276-78.

100) Murphy-Boesch J., and Koretsky A.P. 1983. An in vivo NMR probe circuit for improved sensitivity. J.Magn.Reson. 54:526-532.

101) Newsholme, E.A. and Start C. 1973. Regulation in Metabolism. Wiley and Sons Ltd.

102) Noggle J.H. and Schirmer R.E. 1971. The nuclear Overhauser effect: chemical applications. Academic Press.

103) Nunnally R.L., and Hollis D.P. 1979. Adenosine Triphosphate Compartments in living heart: A phosphorus nuclear magnetic resonance saturation transfer study. Biochemistry. 18:3642-3646.

104) Perrin C.L., Johnston E.R. 1979. Saturation-transfer studies of three-site exchange kinetics. J.Magn. Reson. 33:619-626.

105) Perry S., Vander L, McAuliffe J., and Ingwall J. 1986. Myocardial ATP synthesis rates as measured by NMR and oxygen consumption. Abs. Soc. Magn. Reson. Med., Montreal, Pg 139.

106) Petrofsky J.S., and Fitch C.D. 1980. Contractile characteristics of skeletal muscles depleted of phosphocreatine. Pflugers Arch. 384:123-129.

107) Prato F.S., Drost D.J., Keys T., Laxon P., Comissiong B., and Sestini E. 1986. Optimization of signal-to-noise ratio in calculated T1 images derived from two spin-echo images. 3:63-75.

108) Purcell, E.M., Torrey, H.C., and Pound, R.V. 1946. Resonance absorption by nuclear magnetic moments in a solid. Phys.Rev. 69,37.

109) Radda, G.K., AND P.J. Seeley. 1979. Recent studies on cellular metabolism by nuclear magnetic resonance. Annu. Rev. Physiol. 41: 749-769.

110) Redfield A.G., 1955. Nuclear magnetic resonance saturation and rotary saturation in solids. Phys.Rev. 98:1787-1809.

111) Regen D.M., Davis W.W., Morgan H.E., and Park C.R. 1964. The regulation of hexokinase and phosphofructokinase activity in heart muscle. J. Biol. Chem. 239:43-49.

112) Roberts D.V. 1977. Enzyme Kinetics. Cambridge University Press

113) Robinson G., Kuchel P.W. and Chapman B.E. 1985. A simple procedure for selective inversion of NMR resonances for spin transfer kinetic measurements.

J.Magn.Reson. 63:314-319.

114) Rosen B.R., Pykett I.L., and Brady T.J. 1984. Spin lattice relaxation time measurement in two-dimensional nuclear magnetic resonance imaging: corrections for plane selection and pulse sequence. J.Comp. Ass. Tomogr. 8:195.

115) Sanyal G. and Maren T.H. 1981. Thermodynamics of carbonic anhydrase catalysis. J.Biol.Chem. 256:608-612.

116) Schotland J., and Leigh J.S. 1983. Exact solutions of the Bloch Equations with n-site chemical exchange. J.Magn.Reson. 51:48-55.

117) Shoubridge E.A., Bland, J.L., and Radda G.K. 1984. Regulation of creatine kinase during steady-state isometric twitch contraction in rat skeletal muscle. Bioch. Biophys.Acta. 805:72-78.

118) Smith M.B., Briggs R.W., Shoubridge E.A., Hayes D.J., and Radda G.K. 1985. A comparison of in vivo catalysis by creatine kinase in avian skeletal muscles with different fibre composition. Bioch. Biophys. Acta. 846:174-178.

119) Turner, D.C., Wallimann, T., and Eppenberger, H.M. 1973. A protein that that binds specifically to the M-line of skeletal muscle is identified as the muscle form of creatine kinase. Proc.Natl.Acad.Sci. USA 70:702-705.

120) Ugurbil K., Petein M., Maidan R., Michurski S., and From A.H.L. 1986. Measurement of an individual rate constant in the presence of multiple exchanges: application to myocardial creatine kinase reaction. Biochem. 25: 100-107.

121) Ugurbil K. 1985. Magnetization-transfer measurements of individual rate constants in the presence of multiple reactions. J.Magn.Reson.64:207-219.

122) Wallimann T., and Eppenberger H.M. 1985. Localization and function of M-line bound creatine kinase:M-band model and creatine phosphate shuttle. In Cell and muscle motility, vol.6. (Shay J.W. ed) Plenum corp.

123) Wallimann, T. 1975. Creatinekinase-Isoenzyme and myofibrillen-struktur, Ph.D. thesis no 5437, Abstract in English, Eidgenossische Technische Hochschule,Zurick,Switzerland.

124) Watts, D.C. 1973. Creatine kinase. in The Enzymes, Vol.8 (Boyer, P.D. ed.), Academic Press, New York.

125) International Telephone and Telegraph. 1983. Reference data for radio engineers. Howard and Sons Co.

```
C-----------------------------------------------------------------------
C                       APPENDIX  A
C-----------------------------------------------------------------------
C
C
C       PROGRAM MAGTRANS.FOR    2/2/85 REVISED 10/26/85
c
C       THIS PROGRAM WILL       1) CALCULATE EXACT SOL. OF MOD. BLOCK EQS
C                               2) ADD NOISE
C                               3) WRITE THE X,Y PAIRS TO ASCAII FILES
C                               4) CALCULATE INITIAL SLOPES AND ERRORS
C
C
C
C
C
        REAL*4 YA(128),YB(128),YACF(128),XACF(128),ERRA(128),ERRB(128)
        REAL*4 KA,kb,kla,klb,x(128),Y(4,128)
        REAL*4 C(128),RNSE(128)

        TYPE*,'                                         '
        TYPE*,'Ya(inf)=Mag of species A at infinity     '
        TYPE*,'Ya(0)= Mag after pulse (eg after inversion=-1'
        TYPE*,' R=1/T1      K=unidirectional rate constant'
        TYPE*,' similiar for species b '
        TYPE*,'                                         '

        type*,'enter Ya(inf),Ya(0),ka(sec-1),Ra(1/T1sec),kb,Rb '
        accept*,YAi,yao,ka,ra,kb,rb
        ybio=yai*ka/kb
        TYPE*,'                                         '
        type*,' assuming equilibrium I calculate Yb(inf)=',ybio
        Type*,' if this is correct type 0 otherwise enter correct'
        type*,' value, there better be a reason it is not right!'
        accept*,ybi
        TYPE*,'                                         '
        type*,'enter initial value of Yb,  '
        TYPE*,' this will be the same as Yb(inf) generally for selective'
        TYPE*,'pulse on A                                       '
        accept*,ybo
        if(ybi.eq.0)ybi=ybio

c
c
c
c       Calculate Constants See Paper by Led, or Campbell Dobson
c
c       del1=standard text lamda1*-1. del2=std lamda2*-1
c

        alpha=(kb/ka)/(yai/ybi)         !this should be =1. for most apps.
        kla=ra+ka
        klb=rb+kb
        arg= 4.0*ka*kb+(kla - klb)**2
        del1= .5*(-1.* SQRT(ARG)+(kla+klb))
        del2= .5*(1.*sqrt(arg)+(kla+klb))
        c1=((kla-del2)*(yai-yao)-kb*(ybi-ybo)/alpha)/(del2-del1)
        c2=(-1.*(kla-del1)*(yai-yao)+kb*(ybi-ybo)/alpha)/(del2-del1)
        c3=alpha*(-ka*(yai-yao)-(kla-del1)*(ybi-ybo)/alpha)/(del2-del1)
        c4=alpha*(ka*(yai-yao)+(kla-del2)*(ybi-ybo)/alpha)/(del2-del1)

c
c
        type*,' my lambda is a positive value =-1*others  lambda1  =',del1
```

```
      type*,'                          '
      type*,' lambda2  =',del2
      type*,'                          '
      type*,' C1 =',c1
      type*,'                          '
      type*,' C2 =',c2
      type*,'                          '
      type*,' C3 =',c3
      type*,'                          '
      type*,' C4 =',c4
      type*,'                          '


c
c
      type*,' number of points to plot(max 128) and time(sec) of last point'
      type*,'      as n,t '
      accept*,np,tmax
63    type*,' Gaussian noise will be generated  noise(p-p)=5*noise(rms)'
      type*,' enter p-pNoise/Signal based on  Ya(inf)  0 for ideal'
      accept*,xNSR
      type*,' enter random number seed near 10235 '
      accept*,int
c     iNT=10235 !Random number seed for noise
      t=0.0
      f=(1.-2.*exp(-tmax*ra))
      sela=ka+ra

      do 100 i=1,np
      rtwq=float(2*np)
c     tinc= -alog(1.-(1.+f)*exp(t*ra)/(rtwq))/ra !for ideal point spacing
      tinc= tmax*2/rtwq
      ta=-1.*t*del1
      tb=-1.*t*del2
      tsel=exp(-t*sela)

C     GENERATE PSUEDO GAUSSIAN ADD 12 RAN'S SUBTRACT 6
c     Will give numbers between -6 and 6 mean=0
c     gives distribution with sd=1
      ynoise=0.
      do 90 jx=1,12
      ynoise=ran(int)+ynoise
 90   continue
      ynoise=ynoise- 6.0
      ynoise=ynoise/6.0   !to normalize peak to -1 to +1
      RNOISE=xnsr*yai*ynoise !peak to peak noise is XNSR*yai


      ya(i)=yai+c1*exp(ta)+c2*exp(tb)+rnoise
      Y(1,i)=ya(i)
      yb(i)=ybi+c3*exp(ta)+c4*exp(tb)+rnoise
      y(2,i)=yb(i)

c     two selsat cases

      y(3,i) = yai*(ka*tsel+ra)/sela + rnoise
      y(4,i) = yai*(1-2*tsel) + rnoise        'assume ideal flip
      x(i)=t
      RNSE(I)=RNOISE
      t=t+tinc
100   continue

      type*,' Choose  1) Screen display'
      type*,'         2) output file  graph.t'
      type*,'         3) Both '
```

```
        accept*,iq
        if((iq.eq.1).or.(iq.eq.3))Call VTDIS(x,y,2,np)
        if((iq.eq.2).or.(iq.eq.3))call rslnout(x,y,4,np)

        TYPE*,'do you want noise in graph.t ?, y=1,n=0'
        accept*,iyn
        if(iyn.eq.1)call rslout(x,RNSE,RNSE,np)
        type*,'another snr for same data? y=1'
        accept*,iyn
        if(iyn.eq.1)go to 63
ccccccccccccccccccccccccccccccccccccccccccccccccccccccccccccccccccccccccccc
c
102     type*,'to check autocorrelation function rename graph.t file'
        type*,'containing data x, y to autocor.t then $Run Autocor '

ccccccccccccccccccccccccccccccccccccccccccccccccccccccccccccccccccccccccccc
c       initial slope
c
c       initial slope errors
c
        type*,'                                                    '
        type*,' if you do not want initial slope errors type 0'
        accept*,io
        if(io.eq.0)go to 600



200     type*,'enter t1 and t2 from which to calculate initial slope'
        accept*,ts1,ts2
c
        s1=c1*exp(-1.*del1*ts1)+c2*exp(-1*del2*ts1)
        s1=(s1-c1*exp(-1.*del1*ts2)-c2*exp(-1*del2*ts2))/(ts1-ts2)
        s2=c3*exp(-1.*del1*ts1)+c4*exp(-1*del2*ts1)
        s2=(s2-c3*exp(-1.*del1*ts2)-c4*exp(-1*del2*ts2))/(ts1-ts2)
        wqt=yai-yao
        type*,' delta y=yai-ya0   =',wqt
        xkr=s1/wqt
        xyr=-s2/wqt
        type*,'initial slope of selected species=',s1,'k+R=',xkr
        type*,'initial slope of non-selected species=',s2,'k=',xyr
        calR=xkr-xyr
        type*,'calculated R=1/T1 is=',calR
        type*,'actual k=',ka,'     actual R=1/t1  =',ra
        routo=(ka-xyr)/ka
        type*,'fractional error=(K-kexp)/K=',routo
        routo=(ka+ra-xkr)/(ka+ra)
        type*,'fractional error=(kla-klaexp)/kla= ',routo
c       Apply correction obtained from experimental k,t1

        type*,'                    '
        type*,' apply correction using experimental k,T1'
        routo=Ea(ts1,ts2,calr,xyr)
        rkfix=xyr/(1.-routo)
        type*,'ea=',routo,'   recalculated ka=',rkfix
        routo=E1a(ts1,ts2,calr,xyr)
        rk1fix=xkr/(1.-routo)
        type*,'e1a=',routo,'   recalculated kla=',rk1fix
c
        routo=(ka-rkfix)/ka
        type*,'fractional error=(K-kexp)/K=',routo
        routo=(ka+ra-rk1fix)/(ka+ra)
        type*,'fractional error=(kla-klaexp)/kla= ',routo

        type*,'                    '
        type*,' second iteration'
```

```
      c2r=rk1fix-rkfix
      routo=Ea(ts1,ts2,c2r,rkfix)
      rkfix=xyr/(1.-routo)
      type*,'ea=',routo,'   recalculated ka=',rkfix
      routo=Ela(ts1,ts2,c2r,rkfix)
      rk1fix=xkr/(1.-routo)
      type*,'ela=',routo,'   recalculated kla=',rk1fix
c
      perea=ea(ts1,ts2,ra,ka)
      perela=ela(ts1,ts2,ra,ka)
      type*,'ideal ea=',perea,'    ela=',perela
      routo=(ka-rkfix)/ka
      type*,'fractional error=(K-kexp)/K=',routo
      routo=(ka+ra-rk1fix)/(ka+ra)
      type*,'fractional error=(kla-klaexp)/kla=',routo

      type*,'                    '
      type*,' Another go type 1'
      accept*,yans
      if(yans.eq.1)go to 200


      type*,'                    '
      type*,' plot errors '



      type*,' assuming slope is calculated from two early points '
      type*,' enter earliest of the two( in seconds) '
      accept*,t1
      type*,'enter the maximum spacing between t2 and t1 to be plotted (sec)'
      accept*,tmax


      fix=.0000001  ! kludge to keep from blowing up at 0

      tinc=tmax/float(np)

c     error will be plotted versus tau=t2-t1 , the point spacing

      yd=yai-yao




      do 300 j=1,np


      tau=(j-1)*tinc + fix
      t2=tau+t1
      A1=(t2**2-t1**2)/(2.*tau*yd)
      ya1=a1*(c1*del1**2+c2*del2**2)/kla
      yb1=a1*(c3*del1**2+c4*del2**2)/(alpha*ka)

      a2=(t2**3-t1**3)/(6.*tau*yd)
      ya2=a2*(c1*del1**3+c2*del2**3)/kla
      yb2=a2*(c3*del1**3+c4*del2**3)/(alpha*ka)

      a3=(t2**4-t1**4)/(24.*tau*yd)
      ya3=a3*(c1*del1**4+c2*del2**4)/kla
      yb3=a3*(c3*del1**4+c4*del2**4)/(alpha*ka)

      a4=(t2**5-t1**5)/(120.*tau*yd)
      ya4=a4*(c1*del1**5+c2*del2**5)/kla
```

```
      yb4=a4*(c3*del1**5+c4*del2**5)/(alpha*ka)


      ya(j)=1.+ya1-ya2+ya3-ya4        !fractional error  measured/actual
      yb(j)=-1.*(1.-yb1+yb2-yb3+yb4)
      y(1,j)=(1.0-sqrt(ya(j)**2))*100.        !to give percent error
      y(2,j)=(1.0-sqrt(yb(j)**2))*100.
      x(j)=tau
      r1=sqrt(ya1*ya1)
      r2=sqrt(ya2*ya2)
      r3=sqrt(ya3*ya3)
      r4=sqrt(ya4*ya4)
      r5=sqrt(yb1*yb1)
      r6=sqrt(yb2*yb2)
      r7=sqrt(yb3*yb3)
      r8=sqrt(yb4*yb4)
      if((r4.gt.r3).or.(r3.gt.r2).or.(r2.gt.r1))type*,'check convergence'
      if((r8.gt.r7).or.(r7.gt.r6).or.(r6.gt.r5))type*,'check convergence'


300   continue

      type*,' Choose  1) Screen display'
      type*,'         2) output file '
      type*,'         3) Both '
      accept*,iq
      if((iq.eq.1).or.(iq.eq.3))Call VTDIS(x,y,2,np)
      if((iq.eq.2).or.(iq.eq.3))call rslnout(x,y,2,np)

c
c     final error after correction w=(k - Kexp/(1-ea(kexp,k1aexp))/k
c     where kexp=k(1-ea(k,k1a)
      type*,' output file graph.t wiht final errors after correction'

      ts1=t1
      tsmin=1.05*t1

      tinc=(tmax-tsmin)/float(np)

      do 500 ip=1,np
            ts2=tsmin+(ip-1)*tinc

c     calculate what estimated k,k1 would be
            rexk=ea(ts1,ts2,ra,ka)
            rexk1a=ela(ts1,ts2,ra,ka)
            exk=ka*(1.-rexk)        ! k from initial slope
            exk1=(ka+ra)*(1.-rexk1a)        !k1a from initial slope
            exr=exk1-exk    ! r=1/t1 from initial slope
            fea=ea(ts1,ts2,exr,exk)
            fela=ela(ts1,ts2,exr,exk)
            Frerk=(rexk-fea)/(1.-fea)
            frerk1=(rexk1a-fela)/(1.-fela)
            y(1,ip)=frerk
            y(2,ip)=frerk1
            x(ip)=ts2
500   continue
      call rslnout(x,y,2,np)

      do 550 it=1,np
            ts2=tsmin+(it-1)*tinc

c     calculate what estimated k,k1 would be
            rexk=ea(ts1,ts2,ra,ka)
            rexk1a=ela(ts1,ts2,ra,ka)
            exk=ka*(1.-rexk)        ' k from initial slope
```

```
C=======================================================================
C                        APPENDIX B
C-----------------------------------------------------------------------
C
C       Welcome to CALLVOXMAG the NMR exchange reaction simulation
C       Program. To visualize the Magnetizations of two exchanging nuclear
C       Species (MA and MB) after logging into the VAX type $ Run CALLVOXMAG
C       W's are frequencies (in hertz) and H's are field strengths in Gauss.
C       Rate constants and relaxations are in sec-1, and secs. The results
C       are stored in files GRAPH.T. To visualize the plots you can use RS1
C       or crudely look at the output on a VT100 with VTDIS.for.
C
C
        REAL*4 MA(3),MB(3),MO(2),K(2),RA(2),RB(2),W(3)
        REAL*4 X(128),Y(4,128),TA(8),H1a(8)
        integer*4 P(3)

        TYPE*,'ENTER RATIO A TO B (EG. 2)'
        ACCEPT*,AB
        TYPE*,'ENTER GAMMA IN HERTZ/GAUSS (EG 4200)'
        ACCEPT*,GAM
        TYPE*,'ENTER WA AND WB AND SPECTROMETER FREQ IN HERTZ  WA,WB,W'
        TYPE*,'   (EG 4.2E6,4.2005E6,4.2005E6)  TO SAT PEAK B '
        ACCEPT*,W(1),W(2),W(3)
        TYPE*,'ENTER H0 IN GAUSS (EG 1000) FOR ABOVE EG'
        ACCEPT*,HO


10      type*,'enter number of increments where h1 has different values'
        TYPE*,' EG. 2 '

        accept*,P(1)
        do 12 j=1,p(1)
        type*,'enter value of H1(gauss) and length(secs) of increment#',j
        TYPE*,' (EG .1,1  FOR SAT PULSE   0,5 TO WATCH RELAXATION)'
        accept*,H1a(j),TA(j)
12      continue

        P(2)=409600
        TYPE*,'ENTER T1,T2,KAB OF NUC A IN SEC,SEC,1/SEC (EG 1,.01,1)'
        ACCEPT*,RA(1),RA(2),K(1)
        RA(1)=1./RA(1)
        RA(2)=1./RA(2)
        TYPE*,'ENTER T1,T2,KBA OF NUC B IN SEC,SEC,1/SEC (EG 1,.01,2)'
        ACCEPT*,RB(1),RB(2),K(2)
        RB(1)=1./RB(1)
        RB(2)=1./RB(2)

        MO(1)=1.
        MO(2)=1./AB
C
C       ASSUME INITIALLY RELAXED
        MA(1)=0.
        MB(1)=0.
        MA(2)=0.
        MB(2)=0.
        MA(3)=MO(1)
        MB(3)=MO(2)
        BETA=0.
        np=64
        P(3)=np
        CALL VOXMAG(HO,GAM,H1a,BETA,MO,MA,MB,RA,RB,K,W,Ta,P,np,X,Y)
        type*,'another go? yes=1,no=0'
        accept*,ians
        if(ians.eq.1)go to 10
```

```
      STOP
      END

ccccccccccccccccccccccccccccccccccccccccccccccccccccccccccc
      SUBROUTINE VOXMAG(HO,GAM,H1A,BETA,Mo,MA,MB,RA,RB,k,W,ta,P,np,X,Y)
ccccccccccccccccccccccccccccccccccccccccccccccccccccccccccc
c     Eric McFarland  7/6/85
c     This is a rework of KINSIM.FOR to model exchange reactions
c     during arbitrary pulses in arbitrary h1 fields. A modified
c     2nd order R-K method is used to calculate the behavior of the system
c     of coupled equations.
c
c     H0,H1A =Magnitude of static, and RF fields, H1A(i)=h1 during time Ta(i)
C     GAM= GYROMAGNETIC RATIO IN HERTZ/GAUSS
c     BETA= angle H1 makes with x axis in main reference ROTATING frame
c     Mo(2)=equilibrium magnetizations of species A(Mo(1)), B(Mo(2))
c     MA(3)=intial value of A magnetization IN THE ROTATING FRAME.
C             if relaxed=(0,0,Mo(1)),MA(1)=in phase,u vector, MA(2)=v
c           the final value of MA(3) is put in here and returned
c     MB(3)=initial B magnetization.....
c     RA(2),RB(2)= 1/T1 ((1)) and 1/T2 (2) 's of species A and B
c     K(2)= KAB as K(1) and KBA as K(2)
c     W(3)= WA, WB, and, W of excitation pulse, where W is freq in hertz
c           wa and wb are resonance freqs of a and b
c     T(i)= length of ith increment during which h1 is on with value H1A(i)
c     P = parameter array with integers P(1)=ntinc,P(2)=nt,P(3)=np
c     ntinc= number of h1 intervals
c     nt= maximum number of time steps to examine. Program will try
c             to be efficient and start by looking at 64 points
c     np=number of points to plot with rslout
c     freak=precentage change in mag to trigger smaller time step
C     Y= OUTPUT ARRAY
ccccccccccccccccccccccccccccccccccccccccccccccccccccccccccc
c
      real*4 Mo(2),MA(3),xma(3),xmb(3),MB(3),RA(2),RB(2),K(2),W(3)
      REAL*4 X(np),Y(4,NP),H1A(8),TA(8)
      Integer*4 P(3),nsuc(8),ntry(8)

      RPIE=3.14159265
      GAM=GAM*2.*RPIE          !CONVERT TO RADS
      GAMA=W(1)/H0
      GAMB=W(2)/H0
      np=P(3)
      nt=P(2)
      ntinc=P(1)
      np1=np-1
      rnp=float(np-1)
      TIME=0.
      freak=(0.10)**2  !for 10% change
      regtime=0.
C
C
C     Here is where we step through each of the ntinc time divisions
c     where during each H1 remains constant.
C
C


      do 200 jm=1,ntinc

c
c     Set up time increments for jm interval
```

```
c
      ntry(jm)=0
      nsuc(jm)=0      !counters to check efficiency
      t=ta(jm)
      REGTIME=TA(JM)+REGTIME
      h1=h1a(jm)
      pltsc=t/rnp
      stsc=pltsc
      rplot=0
      inp=1
      iacq=0
      tsc=stsc
c
c
c
c
c
C
      do 100, i=1,nt

            dmza=(MO(1)-MA(3))*RA(1)+GAM*H1*MA(2)-K(1)*MA(3)+k(2)*MB(3)
            dmzb=(MO(2)-MB(3))*RB(1)+GAM*H1*MB(2)-K(2)*MB(3)+K(1)*MA(3)
            DMXA=-(W(3)-W(1))*MA(2)-MA(1)*(RA(2)+K(1))+MB(1)*K(2)
            DMXB=-(W(3)-W(2))*MB(2)-MB(1)*(RB(2)+K(2))+MA(1)*K(1)
            DMYA=(W(3)-W(1))*MA(1)-MA(2)*(RA(2)+K(1))+MB(2)*K(2)-GAM*H1*MA(3
            DMYB=(W(3)-W(2))*MB(1)-MB(2)*(RB(2)+K(2))+MA(2)*K(1)-GAM*H1*MB(3

c           check stability

45          xMA(1)=MA(1)+DMXA*TSC
            x1=((xma(1)-ma(1))/mo(1))**2
            xMB(1)=MB(1)+DMXB*TSC
            x2=((xmb(1)-mb(1))/mo(2))**2
            xMA(2)=MA(2)+DMYA*TSC
            x3=((xma(2)-ma(2))/mo(1))**2
            xMB(2)=MB(2)+DMYB*TSC
            x4=((xmb(2)-mb(2))/mo(2))**2
            xMA(3)=MA(3)+DMZA*TSC
            x5=((xma(3)-ma(3))/mo(1))**2
            xMB(3)=MB(3)+DMZB*TSC
            x6=((xmb(3)-mb(3))/mo(2))**2
            ntry(jm)=ntry(jm)+1
      if((x1.gt.freak).or.(x2.gt.freak))go to 60
      if((x3.gt.freak).or.(x4.gt.freak))go to 60
      if((x5.gt.freak).or.(x6.gt.freak))go to 60
            go to 70
60    continue
      tsc=tsc*.1
      go to 45        !UNSTABLE DECREASE TIME INC.

c     finish second part of R-K

70          continue
            nsuc(jm)=nsuc(jm)+1
            xdmza=(MO(1)-xMA(3))*RA(1)+GAM*H1*xMA(2)-K(1)*xMA(3)+k(2)*xMB(3)
            xdmzb=(MO(2)-xMB(3))*RB(1)+GAM*H1*xMB(2)-K(2)*xMB(3)+K(1)*xMA(3)
            xDMXA=-(W(3)-W(1))*xMA(2)-xMA(1)*(RA(2)+K(1))+xMB(1)*K(2)
            xDMXB=-(W(3)-W(2))*xMB(2)-xMB(1)*(RB(2)+K(2))+xMA(1)*K(1)
            xDMYA=(W(3)-W(1))*xMA(1)-xMA(2)*(RA(2)+K(1))+xMB(2)*K(2)
            xdmya=xdmya-GAM*H1*xMA(3)
            xDMYB=(W(3)-W(1))*xMB(1)-xMB(2)*(RB(2)+K(2))+xMA(2)*K(1)
            xdmyb=xdmyb-GAM*H1*xMB(3)
```

```
              qpl=time-rplot*pltsc

              if(qpl.lt.0.)go to 73
              if(inp.gt.np)go to 73
              rplot=rplot+1.
              X(Inp)=TIME
              Y(1,Inp)=MA(3)
              Y(2,Inp)=MB(3)
              Y(3,INP)=MA(1)
              Y(4,INP)=MB(1)
              iacq=inp
              inp=inp+1

c       second order Runga-Kutta Solutions

73            MA(1)=MA(1)+0.5*tsc*(dmxa+xdmxa)
              MB(1)=MB(1)+0.5*tsc*(dmxb+xdmxb)
              MA(2)=MA(2)+0.5*tsc*(dmya+xdmya)
              MB(2)=MB(2)+0.5*tsc*(dmyb+xdmyb)
              MA(3)=MA(3)+0.5*tsc*(dmza+xdmza)
              MB(3)=MB(3)+0.5*tsc*(dmzb+xdmzb)

              TIME=TIME+TSC

              if(time.gt.REGTIME)go to 105
              tsc=stsc

100     CONTINUE

105     CALL RS1NOUT(X,Y,4,iacq)

        DO 106 JK=1,NP  !ZERO DISPLAY MATRICES
        X(JK)=0.
        Y(1,JK)=0.
        Y(2,JK)=0.
        Y(3,JK)=0.
        Y(4,JK)=0.

106     CONTINUE
        type*,'number of attempted time steps=',ntry(jm),'in loop#',jm
        type*,'number of successful time steps=',nsuc(jm)
200     continue
        RETURN
        END



C       AUTHOR:Eric McFarland
c       THIS SUBROUTINE PREPARES POINTS X,Y1,Y2 TO BE PLOTTED BY RS1
C       TO USE 1) GET INTO RS1 AND USE #CALL $READ_FREE OR FREE("FN","TAB")
C              2) HAVE LAYOUT GIVING LENGTH OF VALUES

        SUBROUTINE RS1NOUT(X,Y,L,N)
        DIMENSION X(N),Y(L,N)
        DATA ICHAR/' '/
        OPEN(UNIT=4,NAME='voxmag.T',TYPE='NEW',FORM='FORMATTED')
        DO 10 I=1,N
 105    FORMAT(F12.6,A1,F12.6,A1,F12.6,A1,F12.6,A1,F12.6)
        WRITE(4,105)X(I),ICHAR,Y(1,I),ICHAR,Y(2,I),ICHAR,Y(3,I),ICHAR,Y(4,I)
  10    CONTINUE
        CLOSE(UNIT=4)
        RETURN
        END
```

```
              exkl=(ka+ra)*(1.-rexkla)        !kla from initial slope
              exr=exkl-exk    ! r=l/tl from initial slope
              fea=ea(ts1,ts2,exr,exk)
              fela=ela(ts1,ts2,exr,exk)

              zqa=ka*(1.-fea)
              zql=(ka+ra)*(1.-fela)

              trma=1./(1.-fea)**2
              tbar=ts2/2.+ts1/2.

              trmb=(2.*exkl*tbar-fea)**2
              trmc=(tbar*(2.*exkl+4.*exk)-fea)**2
              frerk=(trma+trma**2*(trmb+trmc))/(tbar-ts1)


              y(1,it)=frerk
              y(2,it)=frerk
              x(it)=ts2


550           CONTINUE
              call rslnout(x,y,2,np)

600           continue
              stop
              end


              Function Ea(qto,qtl,qR,qrK)
              q=qtl/qto
              qzi=qrk/qr
              qb=qto*qR
              qt=.25*qb*(q+1.)*((2.*qzi+1.)**2-1.)/qzi
              Ea=qt-(qb**2/12.)*((q**3-1.)/(q-1.))*(((2.*qzi+1.)**3)-1.)/qzi
              end

              Function Ela(to,tl,R,rK)
              tau=tl/to
              zi=rk/r
              b=to*R
              t=.25*b*(tau+1.)*((2.*zi+1.)**2+1.)/(zi+1.)
              Ela=t-(b**2/12.)*((tau**3-1.)/(tau-1.))*((2.*zi+1.)**3+1.)/(zi+1.)
              end
C-------------------------------------------------------------------------
C
C
C
```

Sample Histogram from a Set of Random Noise